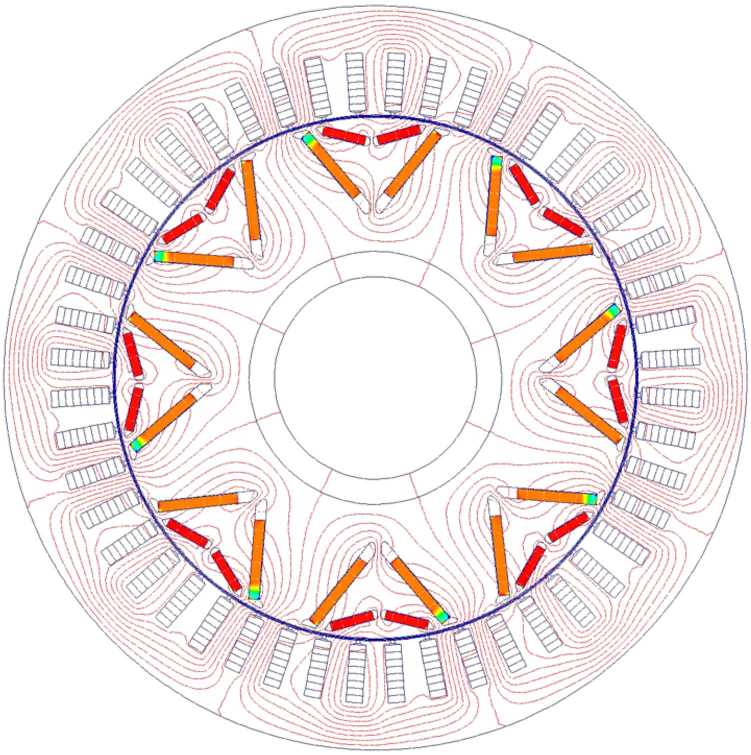

Design and Evaluation of a HRE-Free PMSM Rotor for Heavy-Duty Applications

A Combined Literature and Simulation Approach Considering HRE-Free Rotor Design

Master's thesis in Sustainable Electric Power Engineering and Electromobility

NIKOLA MAKELJA
ALEV YUSEIN

DEPARTMENT OF ELECTRICAL ENGINEERING

CHALMERS UNIVERSITY OF TECHNOLOGY
Gothenburg, Sweden 2026
www.chalmers.se

Master's thesis 2026

Design and Evaluation of a HRE-Free PMSM Rotor for Heavy-Duty Applications

A Combined Literature and Simulation Approach Considering HRE-Free Rotor Design

NIKOLA MAKELJA
ALEV YUSEIN

Department of Electrical Engineering
Division of Electric Power Engineering
Chalmers University of Technology
Gothenburg, Sweden 2026

Design and Evaluation of a HRE-Free PMSM Rotor for Heavy-Duty Applications
A Combined Literature and Simulation Approach Considering HRE-Free Rotor Design
NIKOLA MAKELJA
ALEV YUSEIN

Supervisor: Rasmus Andersson, Volvo Group Trucks Technology
Supervisor: Emil Callerfjord, Volvo Group Trucks Technology
Examiner: Torbjörn Thiringer, Department of Electrical Engineering

Master's Thesis 2026
Department of Electrical Engineering
Division of Electric Power Engineering
Chalmers University of Technology
SE-412 96 Gothenburg
Telephone +46 31 772 1000

Cover: Radial cross section of PMSM with partly demagnetized magnets

Typeset in LaTeX
Printed by Chalmers Reproservice
Gothenburg, Sweden 2026

Design and Evaluation of a HRE-Free PMSM Rotor for Heavy-Duty Applications
A Combined Literature and Simulation Approach Considering HRE-Free Rotor Design
NIKOLA MAKELJA
ALEV YUSEIN
Department of Electrical Engineering
Division of Electric Power Engineering
Chalmers University of Technology

Abstract

Permanent magnet synchronous machines (PMSMs) are widely used in heavy-duty electric powertrains due to their high efficiency and torque density. However, conventional NdFeB rotor magnets often contain heavy rare earth elements (HREs), such as dysprosium and terbium, to improve coercivity and in turn thermal stability. This thesis evaluates the feasibility of removing HREs from NdFeB magnets in a double-layer V-shaped PMSM rotor. The work combines a sustainability analysis of rare earth elements (REEs) with electromagnetic simulations in Ansys Motor-CAD, including magnet screening, demagnetization assessment, custom magnet evaluation, rotor geometry studies, optimization, and benchmarking against the original HRE-based reference design.

The sustainability analysis shows that reducing HRE content can lower material cost, reduce environmental burden, and decrease dependence on critical REEs. However, HRE reduction does not remove all sustainability challenges, since REE supply remains affected by geopolitical concentration, processing capacity, environmental risks, and low recycling rates. The simulation results show that replacing the original HRE-based magnet with available HRE-free magnets in the unchanged rotor geometry is not sufficient to meet both torque and demagnetization requirements. At 140°C under short circuit conditions, the original HRE-free 45SH and 42SH rotor cases reached only approximately 335 Nm and 320 Nm after demagnetization, compared with approximately 505 Nm for the HRE-based reference design. High intrinsic coercivity, and strong coercivity retention at elevated temperatures are critical for limiting irreversible demagnetization under short circuit condition. Rotor geometry optimization significantly improves the HRE-free designs, especially through increased magnet thickness up to 6.00 mm, but introduces trade-offs between demagnetization resistance, torque performance, and magnet weight. Overall, the results show that an HRE-free PMSM rotor application is possible only if magnet material properties and rotor geometry are designed together.

Keywords: PMSM, HRE-free magnets, demagnetization, coercivity, remanence, sustainability, rare earth elements (REEs)

Acknowledgements

First and foremost, we would like to express our sincere gratitude to our supervisors Rasmus Andersson and Emil Callerfjord from MDS EM at Volvo GTT, for their guidance, support, and valuable technical knowledge throughout this thesis work. Their feedback and engagement have been highly appreciated and have contributed greatly to the development of this project. We are also grateful to the MDS EM team for their support and welcoming environment during the thesis period.

Our sincere thanks also go to Torbjörn Thiringer for his valuable feedback and insightful discussions during the thesis, which have helped improve both the technical content and the overall quality of the work.

We are also grateful to Tommy Andersson from Sura Magnets AB and researcher Anders Nordelöf for taking the time to share their knowledge and perspectives. Their insights contributed significantly to the sustainability review.

In particular, we would like to thank the product and strategy leaders within VSF at Volvo GTT for their encouragement, support, and valuable contacts. Their guidance and network contributed to identifying this thesis opportunity and enabling the connection to the project.

Finally, we would like to thank our families and friends for their encouragement, patience, and support throughout our studies and during the thesis period. One of the authors would also like to express sincere gratitude to her partner, Alpcan Musa Yilmaz, for his continuous support and understanding.

Nikola Makelja, Gothenburg, Sweden, 2026
Alev Yusein, Gothenburg, Sweden, 2026

Contents

1

Introduction

This chapter introduces the background and motivation for the thesis. It presents the challenges related to heavy rare earth elements in permanent magnet synchronous machine (PMSM) rotor magnets and explains why HRE-free magnet solutions are of interest for heavy-duty electric machine applications. The chapter also defines the aim, limitations, previous work, and societal, ethical, and ecological aspects of the study.

1.1 Problem Background

The transition to electrified transportation has led to a rapidly increasing demand for high-performance electric machines. PMSMs are widely used in automotive and heavy-duty applications due to their high efficiency, power density, and controllability. However, many PMSMs rely on permanent magnets that contain heavy rare earths (HREs). These are added to improve thermal stability and coercivity of the magnets, whereas light rare earths (LREs) are added for higher remanence, or magnet strength. Despite their technical benefits, the use of HRE materials presents several critical challenges. These elements are classified as critical raw materials due to their limited global supply, high price volatility, and concentration of production in a small number of countries, particularly China [1]. This creates supply chain vulnerabilities and geopolitical risks, especially for companies with global manufacturing operations. There is, however, potential to develop rare earth resources outside China, including in Northern Europe, which could contribute to a more diversified supply chain in the future. In addition, the environmental impact associated with rare earth mining and refining is significant, often involving toxic waste, radioactive by-products, and extensive water and energy use. These environmental concerns contradict the sustainability goals of the electrification movement.

1.2 Aim

The aim of this thesis is to evaluate the feasibility of removing heavy rare earth elements (HREEs) from NdFeB permanent magnets in a PMSM for heavy-duty applications. The work is divided into two main parts: a sustainability analysis and a simulation analysis.

The sustainability analysis evaluates whether reducing or removing the use of HREEs can improve the sustainability of PMSM rotor designs for heavy-duty applications. The analysis considers

- the availability of REEs, with focus on the difference between light and heavy REEs, geographical distribution, European dependency on imports, and potential supply sources outside China.
- the material cost of REEs, including the price difference between light and heavy REEs.
- the environmental impact of RE production, including mining, processing, greenhouse gas emissions, energy use, water consumption, waste handling, and challenges related to radioactive by products.
- the supply chain resilience of REEs, including geopolitical risks, recycling and reuse of permanent magnets, and European strategies for reducing supply vulnerability.

The simulation analysis investigates whether an HRE-free rotor design based on the double-layer V-shaped reference PMSM can fulfill the electromagnetic requirements while limiting irreversible demagnetization under worst-case short circuit and normal operating conditions. The evaluation is based on key performance indicators such as torque, back EMF, short circuit current response, and irreversible demagnetization ratio. The main objective is to maintain a torque above 500 Nm after the demagnetization assessment while keeping the irreversible demagnetization ratio below 10%. This part investigates

- available HRE-free NdFeB magnet grades from different material sources.
- the influence of remanence and intrinsic coercivity on machine performance and demagnetization behaviour.
- the required combination of remanence and intrinsic coercivity for a custom HRE-free magnet design.
- the influence of rotor geometry modifications on demagnetization and electromagnetic performance.
- the optimization of rotor geometry parameters to identify a suitable HRE-free rotor design with a target magnet weight below 4.5 kg.
- the benchmarking of selected HRE-free magnet and rotor designs against the original HRE-based reference rotor.

1.3 Limitations

The scope of this thesis is limited to the investigation of HRE-free permanent magnet rotor designs for a PMSM intended for heavy-duty applications. The main limitations for the work are summarized as follows

- The thesis does not aim to eliminate rare earth elements completely. The focus is limited to removing heavy rare earth elements from NdFeB-based permanent magnets.

- The sustainability analysis is limited to the permanent magnets and the materials used in them. Other machine components, such as the stator, windings, housing, cooling system, and power electronics, are not included.

- The sustainability study is mainly focused on Europe. Global supply chain structures, and non-European policy aspects are therefore not investigated in detail.

- The economic comparison is limited to material related cost aspects. Production cost, tooling cost, recycling cost, and full life cycle cost are not evaluated in detail.

- Only rare earth based PMSM rotor alternatives are considered. Other machine concepts, such as ferrite magnet machines, electrically excited synchronous machines, induction machines, and synchronous reluctance machines, are outside the scope.

- Only rotor-related design changes are investigated. The stator geometry, winding configuration, cooling arrangement, and overall machine architecture are kept unchanged from the reference machine.

- The electromagnetic evaluation is based on simulations in Ansys Motor-CAD. No physical prototype is built or experimentally tested.

- The demagnetization analysis is performed at selected fixed magnet temperatures. Detailed thermal modeling, cooling strategies, and methods for reducing magnet temperature are not included.

- The study is based on selected operating points, including worst-case demagnetization conditions. Full drive-cycle analysis, long-term operational loading, and ageing effects are not investigated.

- PWM current ripple, inverter switching effects, and current harmonics are not included in the simulations.

- The magnet material data is based on available temperature-dependent data from selected sources. Uncertainties related to supplier variation, manufacturing tolerances, batch variation, and long-term degradation are not considered in detail.

- Mechanical aspects such as rotor stress, vibration, noise, fatigue, and manufacturability are not studied
- The benchmarking is limited to the available reference PMSM model. Therefore, the conclusions are specific to the investigated topology, material data, and operating conditions.

1.4 Previous Work

The research on HRE-free PMSMs is ongoing and previous studies have been found, however none touch upon heavy-duty applications [2], [3], [4], [5], [6], [7], [8]. Previous studies are limited to lower power applications and they have been made for different topologies of the PMSMs, including surface mounted permanent magnets (PMs) [5], [4], interior PMs [6], [7], [8], outer rotor PM traction motors [2] and PM-assisted synchronous reluctance machine [3]. Even though the literature does not provide details on heavy-duty applications, they do provide insight on problems that may occur regarding demagnetization when there are no HRE elements present in the PMs.

In [7], segmented magnets are used to address the problem of demagnetization. The segment closest to the d-axis is thicker due to the corners being most prone to demagnetization, while [6] uses bonded rare earth magnets where the reluctance torque is used more effectively by using a an asymmetric arrangement of the magnets. This to match the performance of machine utilizing sintered magnets. In [2], a Halbach array arrangement of the magnets is used to address the demagnetization. Lastly, [8] suggests a design with two different magnet grades, where the magnets closest to the air gap have a lower B_r compared to the magnet closer to the machine axis. Notably, the implemented solutions used in different studies are aimed to change the behavior of the field in order to avoid demagnetization.

1.5 Societal, Ethical and Ecological Aspects

Permanent magnet synchronous machines are important for the electrification of the transport sector, especially in heavy-duty vehicles where high efficiency, high torque density, and reliable operation are required. By enabling more efficient electric powertrains, these machines can contribute to reduced fossil fuel use and lower greenhouse gas emissions. In this thesis, the focus is on an heavy rare earth free PMSM rotor, where the aim is to reduce the dependence on heavy rare earth elements while still maintaining the required machine performance.

From a societal perceptive, reducing the use of heavy rare earth elements can improve supply chain resilience. These materials are associated with limited availability, price variations, and strong dependence on a small number of supplier countries. For vehicle manufacturers, this can create uncertainty in production and long-term planning. An HRE-free rotor design could therefore reduce the vulnerability connected to critical raw materials. However, the design must still meet the performance and safety requirements of heavy-duty applications, since reduced robustness or increased demagnetization risk could lead to shorter component lifetime or higher material use.

From an ethical perspective, the use of rare earth elements raises concerns related to how these materials are extracted and processed. Although electric vehicles can reduce emissions during operation, the production of rare earth materials may involve environmental damage, high energy use, water consumption, and waste handling challenges. Heavy rare earth elements, such as dysprosium and terbium, are often used to improve temperature stability of NdFeB magnets. Reducing the need for these elements is therefore relevant, since it may lower the dependence on material supply chain where environmental and social conditions can be difficult to control.

From an ecological perspective, removing HRE elements from the rotor magnets has the potential to reduce the environmental burden related to magnet production. This is important because the sustainability of electrification should be evaluated not only during vehicle operation, but also across the full material and manufacturing chain.

2

Collection of known usable theory

This chapter introduces the theoretical background needed for the thesis. First, rare earth elements and magnetic materials are described. The chapter then presents the basic magnetic principles related to magnetization, hysteresis, coercivity, and demagnetization. Finally, the electromagnetic concepts and PMSM theory required for the simulation analysis are introduced.

2.1 Rare Earth Elements

Rare earth elements (REEs), also known as rare earth metals or simply rare earths are not found in their native form but occur within minerals such as oxides [9],[10]. REEs are a group of 17 closely related elements consisting of scandium (Sc), yttrium (Y), and the 15 lanthanides, which are typically drawn as a separate row below the periodic table [9]. The REEs are commonly divided into two groups: light rare earth elements (LREEs) and heavy rare earth elements (HREEs), which are summarized in Table 2.1. Monazite, which mainly contains LREEs, is the most frequently occurring REE bearing mineral. The LREEs generally include elements from lanthanum (La) to samarium (Sm), whereas the HREEs consist of yttrium (Y) and elements from terbium (Tb) to lutetium (Lu)[9].

REEs are often associated with a carbonate rock known as carbonatite. Carbonatite is an igneous rock, meaning a rock formed through the solidification of molten material (magma or lava), that is generally intrusive and consist of more than 50% carbonate minerals. Carbonatites are related to continental alkaline igneous rock that belong to a group of rare igneous rocks. Alkaline rocks are important because they contain high concentration of incompatible elements, such as the REEs [9]. Carbonatites are typically enriched in LREEs, whereas alkaline igneous rocks may contain relatively higher proportions of HREEs [11]. Key geological terms used in this context are summarized in Table 2.2.

Table 2.1: Rare Earth Elements classification

Atomic Number	Name	Label
Light Rare Earth Elements (LRE)		
57	Lanthanum	La
58	Cerium	Ce
59	Praseodymium	Pr
60	Neodymium	Nd
61	Promethium	Pm
62	Samarium	Sm
63	Europium	Eu
64	Gadolinium	Gd
Heavy Rare Earth Elements (HRE)		
65	Terbium	Tb
66	Dysprosium	Dy
67	Holmium	Ho
68	Erbium	Er
69	Thulium	Tm
70	Ytterbium	Yb
71	Lutetium	Lu

Table 2.2: Summary of geological terms related to REE deposits

Term	Description	HRE content
Igneous rock	Formed from solidified magma or lava.	Depends
Carbonatite	Igneous rock with >50% carbonate minerals, often REE-rich.	Low
Alkaline rocks	Igneous rocks enriched in alkali elements and REEs.	High
Incompatible elements	Elements that remain in the melt during crystallization.	Not specific

2.2 Soft and Hard Magnetic Materials

Most magnetic materials can be divided into one of two groups, magnetically soft and magnetically hard. The soft materials are easy to magnetize and demagnetize, while the hard materials are as the name suggests hard to magnetize and demagnetize [12, Ch. 13.1]. Soft magnetic materials are characterized by their high permeability. Hard magnetic materials however, are used to create permanent magnets which have high coercivity as one of their main requirements. The reason for this is that once it is magnetized, it shall be able to resist demagnetization from stray fields, including its own demagnetizing field. As seen in Fig. 2.1, in the case of the soft magnetic materials, the magnetic field strength, H is small compared to magnetic polarization, J and thus B and J are practically the same according to

$$B = J + \mu H \tag{2.1}$$

where μ

$$\mu = \mu_0 \mu_r \tag{2.2}$$

and μ_0 is the permeability of free space and μ_r is the relative permeability of the material [12, Ch. 1.8]. For the hard magnetic materials the magnetic flux density, B and J are very different due to H being big in comparison to J. The quantities $\boldsymbol{B}$, $\boldsymbol{H}$, and $\boldsymbol{J}$ are introduced in more detail in Section 2.3.

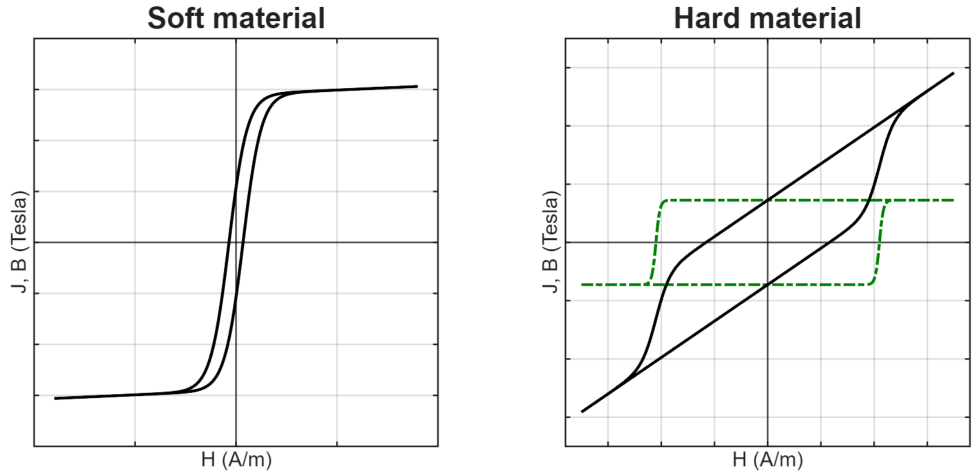

Figure 2.1: Magnetization characteristic of soft and hard magnetic materials showing the relationship between magnetic field strength $\boldsymbol{H}$ and magnetic flux density $\boldsymbol{B}$ and polarization $\boldsymbol{J}$

2.3 Magnetic Fundamentals

Electric vehicles and many other clean energy applications heavily depend on permanent magnets based on REEs [13]. These magnets support the efficient transformation of electrical energy into mechanical motion. Under this section, the fundamental physical principles governing permanent magnets are introduced. First, basic magnetic theory is presented, including the origin of magnetic fields, magnetization, and domain behavior. This is followed by an explanation of magnetic hysteresis, which describes how magnets respond to an external magnetic field and how key properties such as remanence and energy product are defined. Finally, demagnetization mechanisms are examined, with emphasis on thermal effects, coercivity, and operating conditions relevant for electric machine applications.

2.3.1 Magnetization and Magnetic Domains

There are two ways to generate a magnetic field. First by applying electric currents and secondly, using magnetic substances. In the first case, magnetic field is produced by either electric charges that move and in the second case, by the magnetic moments inside magnetic substances at an atomic scale [12, Ch. 1.3]. A magnetic field that passes through a surface is called magnetic flux [12, Ch. 1.7]. The strength of the field itself is denoted as magnetic field strength (H) and has the unit A/m, hence relates to the field from the moving electric charges [12, Ch. 1.8]. The unit A/m describes the strength of a 1 A current moving in a circle with a diameter of 1 m, as illustrated in Fig. 2.2. The intensity of the field that is produced by the elemental magnetic moment is called magnetization (M). All magnetic moment *(m)* per unit volume summed gives M [12, Ch. 1.4]. Closely related to the magnetization is the magnetic polarization J, defined as

$$J = \mu_0 M \tag{2.3}$$

and has the unit T and represents the magnetic contribution from the material itself. The magnetic moment is due to the motion of the electrons around the nucleus of the atom [12, Ch. 3.2]. Due to the strong interaction between the magnetic moments inside of magnetic materials, spontaneous alignment of the magnets is permitted. Essentially, H is associated with currents and M with matter. The sum of H and M gives the magnetic field *(B)*. This results in

$$B = \mu H + \mu M \tag{2.4}$$

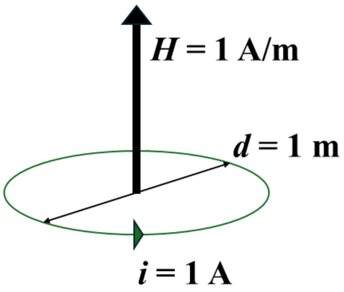

Figure 2.2: llustration of the relationship between electric current and magnetic field strength H. A current flowing through a conductor produces a magnetic field around it.

Magnets can be divided into small regions, called magnetic domains [12, Ch. 4.1]. In each domain, the magnetic points in the same direction while the different domains of the magnets may point in different directions depending on how magnetized it is. The Curie temperature (T_c) is the characteristic temperature and below this the magnetic moments are aligned spontaneously [12, Ch. 8.2]. Below the Curie temperature T_c, a ferromagnetic material divides into magnetic domains. Magnetic anisotropy determines the preferred direction of magnetization within these domains [12, Ch. 7]. In an unmagnetized ferromagnetic material, the magnetic domains are arranged in different directions in order to minimize the internal magnetic energy, as illustrated in Fig. 2.3. As a result, the net magnetization of the material is close to zero. There is more energy needed for the material to be fully magnetized compared to when it is not [12, Ch. 9].

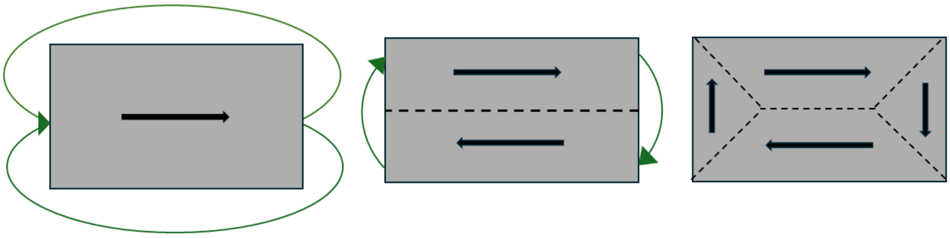

Figure 2.3: Minimization of internal energy

2.3.2 Hysteresis

Magnetic materials can be magnetized by applying an external magnetic field. The magnetization process is illustrated in Fig. 2.4. Starting from an initially unmagnetized state, the magnetic domains begin to align with the applied field as the field strength increases, as shown by point (1) [12, Ch. 9.7]. The alignment process during magnetization is illustrated in more detail in Fig. 2.5.

At the point where the applied field is so high that all domains are oriented in the same direction, saturation is reached. When the magnetic material is saturated, a further increase of the applied field will not have any effect [12, Ch. 1.7]. This is seen at point (2) in Fig 2.4.

When the applied field is zero, the residual magnetization, or remanence (B$_r$), is not zero [14], as seen at point (3) in Fig. 2.4. This is the magnetization that is left when no external field is applied and is often referred to as how strong the magnet itself is. An analogy to the fact that a magnetized magnet wont ever lose its magnetic energy spontaneously is a mass that has been lifted up and put down on a table of a certain height. This mass will keep its potential energy until its pushed off of the table. The same principle works for magnetization.

By applying a negative field from the saturation point, there will be a rotation of the magnetization that is reversible. Furthermore, the growth of reverse domains will decrease the magnetization, as seen at point (4). By removing the applied field or reversing the field, the hysteresis curve is obtained [12, Ch. 1.9].

The point where the product between H and B is at its maximum value is called the maximum energy product (BH$_{max}$) [15]. This indicates the highest energy density a magnet can store and release, i.e the point where it has the highest energy per volume unit. BH$_{max}$ is usually used to indicate the grade of the magnet. The product is illustrated in Fig. 2.6.

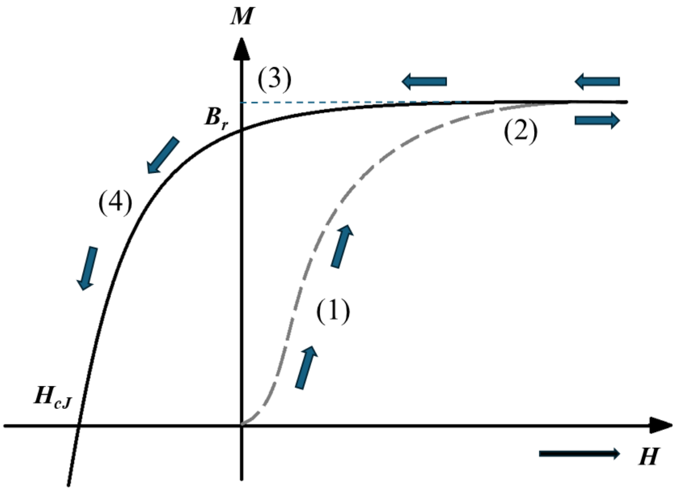

Figure 2.4: Magnetization and demagnetization showing domain alignment, saturation, remanence, and demagnetization.

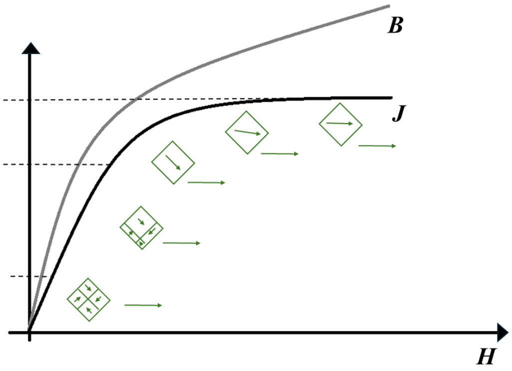

Figure 2.5: Alignment of magnetic domains during magnetization. As the applied magnetic field increases, the domains rotate and align with the field direction.

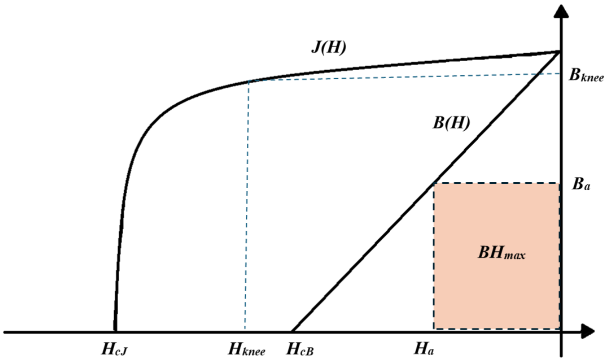

Figure 2.6: Demagnetization curve of a PM illustrating BH_{max}. The shaded region represents the largest $B \cdot H$ product.

2.3.3 Coercivity and Demagnetization

In order to reduce M, to zero, a reverse field has to be applied up to the coercivity (H_{cJ}) of the magnet [12, Ch. 1.9]. The coercivity is the ability of the magnet to withstand a external magnetic field without getting demagnetized [16]. The properties of the magnets, B_r and H_{cJ}, have a thermal behavior. This is described by the reversible temperature coefficients (RTCs), α_{B_r} and $\beta_{H_{cJ}}$, which are for B_r and H_{cJ} respectively [17]. For Nd-based magnets, both coefficients become negative with increasing temperature, meaning a loss of magnetic strength, or remanence, and coercivity.

As long as the temperature is below T_c, the effect is reversible, meaning that the properties recover whenever the temperature drops. Usually it is a combination of the temperature and reverse fields. Transient events such as short circuit currents can lead to irreversible demagnetization of the permanent magnet [18]. In applications such as electric vehicles, HRE elements are used in the magnets in order to increase the coercivity [19]. By increasing the coercivity, there needs to be a larger external field to demagnetize it. Thus the magnet handles larger currents and higher temperatures without demagnetizing [16].

Furthermore, the coercivity of the magnet is dependent on the size of the grains [20]. By decreasing the size of the grains in the production process, the coercivity increases to a maximum value [21]. If the size is further decreased past a certain critical size, it will have the opposite effect and instead a decrease of coercivity will happen. A general waveform on the relationship between the coercivity and grain size is shown in Fig. 2.7.

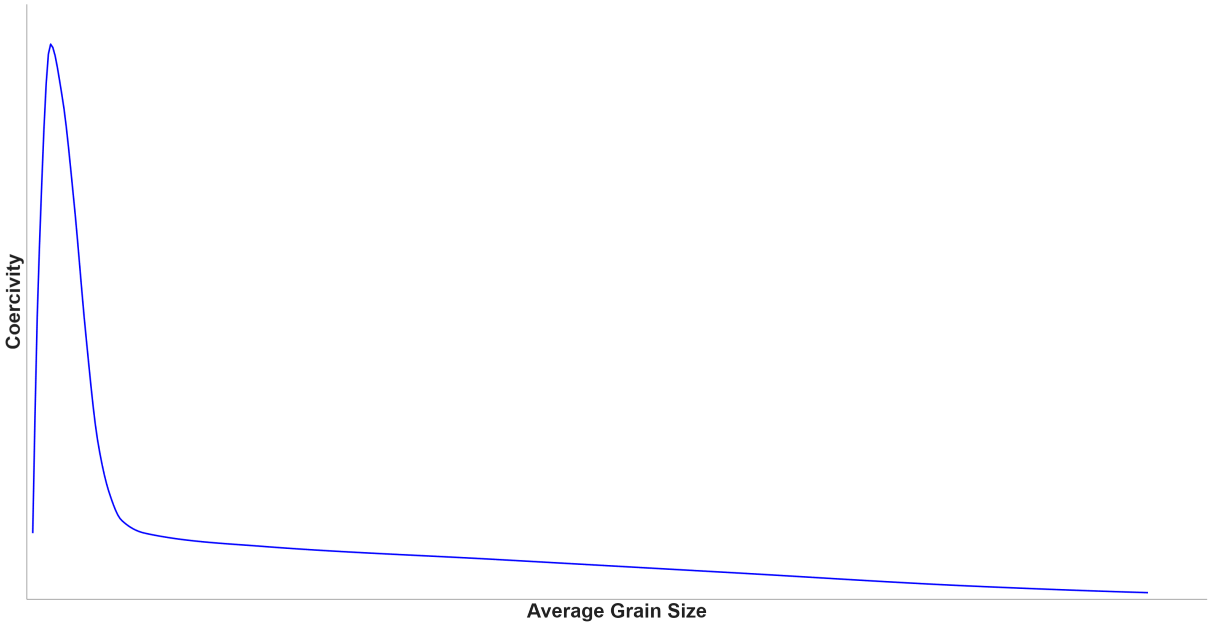

Figure 2.7: Coercivity as a function of average grain size.

If a permanent magnet is in free space, i.e an open magnetic circuit, then there will be a demagnetization field (H_d) created in order to try and minimize the internal energy

[12, Ch. 2.7]. However, if put in a closed magnetic circuit, for example a piece of iron with high permeability, then the demagnetization field will be zero [12, Ch. 2.6]. These cases are illustrated in Fig. 2.8. The point in the hysteresis loop where H_d is located indicates the working point of the magnet, seen in Fig. 2.9 [12, Ch. 2.5]. This depends on the circuit itself, the geometry of the magnet, temperature, the material of the magnet and whether there is an external field applied.

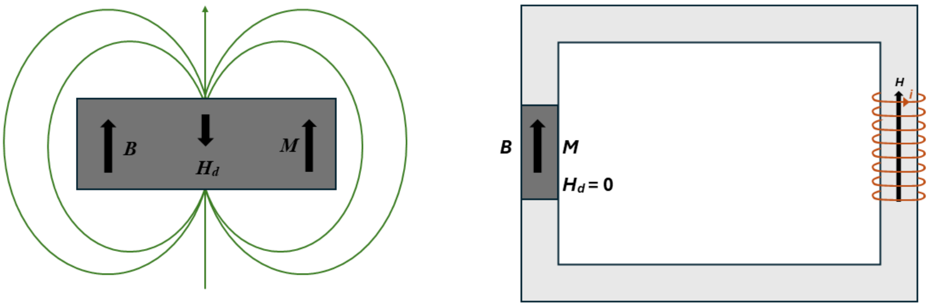

Open circuit: $H_d \neq 0$ **Closed circuit:** $H_d = 0$

Figure 2.8: Magnet in an open magnetic circuit (left) and in a closed magnetic circuit (right).

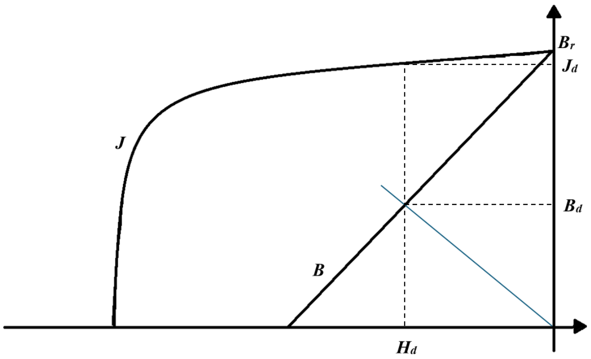

Figure 2.9: Demagnetization curve showing the working point of a permanent magnet under a demagnetizing field.

It is possible to apply a negative magnetic field without causing permanent demagnetization [22]. However, there is a knee point for which any demagnetization further below that point causes permanent demagnetization of the magnet. When a magnet is permanently demagnetized, it will have lower remanence, and in this case the effect is not reversible.

2.4 NdFeB Magnets

NdFeB magnets are often used in electric machines because they can provide strong magnetic performance in a compact design. In PMSMs, the magnets create the rotor magnetic field, which has a direct influence on torque production, efficiency, and the risk of demagnetization. Since this thesis investigates the reduction or removal of HREs in NdFeB-based rotor magnets, the classification and manufacturing of these magnets are introduced in the following sections.

2.4.1 Classification of NdFeB Magnets

NdFeB magnets are classified using a standardized notation that provides information about the material type, magnetic performance, and resistance to demagnetization [23]. This notation typically consists of a letter, a numerical value, and in some cases an additional suffix.

The first letter, “N”, indicates that the magnet is based on neodymium-iron-boron. The numerical value below defines the magnet grade and is directly related to the maximum energy product, $(BH)_{\max}$. Magnets with higher grade numbers generally exhibit stronger magnetic performance and are therefore suitable for applications requiring high power density.

In addition to the numerical grade, suffixes such as M, H, SH, UH, EH and AH indicate different levels of intrinsic coercivity, H_{cj}. This parameter describes the magnet’s resistance to demagnetization, for example when exposed to elevated temperatures. Each suffix corresponds to a minimum coercivity level. The suffixes represent increasing levels of intrinsic coercivity, with M corresponding to the lowest level, followed by H, SH, and UH. A higher coercivity level implies that the magnet is more stable and can maintain its magnetic properties under more demanding operating conditions.

For example, a magnet labeled N45SH consists of a neodymium-based material with a relatively high $(BH)_{\max}$ value and an increased coercivity level. This makes it suitable for applications where both strong magnetic performance and good thermal stability are required, such as in electric machines and automotive systems. The structure of the grading notation is illustrated in Fig. 2.10, where the material type, magnetic grade, and coercivity level are separated for clarity.

N45SH

N	45	SH
Material	Grade	Coercivity

Figure 2.10: Illustration of NdFeB magnet grade notation

2.4.2 Manufacturing of NdFeB Magnets

The manufacturing process of a permanent magnet is divided into several steps as seen in Fig. 2.11. First the raw materials are obtained, including the LREs. For instance the production of NdFeB consists of raw materials that are melted together in a vacuum or inert gas atmosphere [24]. This prevents oxidation and ensures a clean alloy. The molten alloy is then rapidly cooled using strip casting, where the liquid metal is poured onto a rotating, water cooled wheel. This fast cooling produces thin metal flakes with a fine and uniform microstructure and prevents the formation of unwanted iron rich phases that would reduce magnetic performance.

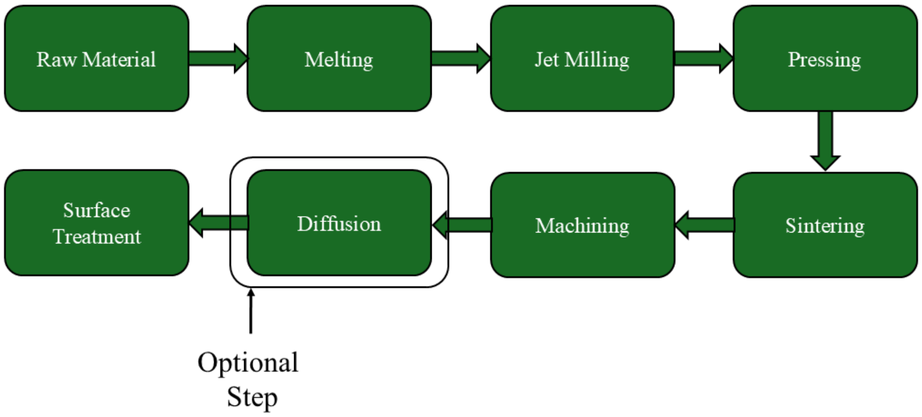

Figure 2.11: Main steps in the manufacturing process of NdFeB magnets.

Next, the brittle flakes are broken down into powder through a process called hydrogen decrepitation [24]. Hydrogen enters the material along grain boundaries, creating internal stresses that cause the flakes to crack and break apart. The material is then mechanically milled with jet milling to produce very fine powder particles, typically a few micrometers in size.

The fine powder is then pressed into a desired shape while exposed to a strong magnetic field [24]. This aligns the particles in the same direction. After pressing, the compacted powder is sintered at high temperature in a vacuum or inert gas. During sintering, the particles bond together and the magnet becomes dense and mechanically strong. The temperature and time are controlled to achieve high density without excessive grain growth. An additional heat treatment is applied after sintering to optimize magnetic properties such as coercivity and hysteresis behavior.

During sintering, the magnet shrinks significantly and unevenly depending on the alignment direction [24]. Therefore, machining is required to achieve the final dimensions and flat surfaces. Cutting, grinding, or electrical discharge machining is used to shape the magnet. Sharp edges are rounded, often using vibratory finishing, to improve surface quality and ensure uniform coating in later steps.

Once the magnet has its final shape, it is magnetized using a strong external magnetic field [24]. This step permanently aligns the magnetic domains, turning the material into a functional permanent magnet.

To improve high temperature performance, dysprosium (Dy) diffusion may be applied [24]. Instead of adding dysprosium throughout the entire magnet, a thin Dy rich layer is applied to the surface and diffused along the grain boundaries during heat treatment. This significantly increases coercivity and operating temperature while minimizing the amount of expensive and critical dysprosium used.

An alternative approach to increase coercivity while minimizing HRE content is the so called two powder method [25]. In this technique, two powders with different particle sizes are used. First standard NdFeB composition, while a second finer powder contains Dy or Tb and exhibits higher magnetocrystalline anisotropy. During sintering, the finer powder melts first due to its higher surface energy. This enables a homogeneous redistribution of HREE along the grain boundaries. In contrast to conventional grain boundary diffusion processing, no additional diffusion step after sintering is required.

Traditionally, instead of adding HRE elements with diffusion or the two powder method, they are added in the beginning along with the other raw materials when alloying [26]. With the traditional method the magnets will have a homogeneous distribution of the HRE elements, but the usage of HRE is less efficient and more material is used compared to the other cases. When doing diffusion the HRE element only enters the grain boundary phase or in the surface layer which explains why the effect on the remanence is lower compared to the traditional way. It can however, still be enough to prevent demagnetization of the magnet.

2.5 Electromagnetics

This section introduces the basic electromagnetic principles relevant to electrical machines. First, the magnetic circuit concept is presented to describe how magnetic flux is produced and distributed in the machines. Then, the principle of electromagnetic induction is introduced through the concept of back electromotive force (EMF).

2.5.1 Magnetic Circuit

The path of the magnetic field in a machine can be simplified as a equivalent magnetic circuit, where magnetic calculations that are equivalent to electric circuit analysis can be performed [27]. Magnetic circuit analysis is used when sizing the magnetic components of an electromagnetic device. The magnetic circuit consists of an magneto motive force (MMF) which is denoted by $\mathscr{F}$, a reluctance $\mathscr{R}$ (H^{-1}) and a magnetic flux ϕ (Wb). These are equivalent to the electro motive force (EMF), denoted by V, resistance R (Ω) and current I (A) respectively.

What drives the magnetic flux in the circuit is the MMF [27]. The relation between the MMF and the flux is given by

$$\mathscr{F} = \phi\mathscr{R} \tag{2.5}$$

There are two ways to produce an MMF with external sources. Firstly by current excitation in windings or by PM excitation, which is used in PMSMs [27]. The MMF from permanent magnet excitation is given by

$$\mathscr{F} = H_c t_{mag} \tag{2.6}$$

where H_c is the coercive field strength and t_{mag} is the length of the flux path through the magnet, which in this case corresponds to the magnet thickness.

Furthermore, the reluctance is the difficulty the flux experiences as it flows through the circuit and is expressed as

$$\mathscr{R} = \frac{l}{\mu A} \tag{2.7}$$

where l is the length of the circuit and A is the cross sectional area that the flux flows through [27]. When doing the magnetic circuit analysis, the different components with different relative permeability will have their own reluctance which are then summed together for a total reluctance, similar to resistors in series.

Lastly, the flux (ϕ) passing through a cross sectional area A that is placed in a magnetic field B is given by

$$\phi = BA \tag{2.8}$$

For permanent magnet excitation however, (2.8) can be written as

$$\phi_0 = B_r A \tag{2.9}$$

where ϕ_0 is the remanent flux of the permanent magnet and is dependent on the remanence B_r of the permanent magnet.

The magnetic flux is proportional to both the cross sectional area it flows through and the *MMF* [27]. Depending on the selection of the core material, the flux can be contained inside the circuit but there will be some leakage flux. In contrast, in electric circuits there can be no current flow without a complete circuit, while magnetic flux is able to flow in the air surrounding the circuit.

For permanent magnets, (2.5) and (2.6) can be combined into

$$\phi = \frac{\mathscr{F}}{\mathscr{R}} = \frac{H_c}{\mathscr{R}} t_{mag} \tag{2.10}$$

which shows that the flux through the magnet is proportional to the thickness of the magnet. This can be further linked to the flux linkage (Ψ) that is given by

$$\Psi = N\phi \tag{2.11}$$

where N is the number of turns in the windings. Thus, it can be concluded that both the flux linkage and the flux is proportional to the thickness of the magnets.

2.5.2 Back Electromotive Force

The operation of electrical machines is fundamentally based on Faraday's law of electromagnetic induction [27]. According to this law, a voltage is induced in a closed loop when the magnetic flux linking the loop changes with time. The induced EMF is given by

$$e = -\frac{d\phi}{dt} \tag{2.12}$$

where e is the induced voltage. The induced voltage can therefore be written as

$$e = -\frac{d(BA)}{dt} \tag{2.13}$$

In rotating electrical machines, the magnetic field distribution relative to the stator windings varies with time due to rotor motion. As the rotor rotates, the magnetic flux linking the stator coils changes, which induces a voltage according to Faraday's law. This induced voltage is referred to as the back electromotive force (back EMF) since it opposes the applied stator voltage.

2.6 Permanent Magnet Synchronous Machine

Permanent magnet synchronous machines (PMSMs) are commonly used in modern electric drive applications due to their high efficiency [27]. In a PMSM, the rotor contains permanent magnets that create a magnetic field, while the stator windings are supplied with three phase currents that generate a rotating magnetic field. The interaction between these magnetic fields produces the electromagnetic torque that drives the machine.

Different rotor configurations can be used in PMSMs depending on the desired electromagnetic and mechanical performance. Common examples include V shaped, U shaped, and surface mounted magnet topologies, see Fig. 2.12.

To better understand and analyze the behavior of a PMSM, several electromagnetic concepts and mathematical models are used. The following subsections therefore describe the main principles that govern the operation of the machine.

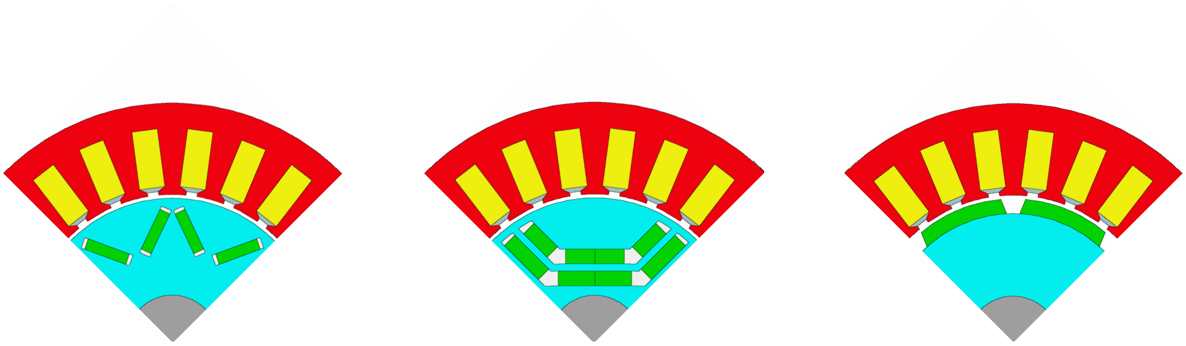

(a) V-shaped rotor (b) U-shaped rotor (c) Surface-mounted rotor

Figure 2.12: Different PMSM rotor magnet topologies.

2.6.1 DQ Model

The voltage that gets fed into the PMSM from the inverter are three phase voltages [27]. In order to simplify the analysis of the PMSM the three phase system is transformed first into the $\alpha\beta$-system. This is a stationary system which is observed from the outside. This system is lastly transformed into a dq-system which is a rotating system, however it is observed from inside the system, meaning that the machine can be analyzed with DC quantities. In the dq reference frame, the stator voltage (u_s) equations of a PMSM can be written as

$$u_{sd} = R_s i_{sd} + L_{sd}\frac{di_{sd}}{dt} - \omega_r L_{sq} i_{sq} \tag{2.14}$$

$$u_{sq} = R_s i_{sq} + L_{sq}\frac{di_{sq}}{dt} + \omega_r L_{sd} i_{sd} + \omega_r \psi_{PM} \tag{2.15}$$

where R_s is the stator resistance, L_{sd} and L_{sq} are the d and q axis inductances, ψ_{PM} is the permanent magnet flux linkage and ω_r is the electrical angular speed of the rotor.

2.6.2 Short Circuit Theory

One of the most severe fault conditions in electric machines is a short circuit, which produce large currents, up to several times larger than the rated current [28]. During a short circuit the terminal voltage becomes zero, which when put into (2.14) and (2.15) gives

$$0 = R_s i_{sd} + L_{sd}\frac{di_{sd}}{dt} - \omega_r L_{sq} i_{sq} \tag{2.16}$$

$$0 = R_s i_{sq} + L_{sq}\frac{di_{sq}}{dt} + \omega_r L_{sd} i_{sd} + \omega_r \psi_{pm} \tag{2.17}$$

In the worst case operating condition, at maximum torque and base speed, see Fig. 2.13, the machine has a high back EMF. This, coupled with low impedance in the stator, produces the maximum possible short circuit current, thus it is referred to as the worst case condition.

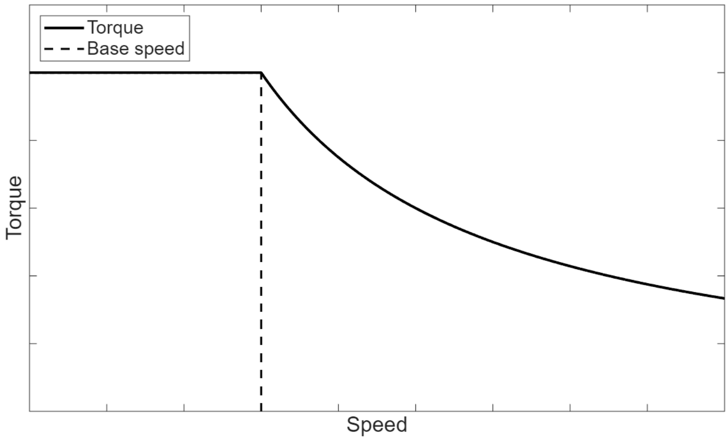

Figure 2.13: Torque speed characteristic showing the constant torque region, base speed and field weakening operation.

In PMSM drives in electric vehicles, a standard safety system that is used is active-short circuit (ASC) [18]. This protective measure is used to prevent catastrophic failure. Optimally, a shutdown of the inverter is preferred. What makes it a safe state is that its a transient where the torque drops to close to zero within milliseconds. However, such a shutdown cannot be applied at all speeds because of the risk of dangerous uncontrolled generation. The disadvantage with ASC is the risk of irreversible demagnetization of the PMs and risk of damaging the inverter. The torque pulsations of such an event is also a possible danger for the driver and can potentially stress mechanical structures.

2.6.3 Torque Production

In the dq reference frame, the torque of a PMSM can be expressed as

$$T_e = \frac{3p}{2}\left(\psi_{PM} i_q + (L_{sd} - L_{sq}) i_{sd} i_{sq}\right) \tag{2.18}$$

where p is the number of pole pairs [27].

The first term represents the electromagnetic torque produced by the interaction between the stator current and the permanent magnet flux. The second term represents the reluctance torque, which arises due to the difference between the d- and q-axis inductances.

In interior PMSMs, the rotor structure creates magnetic saliency such that $L_d \neq L_q$. This difference in inductance allows an additional torque component, known as reluctance torque, to be generated. As a result, the total torque in an interior PMSM is the sum of the electromagnetic torque and the reluctance torque. Depending on the current angle, these two components contribute differently to the total torque [29]. Maximum torque is obtained when both components contribute positively, see Fig. 2.14

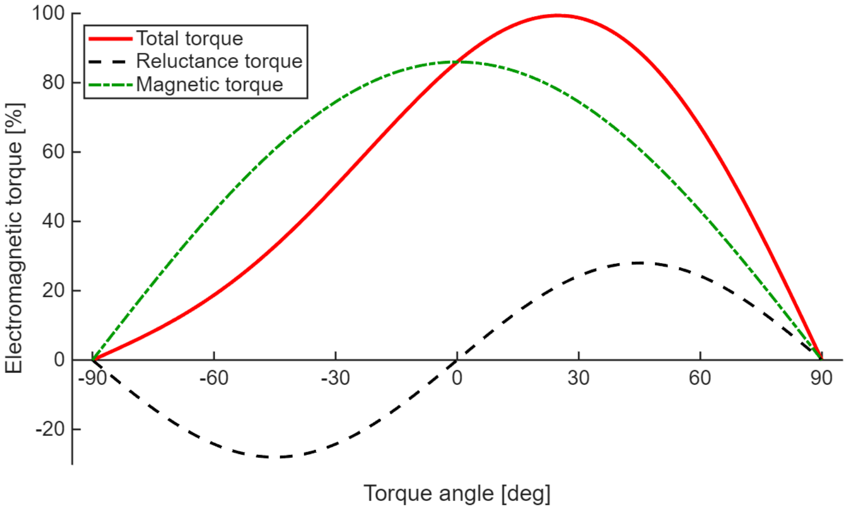

Figure 2.14: Magnet torque, reluctance torque, and total torque as a function of torque angle, with the q-axis used as the reference direction.

2.6.4 Maximum Torque Per Ampere (MTPA)

In the dq reference frame, an important objective is to determine how the stator current should be distributed between the d- and q-axes in order to maximize torque production for a given current magnitude [27]. This operating condition is commonly referred to as a Maximum Torque Per Ampere (MTPA) [30]. The MTPA strategy ensures efficient utilization of the available current and is typically applied in the constant torque region, i.e., below base speed, before the onset of field weakening.

The magnitude of the stator current vector can be expressed as the combination of its d- and q-axis components as

$$I_{mag} = \sqrt{i_{sd}^2 + i_{sq}^2} \tag{2.19}$$

To parameterize the current vector, the angle β is introduced as the angle between the stator current vector and the q-axis. The current components can then be written as

$$i_{sd} = I_{mag} \cos(\beta) \tag{2.20}$$

$$i_{sq} = I_{mag} \sin(\beta) \tag{2.21}$$

By substituting these expressions into the electromagnetic torque equation presented in Section 2.6.3, the torque can be expressed as a function of the current angle β. The optimal operating point is obtained by maximizing the torque with respect to β, which leads to the condition

$$\frac{dT_e}{d\beta} = 0 \tag{2.22}$$

Solving this expression results in the following relation for $\cos(\beta)$

$$\cos(\beta) = -\frac{\psi_m}{4(L_{sd} - L_{sq})I_{mag}} - \sqrt{\frac{1}{2} + \left(\frac{\psi_m}{4(L_{sd} - L_{sq})I_{mag}}\right)^2} \tag{2.23}$$

This expression defines the MTPA trajectory for a given machine, where the torque per ampere is maximized [30]. The corresponding current angle β determines the optimal balance between the magnet torque and the reluctance torque contributions. In the current plane, the MTPA trajectory represents the locus of operating points that achieve maximum torque for each current magnitude.

2.6.5 Field Weakening

Field weakening is used to extend the operating speed range beyond the base speed [27]. At low and medium speeds, the stator voltage is below the inverter voltage limit and the motor can operate with MTPA. However, as the rotor speed increases, the back EMF also increases since it is proportional to the rotor speed.

When the base speed is reached, the induced back EMF approaches the maximum available stator voltage. As a result, the voltage limit of the inverter is reached and further increase in speed cannot be achieved without modifying the flux in the machine.

This behavior can be understood from the stator voltage equations in the dq reference frame given in (2.14) and (2.15). In particular, the term $\omega\psi_{PM}$ in (2.15) increases with electrical speed and contributes to the rising stator voltage.

To enable operation at higher speeds, a negative d axis current i_d is applied. This current produces a magnetic field that opposes part of the permanent magnet flux. As a result, the effective air gap flux is reduced, which lowers the back EMF and allows the motor to operate at speeds above the base speed without exceeding the inverter voltage limit.

This operating principle is illustrated in Fig. 2.13. At speeds below the base speed, the motor operates in the constant torque region where the voltage limit of the inverter is not reached. Once the base speed is exceeded, field weakening control is applied, and the torque decreases with increasing speed.

3

Case set up - Sustainability

The literature review focuses on the sustainability aspects of REEs and is divided into four main sections:

- Availability of REEs
- Raw Materials Cost
- Environmental Impact of REEs
- Supply Chain Resilience

and each section addresses a specific aspect of rare earth use in order to provide a comprehensive understanding of the topic. The selection of these themes is based on their relevance to the key sustainability challenges associated with REE-based PM, particularly in electric machine applications.

The analysis is primarily based on a combination of peer-reviewed scientific literature, reports from European Commission, and policy documents such as the Critical Raw Materials Act. In addition to the literature sources, qualitative insights from industrial interviews have also been included as a complementary part of the analysis. The interview material is not used as stand-alone evidence, but rather to support and contextualize findings from the literature.

In the section on availability, potential REE suppliers outside of China are identified. The geographical distribution and supply structure of REEs are reviewed with a focus on Europe's dependency on imports. Existing mining operations, planned projects, and identified but not yet exploited deposits are included. The sources are assessed from a strategic supply perspective as well as with respect to environmental, social, and governance considerations, in line with EU's sustainability objectives.

The cost section is based on an analysis of costs relative to the normalized price of lanthanum. This has been done in order to clearly state how much the prices differ between the HREs and LREEs. Furthermore, the cost of different manufacturing processes are identified and whether it is possible to cut costs by using different methods.

In the section on environmental impact, the impact of REE production is analyzed together with studies and reports from the European Commission to assess the environmental consequences of REE production. The analysis covers different stages of the value chain, including mining and processing, with a focus on greenhouse gas emissions, water consumption, and energy use. Additionally, environmental challenges due to the presence of radioactive elements in RE bearing minerals are considered. The role of electricity mix influencing the sustainability of REE production is also evaluated.

Lastly, in the section on supply chain resilience, strategies to reduce supply risks for REEs are reviewed. The analysis focuses on recycling and reuse of permanent magnets, including current recycling rates, technical challenges, and design related aspects that influence recyclability. In addition, to mitigate the supply chain risks it is considered in the context of European Commission initiative.

4

Sustainability Analysis

Sustainability is a broad and sometimes ambiguous concept that has been defined in several ways across different contexts. The term has developed a range of more specific meanings, which is why sustainability is often discussed through its underlying principles rather than through one single universal definition [31]. At its core, sustainability concerns the conditions under which society can function over time without depleting natural resources or causing long-term damage to the environment. In this sense, sustainability is closely linked to how resource usage is managed, so that human development can continue without undermining ecosystems and the foundations for life [31].

In this chapter, sustainability is analyzed and discussed through the lens of REEs where questions of availability, cost and environmental impact become central. In particular, supply concentration and geopolitical dependence influence how sustainable and resilient the value chain can be according to the European commission.

4.1 Material Availability

As stated in the problem background, the production of REEs is concentrated in a small number of countries, where the main country is China. Critical raw materials (CRMs) are materials that for Europe are of utmost economic importance. Included in CRMs are the REEs, for which the demand is expected to increase six-fold by 2030 and as much as seven-fold by 2050 [32]. At this moment, Europe is heavily reliant on imports. In a study on CRMs for the EU in 2023 it is stated that the main suppliers of REEs to the EU is China [33]. In particular, China accounts for 100% of the HREE share and 85% of the LREE share. Another study shows that 98% of the RE magnet demand is met by Chinese import [34]. Due to this, the Critical Raw Materials Act (CRMA) was created to address the challenges of CRMs. The aim is a secure and sustainable supply of CRMs and to make the EU more independent of import from outside [35].

Recent discoveries, such as the identification of the Per Geijer REE deposit in Kiruna in northern Sweden, demonstrates the potential to improve European access to rare earth resources in the long term [36]. The Per Geijer deposit has previously been described as the largest known rare earth element-deposit in EU with exceeding one million tonnes of rare earth oxides deposit. The deposit is considered to be important for future supply share especially for electric motors since the demand is expected to increase. However, mining and processing operations are not expected to commence in the near term because of the complexity of the path from discovery to mining. The process includes mining permits and assessing environmental impact. Based on the permitting timelines in the mining industry, commercial mining and deliveries of raw material are not expected to begin until after the 2030s. In parallel LKAB is planning a circular industrial park in Luleå for extraction and processing of rare earth elements where the production is expected to start 2027. Even though the Kiruna area has been mined for many years, the discovery of rare earth elements is quite recent.

In addition to the Kiruna area, other rare earth element occurrences have been identified in Sweden [37]. One example is Norra Kärr in southern Sweden, which is classified as a rare earth element resource. The deposit is associated with alkaline igneous rock. Furthermore, there are other locations that have been identified such as Norberg, Olserum and Riddarhyttan-Bastnäs.

Additional efforts are also being made to strengthen REE processing capacity in Northern Europe. A Norwegian company called REEtec AS involving technology for separation aims to establish a more complete value chain using energy efficient and low emission technologies [38]. The first processing facility was expected to be operational in the mid 2020s, while additional capacity is planned later in the decade to handle material from future mining operations in Sweden. These developments represent an important step toward reducing Europe's dependence on external processing, particularly from China. At the moment, 100% of the processing is imported to EU [33]. However, the availability of separated REEs from these facilities remains dependent on the successful and timely development of upstream mining project. As a result, although processing capacity in Europe might start improving, it does not eliminate the short- to medium-term supply risks connected with REEs.

In addition to the findings from the literature, an interview made with Anders Nordelöf[1] provides further insight into the challenges of developing a European RE supply chain. In Europe, projects related to mining and processing often take longer time due to strict environmental regulations and democratic processes, where local communities can influence or delay decisions. While these processes are important from a sustainability perspective, they also slow down the development of domestic production. This can increase the risk that Europe becomes dependent on other regions. At the same time, countries such as China have built up their RE industry over several decades, which has allowed them to develop both technical knowledge and efficient production systems.

---

[1] Anders Nordelöf, Professor at VTI and Visiting Researcher at Chalmers, Gothenburg, 2026-02-26

However, there are several projects around the world, as seen in Fig. 4.1 [39]. According to [40], there are also several other projects outside of China, some of which are in the US as well as Brazil, Russia and Vietnam. There are also locations in Africa, specifically in South Africa, Uganda and Angola.

Figure 4.1: Locations of REE projects around the world. Adapted from *Simplified World Map* by Guilherme de Souza Vieira, licensed under CC BY-SA 3.0. Markers added by the authors [39].

Another perspective on REEs is the supply risks provided by the EU founded REEsilience project that takes into account environmental, social and governance (ESG) risk perspectives [41]. The study explains that environmental risks are mainly concentrated in ecologically sensitive regions such as Brazil, Central Africa, and Southeast Asia, while social risks are more pronounced in densely populated areas, particularly in parts of Africa and South Asia. Governance related risks follow broader institutional patterns, with countries such as those in Scandinavia, Canada and Australia exhibiting the lowest risks levels. Going forward, it is expected that Canada will be one of the global leaders in the REE production, as they rank among the top countries with rich deposits of REEs [42]. There is ongoing research on potential environmental risks that are associated with the ongoing development of REE production in Canada, showing incentive of environmental assessment and mitigation of harm. Some of the sites with REE deposits include Nechalacho and Strange Lake.

Australia is well placed to be a major supplier of REEs due to having a wide range of deposits containing REEs [43]. The deposits are divided into different groups, where Carbonatite is one of them. There are several significant carbonatite related deposits of which Mount Weld is included and is significant. This deposit has been in active mining since 2007 and there are claims that it has the highest grade REE deposit globally [44]. Australia stood for 4% of the global production of rare earth oxides (REOs) in 2022 [40]. Outside of Mount Weld there are other locations such as the Olympic Dam, Dubbo, Nolans Bore and Yangibana [40], [44].

In June 2024 the Norwegian company called Rare Earths Norway (REN), has announced a mineral resource of 8.8 million tones of total rare earth oxides [45]. Which shows that the Fen Carbonatite Complex in Norway contains the largest known rare earth element deposit in continental Europe, even larger than the Per Geijer deposit.

There have been several deposits identified all over Europe, for some which need more exploration. In Greenland and Finland there are several places with identified deposits of Carbonatite type while others are of Alkaline igneous rock [37]. However, the locations in Finland that have been identified still need some exploration but economic resources are likely to be present. Some of the identified locations are Katajakangas, Korsnäs and Sokli. Regarding Greenland, there are two locations that are compliant with the reporting codes JORC or NI-43–101. These are frameworks for mineral resource reporting, meaning they have a formal estimate of the REE resources. These two locations are called Sarfartoq and Motzfeldt. The rest still require some exploration [37].

There is also extraction going on in Myanmar, near the border to China. However, there are several problems since environmental regulations are almost non existent there [46]. Due to this, the companies responsible for mining have no obligations to do assessments on environmental impact or to develop strategies in order to mitigate potential harm. Furthermore, due to the political state in Myanmar, organizations perceive the extraction as means of financial resistance first and foremost. This is done in order to handle pressure from the military state of Myanmar. Regarding the lack of harm mitigation strategies and assessments on the environmental impact, miners have reported negative health effects. Moreover, there have been reports of contamination of land and local water sources due to toxic chemicals that are used in the extraction process [46]. In 2014 it was recorded that 96.1% of the population in Chipwe Township, which has the largest concentration of REE extraction, relied on untreated water as their main source of drinking water and other domestic needs. This is a problem from a trade point of view, as Chinese traders are concerned about the toxicity levels of the crops from farmers who live near the mining sites [46]. Due to the environmental impact and the harm caused to the residents and workers near the mining sites in Myanmar, using Myanmar as an alternative REE source to China is counterintuitive from an CRMA and sustainability perspective.

In addition to China, India is also classified as one of the primary countries for rare earth elements, accounting for approximately five percent of the total world REE reserves [47]. India primarily exploits monazite as its main rare earth resource, which predominantly contains light rare earth elements. Consequently, the country will remain heavily dependent on imports to meet its demand for heavy rare earth elements.

Given its substantial reserves, India could potentially serve as an important supplier of REE to regions such as the European Union. However, extensive mining and production activities have resulted in significant environmental and health impact. Processes including mineral processing can release dust that contains REE. These emissions pose risk to surrounding soil, water, human health etc. thereby limiting the sustainability and scalability of REE production in the country which in turn goes against the CRMA [47],[35].

As noted, Europe has significant potential for the availability of rare earth elements, particularly in the northern regions of the EU. Moreover, due to its long mining history, the EU hosts numerous old and abandoned mining sites as well as large volumes of mine tailings [48]. To date, many of these sites have not been systematically assessed to determine whether they contain recoverable and economically valuable raw materials.

Under the Critical Raw Materials Act, the European Commission is granted the authority to require active mining operations to assess the recovery potential of critical raw materials from their waste streams. For closed and abandoned mines, the member states are responsible for collecting relevant data, conducting targeted sampling campaigns, and publishing information on the critical raw material content of mine waste and tailings in openly accessible databases. This framework aims to improve transparency, enable the identification of promising recovery opportunities, and support the development of secondary raw material supply within the EU [48].

4.2 Material Cost

The cost of REEs is affected by a balancing problem related to the demand for different co-products [49]. Some co-products have higher demand, and are often more scarce, which leads to oversupply of less demanded co-products due to being present in the deposits [50]. Due to the dynamic of supply and demand, as well as geopolitics and speculation in the market, REEs are subject to noteworthy fluctuations in price.

HRE elements tend to be a fraction of the total ores that are mined. In the Bayan Obo mine in China, the LRE element Neodymium stands for 18.6% of the total rare earth oxides (REOs), while the HRE elements are below 1%, if they even exist. Similarly, in the Ionic clay ore REEs are at most a few percent of the whole ore [50]. Due to the limited supply, the price will increase as a result of the high demand.

It also means there is a significant difference in the cost between most light rare earth oxides (LREOs) and heavy rare earth oxides (HREOs). When looking at the 3-year average price of the different elements, where the price of Lanthanum is normalized. The price of the rest are compared to the normalized price of Lanthanum oxide. LREOs, such as Neodymium and Praseodymium, have averaged around 100 between 2021 and 2024. During the same period HREOs, such as Dysprosium and Terbium, have averaged around 400 and 1800, respectively [50]. The prices of HREs are notably higher than LREs. As shown in Fig. 4.2, the prices of HREOs are significantly higher than those of LREOs.

Based on an interview with Anders Nordelöf[1], co-author of the referenced study, the normalization of prices relative to lanthanum was used to enable comparison between different datasets and time series, while reducing the influence of inflation and inconsistencies in available price data.

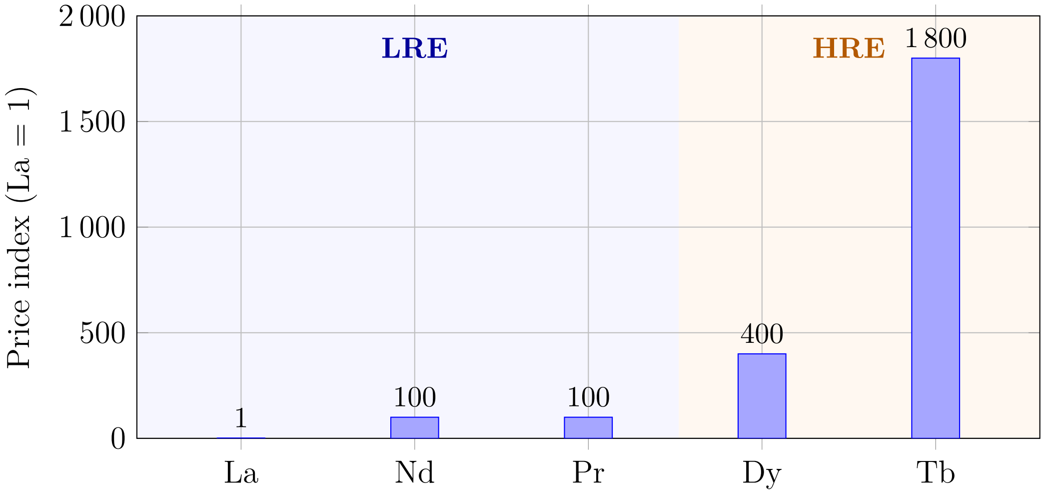

Figure 4.2: Relative average prices of selected rare earth oxides between 2021 and 2024 normalized to the price of lanthanum oxide.

Another way of reducing the HRE content and thereby potentially also the cost is to modify the manufacturing process. As discussed in Section 2.4.2, several manufacturing approaches have been developed to reduce the required HRE content. One example is the grain boundary diffusion process, where HRE elements are diffused into an already sintered magnet instead of being added uniformly during alloying [26],[14]. This approach concentrated the HRE elements at the grain boundaries where they are most effective in improving coercivity, allowing the total amount of HRE material to be reduced and thereby lowering the overall cost of the magnet.

In addition to the literature, insights from an interview with Anders Nordelöf[1] indicates that the price of REE is mainly driven by market demand rather than production cost. For example, HREEs such as dysprosium are expensive primarily because they are needed in small quantities but are in high demand. This means that the high price is not only due to the difficulty of extraction, but also because of supply–demand imbalance. As a result, the prices of REE can vary significantly over time depending on market conditions.

4.3 Environmental Impact

The extraction of REEs is associated with direct CO_2 emissions arising from mining activities [51]. Model-based estimates indicate that emissions are expected to increase steadily over time, rising from approximately 71.5 kt in 2010 to about 92.5 kt by 2030.

This trend reflects the growing demand for rare earth materials driven by the expansion of green energy technologies such as electric vehicles.

In addition to direct CO_2 emissions, the total greenhouse gas emissions from REE mining, expressed as CO_2 equivalents, have increased substantially over the past decade [51]. Global emissions have risen by approximately 94% between 2010 and 2020, from around 79 kt CO_2 eq to more than 150 kt CO_2 eq, and are projected to reach nearly 170 kt CO_2 eq by 2030. This projected increase in emissions is illustrated in Fig. 4.3. China accounts for the largest share of these emissions, followed by the US, Myanmar, and Australia. Again, this dominance is primarily explained by China's leading role in primary RE production.

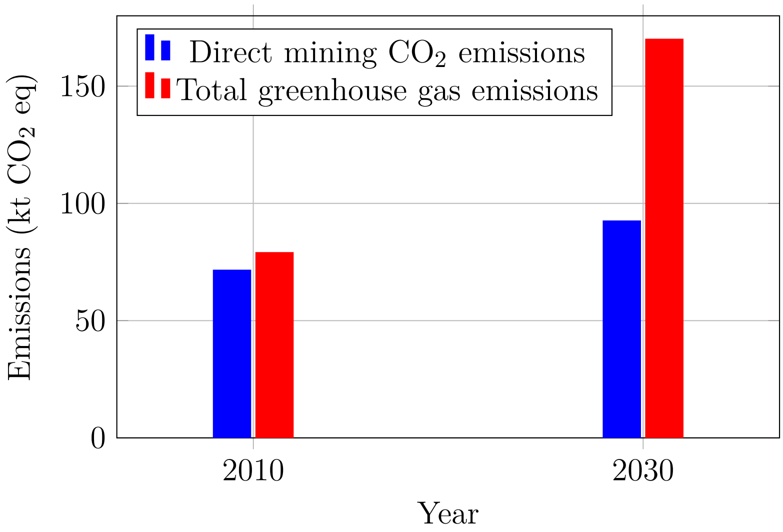

Figure 4.3: Projected greenhouse gas emissions associated with global rare earth element production between 2010 and 2030.

Beyond the mining stage, the processing of REE represents an even more significant contributor to climate impact. CO_2 emissions associated with the processing of both light and heavy REE are projected to increase markedly from 2010 onward [51]. While LREE dominate emissions due to their larger production volumes, processing-related emissions rise across all RE categories as demand increases.

Further, the environmental burden of REOs can be allocated based on their economic value, meaning that REOs with higher economic value are assigned a larger share of the total CO_2 emission [50]. As a result, HREEs such as terbium and dysprosium show significantly higher allocated greenhouse gas emissions compared to LREEs such as praseodymium and neodymium. This difference does not reflect higher physical processing requirements, but rather the market value of HREEs.

From the study in [50], the allocated share of total production emissions per kilogram of a specific REO is presented. This represents all greenhouse gas emissions associated with producing one kilogram of the oxide, including mining, beneficiation and processing and separation steps. For example, terbium oxide reaches approximately 3100 kg CO_2 eq per kg REO, while dysprosium oxide reaches around 800 kg CO_2 eq per kg REO. In contrast, praseodymium oxide and neodymium oxide exhibit substantially lower values, on the order of 200 kg CO_2 eq per kg REO. This difference is illustrated in Fig. 4.4, where HREOs exhibit significantly higher allocated emissions than LREOs.

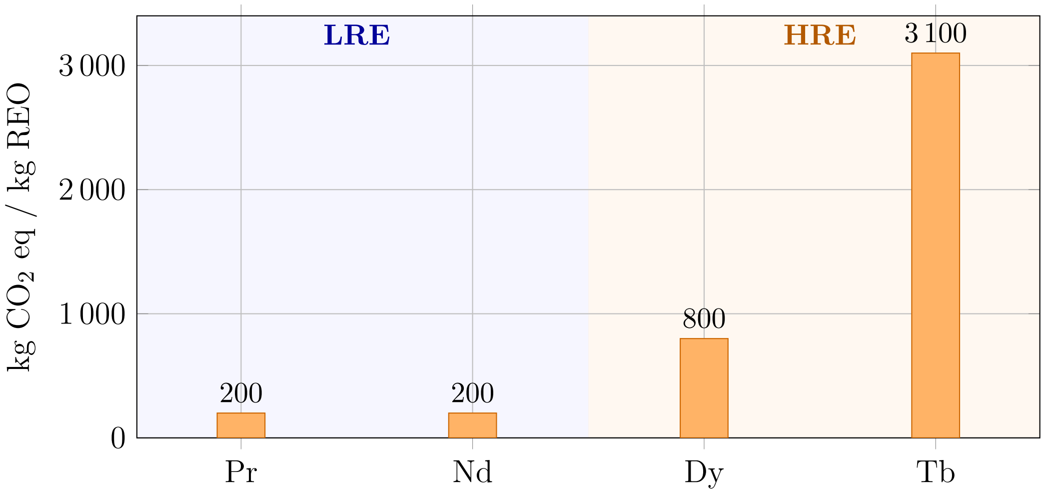

Figure 4.4: Allocated greenhouse gas emissions per kilogram of selected rare earth oxides based on economic allocation.

Due to their similar production routes and comparable economic values, praseodymium and neodymium result in largely similar allocated environmental burdens [50]. Consequently, substituting praseodymium for neodymium in magnet applications does not lead to significant change in the carbon footprint at the material level. However, when assessing the impact at the motor level, where both neodymium and dysprosium are present in the magnets, the allocation effect partially offset each other. As a result, the overall climate impact becomes less sensitive to the choice of allocation year, while the selection of the REO supply route emerges as the dominant factor influencing total greenhouse gas emissions.

An additional aspect highlighted in the interview with Anders Nordelöf[1] the importance of considering both environmental impact per unit mass and total material usage. REE have a high environmental impact per kilogram, mainly due to energy intensive processing and chemical separation. However, the total amount of RE material used in electric machines is relatively small. In contrast, materials such as copper are used in much larger quantities. Even though copper may have a lower impact per kilogram, the total environmental impact can still be significant due to the large volumes required. This shows that both the material intensity and the total mass must be considered when evaluating the overall environmental impact.

Recognizing the trade-offs mentioned with for example HREE compared to LREE, the

CRMA empowers the European Commission to establish information requirements for the environmental footprint of critical raw materials [48]. By increasing transparency of those materials, the Act aims to support informed decision-making, promote more sustainable supply routes, and reduce the overall climate impact of clean energy technology.

Water consumption from REE mining shows a similar upward trend. In mining, water use increases gradually over time, with China's consumption rising from approximately 0.40 million cubic meters in 2010 to an estimated 0.52 million cubic meters by 2030 [51]. However, the processing stage is substantially more water intensive than mining. Global water consumption during REE processing is estimated to be more than twenty times higher than that required for extraction. Between 2010 and 2020 alone, water use in processing increased by over 80% and projections for 2030 indicate total consumption exceeding 20 million cubic meters annually.

In addition to climate-related impact, RE mining and processing pose significant environmental challenges due to the presence of radioactive elements in REE-bearing minerals [51]. If not properly managed, these activities can generate serious environmental and health risks. It has been reported that the production of one tonne of REO may require the handling of up to 1.4 tonnes of radioactive waste in solid, liquid, or gaseous form. The management of radioactive residues is therefore a critical concern and highlights the urgent need for strict regulations and improved safety measures in rare earth mining and processing operations.

In addition to environmental concerns related to extraction and processing, the dependency on REEs has become an important driver for research and innovation within the PM sector. Two recent European Union funded projects, BEETHOVEN and GREENE, explicitly address the need to reduce reliance on critical REE materials. According to those projects the REEs are classified as critical raw materials due to several factors that include significant environmental and social impact associated with production. For example, the production of one tonne of NdFeB magnets has been reported to generate approximately 0.013 tonne of toxic waste, 74m^3 of residual wastewater, 12 000m^3 of process gas, and about one tonne of radioactive waste.

During an interview with the managing director at *Sura Magnets AB*, it was stated that the global demand for NdFeB magnets increased from 248 kt in 2024 to 300 kt in 2026. For comparison, according to *Sura Magnets* China currently exports around 6 500 tons per month. When the environmental footprint is considered, producing the required 500 tons of magnets would generate approximately 6 500 tons of toxic waste, 37 500 cubic meters of contaminated water requiring treatment, 6 000 cubic meters of gas emissions, and about 500 tons of radioactive waste. However, it remains highly uncertain whether a fully non Chinese supply chain for sintered NdFeB magnets exists today. It may even be doubtful, although not entirely impossible.

Considering the energy-intense process of mining and processing REEs, the energy mix that is used is of utmost importance. Globally, the expected energy consumption increase for production of REEs is from 2.55 PJ to 5.47 PJ between 2010 and 2030 [51]. This is due to the increased demand of REEs that has led to an increased production. In China during 2024, the combined share of the grid-mix of electricity was a combined share of 71.3% for coal and oil, of which 52.81% was from coal [52]. By using a sustainable grid-mix, one can make the energy-intense process more sustainable. On the other hand, the energy-mix in for example Sweden in 2024, where there are potential deposits for REE mining, have no fossil fuels [53]. The primary source is hydropower, which accounts for approximately 37.6% of the total production, then comes nuclear and wind power with 28.8% and 24%, respectively. As illustrated in Fig. 4.5, China's electricity production is still largely dependent on fossil fuels, whereas Sweden relies mainly on low carbon electricity sources.

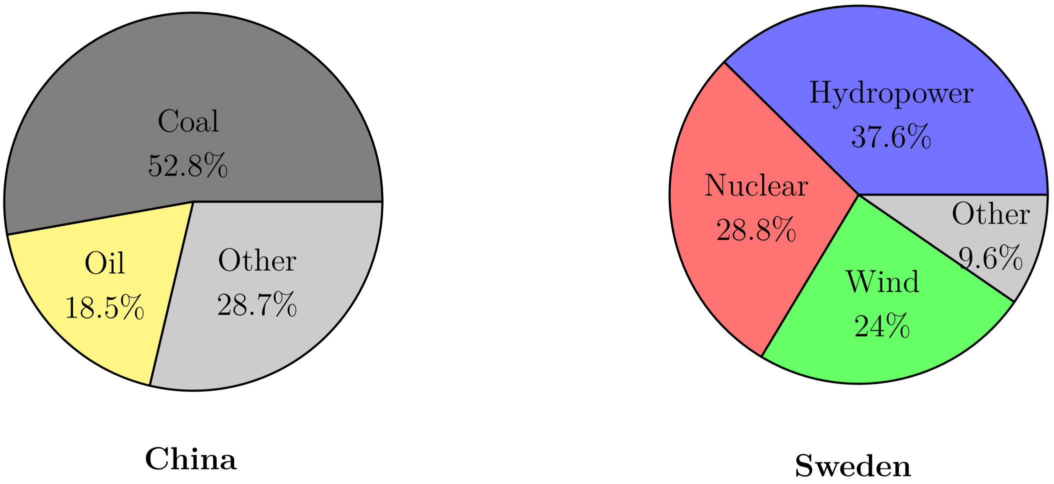

Figure 4.5: Comparison of electricity generation mix in China and Sweden in 2024.

4.4 Supply Chain Resilience

One way to strengthen the RE magnet supply chain is to increase recycling. At the moment, recycling of permanent magnets remains limited. Of all permanent magnet recycling, less than 1% of magnets come from electric machines [54]. The reason for the lack of recycled PMs from electric machines is ineffective collection of PMs, technical difficulties to separate said magnets from the rest of the machine and high expenses. Furthermore, most of the recycling is done in China [55].

There are different ways to separate the magnets from the rest of the machine, but not with ease. One way is to mechanically remove them, at least for surface mounted PMSMs. The problem identified is that the magnets easily could get damaged due to their brittle nature [56]. The same study also tried to separate them thermally. For this approach the problem was the Curie temperature of the magnets which is about 350°C for the

Nd-based magnet compared to the temperature at which the adhesive glue started to get dissolved, around 200°C. Due to this, the magnets were not fully demagnetized and thus there was a risk that the surface mounted magnets would uncontrollably fly out of the machine due to leftover magnetic forces which could cause damage to both the magnets and the heating stove. Furthermore, heavy smoke from the decomposition of the glue is also not environmentally friendly [56].

There are, especially for machine applications, also difficulties with reusing PMs since the dimensions of the magnets are important for the properties. Essentially the dimensions of the magnets are locked to the design of the original machine [54]. Due to the variety in shapes and sizes, an automated disassembly that is efficient enough is hard to achieve [57]. Thus standardization of rotor and magnet designs would improve the possibility of automated disassembly.

In order to make recycling a more viable option, the design of the machines themselves have to take recycling into account. A potential design option is to create segmented magnets [58]. There are several benefits with segmented magnet, but what is to be highlighted is that they are more easily reusable than the standard solid configurations. Usually magnets have a unique shape making reuse difficult, thus small segmented magnets have the potential to be easily manipulated to achieve specific shapes, making reuse easier [58]. This is valid as long as the glue holding the segments can be easily dissolved.

In turn to mitigate supply chain risks, the European Commission has placed increased emphasis on security of supply as a key priority [48]. This approach reflects the need for the EU to remain resilient in the event of import disruptions, for example from dominant supplier countries such as China, or in response to sharp price increases of rare earth elements that may lead to geopolitical risks. To address these challenges, the European Commission promotes the development of more efficient recycling technologies and improve resource efficiency. This to reduce material losses and enable critical raw materials to be reused repeatedly rather than continuously extracted from primary sources. These measures are not voluntary. Companies are required to improve the recovery of critical raw materials from end-of-life products and waste streams, while the member states are responsible for ensuring that effective collection and recycling systems are implemented and maintained [48]. In the case of REE used in electric motors, such measures play a crucial role in enhancing supply security while simultaneously reducing dependence on primary extraction and associated environmental impacts.

Recent industrial developments indicate that some of the previously identified recycling challenges are beginning to be addressed. During an interview with the managing director at *Sura Magnets AB*, the hydrogen based short loop recycling approach developed by HyProMag was highlighted as a promising solution for recovering NdFeB magnets [59]. Where according to HyProMag recycling facilities can establish faster and with lower investment compared to primary production sites. Experiments and industrial validation made by HyProMag shows that magnets produced from hydrogen processed NdFeB powder can reach commercial performance levels. In reported studies, recycled magnets with more than 95 percent recycled content achieved remanence values around 1.3 T and coercivity levels above 1000 kA per meter, corresponding to grades such as N45M and N42M. Further material optimization and blending have enabled coercivity improvements and progress toward higher temperature grades such as UH and EH. These results indicate that recycled magnets can meet the performance requirements of demanding applications, including automotive auxiliary systems. Nevertheless, there is still clear room for improvement. Ongoing research, particularly in grain boundary diffusion using HREE, is expected to further enhance coercivity and thermal stability. This suggests that recycled magnets have additional potential for performance gains in future automotive applications. The technology is also progressing toward industrial deployment. Pilot scale work was first demonstrated at the University of Birmingham in the United Kingdom, followed by a larger demonstration facility at Tyseley Energy Park. Commercial scale up activities are now ongoing through HyProMag operations in Germany and other parts of Europe. These developments suggest that advanced recycling technologies could play an important role in strengthening the resilience and sustainability of the RE magnet supply chain.

Recycling of PM is often discussed as a way to reduce supply risks. However, insights from another interview with Anders Nordelöf[1] show that there are several practical challenges. One major difficulty is collecting and disassembling products as mentioned even according to the literature, especially in applications such as electric vehicles where the magnets are not easily accessible. In Addition, magnets are difficult to handle and must be carefully extracted from the motor to avoid contamination from surrounding materials, which makes it challenging to obtain sufficiently concentrated material streams.

Another challenge is that recycled magnets may have lower performance compared to new materials. This is partly related to the redistribution of elements such as dysprosium, which may no longer be optimally located within the microstructure after recycling. As a result, additional processing or material input may be required to restore performance. However, using HRE-free magnets is a solution to this challenge. Since HRE-free magnets do not use HREEs to enhance its coercivity through GBD, recycling becomes more feasible as the performance of the recycled magnets would be retained.

In addition, according to Nordelöf recycling must be economically competitive with primary production, which is already highly optimized in countries such as China. This means that even if recycling is technically possible, it may still be difficult to implement on a large scale unless it is also cost effective.

Another alternative to strengthen the supply chain resilience is to continue exploring potential deposits and starting mining projects in locations where sufficient deposits already have been found, which have been mentioned in the previous section on availability of minerals. Furthermore, reducing dependence on China for REE separation would be an important step toward strengthening the supply chain. The main strategies for strengthening the resilience of the RE magnet supply chain are summarized in Table 4.1.

Table 4.1: Summary of suggested strategies for strengthening the resilience of the RE magnet supply chain.

Strategy	**Key Challenges**	**Potential Benefits**
Recycling of permanent magnets	Low collection rates, difficult separation of magnets from machines	Reduces demand for primary rare earth extraction
Design for recycling	Requires redesign and standardization of motors and magnets	Improves disassembly and reuse potential
Hydrogen based recycling	Technology still scaling to industrial level	High recycled content magnets with commercial performance
New mining projects	Environmental regulations and long project timelines	Diversifies supply sources outside dominant regions
Reduced dependence on Chinese processing	Need for new separation facilities and infrastructure	Improves supply chain resilience and reduces geopolitical risks

5

Case set up - Simulation

The case set up for simulation describes how the HRE-free rotor alternatives are evaluated from an electromagnetic performance and demagnetization point of view. The analysis is based on a reference PMSM model, where the original HRE-based magnets are replaced by selected HRE-free magnet grades and later combined with rotor geometry modifications.

The simulations are performed mainly in Ansys Motor-CAD. The workflow includes material implementation, short-circuit based demagnetization analysis, rotor geometry studies, optimization, and final benchmarking against the original reference machine.

5.1 Reference PMSM Model

The reference machine in this study is based on a previously developed and evaluated PMSM model and is used as the starting point for all simulations. Only the rotor is studied while the stator is included in the model but kept unchanged in all simulations.

The machine has 8 poles, corresponding to 4 pole pairs, and a double-layer rotor topology, as shown in Fig. 5.1. This design used NdFeB magnets of grade N42UH containing HRE elements.

The rotor consists of two magnet layers per pole arranged in a V-configuration. The inner layer denoted as Layer 1 (L1) contains longer magnets located closer to the rotor center, while the outer layer denoted as Layer 2 (L2) consists of shorter magnets positioned closer to the air gap, as shown in Fig. 5.2.

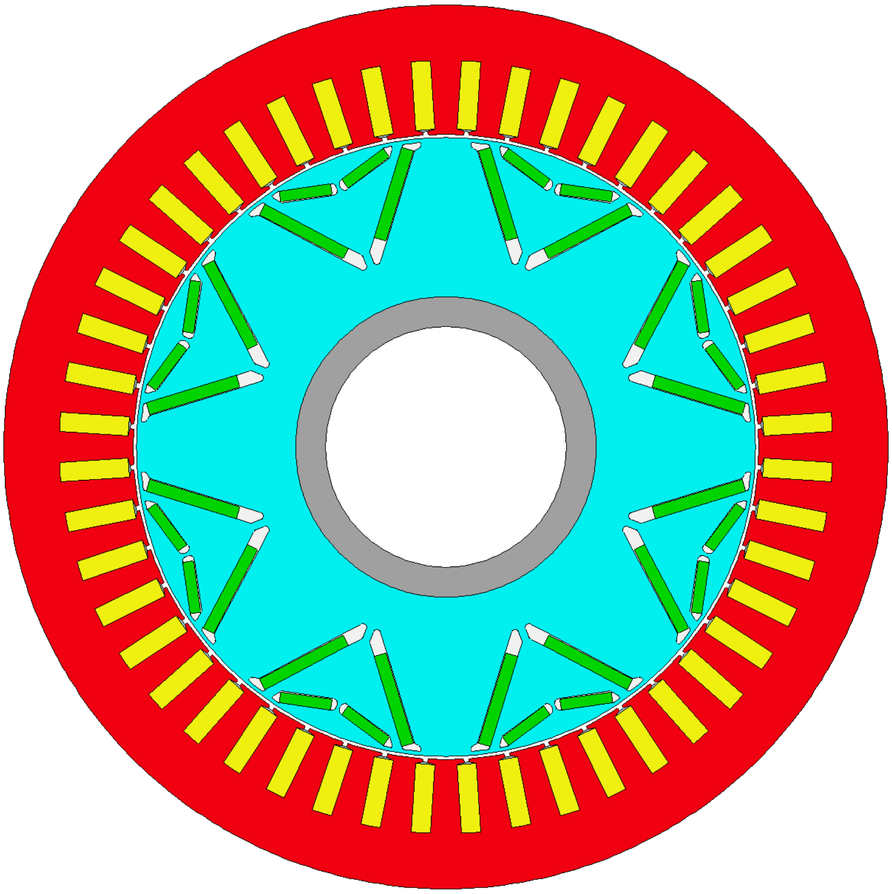

Figure 5.1: Reference PMSM model.

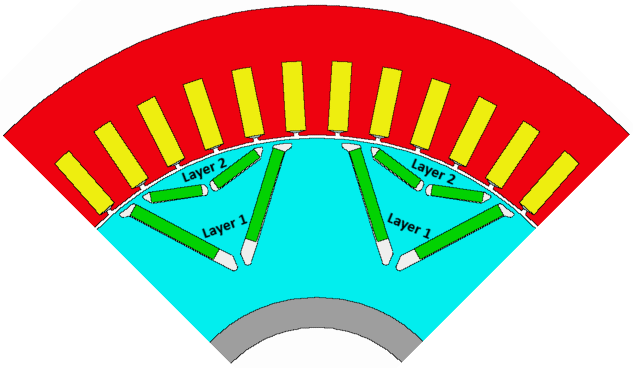

Figure 5.2: One pole pair highlighting Layer 1 and Layer 2

5.2 Magnet Material Data and Implementation

The magnet grades considered in this study are provided as part of an internal material screening. The dataset focuses on HRE-free magnet grades and contains several magnet grades collected from multiple material sources relevant for the investigated machine design.

The occurrence of the identified magnet grades across the reviewed sources is summarized in Table 5.1. Each column represents one source (S1 corresponds to Source 1, S2 to Source 2, and so on). The shaded cells indicate that the corresponding magnet grade is present in that source.

In addition to the grade classification, the provided dataset includes temperature-dependent magnetic properties. In Table 5.1 the values inside the grey cells represent the maximum recommended operating temperature in °C. For each grade, the values of $\boldsymbol{B_r}$ and $\boldsymbol{H_{cj}}$ are available at multiple temperatures. The temperature range varies between the different magnet grades depending on their intended operating condition. The reference temperature for the material data is 20°C, at which the nominal values of $\boldsymbol{B_r}$ and $\boldsymbol{H_{cj}}$ are defined. The corresponding ranges of these properties across the investigated magnet grades are summarized in Fig. 5.3. In addition to the graphical representation at 20°C, the temperature dependent material data for all investigated magnet grades are summarized at selected temperature levels (20°C, 100°C, 120°C, and 140°C) as ranges in Appendix A.

Table 5.1: Occurrence of investigated magnet grades across anonymized sources. Shaded cells indicate presence, and the values inside denote the recommended maximum operating temperature (°C).

Magnet Grade	S1	S2	S3	S4	S5	S6
35SH	150			140		
38SH				140		
40SH	150		180	140		
42SH	150	150	180	140	140	150
45SH	180	150	180	140	180	160
48SH			180			
48H				140		
50SH						160
50H				140		
52H				140		160
52M				140		
54M				140		
N56				140		
N58				140		

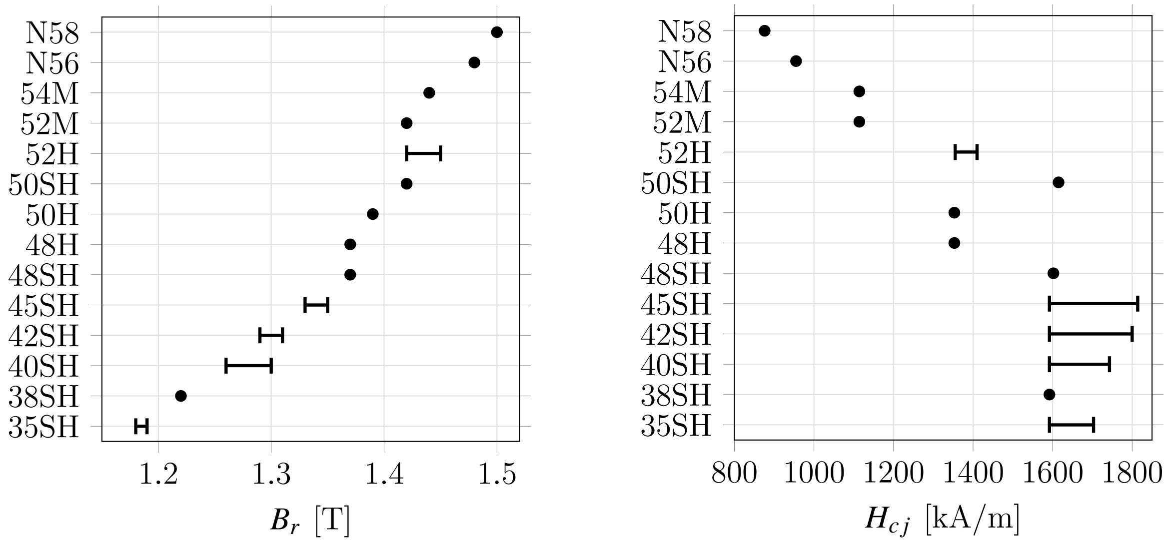

Figure 5.3: Comparison of the variation in B_r and H_{cj} at 20°C for the investigated magnet grades. Horizontal lines indicate value ranges across available sources, while markers indicate single reported values.

To implement this data in Motor-CAD, the temperature dependent material properties are defined manually. For each magnet grade, the available data points for B_r and H_{cj} at specific temperatures are entered directly into the software.

The number of available temperature points varies between the different magnet grades. In some cases, only a limited number of data points are provided, while in the other cases more extensive temperature dependent data is available. As introduced in Section 2.3.3, the variation of B_r and H_{cJ} with temperature is governed by the RTCs, which describe the underlying thermal behaviour of the magnet material.

A quadratic temperature scaling model is used in Motor-CAD to represent the non linear variation of B_r and H_{cJ} with temperature. For each magnet grade with multiple data points are available across a wider temperature range, the model parameters are defined automatically by the software based on the provided data. For magnet grades with more limited temperature data, the available points are entered manually, and the quadratic model is used to interpolate between these values within the specified temperature range. In these cases, the model relies directly on the provided discrete data points.

In Motor-CAD, the quadratic temperature scaling is expressed as

$$B_r(T) = \alpha_0 + \alpha_1 T + \alpha_2 T^2 \tag{5.1}$$

$$H_{cJ}(T) = \beta_0 + \beta_1 T + \beta_2 T^2 \tag{5.2}$$

where α_0, α_1, and α_2 are the coefficients describing the temperature dependence of B_r, while β_0, β_1, and β_2 describe the temperature dependence of H_{cJ}.

5.3 Demagnetization Analysis and Performance Evaluation

An automation script written in Python enables multiple simulations for different magnet grades and temperature conditions in Motor-CAD. For each magnet grade, simulations are performed over a temperature range starting from 100°C up to 140°C, using increments of 10°C. This upper temperature limit is selected as a common threshold that all investigated magnet grades are able to withstand, ensuring a consistent basis for comparison. The overall simulation workflow is illustrated in Fig. 5.4.

The machine is mapped to determine its electromagnetic characteristics over the investigated operating points. For this operating point, Motor-CAD determines the phase advance angle according to the selected MTPA control strategy. The phase advance angle represents the orientation of the stator current vector in the dq reference frame and is equivalent to the current angle β introduced in Section 2.6.4. The phase advance is defined between 0 and 90 degrees in Motor-CAD. At this operating condition, the phase advance is automatically determined to correspond to the MTPA operating point at base speed. In this case, the operating point is calculated from the maximum current. The resulting phase advance is used as input for the short circuit transient simulation.

The short circuit transient simulation is performed in order to determine the maximum demagnetizing current. From this result, the negative peak d-axis current is extracted and used as the current amplitude in the subsequent demagnetization analysis. During the demagnetization run, the phase advance is set to 90°, such that the current vector is aligned with the d-axis to represent a worst-case condition for demagnetization. This case is presented as Short Circuit Condition (SCC) in the thesis. In the simulations the short circuit event is artificially simulated by applying the transient current amplitude in the load cycle, where the transient current amplitude is taken from a short circuit simulation while operating in base speed at maximum current. This is considered worst case in terms of transient short circuit currents.

The demagnetization calculation is performed at high-load conditions corresponding to maximum torque operation and base speed, where the maximum voltage from the battery is extracted. This is where the magnetic loading of the machine is the highest. During field weakening the maximum battery voltage is still utilized however, the magnetic loading decreases due to the negative d-current.

To quantify demagnetization, the ratio between the effective remanent flux density (B_r) after the simulation and the initial B_r is evaluated. This ratio provides a measure of the extent of irreversible demagnetization in the magnets. Since the rotor consists of multiple magnet layers, the demagnetization is evaluated individually for each layer with the help of the Python script. The relative reduction in remanent flux density is calculated as

$$D_i = \frac{B_{r,calc} - B_{r,eff,i}}{B_{r,calc}} \tag{5.3}$$

where $B_{r,calc}$ is the initial remanent flux density and $B_{r,eff,i}$ is the effective remanent flux density of layer i after the demagnetization simulation.

Following the demagnetization step, the impact on machine performance is evaluated through torque and back EMF simulations using custom drive cycle consisting of five electrical cycles. The drive cycle is structured such that the first two cycles correspond to normal operating conditions, the third cycle represent a transient event introducing demagnetization, and the final two cycles again represents normal operation, now after the demagnetization has occurred.

To quantify the performance degradation, cycle two and five are compared, representing the machine behavior before and after the demagnetization event, respectively. For torque, the average value over each cycle is evaluated, while for the back EMF the RMS value is used.

In addition to evaluating the demagnetization under worst-case conditions, the machine performance is also assessed under normal operating conditions. For this purpose, the original maximum operating current 707 A is applied along the d-axis to simulate the worst possible case under normal operation. This case will be presented as Normal Operating Condition (NOC) during the thesis. Again, this is done for maximum torque and base speed. This allows for an evaluation of how irreversible demagnetization affects the machine performance during standard operation.

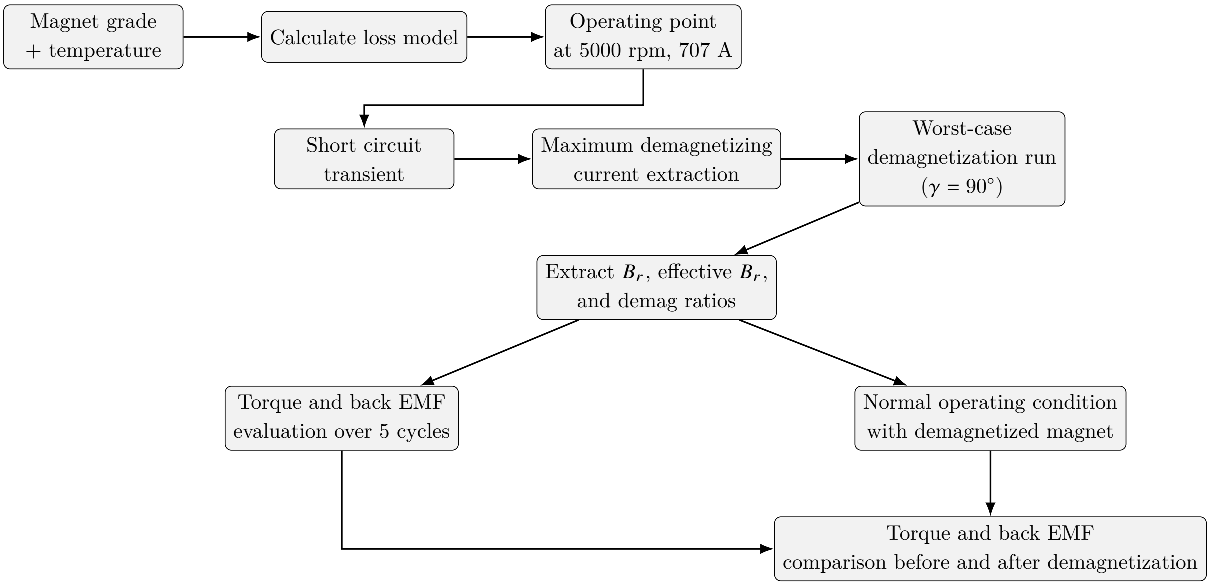

Figure 5.4: Workflow used for automated demagnetization and post-demagnetization performance evaluation in Motor-CAD.

5.4 Custom Magnet Design Based on Demagnetization Requirements

Following the initial evaluation of all investigated magnet grades, a subset of candidates is identified based on their resistance to irreversible demagnetization. From this subset, the magnet grade that demonstrated the highest resistance to irreversible demagnetization is selected as a reference case for further analysis. In this study, the selected reference magnet corresponds to the 45SH grade from one of the sources, with original material properties at 20°C of $\boldsymbol{B_r} \approx 1.34$ T and $\boldsymbol{H_{cj}} \approx 1800$ kA/m.

Based on this reference magnet, a custom magnet material was defined by systematically modifying the $\boldsymbol{B_r}$ and $\boldsymbol{H_{cJ}}$. The purpose of this modification was to investigate the required material properties needed to withstand worst-case demagnetization conditions identified in the previous analysis.

The custom magnet is implemented in Motor-CAD by defining user-specific magnetic material properties. The temperature-dependent behavior of $\boldsymbol{B_r}$ and $\boldsymbol{H_{cj}}$ is adjusted by modifying the coefficients α_0 and β_0 in the quadratic model given in (5.1) and (5.2). Since these coefficients are constant, the changes affect all temperatures equally.

To study the effect of each parameter, separate sweeps of β_0 and α_0 are performed. For the coercivity variation, β_0 is increased, which increased $\boldsymbol{H_{cJ}}$ at 20°C from 1730 kA/m to 2230 kA/m, corresponding to an increment of 50 kA/m per test. For the remanence variation, α_0 is varied, which changed $\boldsymbol{B_r}$ at 20°C from 1.37 T to 0.87 T, corresponding to a decrement of 0.05 T per test.

In addition to the independent parameter sweeps, combined cases are also evaluated by pairing the corresponding β_0 and α_0 values from the individual studies. In the first combined sequence, $\boldsymbol{H_{cJ}}$ is increased stepwise with an increment of 50 kA/m per test while $\boldsymbol{B_r}$ is decreased stepwise with a decrement of 0.05 T per test. In the second combined sequence, both $\boldsymbol{H_{cJ}}$ and $\boldsymbol{B_r}$ increased simultaneously and this case increment of 0.05 T per test for $\boldsymbol{B_r}$. A summary of all considered variations is presented in Table 5.2.

Each variation is defined using 11 test cases, where each test corresponds to a specific set of material properties. For example, Test 1 represents the lowest $\boldsymbol{H_{cJ}}$ value, while Test 11 represents the highest $\boldsymbol{H_{cJ}}$ value. The same test numbering is used consistently when combining $\boldsymbol{H_{cJ}}$ and $\boldsymbol{B_r}$.

The modifications are mainly based on the reference temperature values of $\boldsymbol{B_r}$ and $\boldsymbol{H_{cJ}}$, while the values at other temperatures are adjusted automatically according to the quadratic model. By combining these modifications, custom magnet characteristics are created and evaluated.

The same simulation workflow as described in Fig. 5.4 is applied to the custom magnet. In this way, the demagnetization behaviour and resulting machine performance can be directly compared to the originally investigated magnet grades.

The objective of this step is not to optimize performance under normal operating conditions, but rather to ensure that the magnet material is capable of withstanding worst-case demagnetization scenarios without significant degradation. This allows for the identification of material property requirements for robust magnet design in the investigated application.

Table 5.2: Summary of material property variations used for the custom magnet study at 20°C.

Case	H_{cj} [kA/m]	B_r [T]	Description
H_{cj} variation	1730 → 2230	Constant	Increasing coercivity
B_r variation	Constant	1.37 → 0.87	Decreasing remanence
Combined (trade-off)	Increasing	Decreasing	paired sweeps
Combined (target)	Increasing	Increasing	paired sweeps

5.5 Rotor Geometry Parametric Study

The rotor geometry is modified manually in Motor-CAD in order to study the influence of key design parameters on the demagnetization behaviour. A parametric approach is used, where selected parameters are systematically varied based on the original design at 140°C.

The analysis is primarily based on the previously selected reference magnet, which exhibited the highest resistance to irreversible demagnetization, namely 45SH from S6. In addition, a subset of magnet grades with similarly strong performance is included to enable a comparative evaluation of rotor design sensitivity and required magnet material across different grades. All configurations are evaluated using the same simulation workflow as described in Fig. 5.4. For each case, the demagnetization behaviour, short circuit current, torque, and other relevant electromagnetic quantities are analyzed.

The main parameters investigated are magnet thickness, magnet bar width, magnet separation, pole V-angle, magnet post thickness, web thickness, and web length. The corresponding geometric modifications are illustrated in Fig. 5.5. The modifications are defined relative to the original design values, and the parameters are varied stepwise within a predefined range.

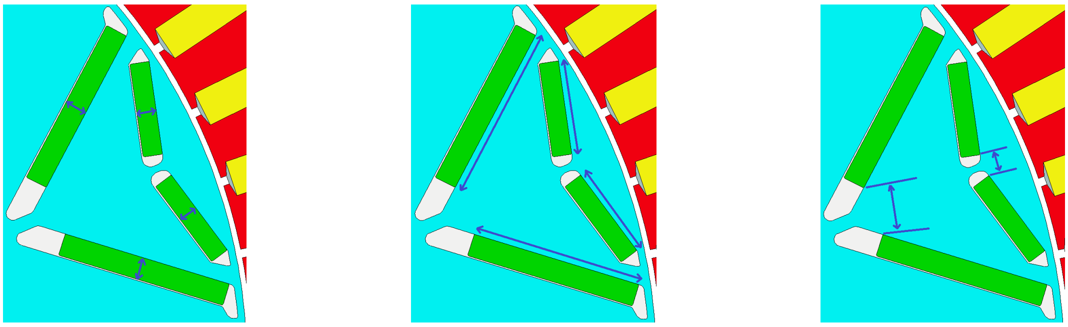

(a) Magnet thickness (b) Magnet width (c) Magnet separation

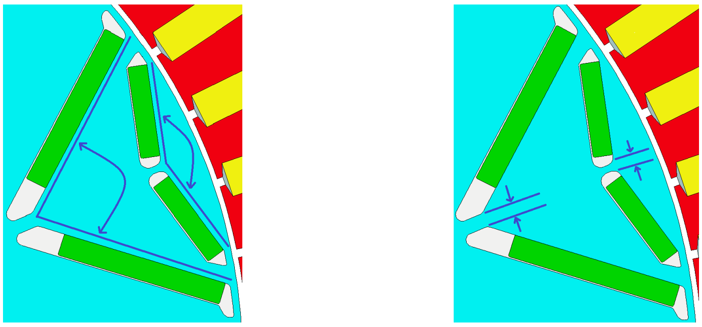

(d) Pole V-angle (e) Magnet post

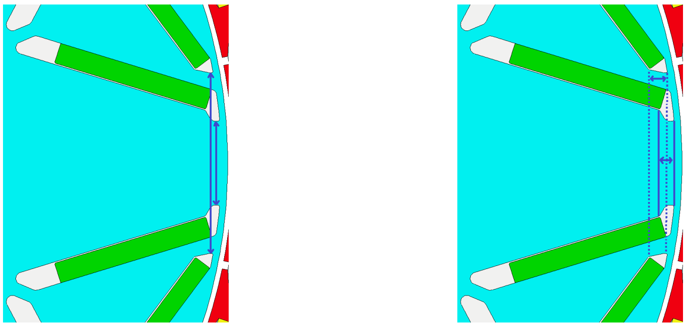

(f) Web thickness (g) Web length

Figure 5.5: Definition of the investigated rotor geometry parameters used in the case set-up.

Individual Rotor Geometry Variations

The magnet thickness was increased in both Layer 1 and 2 in order to improve resistance to demagnetization. The investigated values ranged from 3.2 mm to 5.2 mm for Layer 1 and from 2.8 mm to 4.8 mm for Layer 2, as summarized in Table 5.3. In some cases, the magnet width was reduced simultaneously to maintain a constant area between the thickness and width, in order to keep a constant magnet volume, the concept is illustrated in Fig. 5.6. This allowed the effect of geometry changes to be isolated.

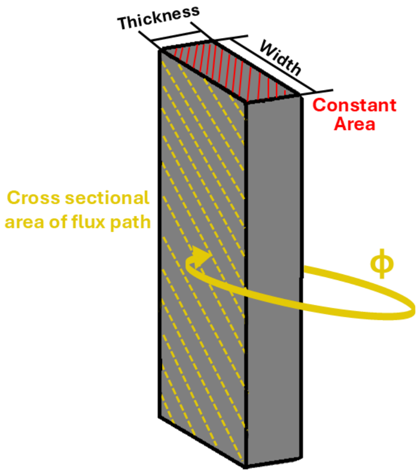

Figure 5.6: Illustration of the magnet geometry showing thickness, width and the constant area. The arrow indicates the direction of the magnetic flux.

The remaining individual variations included magnet separation, pole V-angle, magnet post thickness, web thickness, and web length. These parameters are varied separately for Layer 1 and Layer 2 relative to the original rotor geometry in order to evaluate their individual influence on demagnetization behaviour and electromagnetic performance. The original values and investigated ranges for all individual geometry variations are summarized in Table 5.3.

Table 5.3: Summary of investigated rotor parameter variations

Parameter	Layer	Original	Tested values	Unit
Magnet thickness	L1	3.2	4.0, 4.4, 4.8, 5.2	mm
	L2	2.8	3.6, 4.0, 4.4, 4.8	mm
Magnet width*	L1	25.65	adjusted to keep constant area	mm
	L2	13.94	adjusted to keep constant area	mm
Magnet separation	L1	7.2	7.7, 8.2	mm
	L2	3.2	3.55, 3.9	mm
Pole V-angle	L1	79.1	64, 71.545, 80.95, 82	deg
	L2	151.4	125, 138.2, 160.7, 168	deg
Magnet Post	L1	2	0.5, 3.5	mm
	L2	1	0.2, 2	mm
Web thickness	L1	12.27	8, 22	mm
	L2	27.03	22.26, 31.8	mm
Web length	L1	1.127	0, 2.5	mm
	L2	0.81	0, 2.5	mm

*Magnet width is adjusted in selected cases to maintain a constant magnet area when thickness is varied.

Combined Rotor Geometry Variations

In addition to the individual parameter studies, a set of combined rotor geometry configurations is evaluated on the selected 45SH grade, used as reference. These configurations are constructed by combining parameter values showing promising results in the individual studies presented in Table 5.3. The evaluated combinations are summarized in Table 5.4 and parameters are given for Layer 1 and Layer 2 as L1/L2.

The combinations are defined with increasing complexity. First, individual variations in pole V-angle and web thickness are considered (Combinations 1–3). These are followed by cases where magnet thickness is combined with the selected pole V-angle (Combinations 4–6). In Combinations 7 and 8, web thickness is further included. Finally, in Combinations 9–11, all parameters, including magnet separation in Layer 1, are varied simultaneously.

Table 5.4: Overview of the evaluated combined rotor geometry configurations.

Combination	Pole V-angle L1/L2 [deg]	Magnet thickness* L1/L2 [mm]	Web thickness L1/L2 [mm]	Separation L1 [mm]
1	64 / 125	–	–	–
2	71.5 / 125	–	–	–
3	–	–	19.0 / 31.8	–
4	71.5 / 125	4.4 / 4.0	–	–
5	71.5 / 125	4.0 / 3.6	–	–
6	71.5 / 125	4.6 / 4.2	–	–
7	71.5 / 125	4.4 / 4.0	19.0 / 31.8	–
8	71.5 / 125	4.0 / 3.6	19.0 / 31.8	–
9	71.5 / 125	4.4 / 4.0	19.0 / 31.8	13.2
10	71.5 / 125	4.0 / 3.6	19.0 / 31.8	13.2
11	71.5 / 125	4.4 / 4.0	19.0 / 31.8	15.2

*The magnet width is adjusted according to the corresponding magnet thickness.

5.6 Rotor Geometry Optimization

An optimization of the rotor geometry is carried out with Ansys optiSLang. This is done for several magnets, particularly 45SH, 42SH from one of the sources and a custom magnet with increased H_{cJ} to approximately 2000 kA/m with a constant $\boldsymbol{B_r}$ of 1.34 T. Also, the optimization is done according to the SCC operating case since it is the worst possible case. To do the optimization, Motor-CAD and optiSLang are coupled using Python scripting. The optimization consists of four stages

1. Sensitivity analysis
2. Meta-modelling
3. Optimization
4. Validation

In the sensitivity analysis, a design of experiments is conducted. This is done by a sampling method that generates data sets on performance from Motor-CAD. The sensitivity of the output parameters to variations in the input parameters is then characterized. Following the sensitivity analysis, Meta-models of Optimal Prognosis (MOPs) are built from the results of the first step. The MOPs are used to generate fast and accurate mathematical surrogate models that describe the relationship between the model input parameters and the resulting output objectives and constraints. This step is called Meta-modelling. With the generated meta-models, an optimization step is carried out. Either a local or global optimizer can be used and these can be combined with multiple objectives and constraints. After the optimization step is carried out, the optimum surrogate models based on the MOP are the validated with Motor-CAD.

The chosen input parameters with their current value and range are displayed in Table 5.5. These are the same variables that were varied in Section 5.5 in both Layer 1 and 2, however the bridge thickness and pole arc was additionally included. The bridge thickness is illustrated in Fig. 5.7. A smaller bridge thickness reduces the radial distance between the air gap and the magnet together with the flux barrier region. In contrast, a larger bridge thickness increases this distance, moving the magnet and flux barrier region further inward from the air gap. Bridge thickness was added in order to optimize the distance between the magnets and the air gap. The pole arc, on the other hand, is the angle covered by the magnet layer inner web, measured in electrical degrees. Increasing the pole arc makes the magnet layer wider in the angular direction, so the ends of the layer move further apart. Decreasing the pole arc makes the layer narrower, so the ends move closer together. Criteria for different variables can be set, including performance variables such as torque. The criteria can also be set at specific operating points. Alongside the requirements, up to 3 objectives can be set. The objectives are essentially definitions of outputs that are to be minimized or maximized. Table 5.6 shows the set criteria and objectives.

Table 5.5: Summary of input parameters with their ranges for optimization

Input Parameter	Current Value	Minimum Value	Maximum Value
L1 Pole Arc Ratio	0.80	0.6	0.9
L1 Web Thickness Ratio	0.57	0.2	0.7
L1 Magnet Bar Width Ratio	0.97	0.7	0.99
L1 Web Length Ratio	0.43	0.2	0.7
L2 Pole Arc Ratio	0.70	0.2	0.9
L2 Web Thickness Ratio	0.53	0.4	0.8
L2 Magnet Bar Width Ratio	0.98	0.7	0.99
L2 Web Length Ratio	0.22	0.1	0.5
L1 Magnet Thickness	3.2	3	6
L2 Magnet Thickness	2.8	2.8	4.5
L1 Pole V Angle	79.09	70	150
L2 Pole V Angle	151.4	110	160
L1 Magnet Post	4	2	8
L2 Magnet Post	1	1	8
L1 Magnet Separation	7.2	2	10
L2 Magnet Separation	3.2	3.2	8
L1 Bridge Thickness	1	1	2.5
L2 Bridge Thickness	1	1	2.5

Table 5.6: Summary of optimization objectives and constraints with corresponding targets and limits

Objective/Constraint	Performance Metric	Target/Limit
Objective	Peak Shaft Torque at 3000 rpm	Maximize
Objective	Magnet Weight	Minimize
Objective	Demagnetization Percentage	Minimize
Constraint	Magnet Weight	$\leq$ 4.5 kg
Constraint	Demagnetization Percentage	$\leq$ 10%
Constraint	Peak Shaft Torque at 3000 rpm	$\geq$ 580 Nm

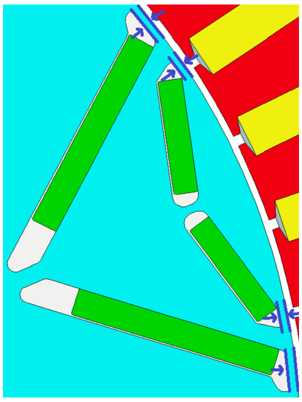

Figure 5.7: The thickness of the bridge between outermost boundary of the magnet layer and rotor surface

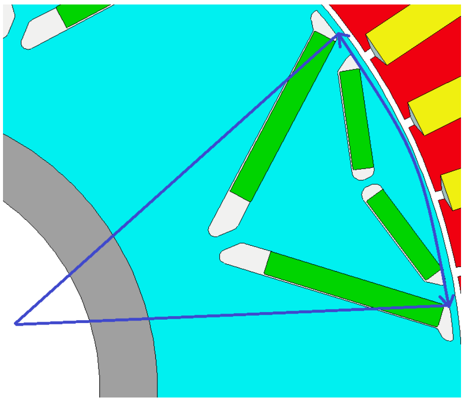

Figure 5.8: The pole arc of the magnet layer inner web in electrical degrees (only for Layer 1 shown)

The exported Python script is edited to add the wanted simulation steps, i.e the demagnetization study. Furthermore, the requirements and objectives are imported to optiSLang. Then the sampling method is selected. The used method is Adaptive Metamodel of Optimal Prognosis (AMOP) and the number of samples is originally chosen as 300. In case more data is needed to improve the meta-model, another sensitivity analysis is added with more samples. To speed up simulations, 12 blackbox licenses were used to be able to run multiple Motor-CAD instances in parallel.

After the simulation of AMOP is finished, the post processing is handled where the estimated sensitivity of output responses to input variables can be visualized. The meta-model can be plotted against two input variables in a surface plot. Here the optimal approximation model is calculated based on sensitivity-based correlation data. This calculation uses the optimal subspace of important variables. How important an input variable is, is quantified by Coefficient of Prognosis (CoP), which is lower than or equal to 100%. CoP is a measure that is based on variance. The higher the CoPs, the more accurate the meta-model predictions become. To increase the CoP, points that are outliers can be deactivated in a residual plot. In the residual plots, it is also possible to find statistical data where the root mean square error for the prediction can be found. This is the relevant measure to determine the quality of the MOP model in the unit of the result. The approximation can be expected to be in the range of ±3 times the root mean square error.

Succeeding the post processing of the AMOP, an optimization can be run based on AMOP. One-click optimization is used and definition of start designs is done manually. The selected start designs are imported from the AMOP simulations and corresponded to designs that are close to, or better than, the defined constraints and objectives. Furthermore, the maximum number of design evaluations is selected to 6000 and in some cases 10000. Lastly, before starting the optimization, the number of best designs to validate is selected as 20.

When the optimization is done, the 20 designs selected as best designs are validated.

5.7 Benchmarking Procedure

In the final step of the simulation workflow, the original reference model is simulated with the N42UH HRE-based magnet using the same procedure described in Section 5.3. This case is used as the reference design for the benchmarking.

The reference design is then compared to the selected HRE-free alternatives. These included the 45SH and 42SH magnets from S6, as well as the custom magnet obtained from the H_{cJ} variation with constant B_r. The custom magnet is defined with H_{cJ}(20°C) of 1980 kA/m and B_r of 1.341 T.

In addition, the optimized rotor designs from Section 5.6 are included in the benchmarking. These consist of the optimized 45SH and 42SH cases from S6, together with two optimized custom magnet designs based on the combined rotor geometry optimization. The purpose of the benchmarking is to compare the original HRE-based reference design with both the non-optimized and optimized HRE-free rotor alternatives, as summarized in Table 5.7.

Table 5.7: Summary of the cases included in the benchmarking study.

Magnet type	Rotor design	Magnet case
Reference, HRE-based	Reference rotor	N42UH
HRE-free alternatives	Reference rotor	45SH
		42SH
		Custom magnet
	Optimized rotor	45SH
		42SH
		Custom magnet 1
		Custom magnet 2

6

Simulation Results and Analysis

This chapter presents and analyses the simulation results used to evaluate the demagnetization behaviour and electromagnetic performance of the investigated HRE-free rotor alternatives. The results include available magnet grades, selected magnet sources, custom magnet variations, rotor geometry studies, optimization, and final benchmarking against the original HRE-based reference design.

Most sections follow the same structure: remaining torque after demagnetization, average torque, back EMF, short-circuit current amplitude, and irreversible demagnetization ratio, expressed as the percentage reduction of the average remanence, $\boldsymbol{B_r}$, in the magnet layers. The results are discussed directly with the figures to connect the observed behaviour to magnet properties, rotor geometry, and operating condition. In the figures, SCC refers to the short-circuit condition, while NOC refers to the maximum normal operating current along the $\boldsymbol{d}$-axis.

Unless otherwise stated, the results are presented as functions of temperature. The rotor geometry studies are instead evaluated at 140°C as functions of the investigated geometry variations. The optimization section differs from the general structure since it focuses on optimized design candidates, parameter influence, Pareto validation, and correlation results. The initial demagnetization study first presents the short-circuit current waveform and repeated short-circuit transients to explain how the demagnetizing current is selected and why one SCC transient is used for the following comparisons.

6.1 Demagnetization Study

This section presents the initial demagnetization study for all available HRE-free magnet grades. The purpose is to evaluate how the different magnets respond to the selected short-circuit demagnetization condition and to identify the most promising candidates for further analysis. Before presenting the main performance results, the short-circuit current waveform and the effect of repeated short-circuit transients are shown.

6.1.1 Short Circuit Response

The short circuit current response was first evaluated in order to understand the transient behaviours during the demagnetization event. In Fig. 6.1 the short circuit current transient is shown for a representative magnet grade at a given temperature. The transient behaviour is consistent across all investigated temperatures and magnet grades, with the main difference being the peak current magnitude, which is the key value. The waveform oscillates considerably until it is damped out after approximately 0.1 s. The figure presented here is only a reference showing the waveform of the short circuit current for the following simulations.

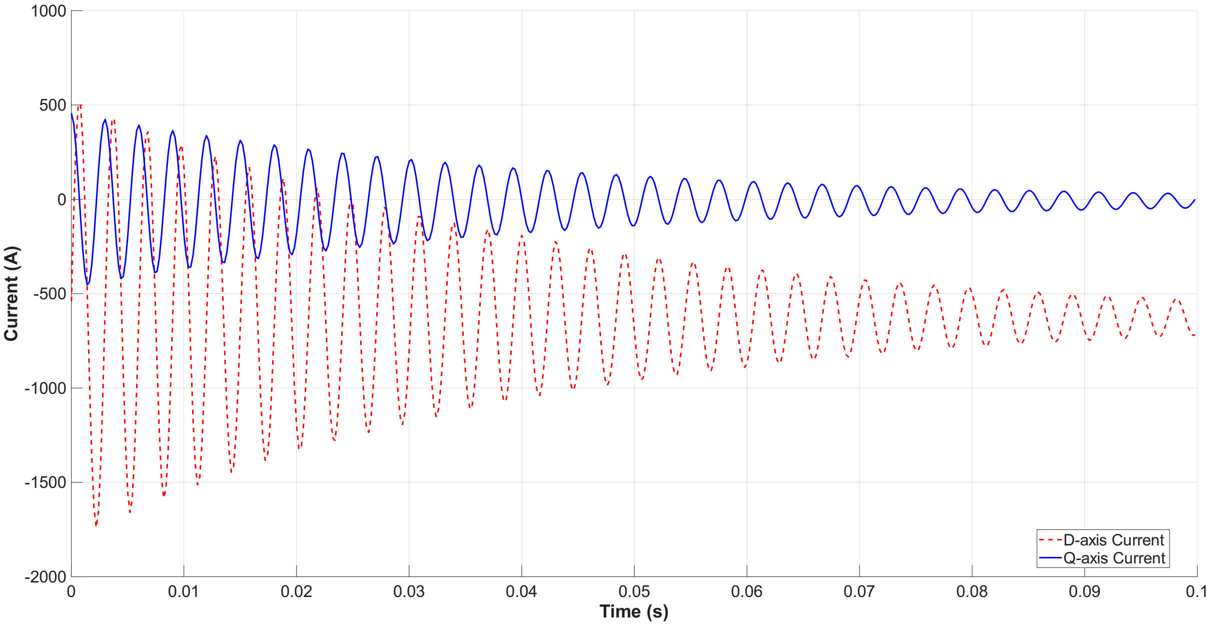

Figure 6.1: Short circuit graphs over time. Dashed line shows d-axis current and solid line shows q-axis current.

Fig. 6.2 presents the transient event from Fig. 6.1 in the i_d-i_q plane, i.e with i_q as a function of i_d. It shows how the current spirals during the transient towards a specific point where it has reached steady state. The oscillatory behaviour seen in the time domain response is therefore also visible in the current plane. This confirms that the short circuit event is a dynamic process where the current components change significantly before the fault response stabilizes.

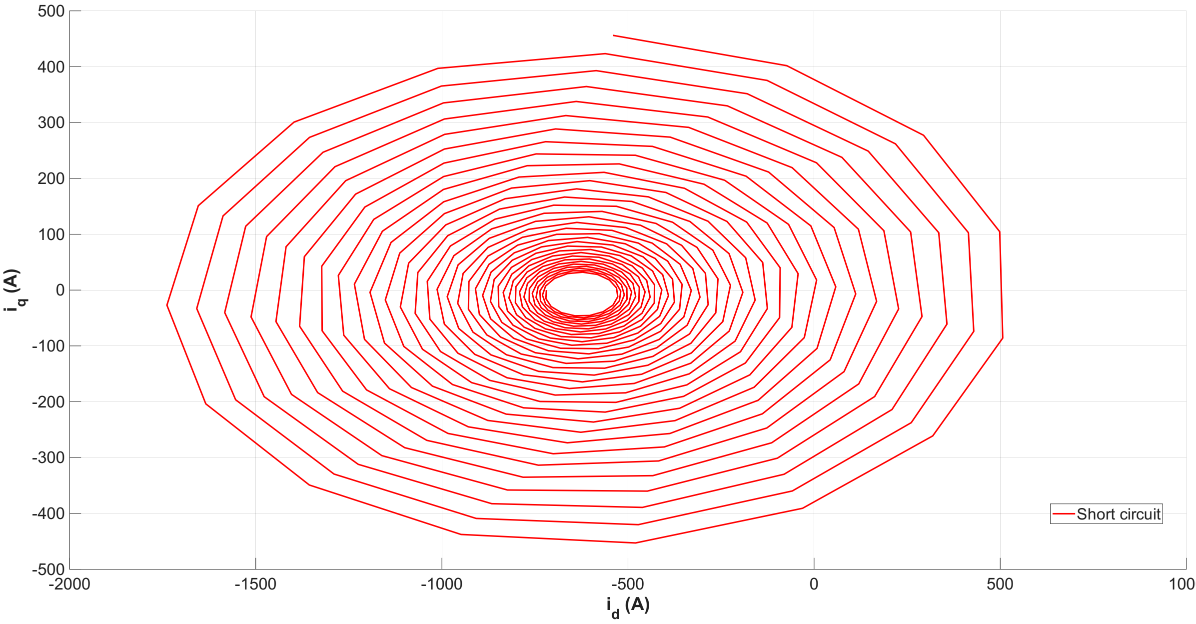

Figure 6.2: Q-axis current as a function of d-axis current during short circuit transient

To investigate whether repeated short circuit events cause additional degradation, three short circuit transients were simulated consecutively, with two cycles of normal operation between each transient. The resulting torque response is shown in Fig. 6.3. The horizontal axis represents the electrical angle, where 360° corresponds to one electrical cycle. During each short circuit event, the average torque drops to approximately 0 Nm. When the machine returns to normal operation, the torque recovers to an average value of approximately 380 Nm.

The torque level after each short circuit transient remains essentially unchanged. This indicates that repeated short circuit events do not cause additional degradation of the machine performance under the studied operating conditions. Consequently, a single short circuit transient is sufficient to represent the worst case demagnetization behaviour for the investigated operating condition. This supports the use of a single SCC based demagnetization event when representing the upcoming results.

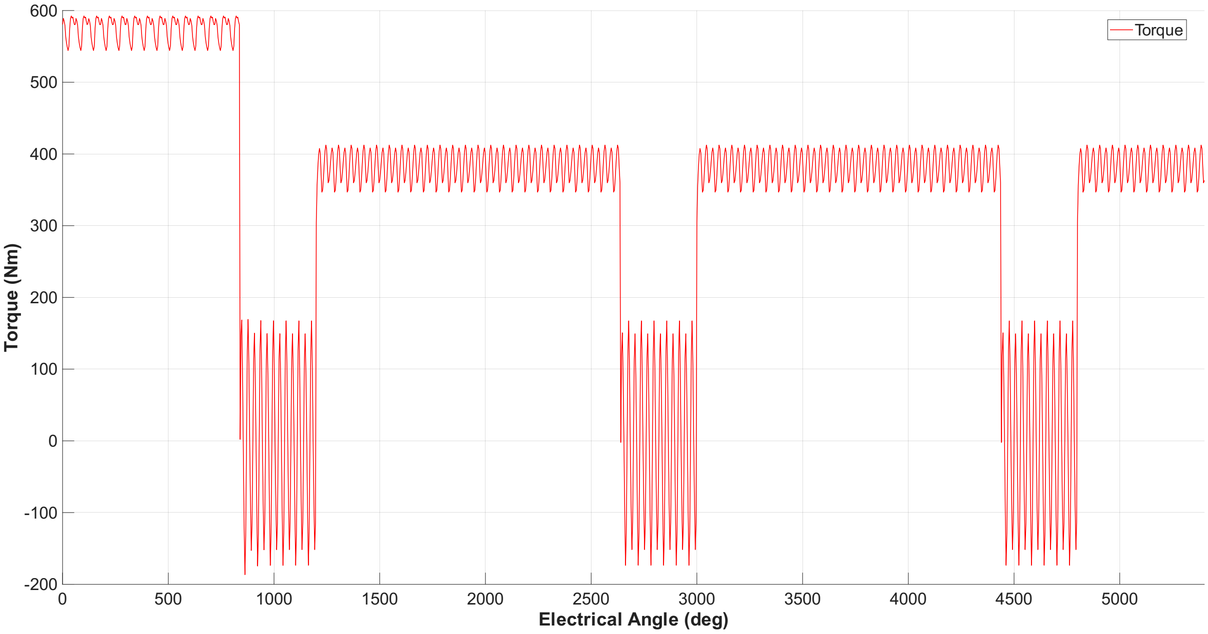

Figure 6.3: Effect on Torque After Three Short Circuit Transients

6.1.2 Torque Response and Influence of Magnet Properties

The torque responses after demagnetization was evaluated for both the short circuit condition (SCC) and the normal operating condition (NOC). This comparison was made in order to investigate how the different magnet grades are affected by irreversible demagnetization and how the remaining torque depends on the magnet material properties, especially remanence and intrinsic coercivity.

Fig. 6.4 illustrates the percentage of the remaining maximum torque after demagnetization during SCC. The figure is divided into two parts, where sources S1–S4 are shown in the left plot and S4-S6 in the right plot, due to the large number of magnet grades from source S4. To clarify, what the plot shows is not the torque retained compared to the absolute maximum torque, but rather the torque retained compared to the maximum torque at a specific temperature.

It is observed that all magnet grades exhibit a reduction in torque already at 100°C, although the magnitude of the decrease varies between the different magnets. With increasing temperature, most magnet grades continue to decrease in torque, typically reaching values between approximately 48% and 55% at 140°C. This indicated that irreversible demagnetization occurs already at relatively moderate temperatures after SCC. As described in Section 2.3.3, demagnetization occurs when when the operating point of the magnet is pushed toward or below the knee point of the demagnetization curve due to the combined effect of reverse magnetic field and reduced intrinsic coercivity, H_{cJ}. Once this happens, part of the magnetization is permanently lost, which directly reduces the effective flux linkage and therefore the torque capability of the machine.

However, several magnets from source S4, particularly those with H and M suffixes such as 48H$_{S4}$, 50H$_{S4}$, 52H$_{S4}$, 52M$_{S4}$ and 54M$_{S4}$, exhibit a behaviour where the torque first decreases and then increases at higher temperatures. A similar trend is also observed for 52H$_{S6}$ and 48SH$_{S3}$. In addition, N56$_{S4}$ and N58$_{S4}$ show an increasing torque with temperature instead of the expected decrease. These deviations are noted, but they are not investigated further since the torque does not recover to a level close to the 500 Nm requirement. The lowest torque values are observed for several H and M grade magnets, reaching approximately 42% of the original torque, while the highest values that reach up to around 68%, are obtained for 45SH$_{S6}$, 42SH$_{S6}$ and 45SH$_{S5}$.

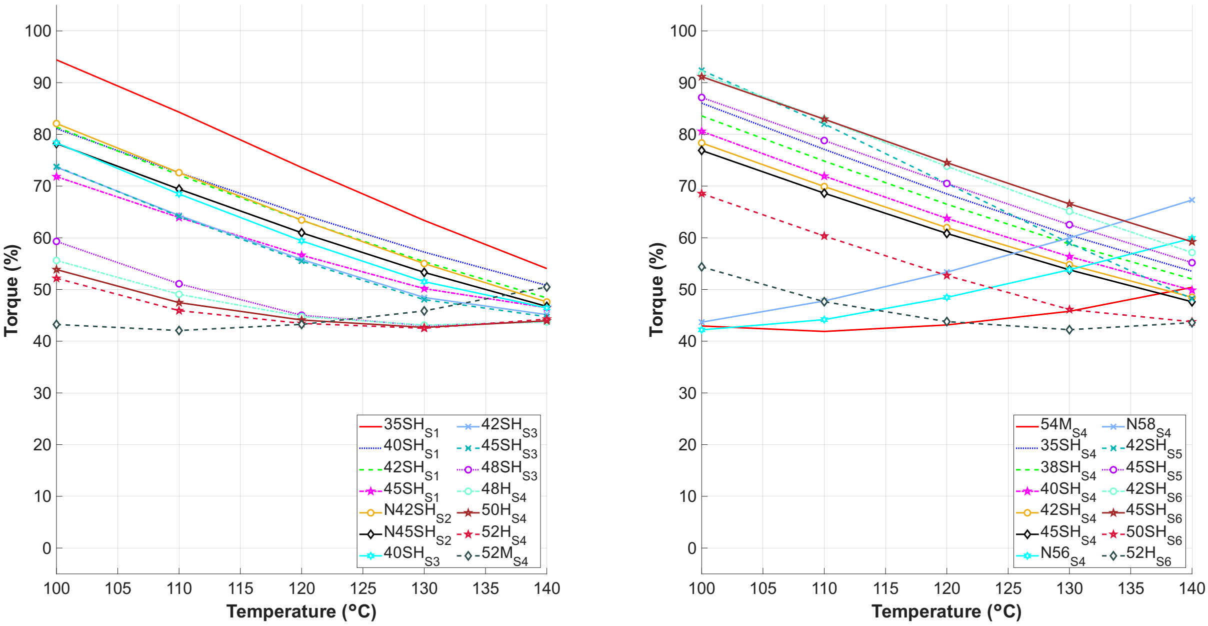

Figure 6.4: Remaining torque as a percentage after demagnetization under SCC for all magnet grades. The subscripts in the legends refer to the magnet sources in Table 5.1.

The observed torque reduction is strongly related to the temperature dependent intrinsic coercivity of the magnets. The XXH and XXM magnet grades show significant torque reduction already at 100°C. Among the magnets included in this study, these magnets have relatively high remanence, with $\boldsymbol{B_r}$ in the range of approximately 1.4 to 1.5 T, but their intrinsic coercivity is comparatively low and decrease rapidly with temperature. For XXH magnets, $\boldsymbol{H_{cJ}}$ decreases from approximately 1300 kA/m at 20°C to around 600 kA/m at 100°C. Similarly, XXM magnets decrease from approximately 1100 kA/m to around 500 kA/m, while NXX magnets decrease from approximately 900 kA/m to around 400 kA/m. This reduction in coercivity means that the magnets lose much of their ability to resist the demagnetizing field generated during the short circuit transient. As a result, the operating point is more easily driven below the knee point, leading to irreversible loss of magnetization.

In contrast, these 42SH and 45SH magnets in the upper end in terms of coercivity show substantially lower torque reduction. The remanence is approximately 1.3 T, but their intrinsic coercivity remains considerably higher at elevated temperatures. At 20°C, $\boldsymbol{H_{cJ}}$ is approximately 1800 kA/m, and even at 100°C it remains close to 900 kA/m. This higher retained coercivity does not completely prevent irreversible demagnetization, but it reduces its extent and helps maintain a more stable magnet operating point. Consequently, the effective flux linkage is better preserved, which explains the smaller reduction in torque. This indicates that, under short circuit fault conditions, retaining sufficient intrinsic coercivity is more important than maximizing remanence.

A deviation from this trend is observed for 48SH$_{S3}$. Although this magnet is classified as an SH grade, its temperature dependent coercivity behaves more similarly to the weaker H and M grades. Its $\boldsymbol{H_{cJ}}$ is approximately 1600 kA/m at 20°C, but decreases to around 600 kA/m at 100°C and approximately 400 kA/m at 140°C. This explains why the torque reduction is significantly larger than for the SH magnets from source S6. The result also shows that the nominal magnet grade alone is not sufficient to predict demagnetization robustness. Instead, the full temperature dependent material data must be considered, including the RTCs and the temperature dependent coercivity model described by (5.2).

It should be noted that the accuracy of the magnet data may vary between the different sources. As described in Section 5.2, some magnets are described by more extensive datasets with several measurement points at each temperature, while other magnets are based on a limited number of values for $\boldsymbol{H_{cJ}}$ and $\boldsymbol{B_r}$ at selected temperatures. Furthermore, it is not clear whether the data comes from serially produced magnets and lab tests. Therefore, differences between magnets of the same nominal grade from different sources may partly be caused by differences in temperature dependence, supplier data quality, and interpolation accuracy.

The case with a NOC is shown in Fig. 6.5. In this case, no magnet grade goes below 60% of the maximum torque. Furthermore, all magnet grades start of by decreasing in torque, but N58$_{S4}$ and N56$_{S4}$ start to increase again after 120°C and 130°C, respectively. Some magnets, notably 35SH$_{S1}$, 35SH$_{S4}$, 38SH$_{S4}$, 40SH$_{S1}$, 40SH$_{S4}$, 42SH$_{S1}$, 42SH$_{S4}$ and 45SH$_{S4}$ do not start decreasing in torque until temperatures above 130°C. Two magnets do not reduce in torque at all, but could possibly be a negligible decrease if any. These magnets are 45SH$_{S5}$, 42SH$_{S6}$ and 45SH$_{S6}$.

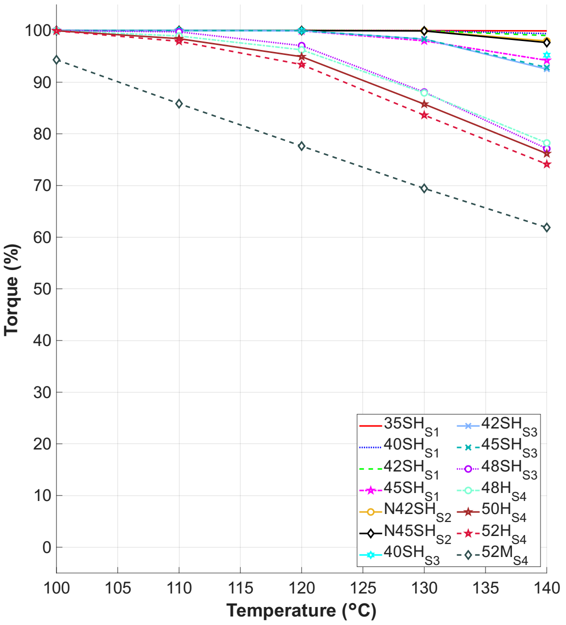

Figure 6.5: Torque behavior for the NOC for all magnet grades. The subscripts in the legends refer to the magnet sources in Table 5.1.

Fig. 6.6 shows the average torque for all magnets under SCC both before and after demagnetization. The trend shows that most magnets have an average torque between 600 Nm and 500 Nm for the whole temperature range except for a few, specifically 52M$_{S4}$, 54M$_{S4}$, N56$_{S4}$ and N58$_{S4}$. After demagnetization all magnets drop below 500 Nm until 140$^{\circ}C$, with the same specific magnets, as well as 48SH$_{S3}$ and 52H$_{S6}$, dropping to approximately 225 Nm.

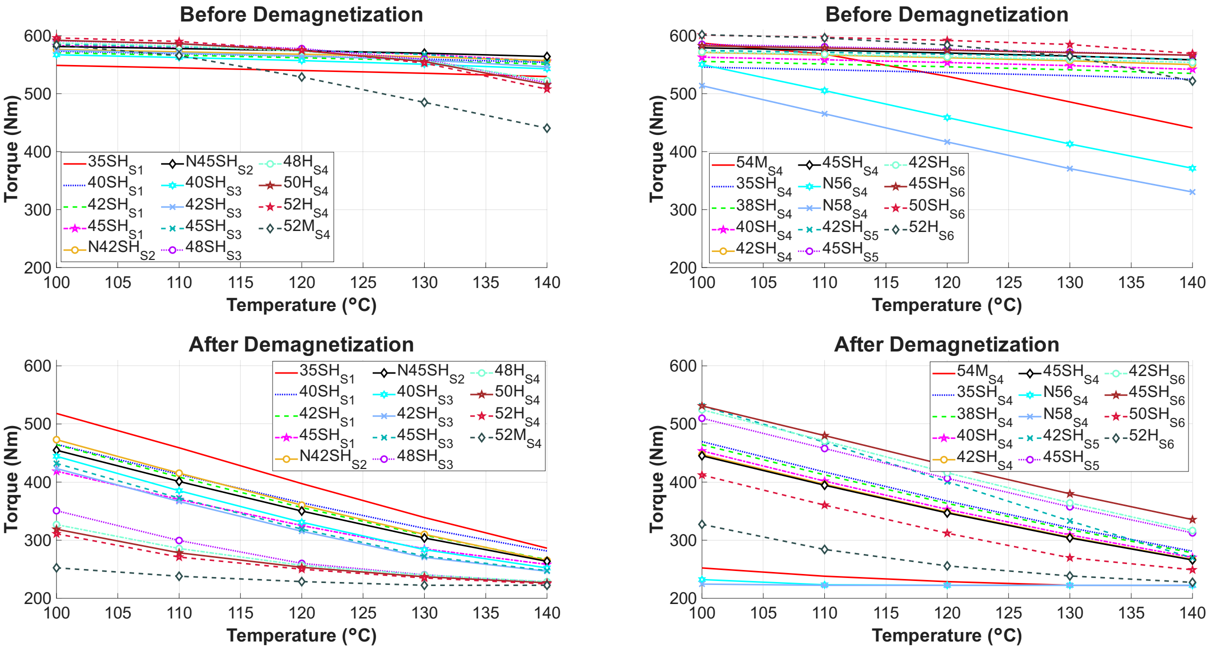

Figure 6.6: Average torque before and after demagnetization under short circuit conditions for all magnets.

In Fig. 6.7 the average torque is shown for NOC. Before demagnetization the torque is identical to Fig. 6.6. After demagnetization, most magnets retain most of their torque, however 48H$_{S4}$, 50H$_{S4}$, 52H$_{S4}$, 52H$_{S6}$, 52M$_{S4}$, 54M$_{S4}$, N56$_{S4}$ and N58$_{S4}$ drop below 500 Nm during the temperature range.

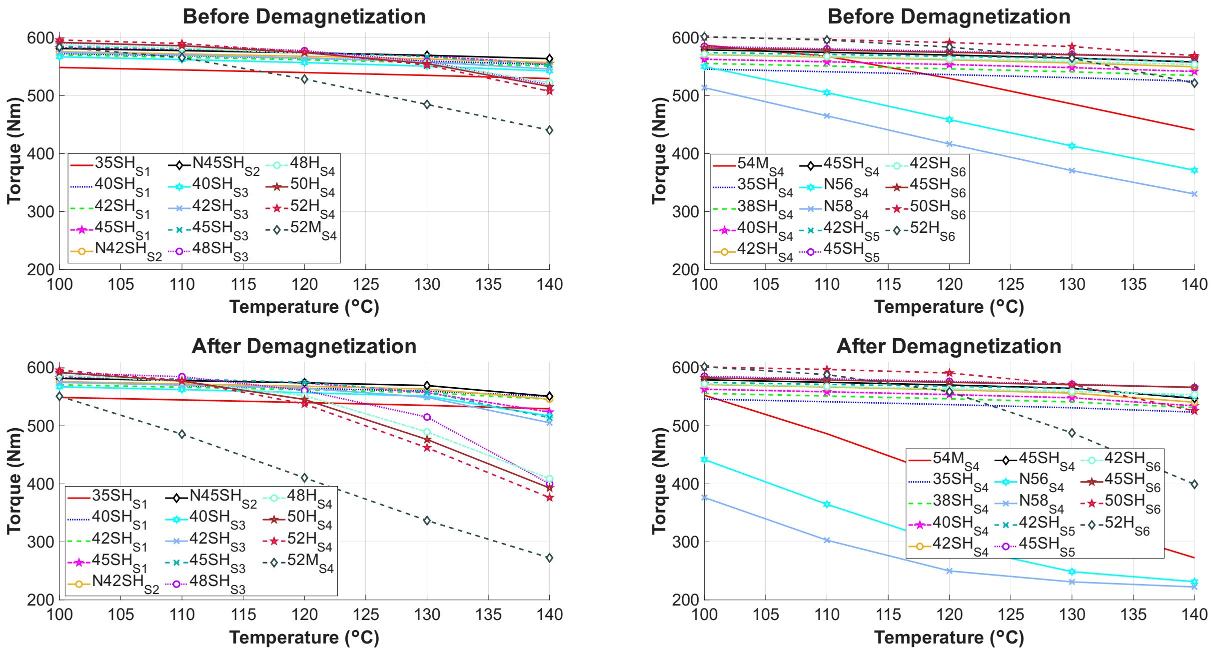

Figure 6.7: Average torque before and after demagnetization under normal operating conditions for all magnets.

A clear difference is therefore observed between the SCC and the NOC. After demagnetization under SCC, the average torque of several magnet grades drops significantly below the required 500 Nm, showing that irreversible demagnetization caused by the fault event can severely compromise the post fault performance. After demagnetization under NOC, the torque generally remains higher, often close to or above 550 Nm, which indicates that partial demagnetization is less severe during standard operation. Nevertheless, the same overall trend is observed in both cases. Magnets with weaker coercivity retention show larger torque degradation, while stronger SH magnets preserve torque more effectively. This confirms that H_{cJ} is a critical parameter not only for limiting irreversible demagnetization during the short circuit transient, but also for maintaining acceptable torque performance after the fault.

6.1.3 Back EMF Response

Fig. 6.8 illustrates the back EMF evolution for SCC for all magnets. Similarily to the torque retention, the back EMF retention is presented compared to the maximum value at the specific temperature. For example N58$_{S4}$ and N56$_{S4}$ are already reduced to 0% at the start of the simulation. All magnets start of with a reduced back EMF, with the highest percentage being approximately 92% at 100°C which is 35SH$_{S1}$. At 140°C, the highest percentage of the original back EMF any magnet has is approximately 27% which is 45SH from S6, meaning that all magnets are reduced to under 30% back EMF. The trend is that all magnets decrease in back EMF, mostly linearly unless it goes to 0%.

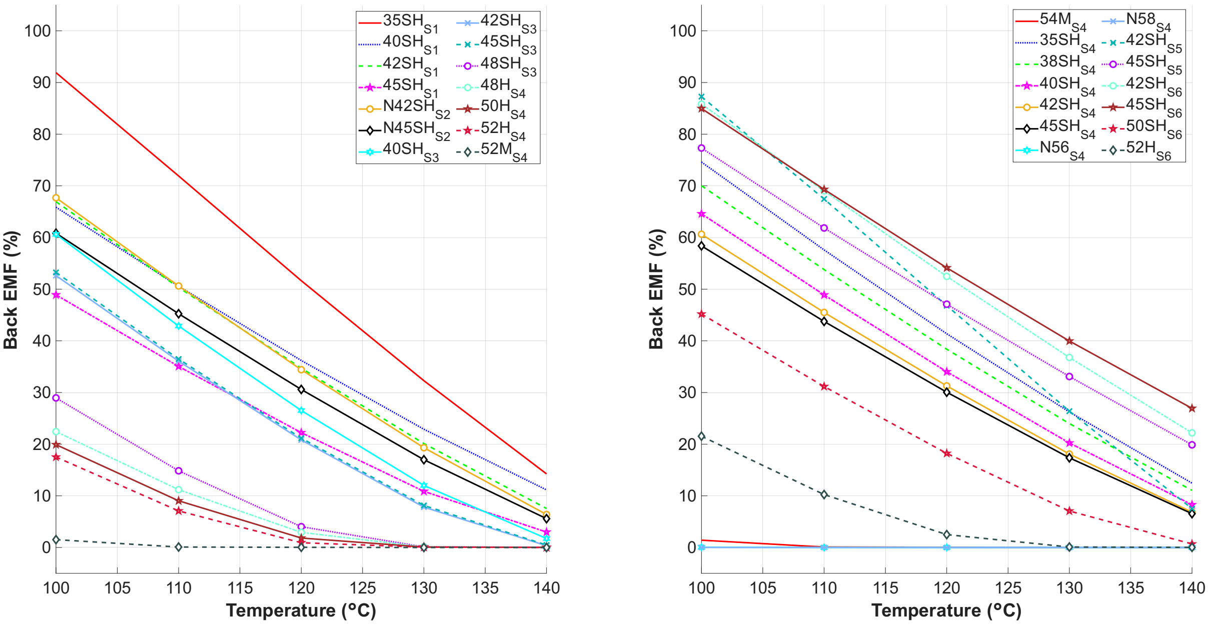

Figure 6.8: Back EMF after demagnetization under SCC for all magnet grades. The subscripts in the legends refer to the magnet sources in Table 5.1.

The same overall material dependent trend is observed in the back EMF response as in the torque response. Magnet grades with lower retained intrinsic coercivity generally show larger reductions, while stronger SH grades retain a larger part of the back EMF. However, the degradation is significantly more severe for back EMF than for torque under short circuit conditions. This difference can be explained by the physical quantities represented by the two responses. The back EMF depends directly on the magnetic flux linkage produced by the permanent magnets. Therefore, a strong reduction in remaining magnetization directly leads to a strong reduction in induced voltage.

The torque response is different because the torque in an interior PMSM does not depend only on the permanent magnet torque component. As described by (2.18), the total torque consists of both the permanent magnet torque and the reluctance torque. Consequently, even if the magnet generated flux becomes very small, a finite torque can still remain due to the reluctance torque contribution and the current excitation. This explains why some of the magnet grades can show almost zero back EMF while still producing finite average torque after demagnetization.

In Fig. 6.9 the back EMF response for NOC along d-axis is shown. Here three magnets decrease negligibly if at all, notably 35SH$_{S1}$, 45SH$_{S6}$ and 45SH$_{S5}$. Several magnets only reduce to 95% or above, specifically 35SH$_{S1}$, 35SH$_{S4}$, 38SH$_{S4}$, 40SH$_{S1}$, 42SH$_{S1}$, 42SH$_{S4}$, 45SH$_{S6}$ and 45SH$_{S5}$. Two magnets reach 0% towards the end, namely N58$_{S4}$ and N56$_{S4}$.

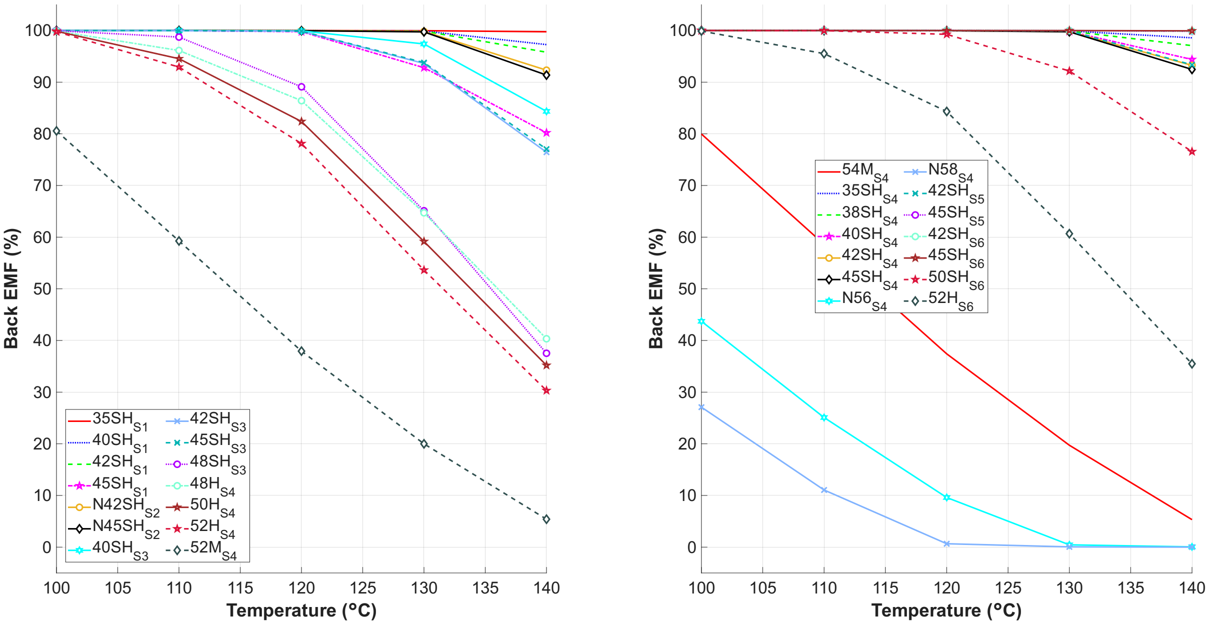

Figure 6.9: Remaining back EMF after demagnetization under NOC for all magnet grades. The subscripts in the legends refer to the magnet sources in Table 5.1.

The comparison between the short circuit condition and the normal operating condition confirms that the short circuit event is the dominant cause of irreversible demagnetization. Under normal operating conditions, most magnets retain a large part of their back EMF, which indicates that the demagnetizing field is not strong enough to severely reduce the magnetization for most grades. Under the short circuit condition, however, the combination of high reverse current and reduced coercivity at elevated temperature pushes the magnets much closer to or below the knee point of the demagnetization curve. As a result, the permanent magnet flux linkage is strongly reduced, leading to a large decrease in back EMF.

6.1.4 Current Response

Fig. 6.10 shows maximum demagnetization current under SCC as a function of temperature for all investigated magnet grades. In general, the demagnetization current decreases with increasing temperature for all magnets, although the rate of reduction varies significantly between materials. Several SH magnets show only a moderate reduction over the studied temperature range and maintain relatively high demagnetization current levels up to 140°C. The highest value is around 1900 A for 45SH from S5 while the lowest is around 900 A for N58 from S4. In contrast, several magnets, particularly grades that end with M and H and without any grade at end such as N56 from S4, show a much stronger decrease with temperature.

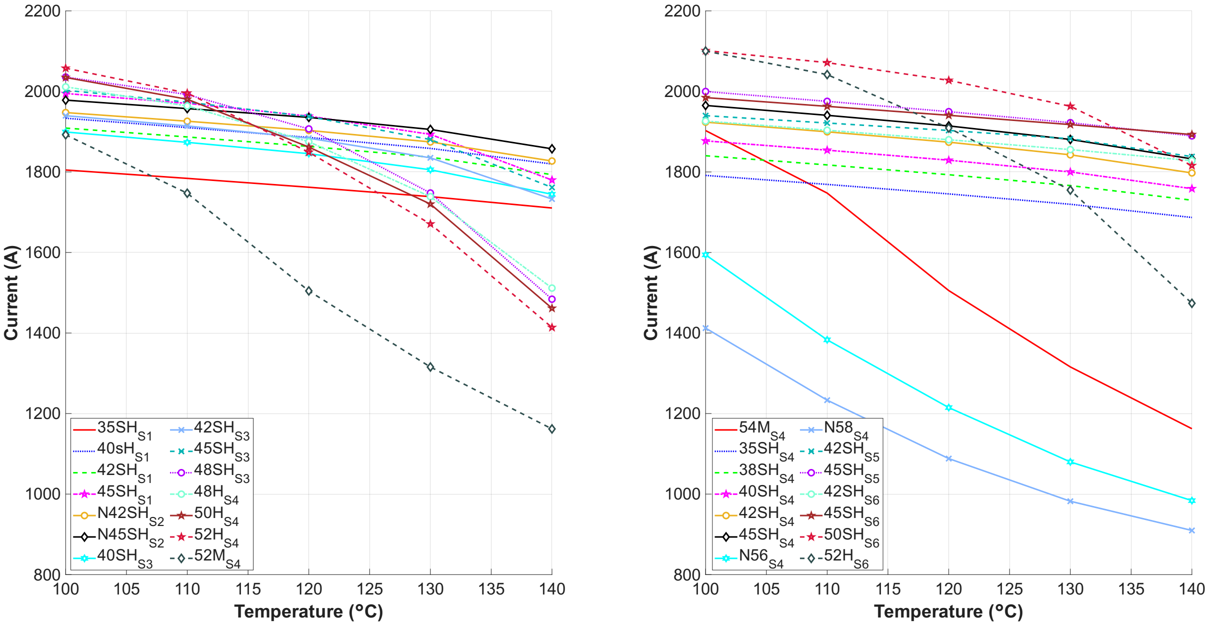

Figure 6.10: Maximum demagnetizing current under SCC for all investigated magnet grades as function of temperature for all magnets.

The reduction in short circuit current should not be interpreted as an improvement in fault robustness. Instead, it is mainly a consequence of the reduced permanent magnet flux linkage with increasing temperature. As the temperature increases, both the remanence B_r and intrinsic coercivity H_{cJ} decrease. This weakens the magnetic state of the rotor and reduces the effective permanent magnet flux linkage, ψ_{PM}. Since the short circuit current is influenced by the induced voltage and the magnetic flux produced by the permanent magnets, a strong loss of magnetization can lead to a lower short circuit current.

Therefore, magnets that maintain higher short circuit current levels with increasing temperature generally also preserve a stronger magnetic state, while magnets showing a strong current reduction often correspond to cases with reduced back EMF and lower remaining torque. This means that a lower current level in the weaker magnet grades does not necessarily indicate a less severe fault condition, but rather that the magnets have already lost a significant part of their magnetic strength due to the larger RTCs of the B_r.

6.1.5 Demagnetization Ratio

One interesting aspect of a demagnetization study is to see the percentage on how much the magnet has been demagnetized. This is evaluated by calculating how much of the average B_r is lost in the magnets. Fig. 6.11 and Fig. 6.12 illustrates this for magnet Layer 1 and 2, respectively. Essentially, the figures show with what percentage of the original B_r it has decreased at each temperature after demagnetization. To clarify further, the increasing curves show that the reduction increases. The trend is an almost linear decrease of B_r in both Layer 1 and 2. This confirms that the irreversible demagnetization becomes more severe as the magnet temperature increases. The reduction is directly connected to the temperature dependent decrease in intrinsic coercivity, $\boldsymbol{H_{cJ}}$, which makes the magnets less resistant to the demagnetizing field during the short circuit transient.

In Layer 1, most magnets retain approximately 20% to 30% of their original $\boldsymbol{B_r}$ at the highest investigated temperature, as shown in Fig. 6.11. In Layer 2, the demagnetization is more severe, with the same magnets retaining only approximately 10% to 20% of their original $\boldsymbol{B_r}$, as shown in Fig. 6.12. This indicates that Layer 2 is more exposed to the demagnetizing conditions during the short circuit event.

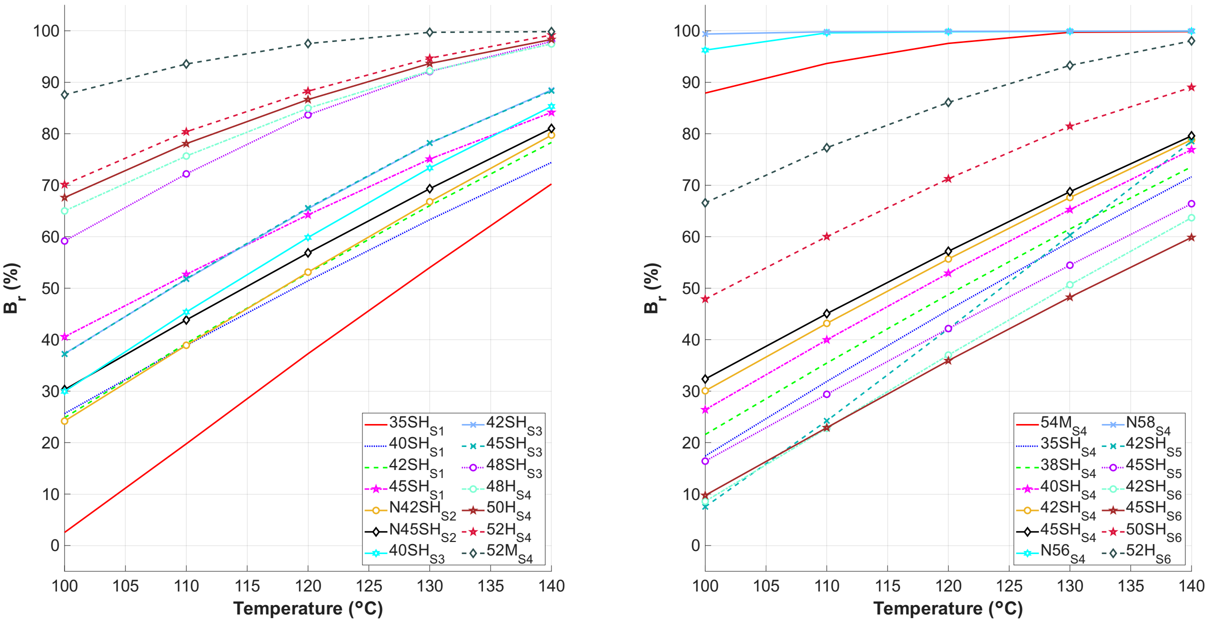

Figure 6.11: Percentage reduction of average B_r after demagnetization as a function of temperature in Layer 1 under SCC for all magnets.

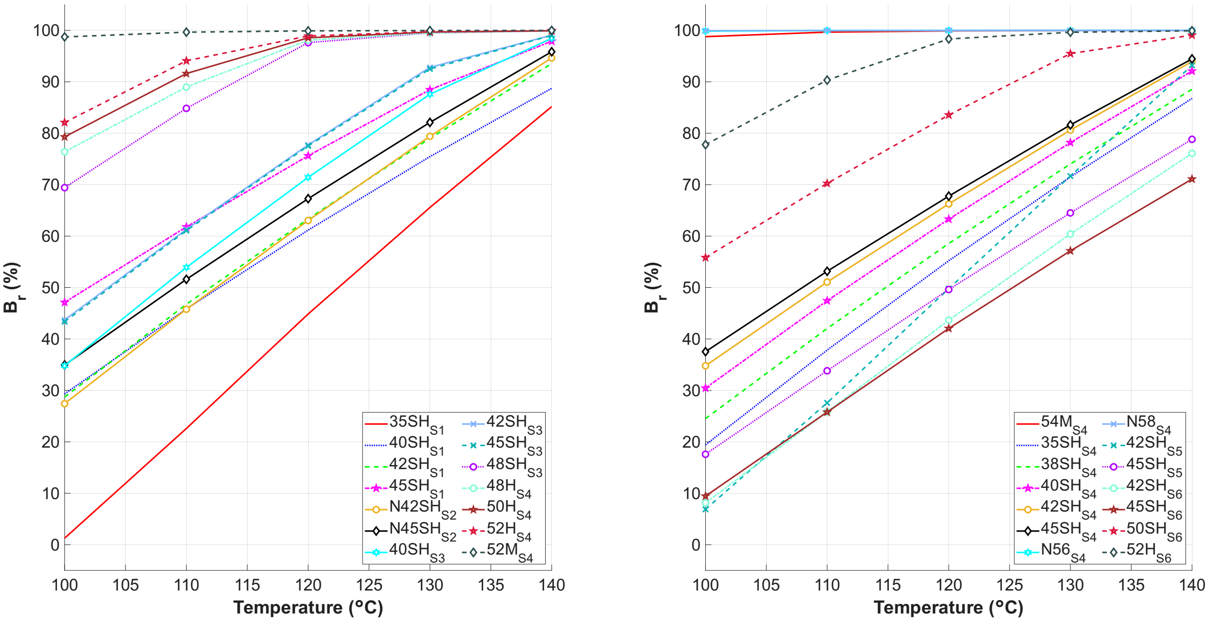

Figure 6.12: Percentage reduction of Average B_r after demagnetization as a function of temperature in Layer 2 under SCC for all magnets.

The demagnetization ratio results provide the clearest indication of the underlying cause of the degradation observed in the torque, back EMF, and current responses. As the remaining average B_r decreases with increasing temperature, an increasing part of the original magnetization is permanently lost. This is consistent with local magnet operating points being pushed below the knee point of the demagnetization curve during the short circuit transient, which causes irreversible demagnetization. The stronger reduction in Layer 2 also explains why the overall machine performance decreases significantly, since the loss of magnetization reduces the effective permanent magnet flux linkage and thereby affects both the induced voltage and torque production.

6.2 Comparison of 45SH Magnet Sources

This section compares the 45SH magnet grade from different material sources. The purpose is to evaluate how much the demagnetization behaviour and electromagnetic performance can vary between magnets with the same nominal grade.

Fig. 6.13 illustrates the remaining torque for the 45SH magnet grade from different sources after SCC and NOC as a function of temperature. Under SCC, all sources show a decreasing torque with increasing temperature. At 100°C, the torque ranges from approximately 72% to 91% depending on the source. As the temperature increases to 140°C, the torque decreases to a range between approximately 45% and 59%. Among the sources, 45SH$_{S6}$ consistently shows the highest torque retention across the entire temperature range, while 45SH$_{S3}$ and 45SH$_{S1}$ exhibit the lowest values. The remaining sources lie between these extremes and follow a similar decreasing trend.

Under NOC, all sources maintain a torque close to 100% up to approximately 120°C. At higher temperatures, a slight decrease is observed for most sources. At 140°C, the torque ranges from approximately 93% to 100%, where 45SH$_{S6}$ remains at 100% while the other sources show minor reductions. This shows again that the NOC is considerably less severe than the SCC for this magnet grade.

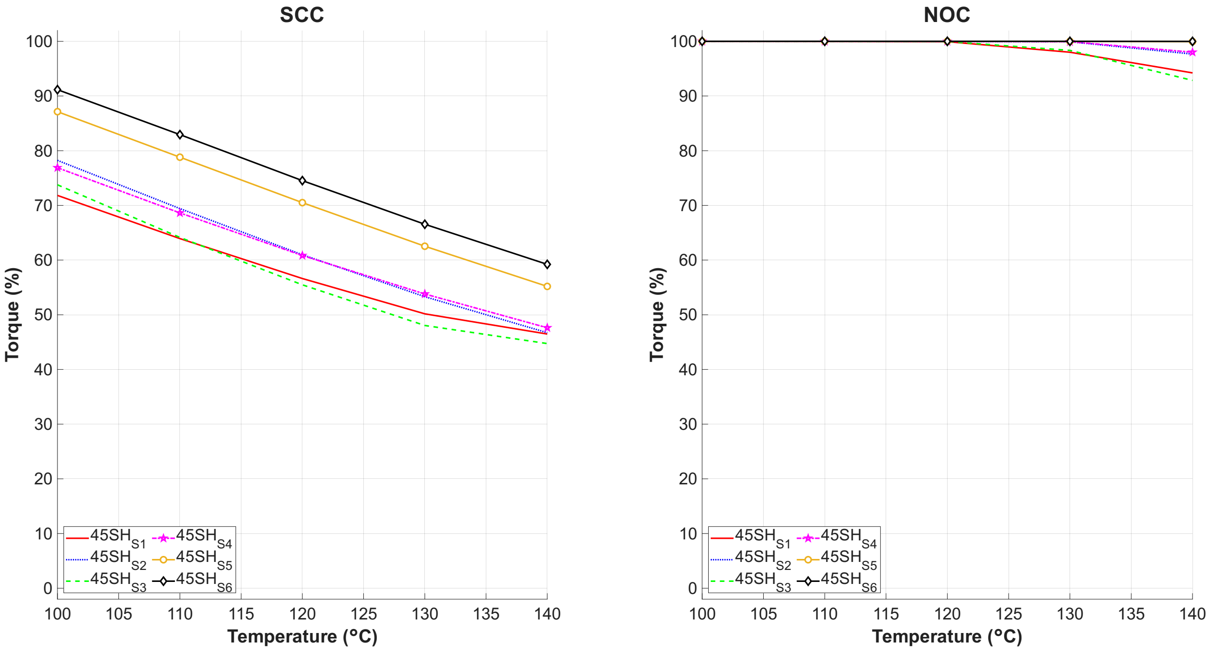

Figure 6.13: Remaining torque after demagnetization for 45SH magnet grade from different sources under SCC and NOC as a function of temperature.

Fig. 6.14 illustrates the average torque before demagnetization, and after demagnetization for SCC and NOC. Before demagnetization, all sources show very similar torque levels over the entire temperature range. The torque decreases slightly with increasing temperature, from approximately 580 Nm at 100°C to around 565-570 Nm at 140°C, with only minor variation between the sources.

After demagnetization under SCC, the torque decreases significantly for all sources and continues to decrease with increasing temperature. At 100°C, the torque ranges from approximately 420 Nm to 530 Nm, while at 140°C it decreases to a range between approximately 250 Nm and 340 Nm. The highest values are observed for 45SH$_{S6}$, followed by 45SH$_{S5}$, while 45SH$_{S3}$ and 45SH$_{S1}$ show the lowest values. This confirms that the short circuit event causes significant irreversible demagnetization and that the severity depends strongly on the material source.

After demagnetization under NOC, the torque remains close to the values before demagnetization. A slight decrease is observed at higher temperatures, where the torque at 140°C ranges from approximately 520 Nm to 570 Nm. The variation between sources is relatively small compared to the SCC case.

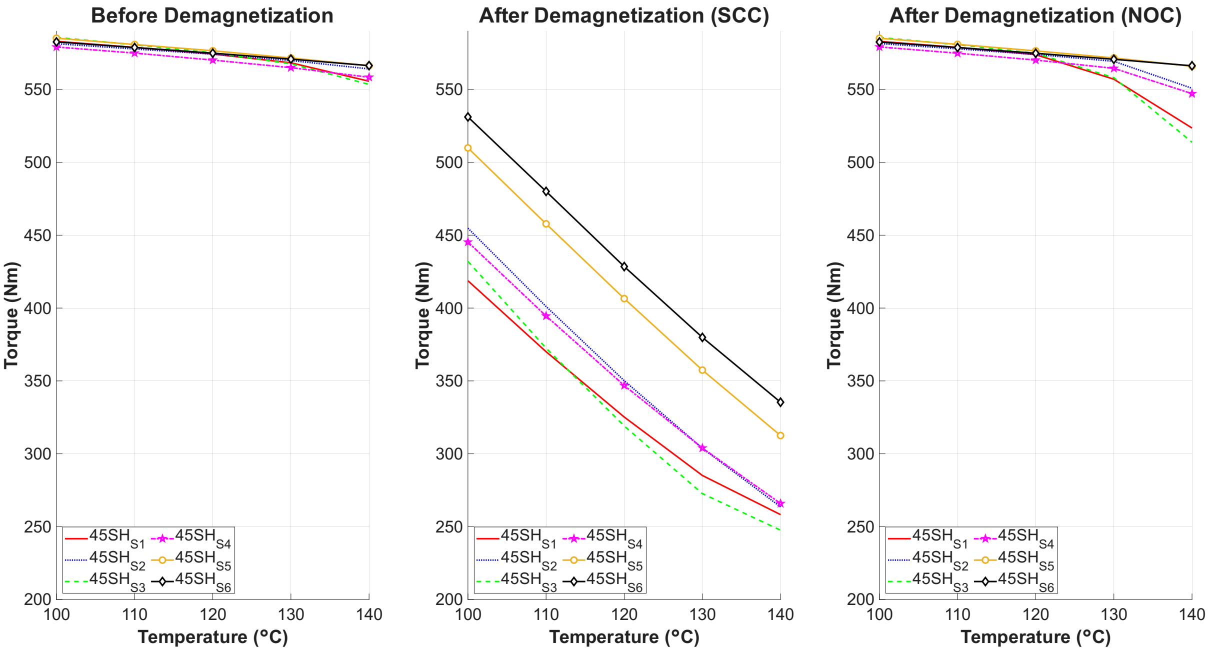

Figure 6.14: Average torque before and after demagnetization under SCC and NOC as functions of temperature for 45SH magnet grade from different sources

Fig. 6.15 illustrates the back EMF retention for the 45SH magnet grade from different sources under SCC and NOC as a function of temperature. Under SCC, all sources show a decreasing back EMF with increasing temperature. At 100°C, the back EMF ranges from approximately 49% to 85%. As the temperature increases to 140°C, the values decrease significantly to a range between approximately 0% and 27%. The highest values are consistently observed for 45SH$_{S6}$, followed by 45SH$_{S5}$, while 45SH$_{S3}$ and 45SH$_{S1}$ show the lowest values across the temperature range.

Under NOC, all sources maintain a back EMF close to 100% up to approximately 120°C. At higher temperatures, a reduction is observed for several sources. At 140°C, the back EMF ranges from approximately 78% to 100%, where 45SH$_{S6}$ remains at 100% while the other sources show varying degrees of reduction. The variation between sources is therefore smaller compared to the SCC case, but more pronounced than for the torque in Fig. 6.13.

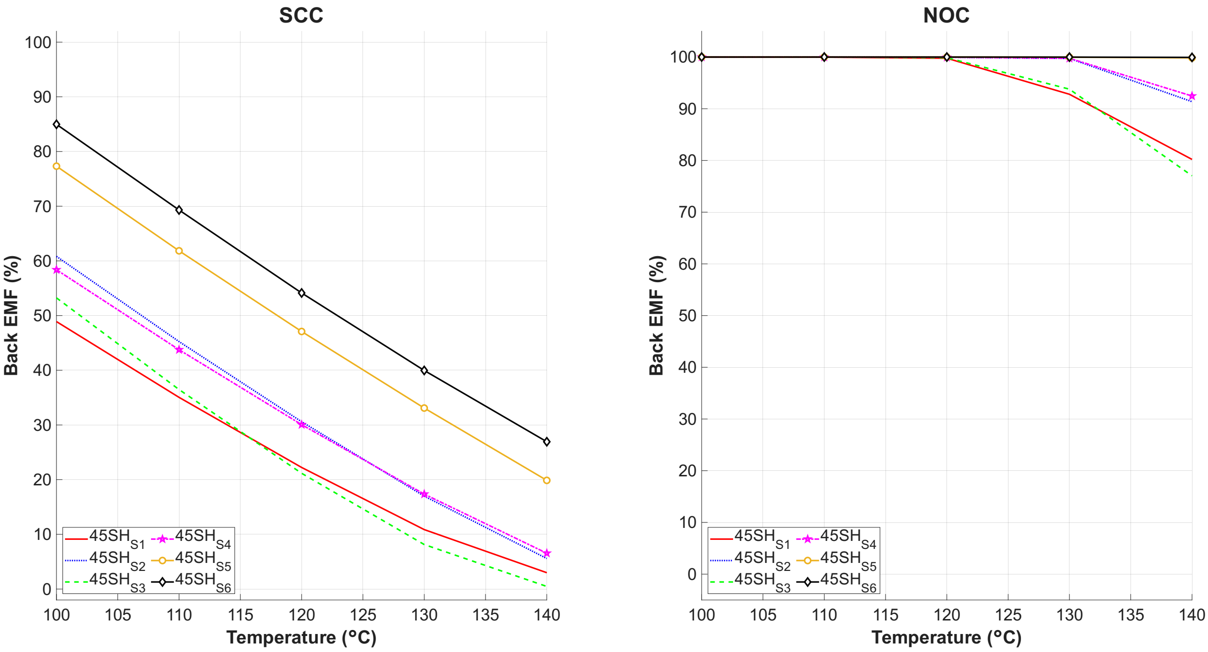

Figure 6.15: Back EMF retention for 45SH magnet grade from different sources under SCC and NOC as a function of temperature.

Fig. 6.16 illustrates the short circuit current amplitude for the 45SH magnet grade from different sources as a function of temperature. For all sources, the current decreases with increasing temperature over the entire range. At 100°C, the current amplitude lies between approximately 1965 A and 2000 A. As the temperature increases to 140°C, the current decreases to a range between approximately 1760 A and 1895 A depending on the source.

At lower temperatures, the variation between the sources is relatively small. However, as the temperature increases, the difference between the sources becomes more pronounced. At 140°C, 45SH$_{S5}$ and 45SH$_{S6}$ show the highest current amplitudes, while 45SH$_{S3}$ and 45SH$_{S1}$ exhibit the lowest values. The remaining sources lie between these extremes and follow a similar decreasing trend.

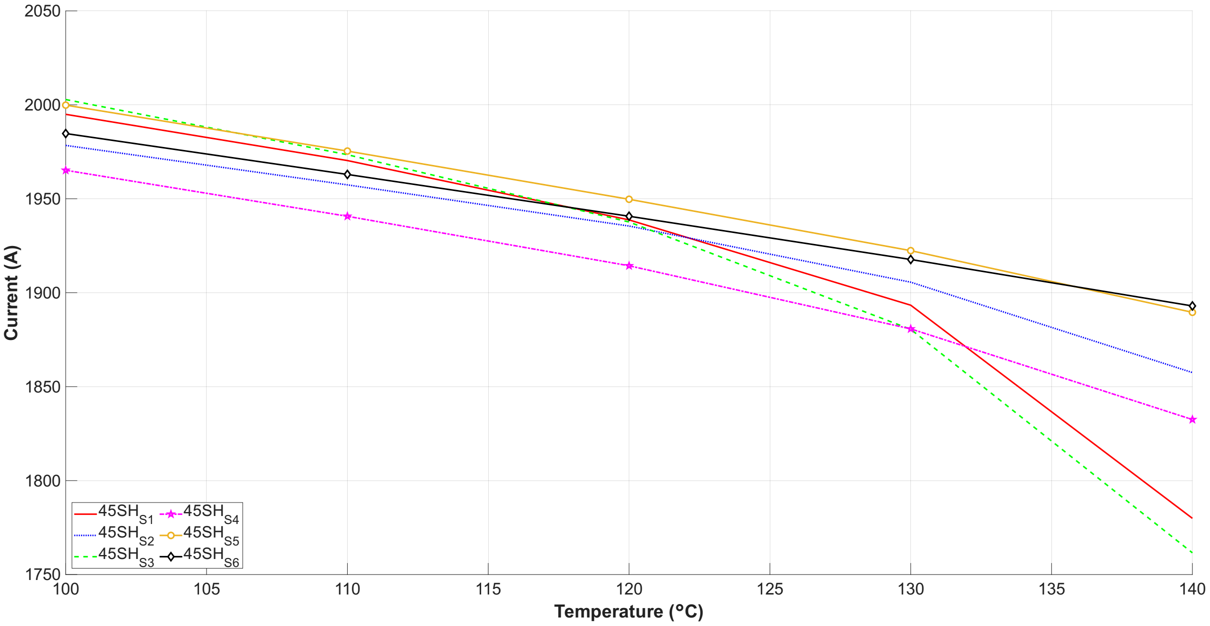

Figure 6.16: Short circuit current amplitude for 45SH magnet grade from different sources as a function of temperature.

Fig. 6.17 illustrated the percentage reduction of the average B_r. For all sources in both layers, the reduction of B_r increases with increasing temperature. In Layer 1, the reduction starts between approximately 10% and 40% at 100°C and increases to a range between approximately 60% and 90% at 140°C. The highest reduction is observed for $45SH_{S3}$, while $45SH_{S6}$ shows the lowest reduction across the temperature range. The remaining sources lie between these values and follow similar increasing trend.

In Layer 2, the same overall behaviour is observed, but with generally higher reduction levels compared to Layer 1. At 100°C, the reduction ranges from approximately 10% to 45%, while at 140°C it increases to approximately 70% to 100%. The highest reduction is again observed for $45SH_{S3}$, while $45SH_{S6}$ shows the lowest values. The variation between sources is more pronounced at higher temperatures.

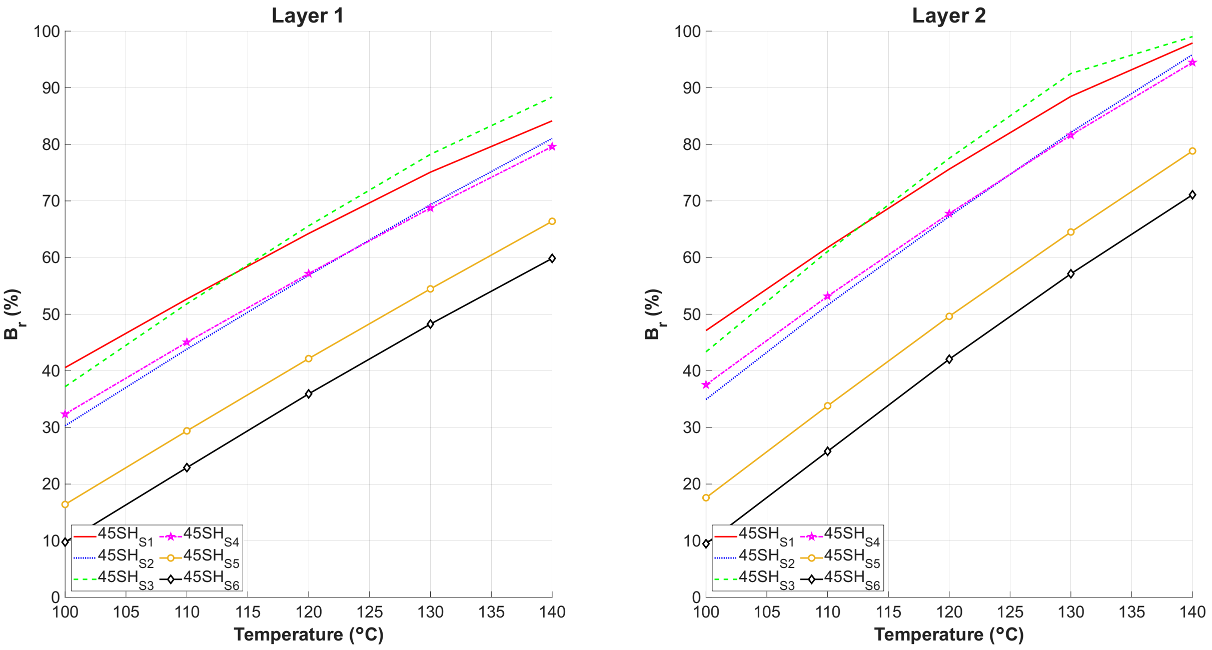

Figure 6.17: Percentage reduction of B_r under SCC and NOC as functions of temperature for 45SH magnet grade from different sources

The comparison of the 45SH magnet grade across different sources further highlights that magnets with the same nominal grade can exhibit significantly different demagnetization behaviour. Although all magnets are classified as 45SH, noticeable variations are observed in torque retention, back EMF, short circuit current and B_r reduction, particularly at elevated temperatures. These differences indicate that the sources specific material properties, especially the temperature dependence of H_{cJ} and B_r, play a critical role. Even small deviations in intrinsic coercivity or its thermal stability can lead to large differences in how the operating point shifts during a short circuit transient. This further shows the importance of taking the RTCs into account when evaluating the demagnetization of the magnets. As a result, some magnets remain further away from the knee point of the demagnetization curve, while others are pushed into irreversible demagnetization.

The layer comparison in Fig. 6.17 also shows that the demagnetization is not spatially uniform within the rotor. Layer 2 generally experiences a larger B_r reduction than Layer 1, especially at higher temperatures. This indicates that Layer 2 is more sensitive to the short circuit event, most likely because it is positioned closer to the air gap and is therefore more directly exposed to the stator magnetic field. During the short circuit transient, this can create stronger local reverse fields near the magnet tips and edges, which increases the risk of irreversible demagnetization.

To further illustrate the FEA result for the 45SH magnet from Source 6, Fig. 6.18 shows the effective remanent flux density distribution at 100°C and 140°C. In the 100°C case, most parts of the magnets are close to the upper part of the colour scale, with values around 1.00 to 1.125 T. Only smaller regions near the magnet edges and corners show visibly lower values. In the 140°C case, a larger part of the magnet area shifts toward the middle and lower part of the scale. Layer 1, is mainly located around 0.48 to 0.72 T, while Layer 2, shows lower values, with several regions around 0.240 to 0.360 T. This indicates that Layer 2 is more strongly demagnetized than Layer 1 in this case. The lower value regions are also more visible near the magnet edges and tips. This supports the results from the torque and back EMF comparison, since local reductions in B_r can still affect the overall machine performance. The colour scale further shows that the displayed maximum B_r value decreases from 1.25 T in the 100°C plot to 1.20 T in the 140°C plot.

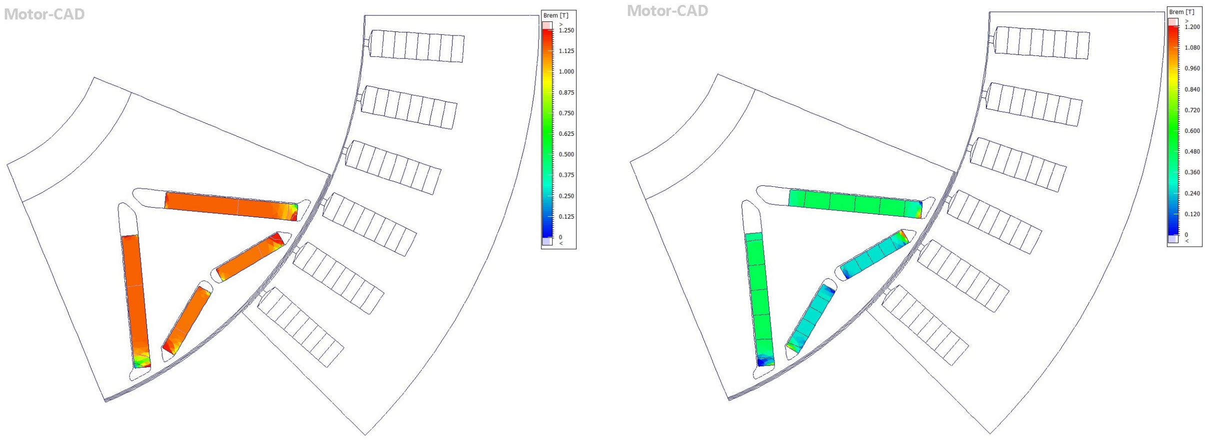

(a): 100°C

(b): 140°C

Figure 6.18: Effective remanent flux density distribution, B_r, for the 45SH magnet from Source 6 at 100°C and 140°C.

6.3 Effect of Remanence at Constant Coercivity

This section investigates the influence of remanence, B_r, while keeping the intrinsic coercivity, H_{cJ}, approximately constant. The comparison is based on SH grades from Source 4, where the magnets have similar H_{cJ} at the reference temperature but different remanence values. With increasing grade from 35SH to 45SH, the remanence increases from 1.18–1.33 T at 20°C.

Fig. 6.19 shows the remaining torque after demagnetization for the SH grades from Source 4 under SCC and NOC along the d-axis. Under SCC, the remaining torque decreases with increasing temperature for all grades. It is also observed that magnets with higher B_r show a larger torque reduction. At 140°C, the remaining torque decreases from approximately 54% for 35SH to approximately 48% for 45SH. The same trend is also observed under NOC, although the reduction is less severe than under SCC. This indicates that a higher B_r leads to a larger decrease in torque.

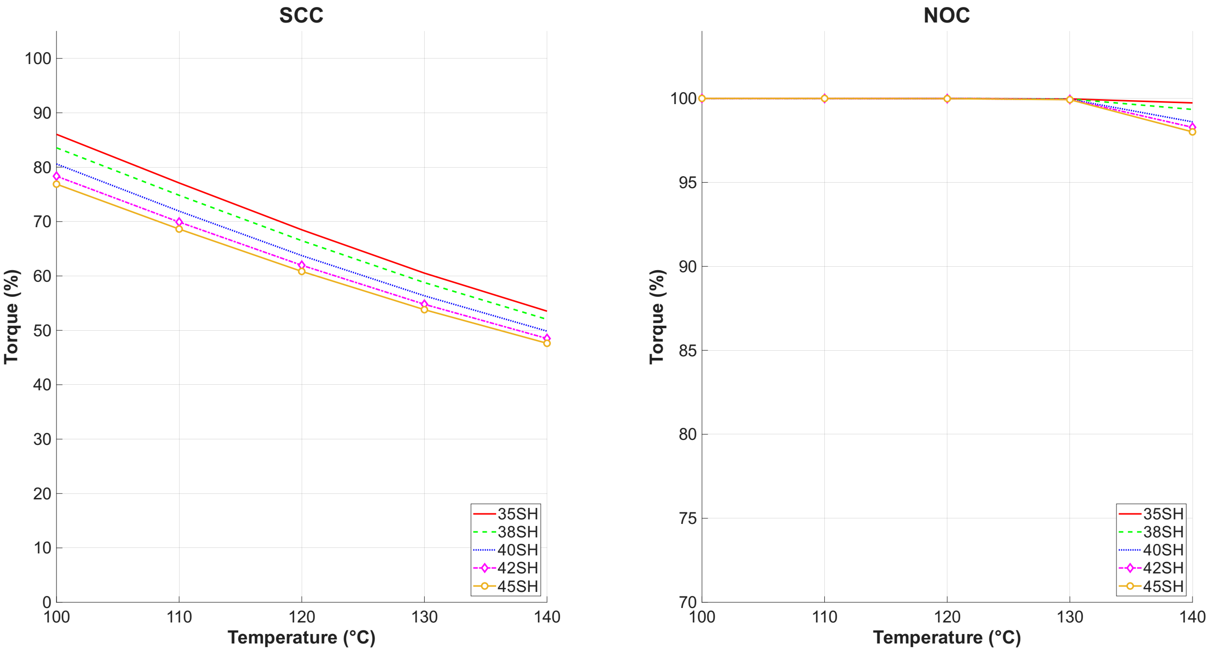

Figure 6.19: Torque reduction for SCC (left) and NOC (right) for all SH grades for S4

In Fig. 6.20 the average torque and short circuit current amplitudes for the different SH grades of S4 are presented. At 100°C the average torque is between 580 Nm and 545 Nm, increasing with magnet grade and at 140°C the torques have gone down to between 558 Nm and 525 Nm. This shows that the higher remanence grades provide higher initial torque before demagnetization.

At 100°C the current amplitude goes from approximately 1790 A to approximately 1960 A when increasing the magnet grade from 35SH to 45SH. The short circuit amplitude decreases with increasing temperature, with the range at 140°C being approximately between 1690 A and 1835 A between the magnet grades. This indicates that higher B_r leads to higher flux linkage, which increases both the initial torque and the short circuit current amplitude.

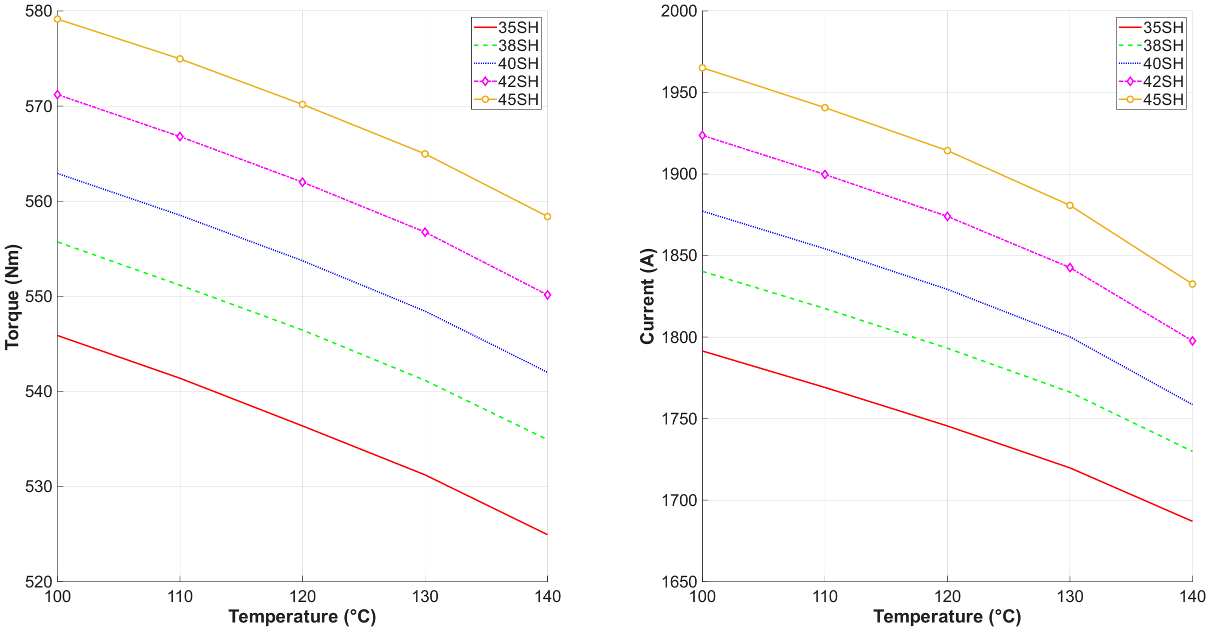

Figure 6.20: Average torque (left) and short circuit current amplitude (right) for different SH grades of S4

Fig. 6.21 illustrates the back EMF evolution for all SH grades of Source 4. The back EMF decreases more with increasing magnet grade. For the SCC case, the back EMF at 140°C goes down from approximately 12% of the original value to approximately 7%. For the NOC the trend is the same, however the decrease when increasing the magnet grade goes from approximately 98% to approximately 92.5%.

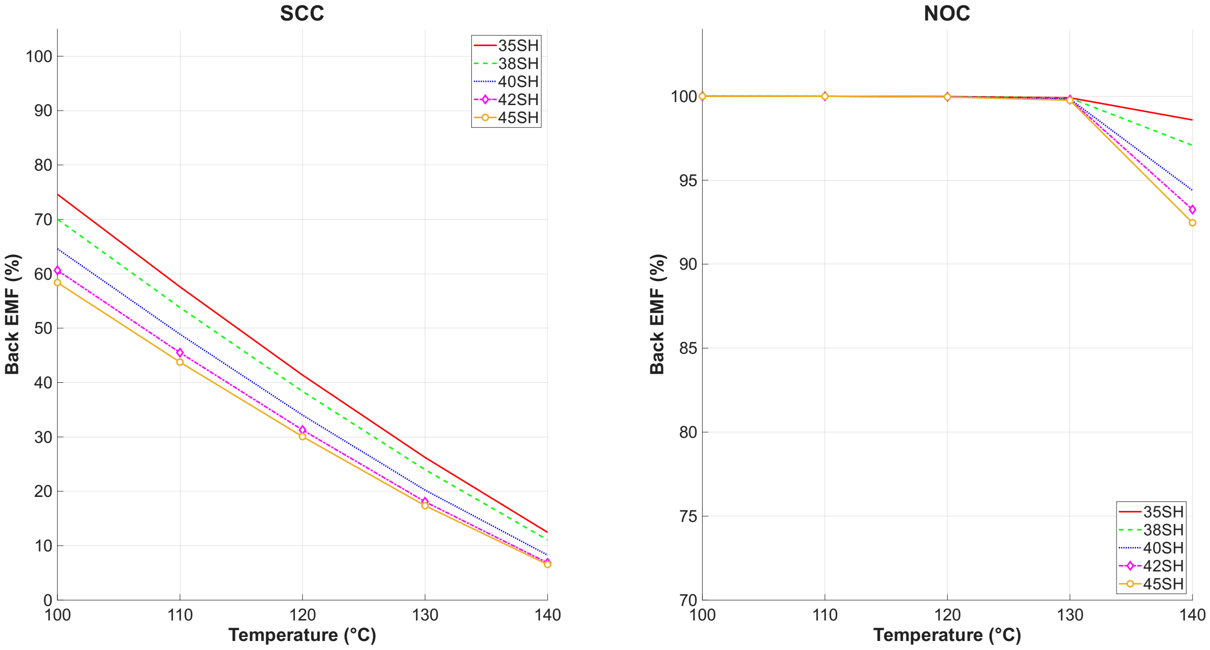

Figure 6.21: Back EMF reduction for SCC (left) and NOC (right) for all SH grades for S4

The percentage reduction of average B_r in Layer 1 and 2 for all SH grades from S4 is presented in Fig. 6.22. For all cases the reduction increases with increasing temperature. In Layer 1 the reduction increases from approximately between 17% and 32% at 100°C to between 71% and 80% at 140°C. The lowest number in the ranges corresponding to the lowest grade (35SH) and highest number corresponding to the highest grade (45SH). Similarily, in layer 2 the reduction increases from approximately between 20% and 37% at 100°C to between 86% and 94% at 140°C. This shows that higher remanence leads to stronger irreversible demagnetization, even when the magnets have approximately the same intrinsic coercivity.

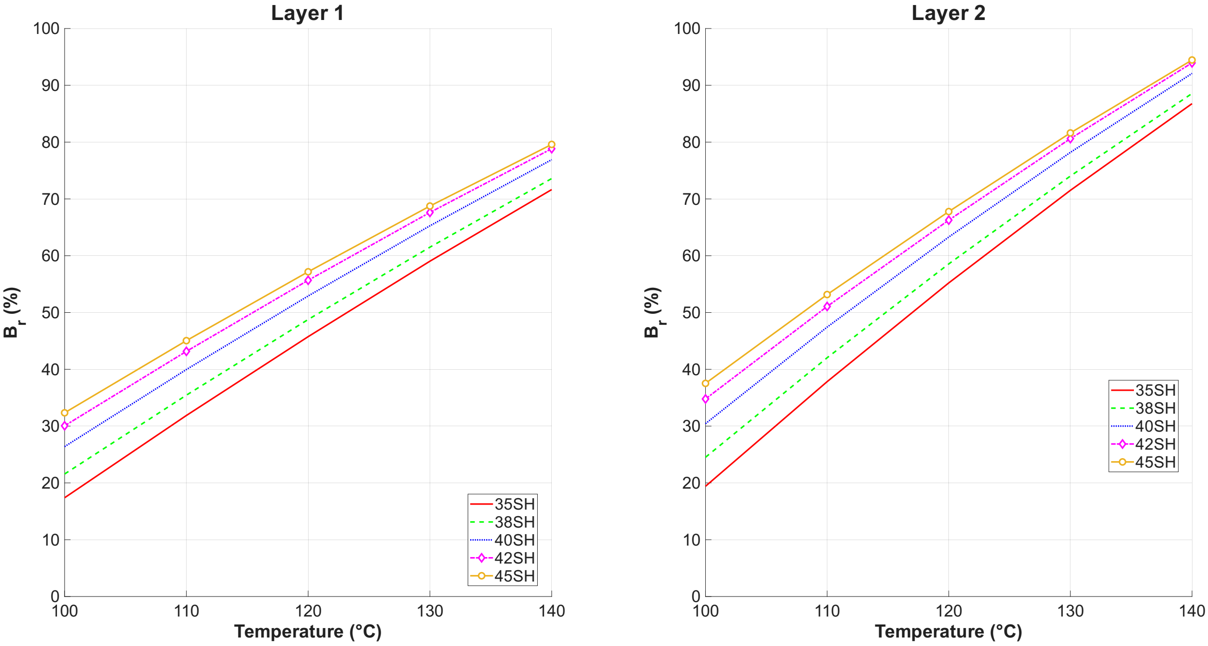

Figure 6.22: Percentage reduction of average B_r in Layer 1 and 2 as a function of temperature for all SH grades for S4

The results indicate that remanence affects the demagnetization behaviour even when H_{cJ} is approximately constant. A higher B_r increases the initial flux and flux linkage, which improves the initial torque. However, during a short circuit transient, this also results in a more demanding magnetic operating condition. Since the coercivity is not increased at the same time, the higher remanence grades are more likely to experience a larger shift of the operating point toward the knee point of the demagnetization curve. This explains why 45SH shows larger demagnetization than 35SH, despite having similar coercivity

Comparison with Increased 35SH Magnet Thickness

The previous figures show a comparison between all SH grades from S4 using the original rotor geometry. The following figures compare 45SH in the original rotor with 35SH in a rotor where the magnet thickness has been increased by 19.4%. The purpose of increasing the 35SH magnet thickness was to obtain torque and short circuit current levels closer to those of the 45SH magnet. This makes it possible to separate the effect of higher remanence from the effect of higher current amplitude.

Fig. 6.23 illustrates the torque behaviour under both SCC and NOC along *d*-axis. For the short circuit operation, the 45SH magnet goes from approximately 86% of the original maximum torque at 100°C to 48% at 140°C, while the 35SH magnet goes from approximately 91% at 100°C to approximately 58% at 140°C. However, in the case with normal operating conditions, 35SH will not reduce in torque while 45SH reduces to approximately 98% at 140°C.

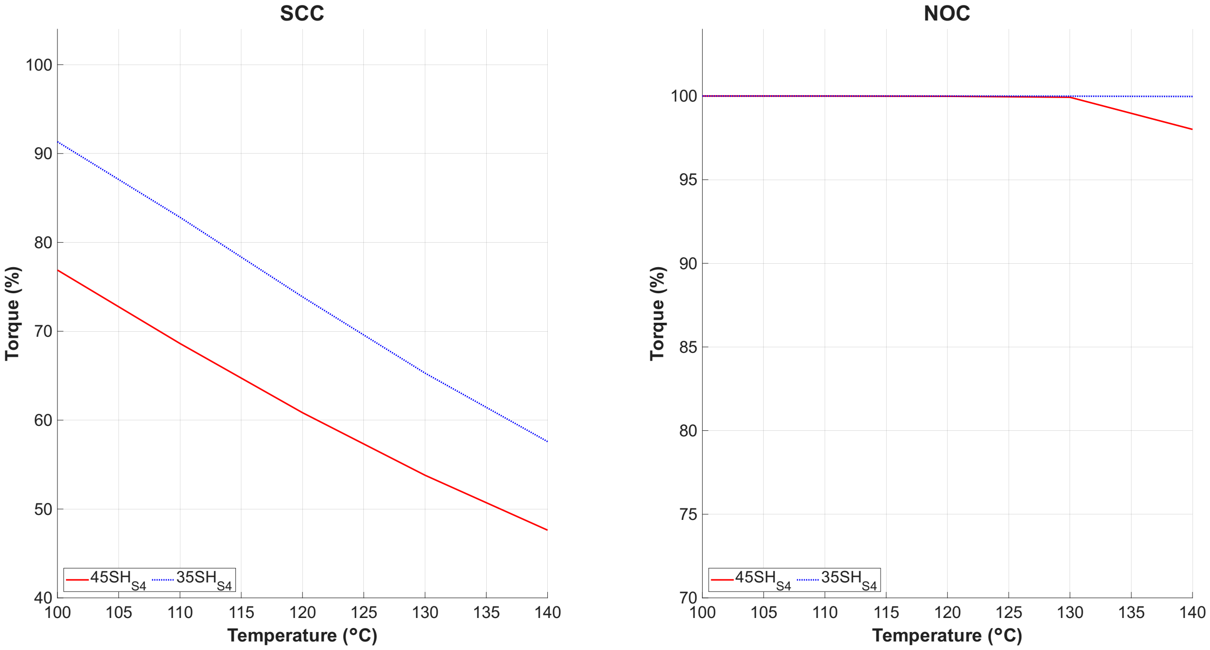

Figure 6.23: Torque behaviour under SCC and NOC along the d-axis with respect to temperature for 45SH$_{S4}$ (original thickness) and 35SH$_{S4}$ (19.4% thicker)

The average torque before the demagnetization with respect to temperature is shown in Fig. 6.24 for the same thicknesses as above. 45SH reduces from 579 Nm at 100°C to 558 Nm at 140°C while 35SH reduces from 566 Nm to 546 Nm between the same temperatures. This confirms that the thicker 35SH case gives torque levels close to the 45SH case before demagnetization.

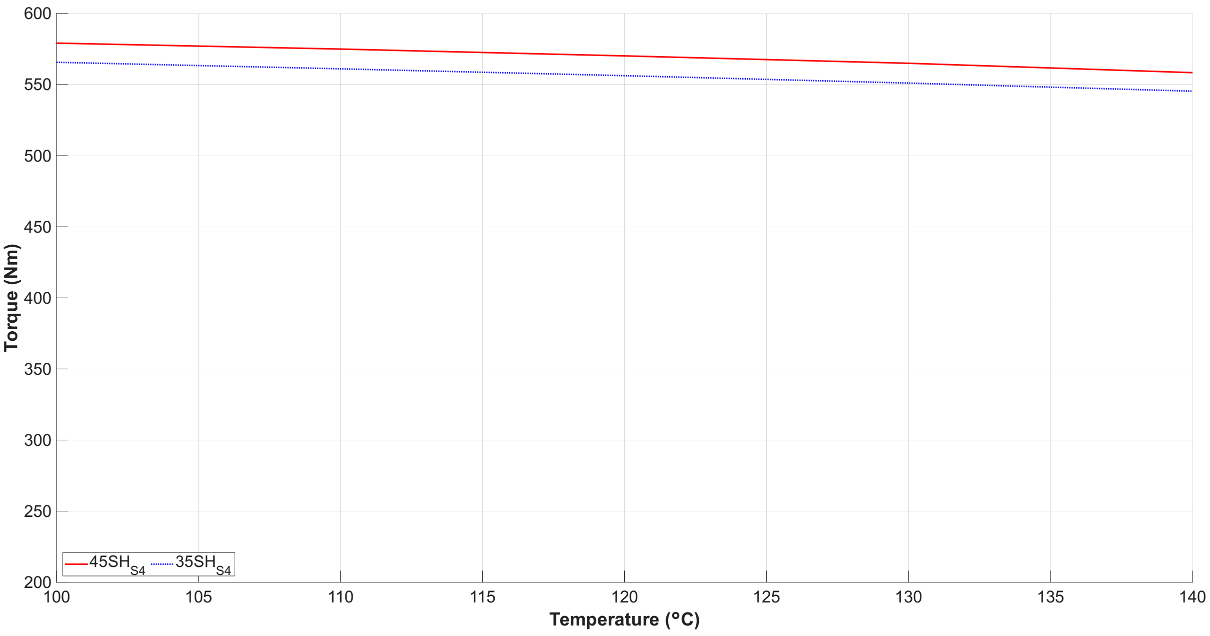

Figure 6.24: Average torque before demagnetization with respect to temperature for 45SH$_{S4}$ (original thickness) and 35SH$_{S4}$ (19.4% thicker)

In Fig. 6.25 the Back EMF behaviour is shown for the same configuration as in Fig. 6.23. Under SCC 45SH reduces from approximately 77% at 100°C to approximately 48% at 140°C. However, under the same conditions 35SH reduces from approximately 91% at 100°C to approximately 58% at 140°C. Under normal operating conditions, 35SH stays at 100% with a negligible drop towards the higher temperatures, while 45SH drops to approximately 92.5% at 140°C.

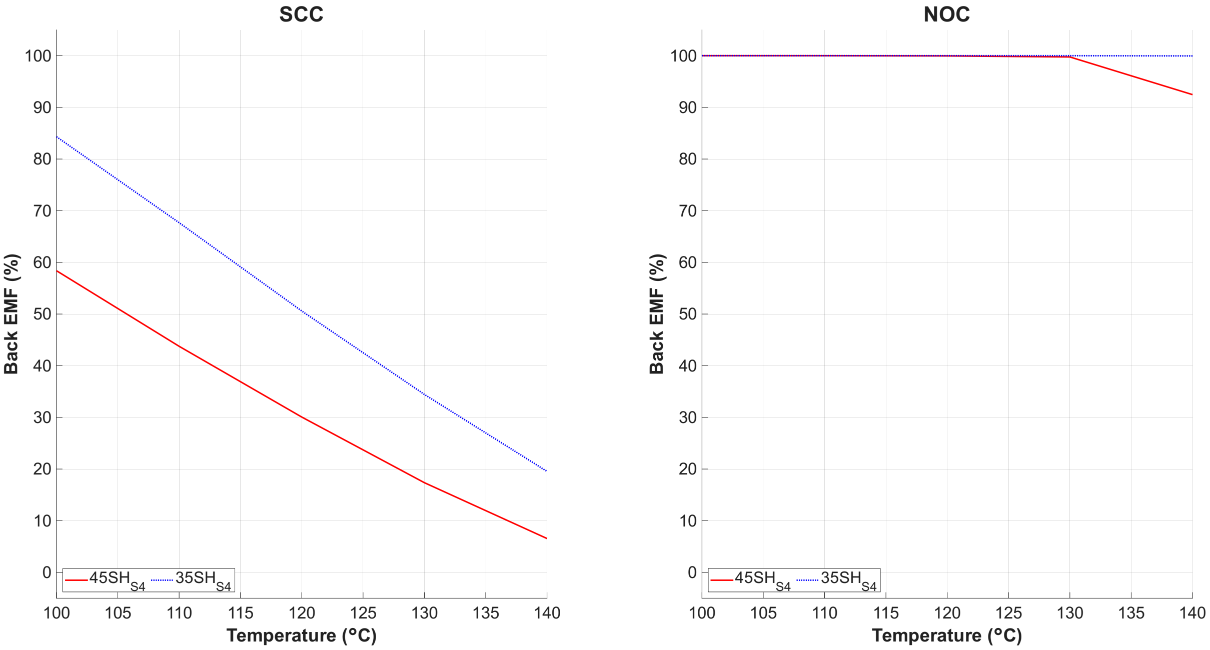

Figure 6.25: Back EMF behaviour under SCC and NOC along the d-axis with resepct to temperature for 45SH$_{S4}$ (original thickness) and 35SH$_{S4}$ (19.4% thicker)

Fig. 6.26 illustrates the short circuit current amplitude for 45SH and 35SH with their respective thicknesses. The short circuit current is marginally higher for 35SH until 130°C where it drops more than the current for 35SH and becomes approximately 15 A lower. The decrease for 45SH is from approximately 1965 A at 100°C to 1830 A at 140°C, while for 35SH it is from approximately 1960 A to 1845 A at the same temperatures. The current is therefore close between the two cases, which supports the use of this comparison for isolating the influence of remanence.

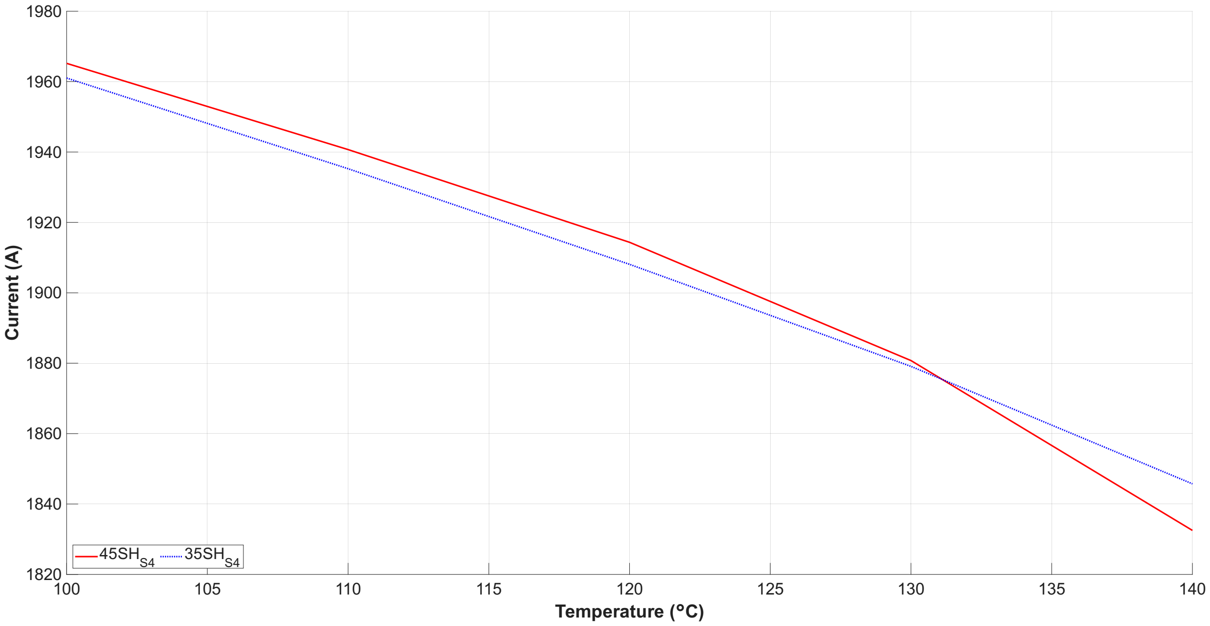

Figure 6.26: Short circuit current amplitude with respect to temperature for 45SH$_{S4}$ (original thickness) and 35SH$_{S4}$ (19.4% thicker)

Fig. 6.27 shows the percentage reduction of the average B$_r$ under short circuit conditions for both Layer 1 and 2. For 35SH, both layers start out at approximately 7% reduction and increase to approximately 65% and 80% for Layer 1 and 2 respectively. For 45SH, the reductions start at 32% and 38% for Layer 1 and 2 and increase to 80% and approximately 94%, respectively.

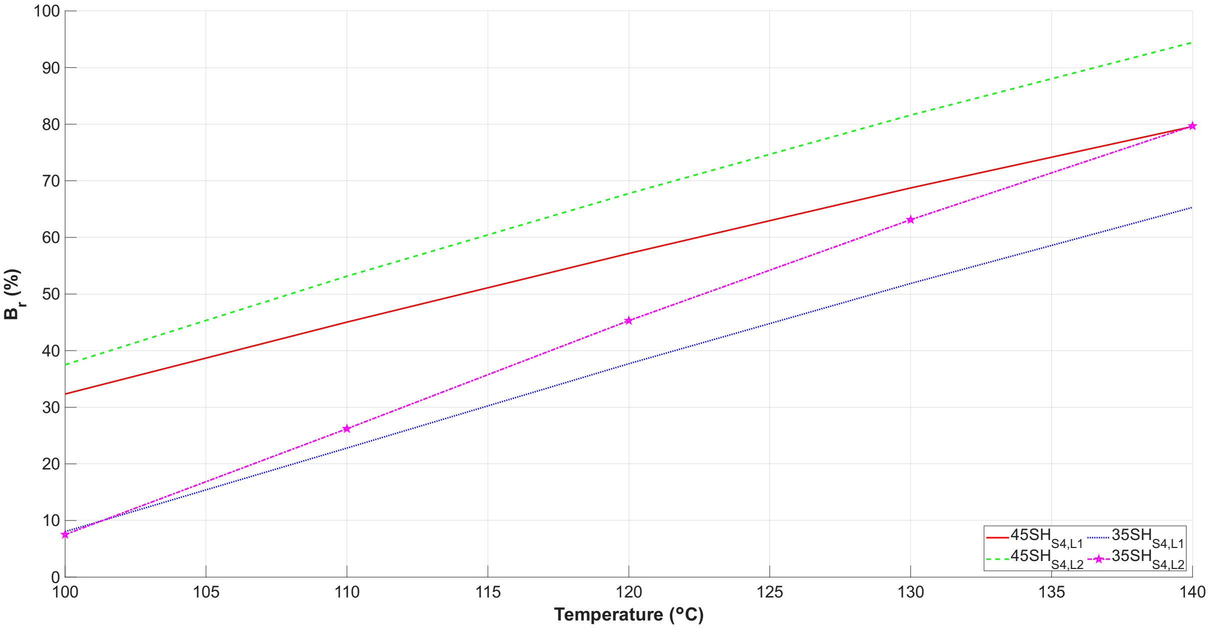

Figure 6.27: Percentage reduction of average B_r after demagnetization under short circuit conditions with respect to temperature for 45SH$_{S4}$ (original thickness) and 35SH$_{S4}$ (19.4% thicker)

Despite the similar torque and short circuit current levels, 45SH still undergoes significantly more demagnetization than the thicker 35SH magnet. This shows that the increased demagnetization observed for higher $\boldsymbol{B_r}$ magnets cannot be explained solely by higher current amplitude. Instead, the higher remanence itself contributes to the increased demagnetization sensitivity. A larger $\boldsymbol{B_r}$ gives a higher initial magnetic flux and shifts the magnet operating point. During the short circuit transient, the reverse magnetic field produced by the stator current acts against the magnetization. When $\boldsymbol{H_{cJ}}$ remains approximately constant, the increased remanence is not accompanied by a corresponding increase in resistance to demagnetization. The operating point is therefore more likely to reach or pass the knee point, resulting in more severe irreversible demagnetization for the 45SH magnet.

Overall, this comparison shows that increasing remanence improves the initial electromagnetic performance, but it also increases the risk of irreversible demagnetization when coercivity is not increased accordingly. For HRE-free magnet selection, this means that high $\boldsymbol{B_r}$ alone is not sufficient. The remanence must be balanced against the available coercivity and the expected short circuit operating condition.

6.4 Custom Magnet Study

This section presents the results from the custom magnet study based on the selected 45SH magnet. The purpose is to investigate how the machine performance changes when the magnet properties are varied systematically around the original design. In this section, the original design refers to the reference case using the selected original 45SH magnet properties in the unchanged rotor geometry. This case is included in the figures and is shown with legend *Original* for reference.

Three custom magnet cases are evaluated. In the first case, H_{cJ} is increased while B_r is kept constant. In the second case, H_{cJ} is increased while B_r is reduced. In the third case, both H_{cJ} and B_r are increased. The case where only B_r is varied while H_{cJ} is kept constant follows the same trend as discussed in Section 6.3 and is therefore not repeated here.

To make the following custom magnet results easier to interpret, the material property values used for each test case are summarized in Table 6.1. The values correspond to the reference temperature of 20°C. The same test numbering is used throughout Section 6.4.

Table 6.1: Custom magnet test cases used in Section 6.4 at the reference temperature of 20°C.

Test	Increased H_{cJ}, constant B_r		Increased H_{cJ}, reduced B_r		Increased H_{cJ}, increased B_r	
	H_{cJ} [kA/m]	B_r [T]	H_{cJ} [kA/m]	B_r [T]	H_{cJ} [kA/m]	B_r [T]
Test 1	1730	1.34	1730	1.37	1730	0.87
Test 2	1780	1.34	1780	1.32	1780	0.92
Test 3	1830	1.34	1830	1.27	1830	0.97
Test 4	1880	1.34	1880	1.22	1880	1.02
Test 5	1930	1.34	1930	1.17	1930	1.07
Test 6	1980	1.34	1980	1.12	1980	1.12
Test 7	2030	1.34	2030	1.07	2030	1.17
Test 8	2080	1.34	2080	1.02	2080	1.22
Test 9	2130	1.34	2130	0.97	2130	1.27
Test 10	2180	1.34	2180	0.92	2180	1.32
Test 11	2230	1.34	2230	0.87	2230	1.37

6.4.1 Increased Coercivity with Constant Remanence

The first custom magnet case investigates the effect of increasing intrinsic coercivity while keeping the remanence approximately constant. The original selected 45SH magnet is used as the reference material. The test cases correspond to increasing H_{cJ} values while maintaining $B_r \approx 1.34$ T. Test 1 represents the lowest coercivity, approximately 1730 kA/m, while Test 11 represents the highest coercivity, approximately 2230 kA/m. The coercivity is increased in steps of 50 kA/m.

Fig. 6.28 shows the torque retention after SCC and NOC. After SCC, increasing H_{cJ} clearly improves the remaining torque after demagnetization. At 100°C the retention goes from approximately 82% to 100%, which is reached by Test 6. From Test 3 onward, the torque retention exceeds that of the original case across the temperature range. This is expected since this is where the coercivity exceeds the reference. The behaviour is similar but shifted upward in y-direction with increasing H_{cJ}. Furthermore, at $140°C$ the retention goes up from 50% to approximately 100% until test 11. During normal operating conditions, the retention increases from approximately 99% to 100% at $140°C$ by Test 3.

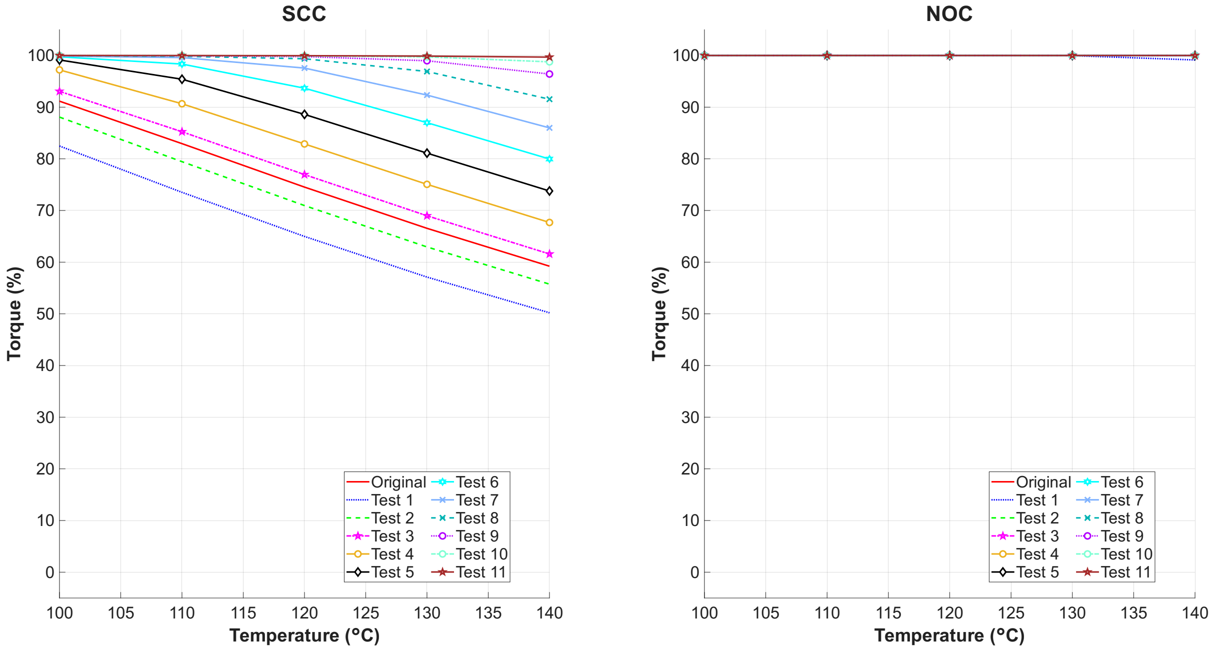

Figure 6.28: Torque retention under SCC and NOC as a function of temperature. Each test indicates increased coercivity with increments of 50 kA/m.

Fig. 6.29 shows average torque before demagnetization and after demagnetization under SCC and NOC. Before demagnetization, all test cases follow nearly the same trend, decreasing slightly from approximately 580 Nm at 100°C to around 565 Nm at 140°C.

After demagnetization under SCC, a clear separation between the rest cases is observed. The lowest test case show the largest torque reduction with increasing temperature, while the higher test cases remain closer to the original torque level. At 140°C, Test 1 decreases to below 300 Nm, whereas the highest test cases remain above approximately 550 Nm.

After demagnetization under NOC, the torque remains almost unchanged compared to the values before demagnetization. All test cases stay close to the original curve across the full temperature range, with only minor deviations at 140°C for the lowest test cases.

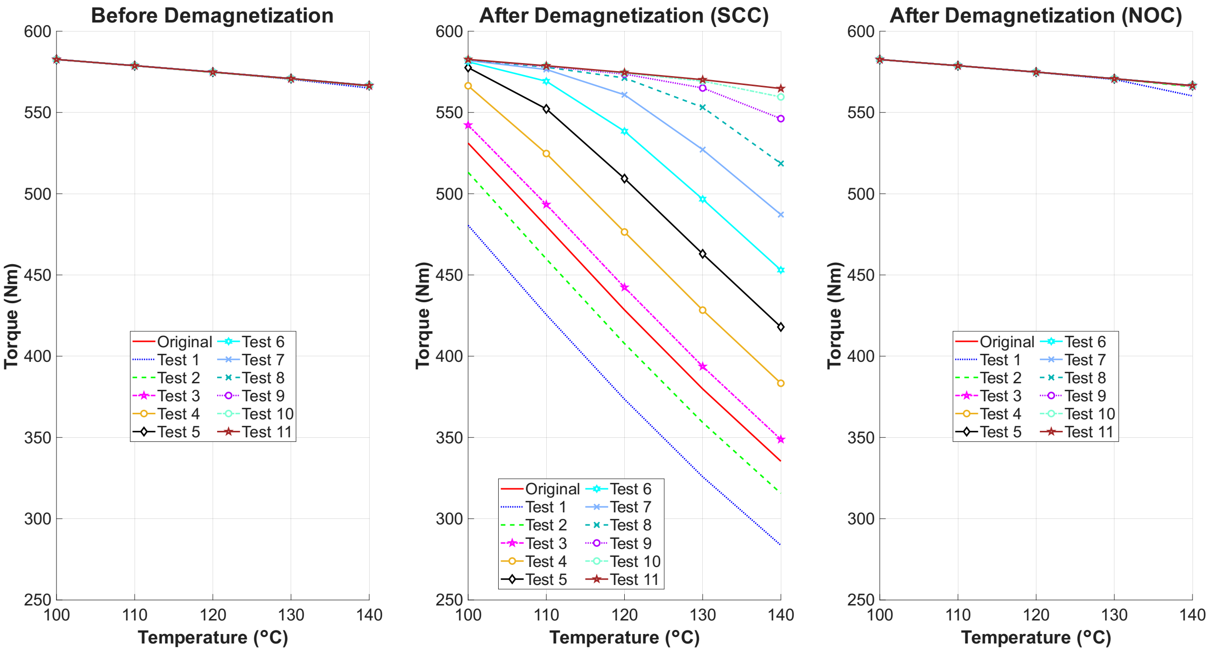

Figure 6.29: Average torque before and after demagnetization for SCC and NOC as a function of temperature. Each test indicates increased coercivity with increments of 50 kA/m.

The back EMF response in Fig. 6.30 shows the same improvement with increasing H_{cJ}. The retention of the back EMF under SCC at 100°C increases from approximately 68% to 100% and at 140°C it goes up from approximately 11% to 98%. Along the temperature range the behaviour is similar but shifted in y-direction when the coercivity is increased. During NOC, the retention at 140°C increases from 96% to 100% by Test 2, but otherwise at 100% over the whole temperature range.

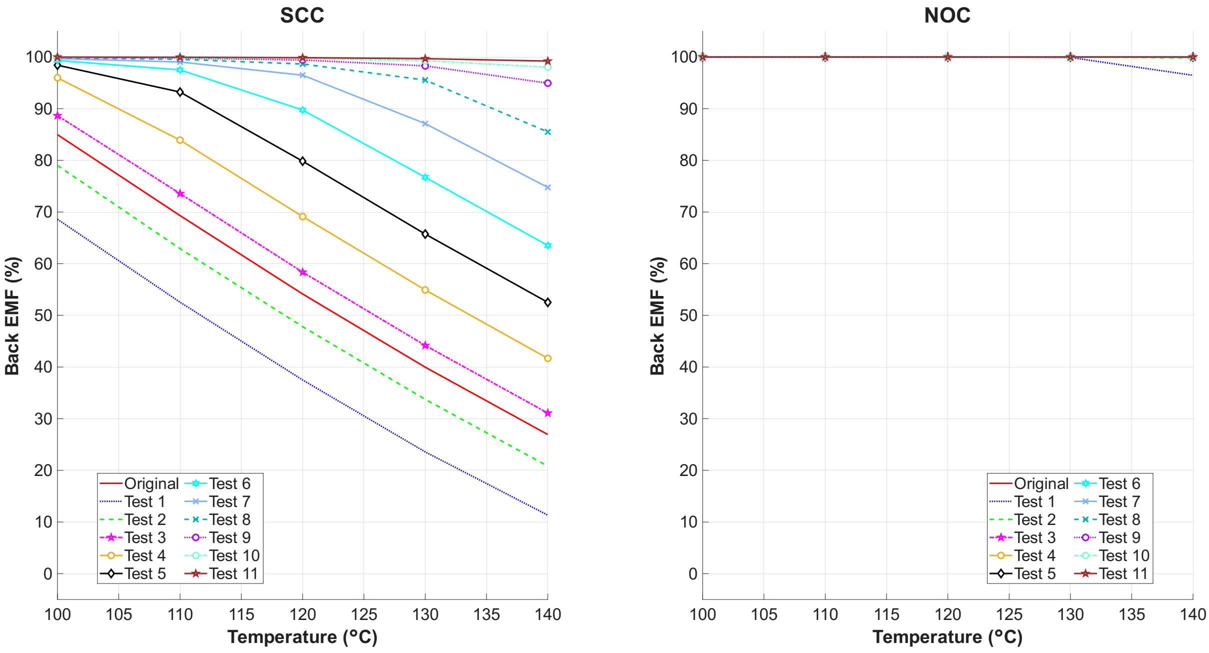

Figure 6.30: Back EMF retention under SCC and NOC as a function of temperature. Each test indicates increased coercivity with increments of 50 kA/m.

Fig. 6.31 shows the short circuit current amplitude as a function of temperature for increasing H_{cj}. As shown, the current decreases from approximately 1985 A at 100°C to around 1875–1895 A at 140°C for all test cases. Only minor differences are observed between the tests, where the lowest test case reaches approximately 1875 A, while the highest test cases remain close to 1895 A at 140°C.

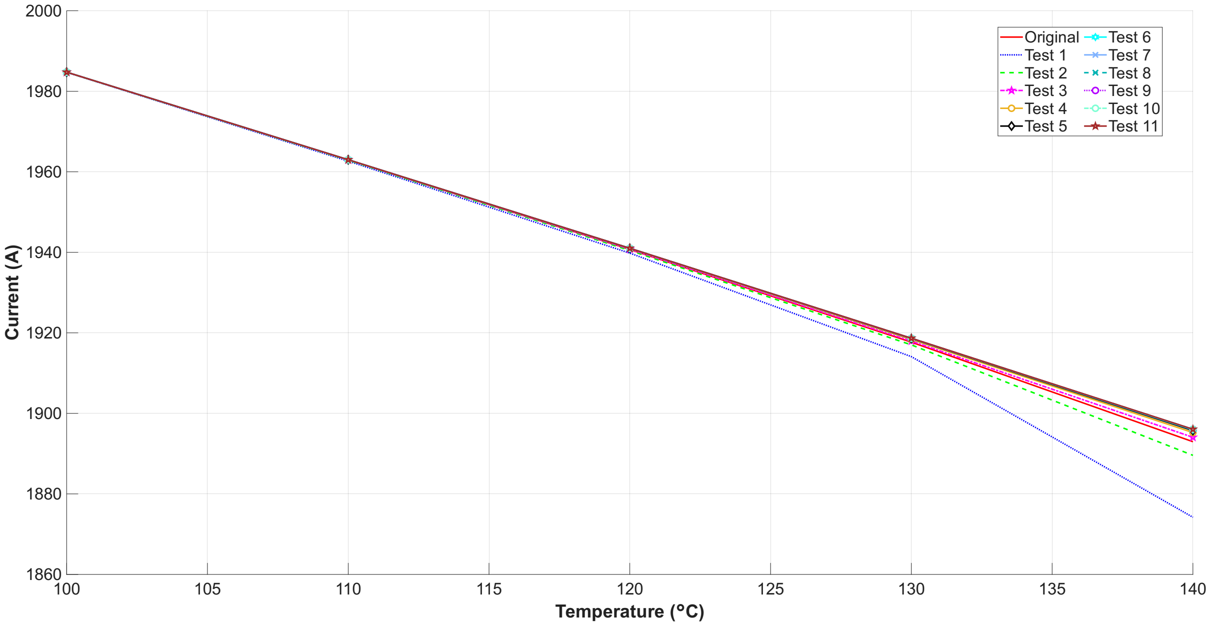

Figure 6.31: Short circuit current amplitude as a function of temperature. Each test indicates increased coercivity with increments of 50 kA/m.

Fig. 6.32 shows the percentage reduction of the average $\boldsymbol{B_r}$ in Layer 1 and 2 for increasing $\boldsymbol{H_{cJ}}$ with constant $\boldsymbol{B_r}$. As shown, the reduction increases with temperature for all test cases and the reduction increases with increasing test index, with the largest values observed at 140°C. At 140°C, the reduction in Layer 1 decreases from approximately 75% for Test 1 to below 10% for the highest test cases. A similar trend is observed in Layer 2, where the reduction is slightly higher across all test cases. This confirms that increasing $\boldsymbol{H_{cJ}}$ directly improves demagnetization resistance.

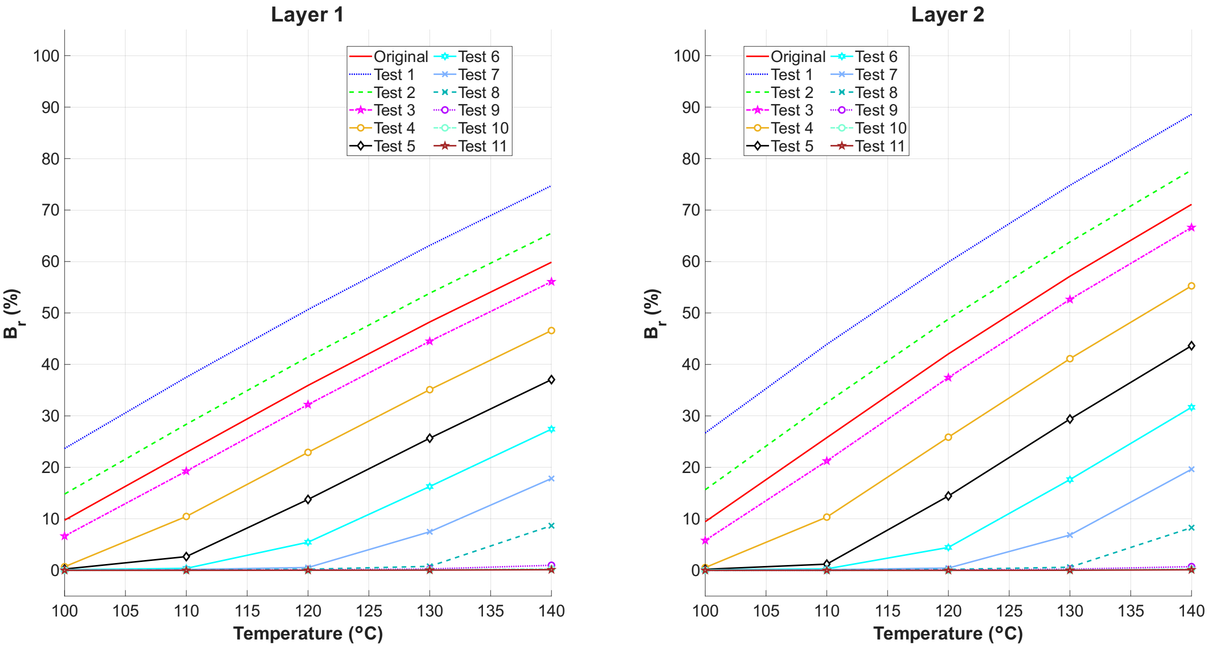

Figure 6.32: Percentage reduction of average B_r in layers 1 and 2 as a function of temperature. Each test indicates increased coercivity with increments of 50 kA/m.

Overall, this case shows that increasing $\boldsymbol{H_{cJ}}$ while keeping $\boldsymbol{B_r}$ constant improves demagnetization resistance without reducing the initial torque capability. The improvement can be explained by the larger distance between the magnet operating point and the knee point of the demagnetization curve. During the short circuit transient, the reverse magnetic field shifts the operating point toward the knee point. For the lower test cases, this shift is sufficient to cause irreversible demagnetization. For the higher test cases, the increased coercivity prevents the operating point from crossing the knee point, which explains the higher torque retention, improved back EMF, and lower $\boldsymbol{B_r}$ reduction.

6.4.2 Increased Coercivity with Reduced Remanence

The second custom magnet case investigates the combined effect of increasing $\boldsymbol{H_{cJ}}$ while reducing $\boldsymbol{B_r}$. In this case, the test indices correspond to paired values from the individual parameter sweeps. Test 1 represents low $\boldsymbol{H_{cJ}}$, approximately 1730 kA/m, and high $\boldsymbol{B_r}$, approximately 1.37 T. Test 11 represents high $\boldsymbol{H_{cJ}}$, approximately 2230 kA/m, and low $\boldsymbol{B_r}$, approximately 0.87 T. The parameter increments are 50 kA/m for $\boldsymbol{H_{cJ}}$ and 0.05 T for

B_r.

As shown in Fig. 6.33, the torque retention under short circuit conditions increases with the test index. Compared to Fig. 6.28, Test 1 and Test 2 show similar behaviour, while higher test cases exhibit improved torque retention. At 140°C, Test 3 increases from approximately 60% to 65%, and Test 4 from below 70% to above 70%. This trend continues for the remaining tests, with the highest test cases approaching 100% in both figures. The differences are most pronounced at higher temperatures. Under normal operating conditions, the torque remains close to 100% for all test cases, with only minor deviations at the highest temperatures.

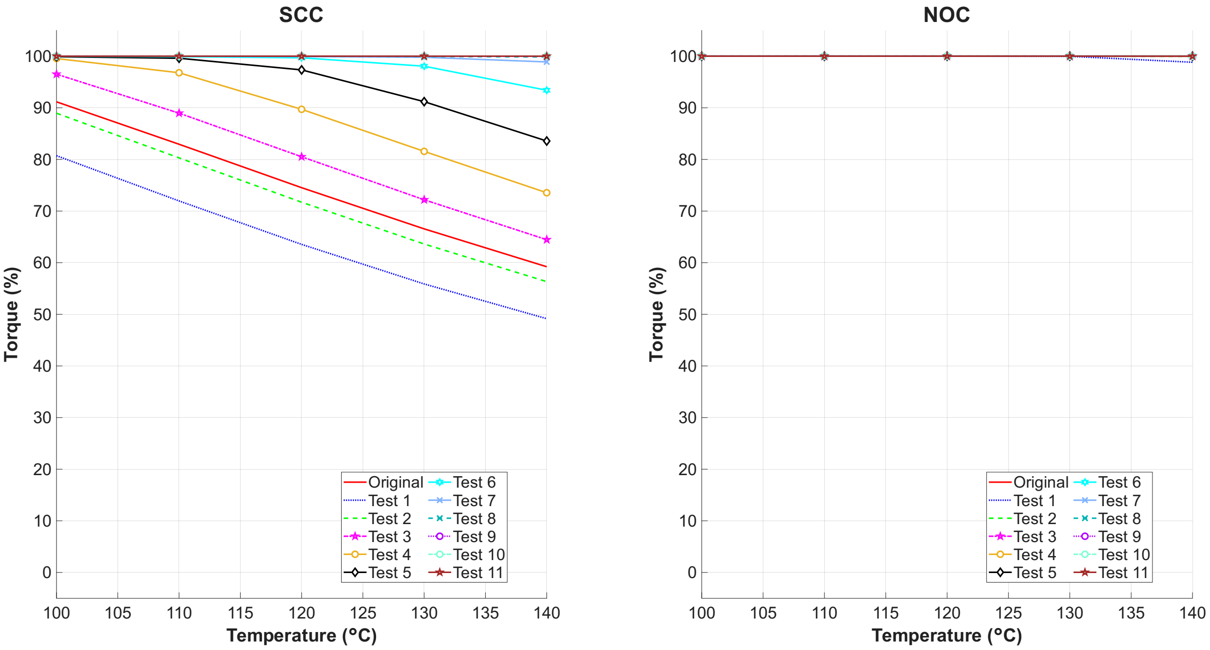

Figure 6.33: Torque retention under SCC and NOC as functions of temperature for combinations of custom magnets with increasing H_{cJ} and decreasing B_r with increments of 50 kA/m and 0.05 T, respectively.

Fig. 6.34 shows the average torque. Before demagnetization, the torque decreases slightly with temperature and with increasing test index, where the lower test cases show higher torque due to higher B_r. After Demagnetization during SCC, the average torque is still higher for the lower test cases at 100°C. This is because B_r is higher at the beginning of the test sequence and decreases with increasing test index. However, Test 1 shows a similar value as in the case with constant B_r, but remains higher than Test 11. Test 2 to Test 4 are above 500 Nm, with Test 4 showing the highest value at around 550 Nm. In contrast, Test 9 to Test 11 are below 500 Nm at the same temperature because of their lower B_r.

At higher temperatures, a different behaviour is observed after demagnetization under SCC. Although the lower index test cases have higher torque at 100°C, they decrease more with temperature. At 140°C, Test 1 to Test 5 drop to around 450 Nm or lower. In contrast, the higher test cases decrease less because of their higher H_{cJ}, and Test 7 and Test 8 remain above 500 Nm at 140°C. This shows the trade-off between initial performance and demagnetization resistance. In addition, Test 3 to Test 5 show slightly higher torque compared to the original case, indicating improved performance in this range since lower tests had started with higher B_r.

Under normal operating conditions is similar to before demagnetization, Test 1 to Test 6 remain above 500 Nm across the full temperature range, including the original case. Test 1 shows slightly higher torque than the original case, while the remaining test cases are lower, particularly at 140°C.

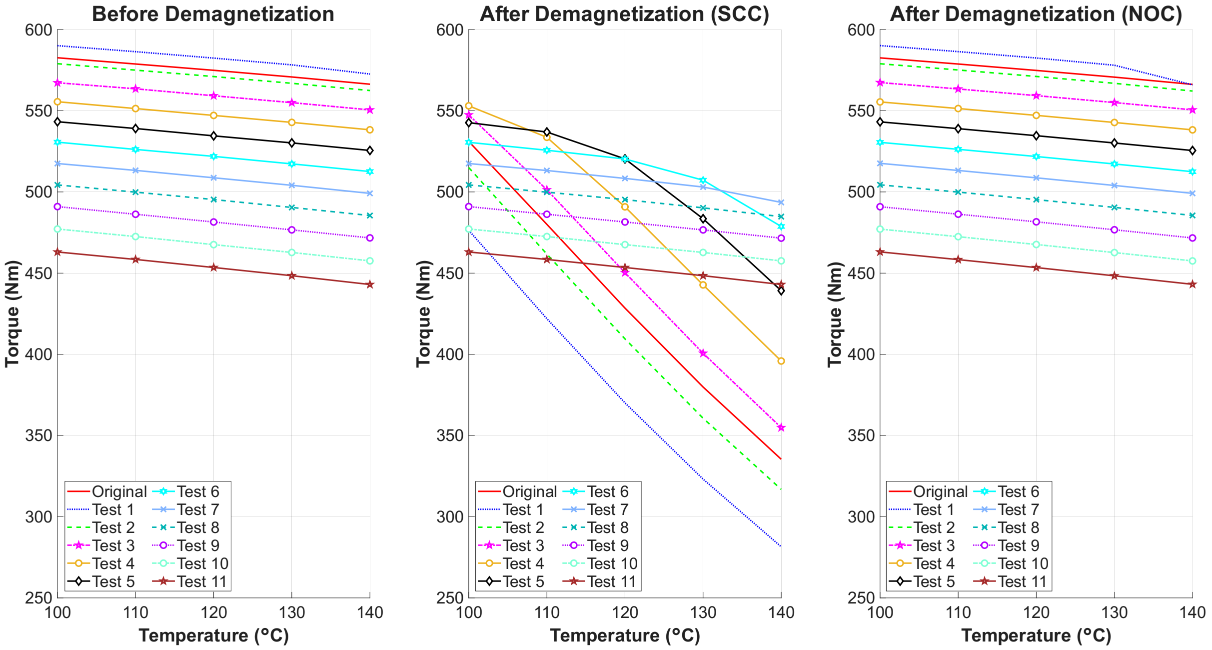

Figure 6.34: Average torque before and after demagnetization under SCC and NOC as functions of temperature for combinations of custom magnets with increasing H_{cJ} and decreasing B_r with increments of 50 kA/m and 0.05 T, respectively.

Fig. 6.35 shows the back EMF behaviour. Compared to the constant B_r case, the lower test cases show similar behaviour, while higher test cases exhibit increased back EMF retention. At 140°C, Test 4 increases from approximately 40% in Fig. 6.30 to around 50% in Fig. 6.35, corresponding to $H_{cJ} \approx 1880$ kA/m and $B_r \approx 1.22$ T. A clear difference is also observed for higher test cases, where Test 7 reaches close to 100% in Fig. 6.35, corresponding to $H_{cJ} \approx 2030$ kA/m and $B_r \approx 1.07$ T, whereas a similar level is reached only around Test 10 in in the constant B_r case. Across the temperature range, the curves shift upward with increasing test index, with the largest differences occurring at higher temperatures. Under normal operating conditions, the back EMF remains close to 100% for nearly all test cases, similar to Fig. 6.30, with only minor deviations at 140°C for the lowest test cases.

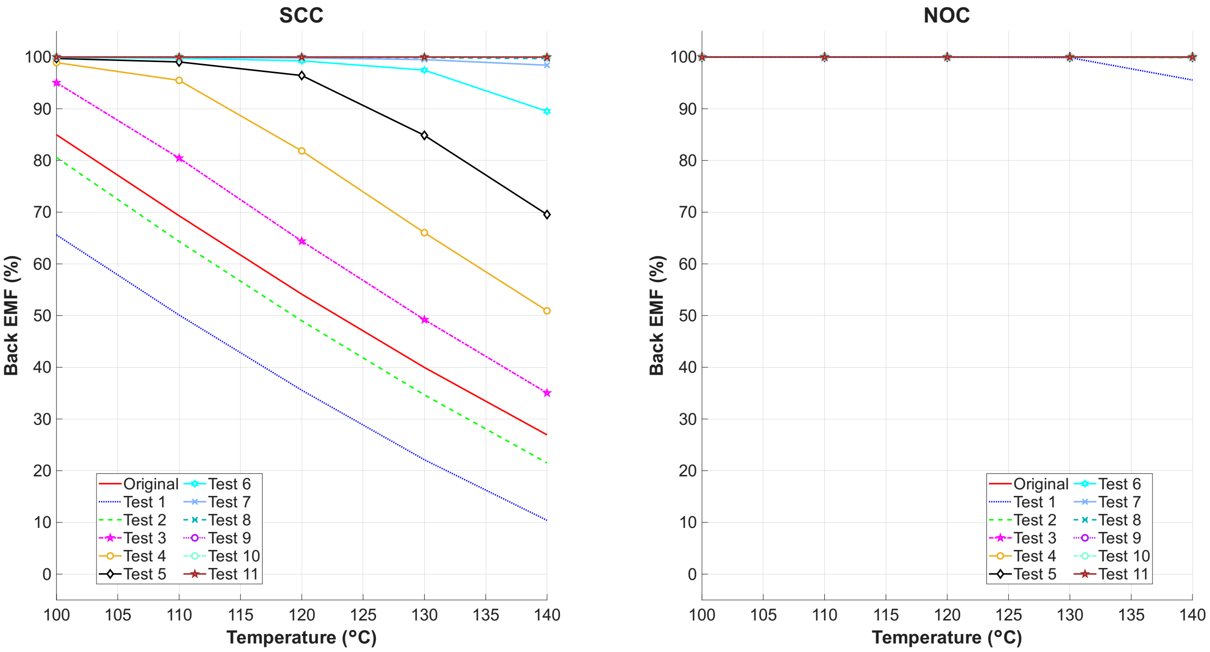

Figure 6.35: Back EMF retention under SCC and NOC as functions of temperature for combinations of custom magnets with increasing H_{cJ} and decreasing B_r with increments of 50 kA/m and 0.05 T, respectively.

Fig. 6.36 shows the short circuit current amplitude, as shown, the current decreases with temperature for all test cases. The lower test cases show higher current levels because they have higher B_r. At 100°C, the current decreases from approximately 2030 A for Test 1 to around 1450 A for Test 11. A similar trend is observed at 140°C, where the current decreases from approximately 1900 A to around 1380 A. The original case follows a similar trend and lies among the lower test cases. Across the temperature range, the curves remain nearly parallel, indicating that the temperature dependence is similar for all test cases.

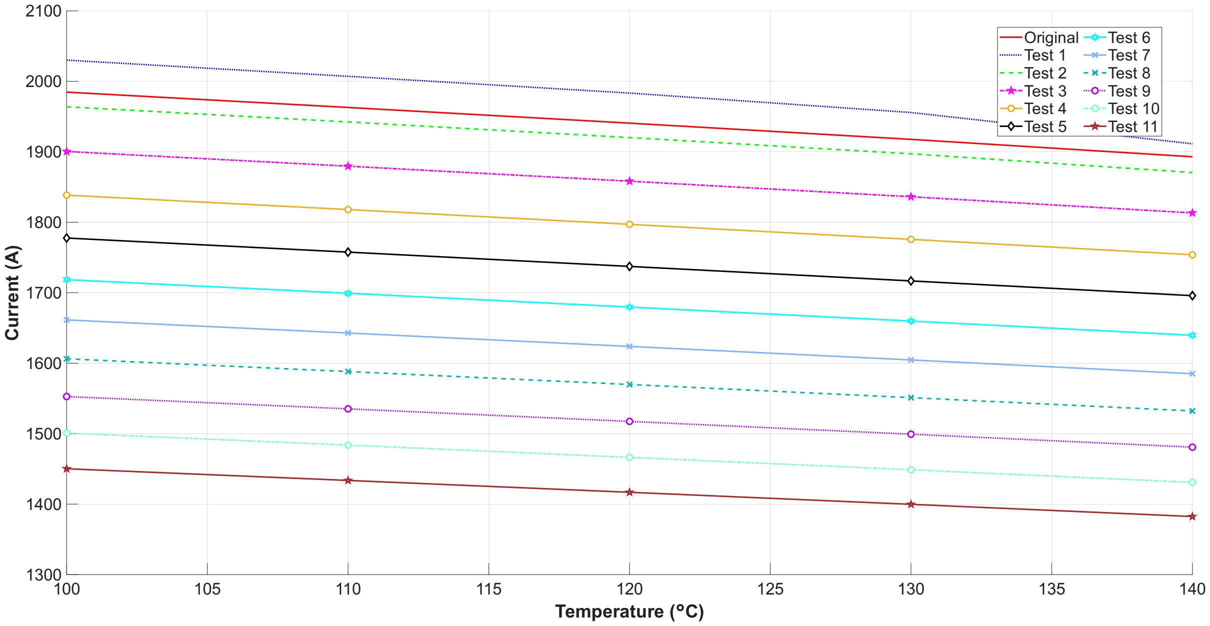

Figure 6.36: Short circuit current amplitude as functions of temperature for combinations of custom magnets with increasing H_{cJ} and decreasing B_r with increments of 50 kA/m and 0.05 T, respectively.

Compared to Fig. 6.32, Fig. 6.37 shows that Test 1 and Test 2 exhibit nearly identical behaviour. Differences become visible from Test 3, where the reduction starts from 0% at 100°C in both layers. At higher temperatures, a lower $\boldsymbol{B_r}$ reduction is observed for the combined case. For example, at 140°C in Layer 1, Test 4 decreases from just below 50% in Fig. 6.32 to below 40% in Fig. 6.37. A similar trend is observed in Layer 2, where the reduction decreases from approximately 55% to around 47%. This behaviour is consistent for higher test indices, where the reduction remains lower in Fig. 6.37 compared to the case with constant $\boldsymbol{B_r}$. The same trend is observed in both layers.

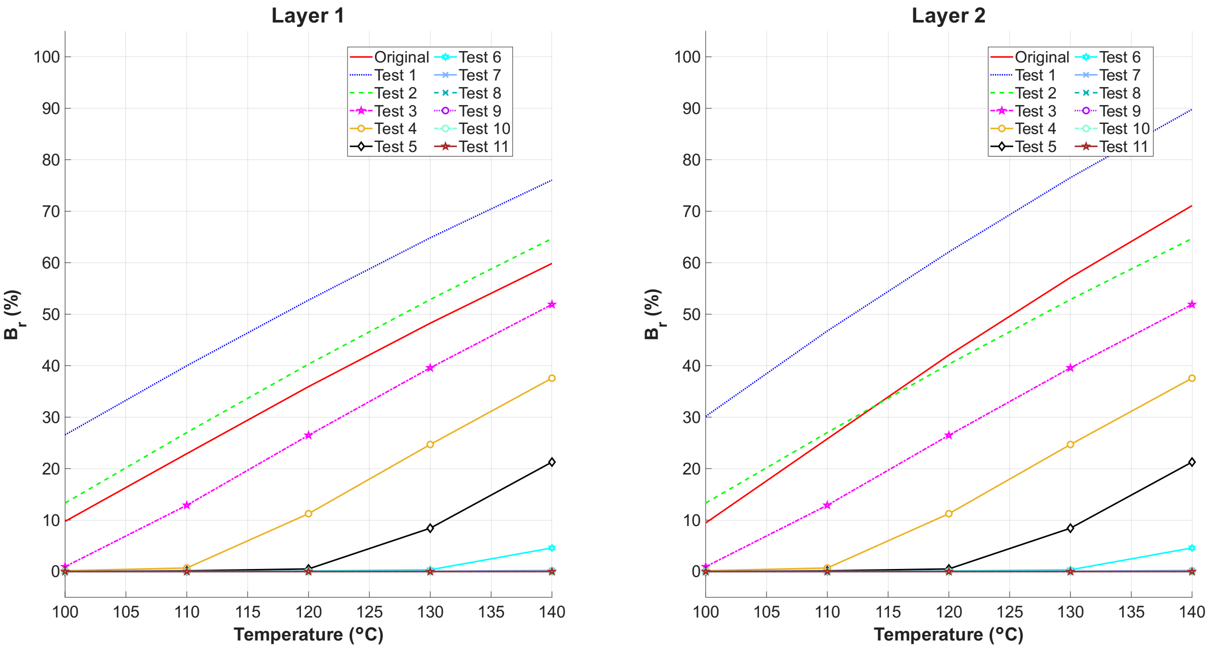

Figure 6.37: Percentage reduction of B_r under SCC and NOC as functions of temperature for combinations of custom magnets with increasing H_{cJ} and decreasing B_r with increments of 50 kA/m and 0.05 T, respectively.

This case shows the trade-off between coercivity and remanence. Increasing H_{cJ} improves resistance to irreversible demagnetization, especially at high temperature. However, reducing B_r lowers the initial flux linkage, which reduces the torque capability before demagnetization and under NOC. Therefore, the best cases are found in the middle of the test range, where H_{cJ} is sufficiently high to limit demagnetization while B_r is still high enough to maintain the required torque.

6.4.3 Increased Coercivity with Increased Remanence

The third custom magnet case investigates the combined effect of increasing both H_{cJ} and B_r. In this case, Test 1 represents low H_{cJ}, approximately 1730 kA/m, and low B_r, approximately 0.87 T. Test 11 represents high H_{cJ}, approximately 2230 kA/m, and high B_r, approximately 1.37 T.

As shown in Fig. 6.38, all test cases start at approximately 100% torque at 100°C, which differs from the behaviour observed in Fig. 6.33 and Fig. 6.28. At higher temperatures, the torque retention remains consistently higher for all test cases. For example, at 140°C, Test 1 retains approximately 73% torque, compared to around 50% in Fig. 6.33. A similar improvement is observed across all test indices, where both intermediate and higher test cases show increased torque retention. The curves are therefore shifted upwards across the entire temperature range, with reduced variation between the test cases compared to the previous figures. Under normal operating conditions, all test cases maintain torque levels close to 100% with no visible differences.

It should be noted that the original curve is included only as a reference and is not part of the Test 1–Test 11 sequence. The test cases are artificial custom magnet definitions where $\boldsymbol{H_{cJ}}$ and $\boldsymbol{B_r}$ are varied together in fixed increments. The original curve, however, uses the actual temperature-dependent material data of 45SH$_{S6}$. Therefore, it does not necessarily follow the same slope as the custom test cases. The different slope indicates that the thermal behaviour of the original magnet data differs from the simplified custom magnet sweep.

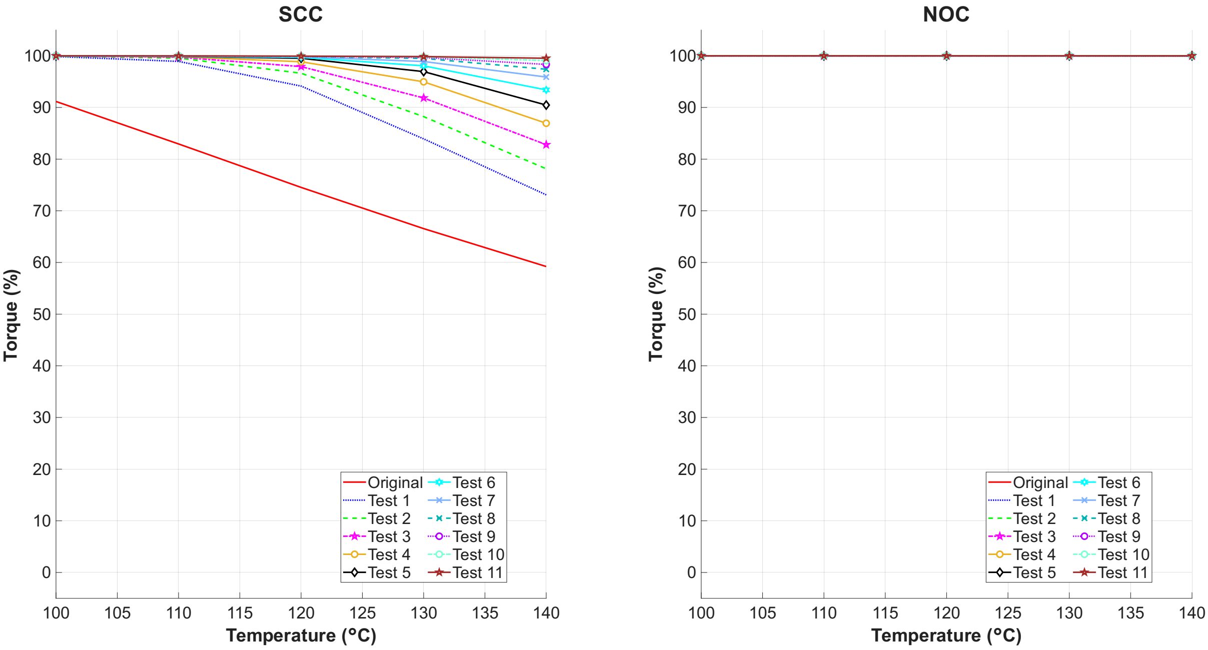

Figure 6.38: Torque retention under SCC and NOC as functions of temperature for combinations of custom magnets with increasing H$_{cJ}$ and increasing B$_r$ with increments of 50 kA/m and 0.05 T, respectively.

Fig. 6.39 shows the average torque for the case where both $\boldsymbol{H_{cJ}}$ and $\boldsymbol{B_r}$ increase. Before demagnetization, the torque decreases slightly with temperature, while higher test cases show higher torque values across the full temperature range. Similar trend is observed for NOC.

After demagnetization under SCC, a clear difference is observed. The higher test cases, especially Test 7 to Test 11, remain above 500 Nm at both 100°C and 140°C. In contrast, the lower test cases, particularly Test 1 to Test 3, are below 500 Nm at both temperatures. In general, the lower test cases show a larger decrease with temperature, while the higher test cases remain more stable. Test cases from Test 6 and above are generally higher than the original case.

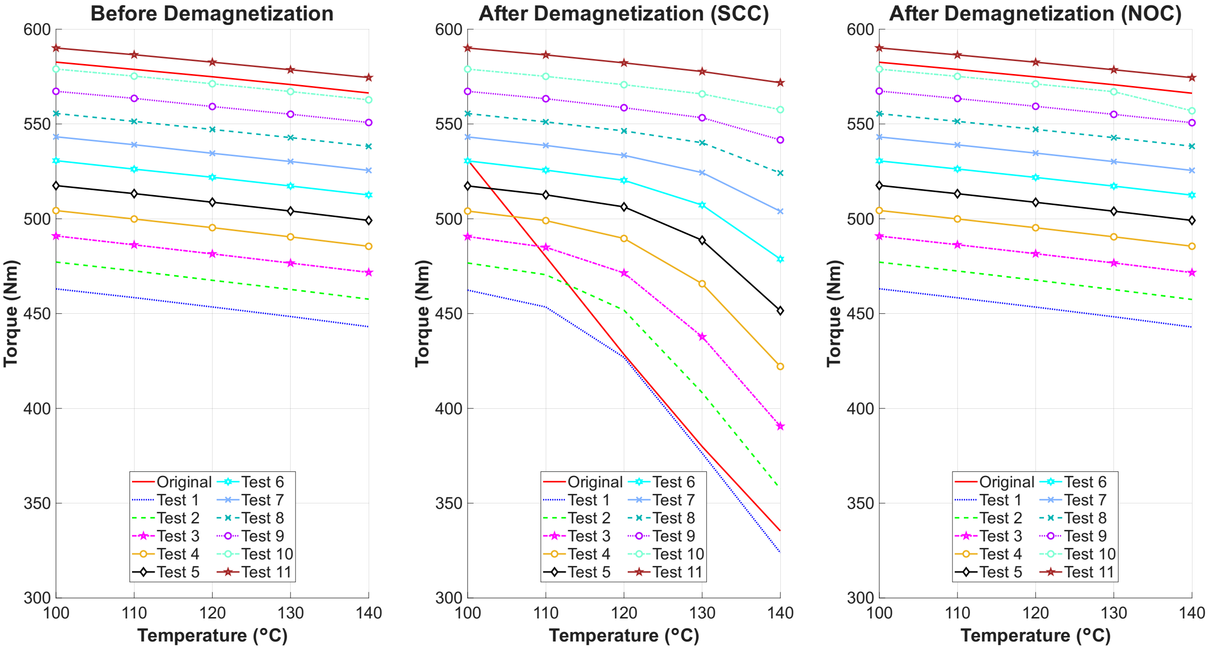

Figure 6.39: Average torque before and after demagnetization under SCC and NOC as functions of temperature for combinations of custom magnets with increasing H_{cJ} and increasing B_r with increments of 50 kA/m and 0.05 T, respectively.

Fig. 6.40 shows the back EMF behaviour for the case where both $\boldsymbol{H}_{cj}$ and $\boldsymbol{B}_r$ increase. As shown, all test cases start close to 100% at 100°C, similar to the torque behaviour. At 140°C, Test 1 retains approximately 40%, whereas it decreases to around 10% in Fig. 6.35. This shows that the lower $\boldsymbol{B}_r$ in Test 1 reduces the demagnetization severity when $\boldsymbol{H}_{cJ}$ is low. As the test index increases, both $\boldsymbol{H}_{cJ}$ and $\boldsymbol{B}_r$ increase, and the intermediate and higher test cases maintain significantly higher back EMF retention. Under NOC, the back EMF remains approximately constant at 100% for all test cases.

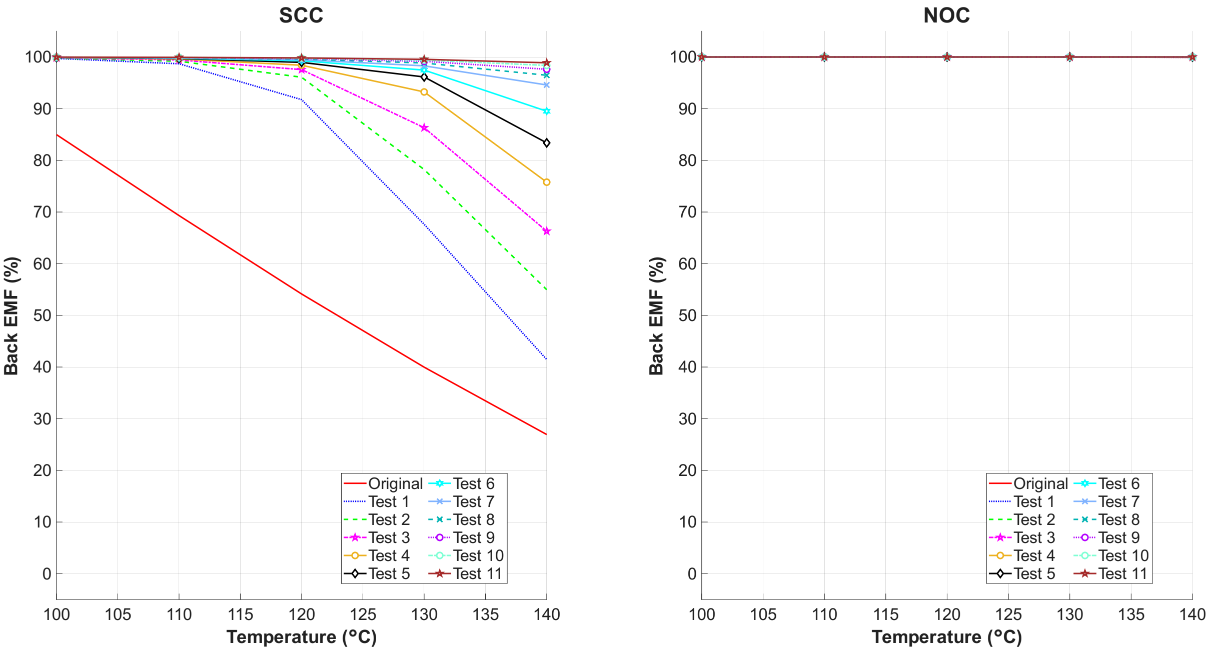

Figure 6.40: Back EMF retention under SCC and NOC as functions of temperature for combinations of custom magnets with increasing H$_{cJ}$ and increasing B$_r$ with increments of 50 kA/m and 0.05 T, respectively.

Fig. 6.41 shows the short circuit current amplitude. The current increases with test index because $\boldsymbol{B_r}$ increases. At 100°C, the current ranges from approximately 1450 A for Test 1 to around 2000 A for the highest test cases. At 140°C, it decreases to approximately 1380 A for Test 1 and remains close to 1900 A for the highest test cases. As in the previous case, the curves remain nearly parallel, indicating similar temperature dependence.

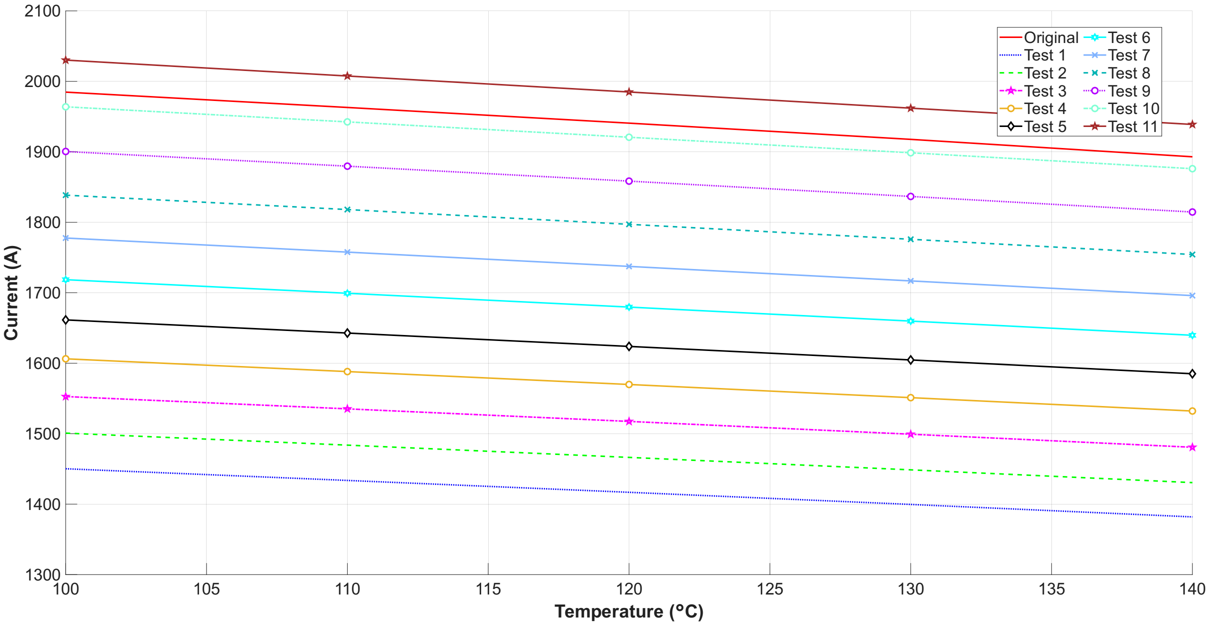

Figure 6.41: Short circuit current amplitude as functions of temperature for combinations of custom magnets with increasing H$_{cJ}$ and increasing B$_r$ with increments of 50 kA/m and 0.05 T, respectively.

Fig. 6.42 shows the percentage reduction of $\boldsymbol{B_r}$. As shown, all test cases start from 0% reduction at 100°C in both layers. At higher temperatures, the reduction increases with temperature, but remains lower compared to the previous cases. At 140°C, Test 1 reaches approximately 40% in Layer 1, showing an improvement compared to the corresponding cases in Fig. 6.37 and Fig. 6.32. As the test index increases, the reduction decreases further, with higher test cases exhibiting only minor reduction. This trend is consistent in both layers, where increasing $\boldsymbol{H_{cJ}}$ and $\boldsymbol{B_r}$ leads to reduced $\boldsymbol{B_r}$ degradation across all test cases. Layer 2 follows the same behaviour as Layer 1 but shows slightly higher reduction values across the full temperature range.

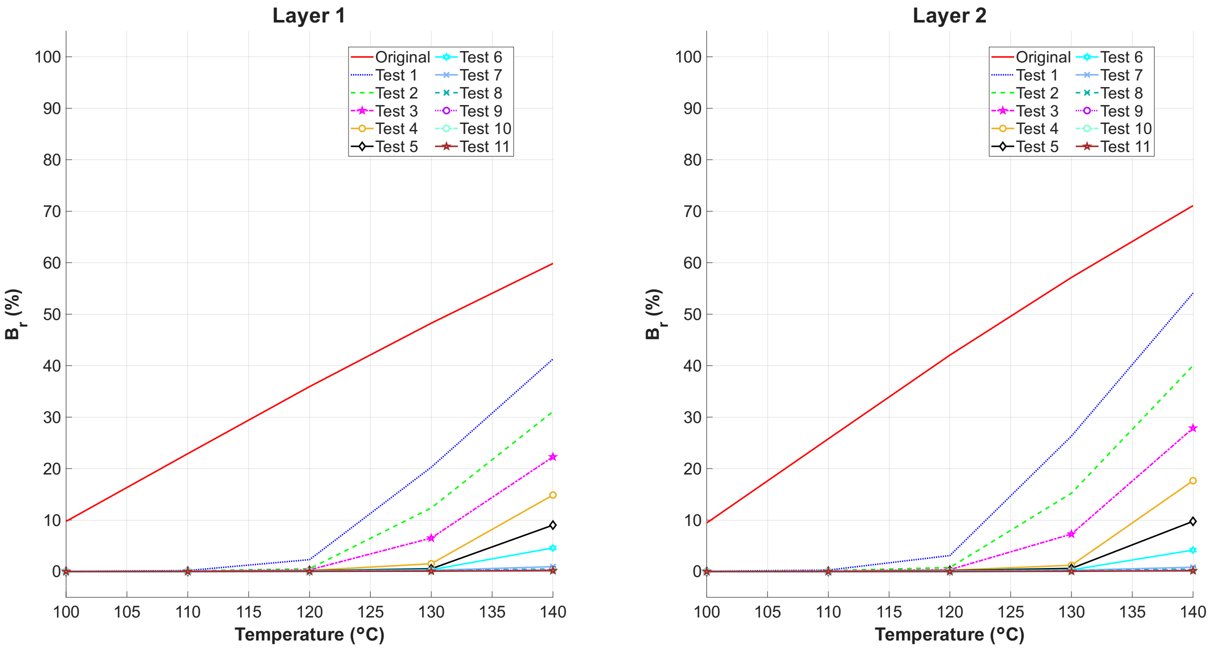

Figure 6.42: Percentage reduction of B_r under SCC and NOC as functions of temperature for combinations of custom magnets with increasing H_{cJ} and increasing B_r with increments of 50 kA/m and 0.05 T, respectively.

This case gives the best overall performance because both the magnetic strength and the demagnetization resistance are improved. Increasing B_r increases the flux linkage and therefore improves the torque capability, while increasing H_{cJ} prevents the operating point from crossing the knee point during the short circuit transient. From approximately Test 6 and above, both parameters are sufficiently high to improve the performance relative to the original design. The higher test cases therefore show higher torque, improved back EMF retention, and reduced B_r degradation across the investigated temperature range.

However, the highest test cases correspond to significantly increased H_{cJ} values compared to the original design. In particular, Test 7–11 approach or exceed approximately 2000 kA/m, which is closer to the coercivity level of UH grade materials than standard SH grade magnets. This indicates that a magnet supplier would need to provide HRE-free magnets with very high intrinsic coercivity to achieve this level of robustness in the unchanged rotor geometry. Such values may not be readily available within current HRE-free magnet classes. Therefore, although the custom magnet study shows that improved material properties can solve the demagnetization problem, it also shows that material development alone may not be realistic. This motivates the rotor geometry study, where the aim is to improve the demagnetization behaviour through design changes rather than relying only on very high coercivity magnet material.

Another possible route to achieving higher H_{cJ} in HRE-free magnets is further improvement of the magnet manufacturing process, for example through grain size refinement. As described in Section 2.3.3, reducing the grain size can increase coercivity up to an optimum value. This suggests that future HRE-free magnet development should focus not only on chemical composition, but also on processing routes that improve coercivity without requiring HRE addition.

6.5 Rotor Geometry Study

This section presents the results from the rotor geometry parametric study at 140°C, based on the previously selected reference 45SH magnet. The purpose of the study is to identify which rotor geometry parameters have the strongest influence on demagnetization behaviour and electromagnetic performance. The study is used as a preliminary step before the rotor geometry optimization.

The geometry parameters are evaluated separately for Layer 1 and Layer 2, except for magnet thickness, where the thickness of both magnet layers is varied simultaneously. The main parameters presented in this section are magnet thickness, pole V angle, and web thickness. Additional parameters, including magnet separation, web length, and magnet post, are presented in Appendix B.

In addition to the individual parameter variations, a set of combined rotor geometry configurations is also evaluated. These configurations are constructed by combining selected parameter values from the individual studies.

6.5.1 Magnet Thickness

Fig. 6.43 shows the torque retention, back EMF retention, and percentage reduction of the average $\boldsymbol{B_r}$ as a function of increasing magnet thickness in both magnet layers. Under normal operating conditions, the torque and back EMF remain at 100% for all investigated thicknesses, which indicates that no noticeable irreversible demagnetization occurs during normal operation.

For SCC, the torque and back EMF retention increases with increasing magnet thickness. The torque increases from approximately 59% retention to approximately 72%, while the back EMF increases from approximately 27% to 44% retention. For the percentage reduction of average B_r, it decreases with increasing magnet thickness. This is because a thicker magnet contains more material in the magnetization direction, which makes the magnet less sensitive to the local reverse field during the short circuit event. The demagnetization is mainly concentrated near exposed regions such as magnet edges and tips, while a larger part of the magnet volume remains magnetized when the thickness is increased. Therefore, the average $\boldsymbol{B_r}$ reduction becomes lower. For Layer 1 it decreases from 60% to approximately 42% and from approximately 72% to 47% for Layer 2.

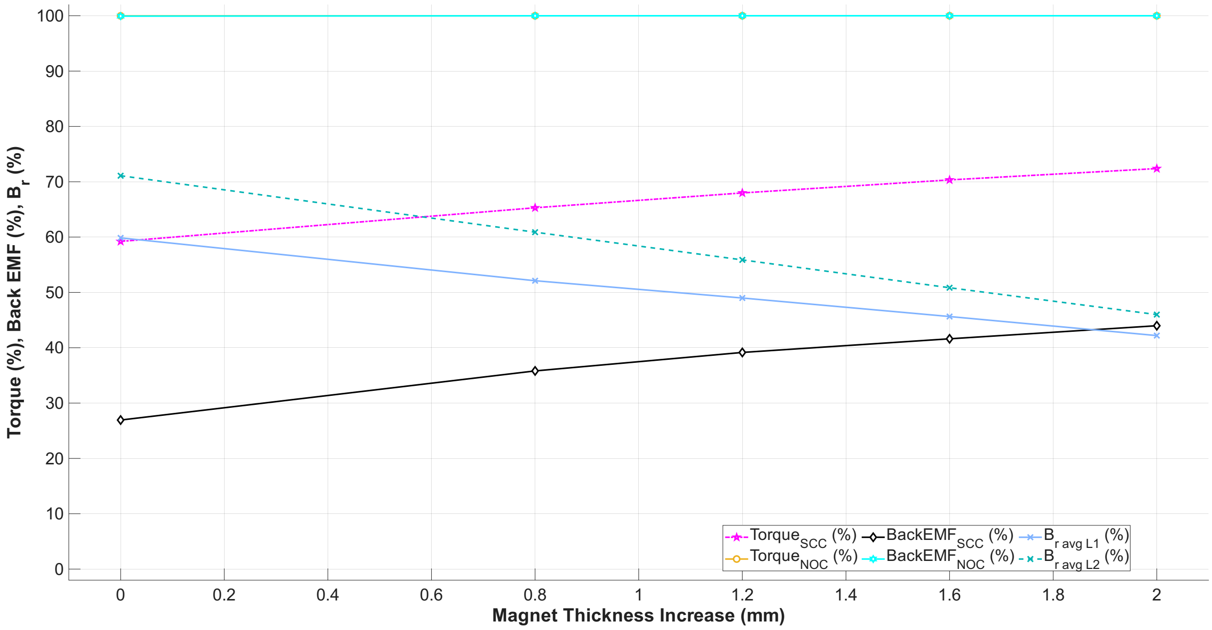

Figure 6.43: Torque and back EMF under SCC and NOC, and reduction of average B$_r$ as function of magnet thickness in Layers 1 and 2, at 140°C.

In Fig. 6.44, the average torque before and after demagnetization is shown for both SCC and NOC, together with the short circuit current amplitude. The torque after demagnetization under NOC is equal to the torque before demagnetization, and both increase from approximately 565 Nm to 610 Nm with increasing magnet thickness. This shows that no noticeable irreversible demagnetization occurs under NOC, while the higher magnet thickness increases the available flux and therefore the torque.

Under SCC, the torque after demagnetization also increases with magnet thickness, from approximately 335 Nm to 440 Nm. Although the short circuit current amplitude increases from approximately 1900 A to 2500 A, the demagnetization is still reduced. This is because the increased magnet thickness gives more magnet material in the magnetization direction, which makes the magnet more resistant to the reverse field during the short circuit event. As a result, a larger part of the magnet remains magnetized even though the fault current is higher.

The comparison between NOC and SCC shows that the benefit of increasing magnet thickness is mainly related to the short circuit case. For the thinnest magnet, the torque difference between NOC and SCC after demagnetization is approximately 230 Nm, from about 565 Nm to 335 Nm. For the thickest magnet, this difference is reduced to approximately 170 Nm, from about 610 Nm to 440 Nm. Thus, thicker magnets do not remove the demagnetization problem but reduce the performance loss caused by SCC. Therefore, increasing magnet thickness is beneficial for SCC robustness, although it also increases magnet weight and short circuit current.

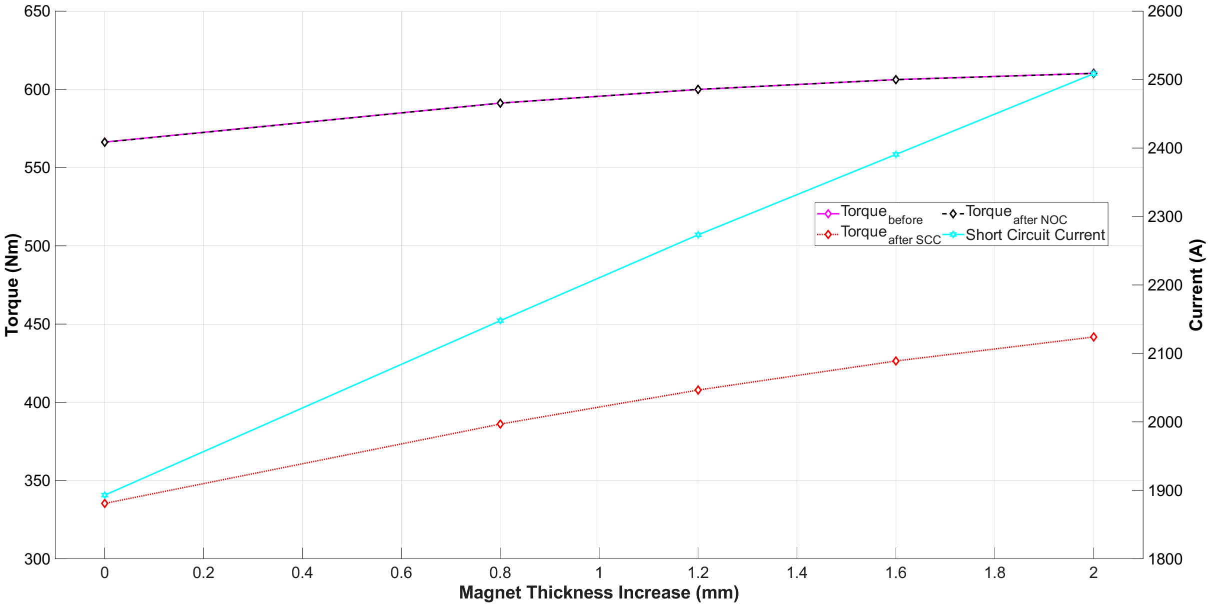

Figure 6.44: Average torque before and after demagnetization due to SCC and NOC (left y-axis, diamond shaped markers) and short circuit current amplitude (right y-axis, hexagram markers) as functions of magnet thickness increase in Layers 1 and 2 at 140°C.

The results show that magnet thickness has a strong influence on both the available magnetic flux and the demagnetization resistance. Increasing the magnet thickness increases the flux linkage, ψ_{PM}, which improves the torque capability. It also means that a larger magnet volume remains magnetized during the short circuit event, reducing the relative loss of B_r. However, the increased flux also leads to a higher short circuit current amplitude, which indicates a stronger electromagnetic interaction during the fault. Magnet thickness therefore improves post fault performance, but at the cost of increased magnet volume and higher short circuit current.

6.5.2 Pole V-Angle

Fig. 6.45 shows the torque retention, back EMF retention, and percentage reduction of the average B_r when the pole V-angle is varied separately in Layer 1 and Layer 2. Under NOC, the torque and back EMF retention remain at 100% throughout the investigated angle range in both layers, which indicates that no noticeable irreversible demagnetization occurs during normal operation.

To the left in Fig. 6.45, the results for Layer 1 are presented. Under SCC, the torque retention decreases from approximately 65% to 60% as the angle is increased. The back EMF retention also decreases from approximately 43% to 28%, although a small local increase is observed around 81° before the curve continues downward. At the same time, the reduction of average B_r increases from approximately 45% to 60% in Layer 1 and from approximately 68% to 71% in Layer 2.

The small local increase in back EMF around 81° is most likely caused by a temporary improvement in the magnetic flux path. Changing the pole V-angle affects both the useful flux linkage and the local demagnetizing field acting on the magnets. At some angles, the magnet orientation can slightly improve how the remaining magnet flux links with the stator winding, which gives a small increase in back EMF. However, when the angle is increased further, the magnets become more exposed to the reverse field during SCC and the average $\boldsymbol{B_r}$ reduction increases. Therefore, the overall trend is still a reduction in both torque and back EMF retention.

To the right in Fig. 6.45, the results for Layer 2 are shown. When the angle in Layer 2 is increased, the torque retention remains between approximately 58% and 62%, with the highest value around 125°. The back EMF retention varies between approximately 27% and 30%, with the highest value occurring at the same angle as the torque. The reduction of average $\boldsymbol{B_r}$ remains within a narrow range, approximately 59% to 60% in Layer 1 and 69% to 72% in Layer 2.

These results show that the pole V-angle does not give a simple monotonic improvement. Instead, it changes the balance between useful air-gap flux and local demagnetizing field. For Layer 1, increasing the angle generally worsens the SCC performance, while for Layer 2 an intermediate angle around 125° gives the best result. This indicates that the pole V-angle can be used to fine tune the field distribution, but it is not as dominant as magnet thickness for improving demagnetization robustness.

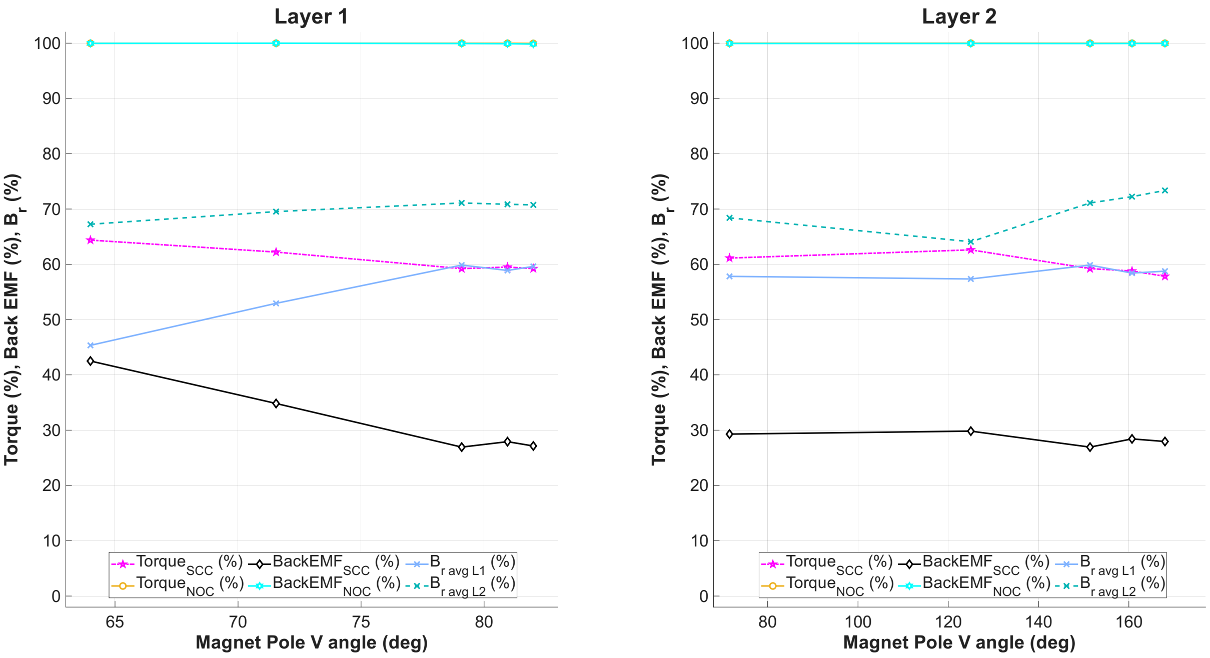

Figure 6.45: Torque and Back EMF under SCC and NOC, and percentage reduction of average B$_r$, as function of varying magnet pole V angle in Layers 1 and 2, at 140°C.

Fig. 6.46 shows the corresponding average torque and short circuit current amplitude. To the left in Fig. 6.46, the results for Layer 1 are shown. The torque before demagnetization and after demagnetization at NOC increase from approximately 530 Nm to 570 Nm with increasing angle. However, the torque after demagnetization under SCC increases by a few Nm at first but then decrease to around 335 Nm from its initial 340 Nm. The short circuit current increases from approximately 1755 A to 1875 A, with a peak of 1890 A at approximately 79°.

To the right in Fig. 6.46, the results for Layer 2 are presented. With increasing angle, the torque before demagnetization and after under NOC stay around 560 Nm with minimal changes. The torque after demagnetization under short circuit conditions increase from 345 Nm to a maximum of 350 Nm at around 125°, before decreasing again with further increasing angle. At the smallest angle, the short circuit current is at 1860 A, which decreases to 1835 A at 125° before increasing up towards 1915 A at the largest angle of around 165°.

The short circuit current does not follow the same trend for the Layer 1 and Layer 2 angle variations. This is because changing the V angle in the two layers affects different parts of the rotor magnetic circuit. When the angle in Layer 1 is changed, the main flux path and the flux linkage are affected more directly, which leads to an overall increase in short circuit current. For Layer 2, the angle variation initially gives a slightly lower current, most likely because the flux linkage and the effective coupling to the stator are reduced. At larger Layer 2 angles, the magnetic path changes again and the current increases. This indicates that the V angle influences both the useful air gap flux and the local field distribution, and that the effect depends on which magnet layer is modified.

The result also shows that the pole V angle alone does not give a clear improvement in SCC robustness. Although an intermediate Layer 2 angle gives a small increase in torque after SCC and a lower short circuit current, the improvement is limited. Therefore, the pole V angle is mainly useful as a fine tuning parameter for the magnetic field distribution, rather than as the main parameter for reducing demagnetization.

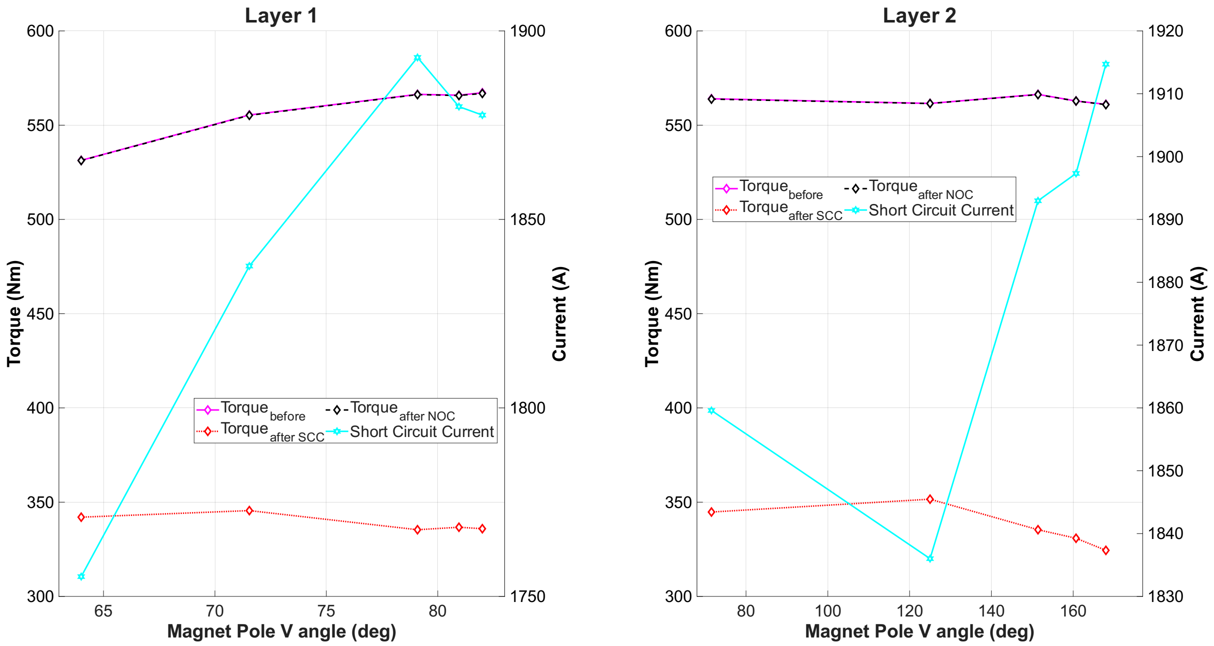

Figure 6.46: Average torque before and after demagnetization under SCC and NOC (left y-axis, diamond shaped markers) and short circuit current amplitude (right y-axis, hexagram markers) as functions of magnet pole V angle in Layers 1 and 2 at 140°C.

The pole V angle mainly affects the direction and distribution of the magnetic field rather than the total flux level. Changing the angle alters how the magnetization direction is positioned relative to the stator magnetic field during the short circuit event. This changes how much of the stator field acts directly against the magnetization of the magnets. Compared with magnet thickness, the influence of pole V angle is therefore more limited. The results show that the pole V-angle should not simply be increased in both layers. Increasing the angle in Layer 1 generally worsens the SCC behaviour, since the torque and back EMF retention decrease and the average $\boldsymbol{B_r}$ reduction increases. For Layer 2, an intermediate angle around 125° gives the best result, with slightly higher torque after SCC and lower short circuit current. Therefore, the pole V-angle is mainly useful as a fine-tuning parameter. In this study, increasing the Layer 1 angle is not beneficial, while a moderate Layer 2 angle can slightly improve the SCC response.

6.5.3 Web Thickness

Fig. 6.47 shows the torque and back EMF retention after demagnetization under SCC, as well as the percentage reduction of average $\boldsymbol{B_r}$, as a function of web thickness, varied separately in Layers 1 and 2. The torque and back EMF retention during normal operating conditions stay at 100% for both investigated cases.

To the left in Fig. 6.47, the results for Layer 1 are shown. Under SCC, the torque retention increases slightly from approximately 59% to 61% with increasing web thickness. Similarly, the back EMF increases from approximately 28% to 32%. The reduction of average $\boldsymbol{B_r}$

decreases from approximately 60% to 49% in Layer 1 and from approximately 71% to 69% in Layer 2.

To the right in Fig. 6.47, the results for Layer 2 are presented. The torque retention shows a similar slight increase, while the back EMF increases from approximately 24% to 28% with increasing web thickness. The reduction of average B_r decreases from approximately 78% to 65% in Layer 1. In Layer 2, the reduction reaches a maximum of approximately 60% and decreases to around 51% at the lowest investigated thickness.

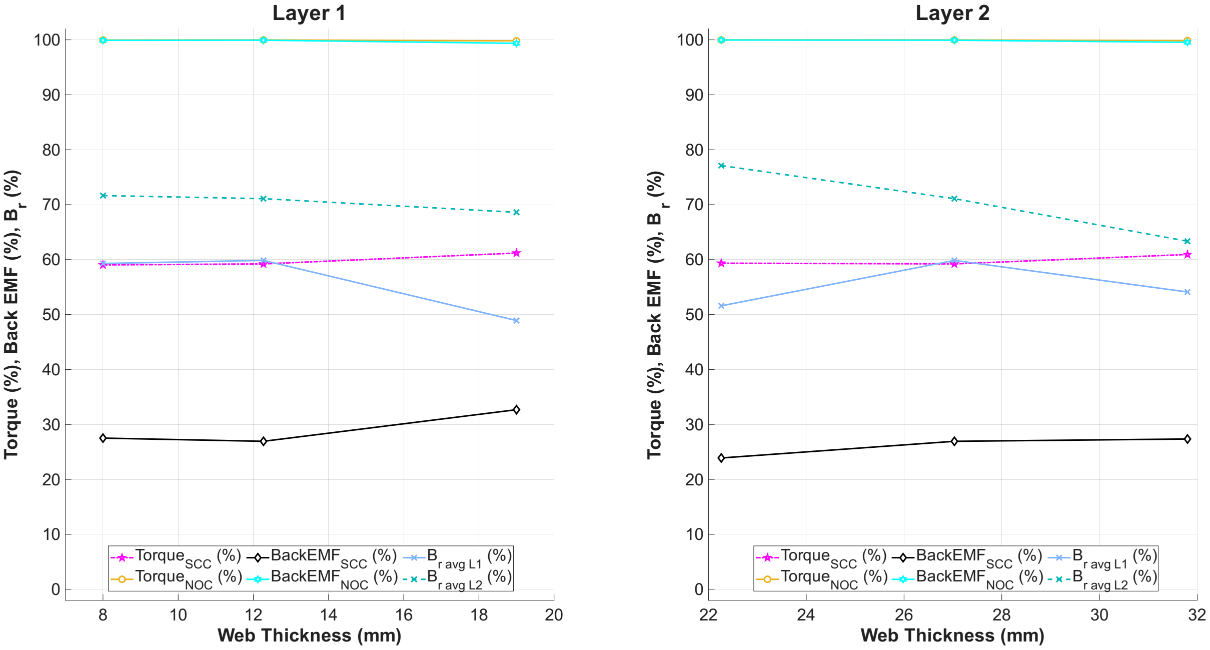

Figure 6.47: Torque and Back EMF behaviour for SCC and NOC and percentage reduction of average B_r with varying web thickness in layers 1 and 2, at 140°C.

The average torque and short circuit current amplitude are shown in Fig. 6.48. To the left in Fig. 6.48, the results for Layer 1 are presented. To the right in Fig. 6.48, the results for Layer 2 are presented. The torque before demagnetization and after demagnetization under NOC varies between approximately 550 Nm and 565 Nm, with a peak at a web thickness slightly above 12 mm. The torque after demagnetization under SCC shows a small increase from approximately 330 Nm to 335 Nm with increasing web thickness. The short circuit current decreases overall from approximately 1875 A to 1855 A, with a peak of around 1893 A at the same thickness where the torque reaches its maximum.

To the right in Fig. 6.48, the results for Layer 2 are shown. The torque before demagnetization and after demagnetization under NOC increases from approximately 540 Nm to 555 Nm, with a peak of around 570 Nm at a web thickness of approximately 27 mm. Under SCC, the torque after demagnetization increases from approximately 325 Nm to 335 Nm with increasing web thickness. The short circuit current initially increases slightly to a peak of approximately 1890 A at around 27 mm, before decreasing significantly to approximately 1810 A at the largest investigated thickness.

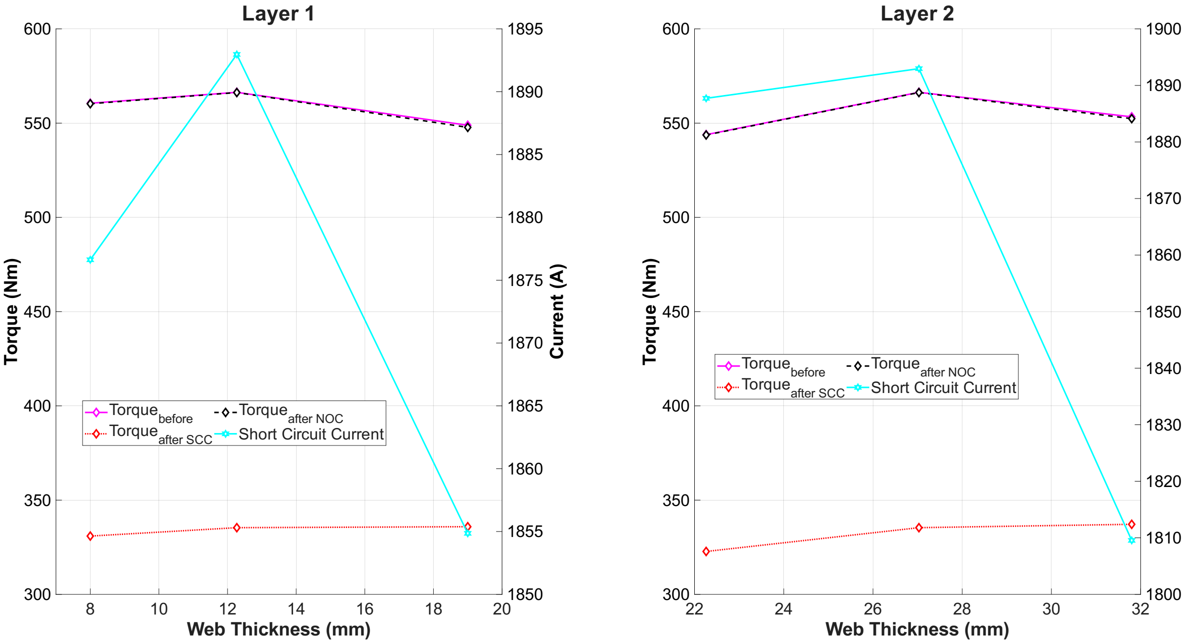

Figure 6.48: Average torque before and after demagnetization due to SCC and NOC (left y-axis, diamond shaped markers) and short circuit current amplitude (right y-axis, hexagram markers) as functions of web thickness in layers 1 and 2 at 140°C.

The web thickness mainly influences the magnetic path inside the rotor. Increasing the web thickness changes the local reluctance and redistributes the flux in the rotor structure. This can reduce local field concentrations and therefore reduce the effective demagnetizing field acting on the magnets. Increasing the web thickness can help reduce demagnetization, but the effect on torque is limited. For Layer 1, increasing the web thickness reduces the average B_r reduction in Layer 1 from approximately 60% to 49%, while the torque after SCC only increases from approximately 330 Nm to 335 Nm. For Layer 2, a larger web thickness also improves the SCC torque slightly, from approximately 325 Nm to 335 Nm, and reduces the short circuit current at the largest investigated thickness. Therefore, increasing web thickness is generally favourable for demagnetization robustness, especially as a supporting parameter. However, it is not strong enough on its own to recover the post-fault torque, and should mainly be used together with more dominant parameters such as magnet thickness.

6.5.4 Combined Rotor Geometry Variations

The results from the individual parameter study show that magnet thickness has the strongest influence on the available flux and post-demagnetization torque, while pole V angle and web thickness mainly affect the local field distribution. Based on these observations, several combined rotor geometry configurations were evaluated. The evaluated configurations correspond to the combinations defined in Table 5.4, and the corresponding

Motor-CAD models are provided in Appendix B.4. The legend *Original* in the figures refers to the the reference case using the selected original 45SH rotor geometry.

The torque behaviour for the combined rotor geometry configurations is presented in Fig. 6.49 for both SCC and NOC as a function of temperature. Under NOC, all configurations, including the original design, maintain a constant torque level of approximately 100% over the entire temperature range from 100°C to 140°C. This confirms that the investigated geometry changes do not introduce additional demagnetization during normal operating conditions and was expected and in line with the previous results.

Under SCC, the torque decreases with increasing temperature for all configurations. The original design shows the largest reduction, decreasing from approximately 91% at 100°C to around 60% at 140°C. Combination 1 and Combination 2 exhibit a similar trend, with torque decreasing to approximately 68% and 65% at 140°C, respectively. Combination 3 reaches approximately 62% at the same temperature and therefore gives only a small improvement compared to the original design.

Combination 5 shows a less pronounced decrease compared to the previous combinations, with torque reducing to approximately 86% at 140°C. Combinations 4, 6, 7, 8, 9, 10, and 11 maintain significantly higher torque levels across the entire temperature range. These configurations remain close to 100% at lower temperatures and exhibit only a minor reduction at higher temperatures. At 140°C, the torque for these combinations remains above approximately 95%, with Combination 10 showing a slightly larger reduction compared to the others within this group. The common feature of these stronger combinations is that magnet thickness is included together with field-shaping parameters such as pole V-angle, web thickness, magnet separation, or magnet post. This means that the designs improve the magnet operating point while also modifying the local field distribution during SCC.

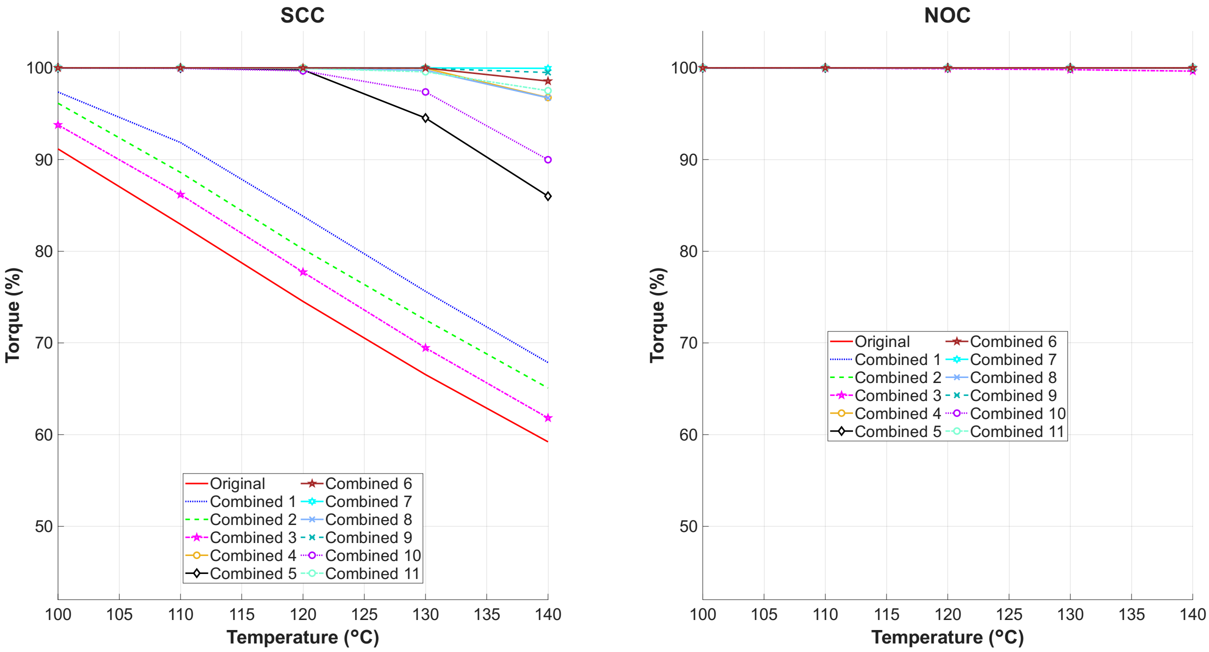

Figure 6.49: Torque retention for combined rotor geometry variations under SCC and NOC as a function of temperature.

The average torque before and after demagnetization is shown in Fig. 6.50. Before demagnetization, all configurations show a gradual decrease in torque with increasing temperature. The original design exhibits the highest torque level across the entire temperature range. Combination 2 and Combination 3 follow similar trends at slightly lower torque levels, while the remaining configurations exhibit lower torque values. After demagnetization under NOC, the torque response remains close to the pre-demagnetization case.

After demagnetization under SCC, a different behaviour is observed. For the original design, Combination 1, Combination 2, and Combination 3, the torque decreases significantly with increasing temperature, reaching values below approximately 360 Nm at 140°C. In contrast the rest of combinations maintain higher torque levels under SCC. However, even though several combined configurations show a strong improvement compared to the original design, none of the evaluated configurations meet the 500 Nm torque requirement at 140°C under SCC. This shows that the combined geometry modifications reduce demagnetization, but are still not sufficient to fully recover the required torque level in the investigated design space.

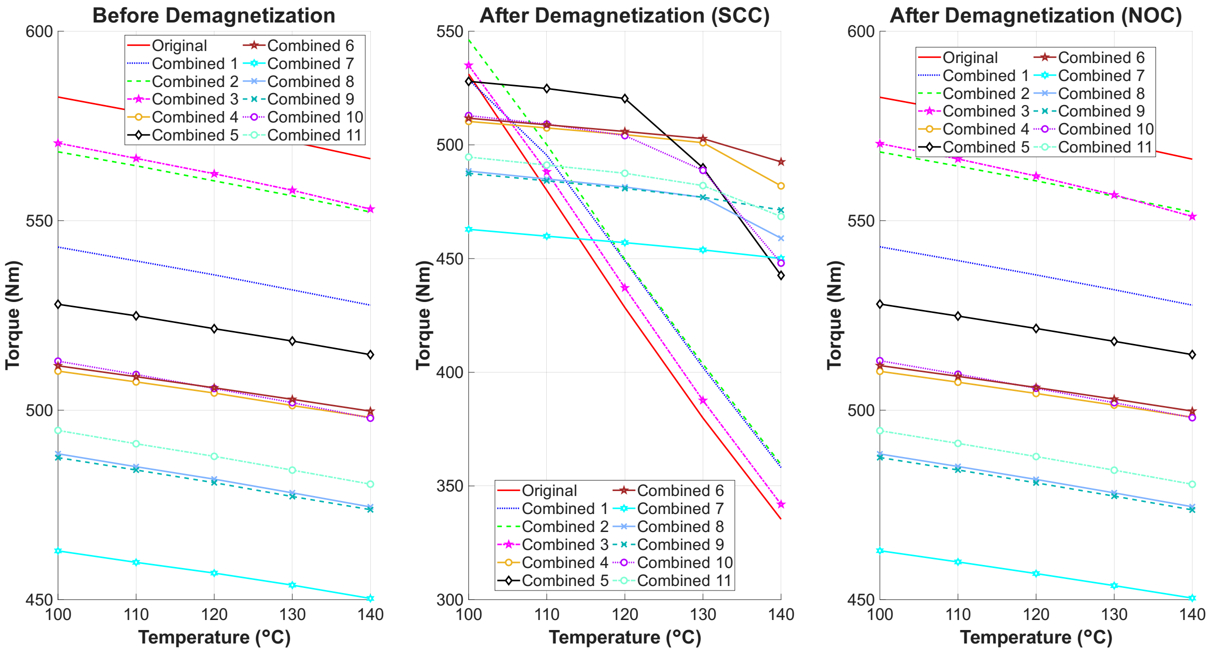

Figure 6.50: Average torque for combined rotor geometry variations before and after demagnetization under SCC and NOC as a function of temperature.

The back EMF behaviour for the combined configurations is presented in Fig. 6.51. Under NOC, all configurations maintain a nearly constant back EMF level close to 100% across the entire temperature range. Only minor deviations can be observed at higher temperatures, where a small reduction is visible for Combination 3, which decreases slightly below 100% at 140°C.

Under SCC, the back EMF decreases with increasing temperature for all configurations. The original design shows the largest reduction, decreasing from approximately 85% at 100°C to around 27% at 140°C. Combination 1 and Combination 2 follow a similar trend, with back EMF decreasing to approximately 45% and 37% at 140°C, respectively. Combination 3 shows a comparable behaviour, reaching approximately 34% at the highest temperature.

Combination 5 exhibits a less severe reduction compared to these configurations, decreasing to approximately 68% at 140°C. Combinations 4, 6, 7, 8, 9, 10, and 11 maintain significantly higher back EMF values over the full temperature range. These configurations remain close to 100% at lower temperatures and show only moderate reductions at higher temperatures. At 140°C, the back EMF for these combinations remains above approximately 90%, with Combination 10 again showing a slightly larger decrease compared to the others within this group. This trend is consistent with the torque retention results and confirms that these geometries are more effective in preserving the magnetization during the short circuit event.

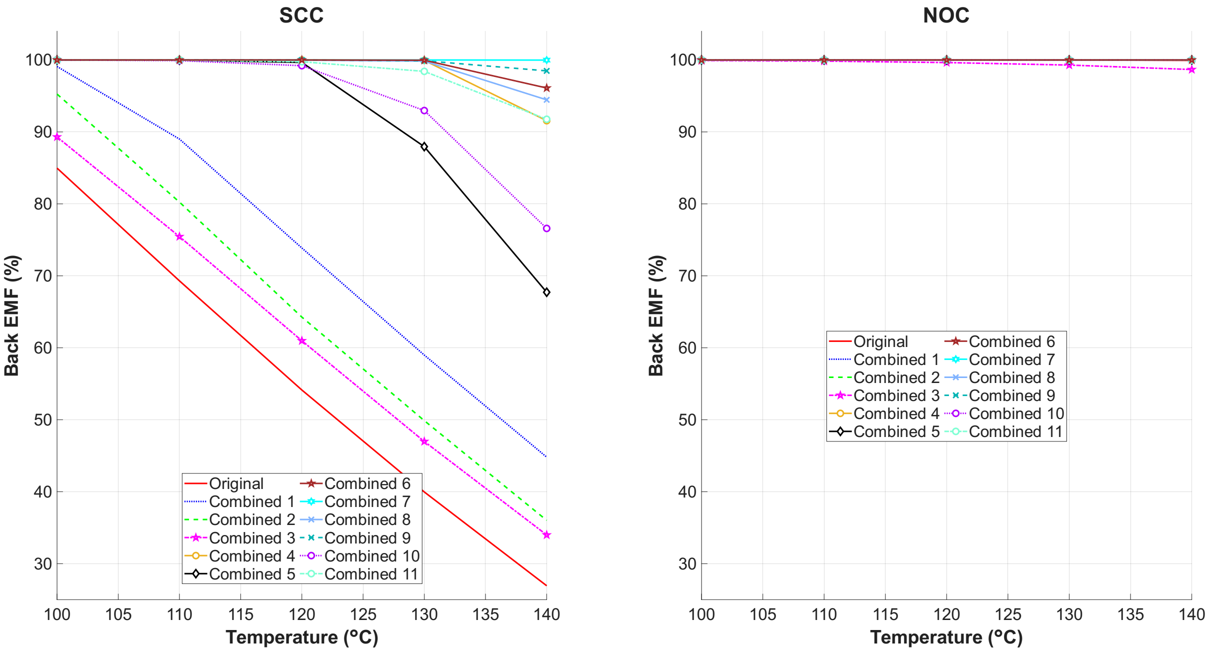

Figure 6.51: Back EMF retention for combined rotor geometry variations under SCC and NOC as a function of temperature.

The short circuit current amplitude is shown in Fig. 6.52. For all configurations, the current decreases approximately linearly with increasing temperature over the investigated range from 100°C to 140°C. The combinations with improved demagnetization behaviour generally show lower short circuit current amplitudes than the original design, decreasing from approximately 1980 A at 100°C to around 1890 A at 140°C. Combination 3 and Combination 2 show similarly high current levels, with values decreasing from approximately 1920 A and 1880 A at 100°C to around 1830 A and 1795 A at 140°C, respectively. Combination 1 follows a similar trend at a lower level, decreasing from approximately 1785 A to 1700 A. Combination 5 shows a moderate current level, decreasing from approximately 1740 A at 100°C to around 1670 A at 140°C.

Combinations 4, 6, 7, 8, 9, 10, and 11 exhibit lower current levels compared to the previously described configurations. Among these, Combination 7 shows the lowest current values across the entire temperature range, decreasing from approximately 1420 A to 1370 A. The remaining configurations within this group lie between approximately 1500 A and 1650 A at 100°C and decrease consistently with temperature.

The lower short circuit current in the improved combinations should not be interpreted as the direct reason for the better demagnetization behaviour. A lower current can occur either because the design has lower effective flux linkage, or because the geometry changes the magnetic coupling during the fault. Therefore, the current must be interpreted together with the torque, back EMF, and B_r reduction results. In this case, the combinations with lower current also retain higher back EMF and show lower average B_r reduction. This indicates that the lower current is not caused by severe magnetic degradation, but rather by a rotor geometry that reduces the effective demagnetizing interaction during SCC. In other words, the improved behaviour is not only due to a lower short circuit current, but due to a better balance between flux linkage, local reverse field, and magnet protection.

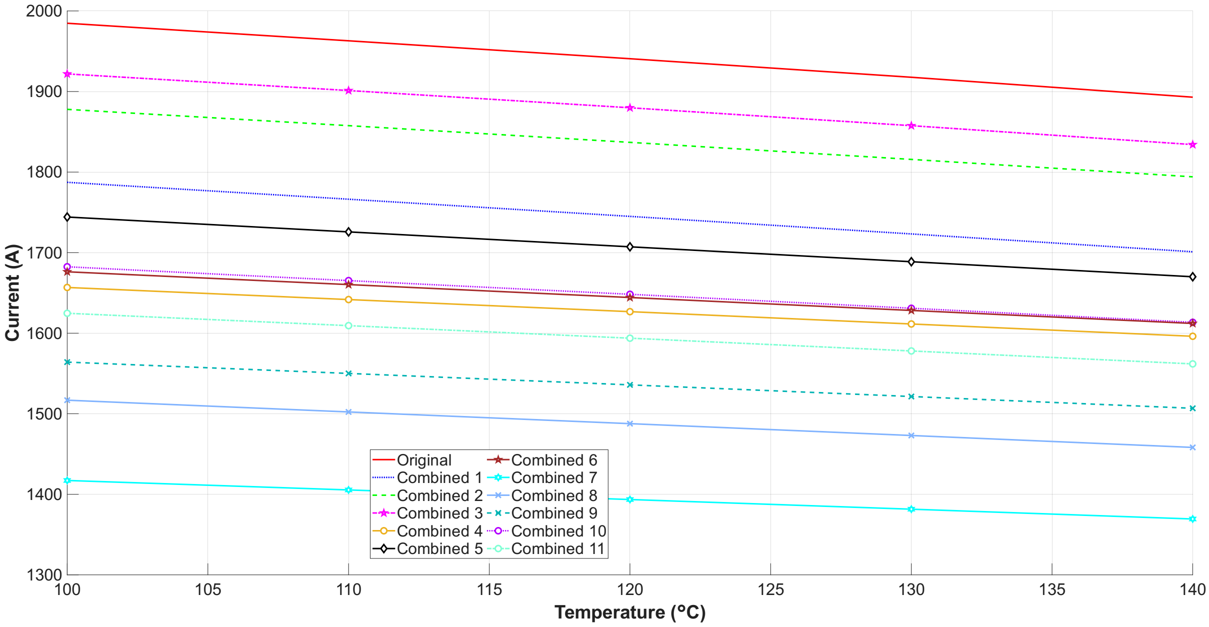

Figure 6.52: Short circuit current amplitude for combined rotor geometry variations as a function of temperature.

Fig. 6.53 shows the percentage reduction of the average $\boldsymbol{B_r}$ in Layer 1 and Layer 2. For both layers, the reduction of $\boldsymbol{B_r}$ increases with increasing temperature for all configurations. The original design exhibits the largest reduction across the entire temperature range in both layers, increasing from approximately 10% at 100°C to around 60% in Layer 1 and approximately 70% in Layer 2 at 140°C.

Combination 1, Combination 2, and Combination 3 show a similar trend with increasing reduction as temperature increases. At 140°C, the reduction reaches approximately 45%, 52%, and 53% in Layer 1, and around 60%, 62%, and 62% in Layer 2, respectively. Combination 5 shows a lower reduction compared to these configurations, with values increasing to approximately 23% in Layer 1 and around 16% in Layer 2 at the highest temperature.

Combinations 4, 6, 7, 8, 9, 10, and 11 exhibit significantly lower $\boldsymbol{B_r}$ reductions in both layers over the full temperature range. For most of these configurations, the reduction remains close to 0% up to approximately 130°C. At 140°C, the reduction for these combinations generally remains below approximately 10% in both layers, with Combination 10 showing a somewhat higher value compared to the others within this group.

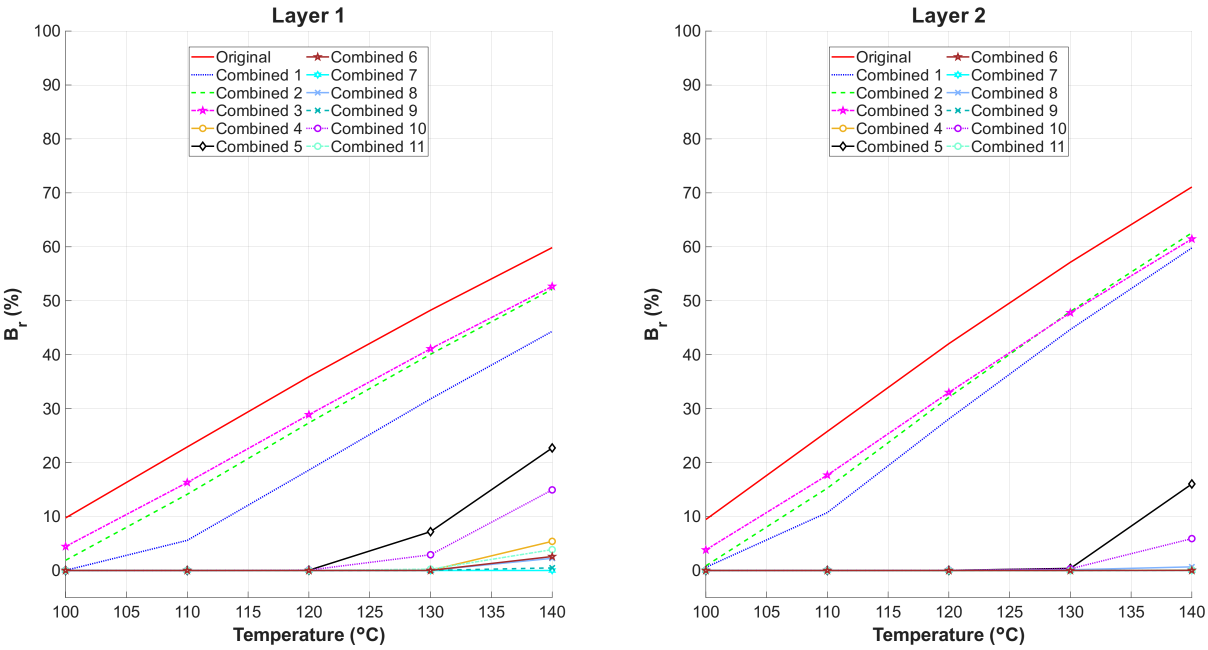

Figure 6.53: Percentage reduction of average B_r in Layer 1 and 2 for combined rotor geometry variations as a function of temperature.

The combined results show that the rotor geometry has a significant influence on the demagnetization behaviour. Configurations where only field distribution parameters are modified, such as Combination 1, Combination 2, and Combination 3, provide limited improvement. Although these changes can reduce the local demagnetizing field, the available flux level and magnet operating point remain relatively close to the original design. As a result, the improvement in torque, back EMF, and $\boldsymbol{B_r}$ reduction is limited.

A stronger improvement is obtained when magnet thickness is included together with other geometric changes. In these cases, the increased magnet thickness raises the available flux level and improves the magnet operating point, while the additional geometry changes reduce the reverse field acting on the magnets. This combination shifts the operating condition both upward and further away from the knee point of the demagnetization curve. This explains why Combinations 4, 6, 7, 8, 9, 10, and 11 show much lower $\boldsymbol{B_r}$ reduction and higher torque and back EMF retention.

The comparison also shows that the performance is not determined only by the number of changed parameters. The selected parameter values are equally important. For example, Combination 10 includes more geometry modifications than Combination 5, but the improvement is not proportionally larger. This is mainly because Combination 10 uses a lower magnet thickness than the strongest combinations. The reduced thickness lowers the available magnetic flux and partly offsets the benefit of the additional changes in field distribution. This shows that magnet thickness remains a dominant parameter even when pole V-angle, web thickness, magnet separation, or other rotor parameters are modified at the same time.

This also explains why some combinations can show low demagnetization but still limited torque. A geometry that reduces the reverse field acting on the magnets can protect the magnetization, but if the magnet volume or effective flux linkage is reduced too much, the post-fault torque remains below the target. Therefore, a good combined geometry must both protect the magnets during SCC and preserve enough useful air-gap flux for torque production.

Although several configurations satisfy the demagnetization criterion of less than 10% average B_r reduction, this does not automatically mean that the torque requirement is fulfilled. Some configurations maintain low demagnetization but still remain below the required 500 Nm after demagnetization under SCC at 140°C. This highlights the main trade-off in the rotor geometry study: reducing irreversible demagnetization does not necessarily guarantee sufficient torque capability.

To further evaluate the spatial distribution of the remaining magnetization, FEA plots were examined for Combination 8 and Combination 11. These two configurations show relatively good average demagnetization behaviour, but they differ in their local B_r distribution. This comparison is important because the average B_r reduction alone can hide local regions with stronger irreversible demagnetization.

Fig. 6.54 shows the effective remanent flux density distribution for Combination 8 at 100°C and 140°C. This configuration includes changes in pole V-angle, magnet thickness, and web thickness, while magnet separation is not included. At 100°C, most parts of the magnets are located close to the upper range of the colour scale, with values mainly around 1.125 to 1.25 T. At 140°C, the overall distribution also remains close to the upper range of the scale, but some local regions at the magnet edges and tips shift toward lower values. The colour scale also shows that the displayed maximum B_r value decreases from 1.25 T at 100°C to 1.20 T at 140°C.

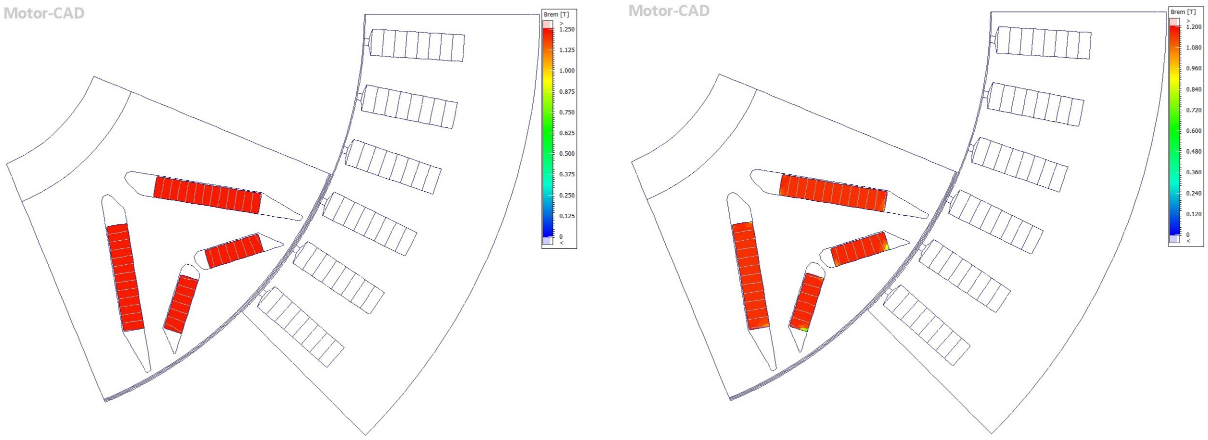

(a): 100°C **(b):** 140°C

Figure 6.54: Effective remanent flux density distribution, B_r, for Combination 8 at 100°C and 140°C after demagnetization under SCC.

The corresponding FEA result for Combination 11 is shown in Fig. 6.55. In contrast to Combination 8, this geometry also includes magnet separation. At 100°C, most of the magnet area is located close to the upper range of the colour scale, with values mainly around 1.125 to 1.25 T. At 140°C, the main magnet regions still remain in the upper part of the scale, but the lower value regions become more visible. The clearest reduction is seen near the lower end of the left Layer 1 magnet , where the values decrease to approximately 0.60 to 0.84 T. Smaller reductions are also visible near near the tip of the right Layer 1 magnet. The colour scale shows that the displayed maximum $\boldsymbol{B_r}$ value decreases from 1.25 T at 100°C to 1.20 T at 140°C.

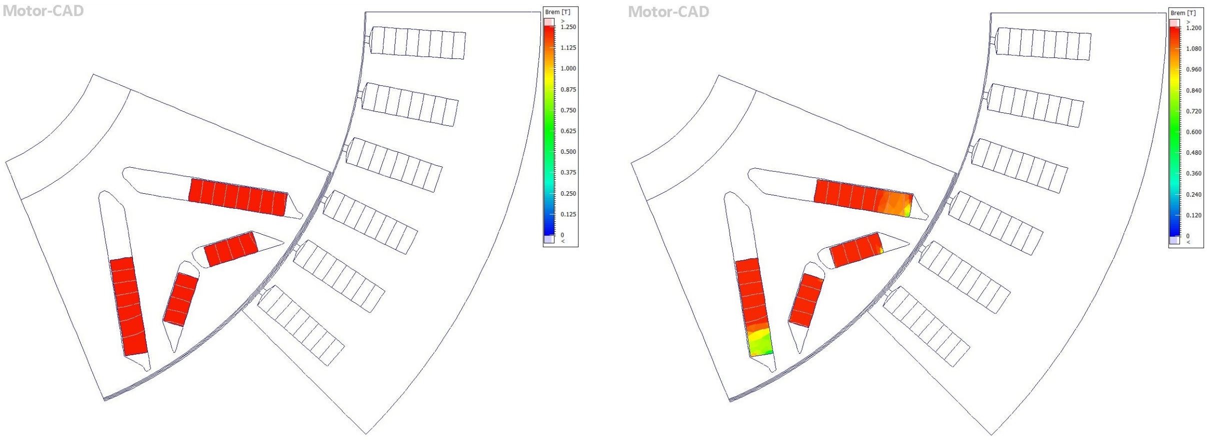

(a): 100°C

(b): 140°C

Figure 6.55: Effective remanent flux density distribution, $\boldsymbol{B_r}$, for Combination 11 at 100°C and 140°C after demagnetization under SCC.

The FEA plots show that the demagnetization is not uniformly distributed within the magnets. For Combination 8, the lower $\boldsymbol{B_r}$ regions are mainly limited to smaller areas near the magnet tips and edges. For Combination 11, where magnet separation is included, stronger local reductions are visible even though the average $\boldsymbol{B_r}$ reduction remains relatively low for both of the combinations. One possible explanation is that the magnet separation in Combination 11 changes the local position of parts of the magnet relative to the air gap, making them more exposed to the stator magnetic field during the short circuit event. This can increase the local reverse field, especially near tips and edges where the field distribution is less uniform.

This shows that magnet separation does not necessarily improve the demagnetization behaviour, even if the average values appear acceptable. It also confirms that average $\boldsymbol{B_r}$ reduction should not be used as the only evaluation criterion. Local FEA results are needed to identify regions where irreversible demagnetization may still occur, especially when evaluating combined rotor geometry changes.

6.6 Optimization of Rotor Geometry

The previous rotor geometry study showed that manual parameter variations can reduce irreversible demagnetization, but that it is difficult to satisfy the torque and demagnetization requirements simultaneously. Therefore, a systematic rotor geometry optimization was performed. The optimization was based on meta-models generated from several hundred Motor-CAD simulations, using the defined objectives and constraints. The optimization was mainly driven by the SCC case, since the previous results showed that NOC did not cause noticeable irreversible demagnetization for the investigated designs

The optimized rotor geometries obtained for the investigated magnet cases are presented in Fig 6.56, and their parameters summarized in Table 6.2. The table lists the physical geometry parameter values and ratios after optimization for all optimized designs, as well as the original values from the reference design.

A general difference can be observed between the optimized selected magnet cases and the optimized custom magnet cases. For the selected 45SH and 42SH magnets, the optimization mainly moves toward thicker and shorter magnets. The Layer 1 magnet thickness increases from 3.20 mm to 6.00 mm for 45SH and to 5.77 mm for 42SH, while the Layer 2 thickness increases from 2.80 mm to 3.93 mm and 4.33 mm, respectively. At the same time, the effective magnet length is reduced. This indicates that the selected magnets require more material in the magnetization direction to reduce irreversible demagnetization during SCC. However, this also increases the magnet weight from approximately 3.00 kg in the original design to 4.08 kg for 45SH and 4.56 kg for 42SH.

For the custom magnet cases, the optimized geometries are less dependent on increasing magnet volume. The Layer 1 thickness increases to 5.43 mm and 5.01 mm, while Layer 2 remains at the original value of 2.80 mm. This means that the custom magnet designs can use relatively longer and thinner magnet regions compared with the optimized 45SH and 42SH cases. The reason is the higher intrinsic coercivity of the custom magnet, which already improves the resistance to irreversible demagnetization. The magnet weights become approximately 4.41 kg and 4.13 kg for the two custom designs.

These differences show that the optimized geometry depends strongly on the magnet material properties. When the magnet material has limited coercivity, the design compensates by increasing magnet thickness, but this increases magnet weight. With higher H_{cJ}, less additional magnet material is needed, especially in Layer 2. Therefore, the optimization does not only increase magnet volume, but balances magnet properties, geometry, torque, demagnetization, and magnet weight.

A similar connection can be made for the pole V-angle. In the manual rotor geometry study, increasing the pole V-angle in Layer 1 did not by itself improve the SCC behaviour, while the Layer 2 angle showed a more favourable response around an intermediate value. In the optimized geometries, the Layer 2 pole V-angle is reduced for all investigated cases, which makes the Layer 2 magnets more V-shaped compared to the original design. This suggests that the optimization uses the Layer 2 angle to improve the local field distribution during SCC. At the same time, the Layer 1 pole V-angle is increased, which indicated that the final design is not determined by one parameter alone, but by the combined effect of both layers.

Other parameters, such as web thickness, web length, magnet post, and bridge thickness, are also changed by the optimization. In the manual parameter study, web thickness for example did not individually give the same improvement as magnet thickness, but they affected the local magnetic path and the demagnetizing field. Their changes in the optimized designs therefore support the conclusion that the rotor geometry must be adjusted as a complete system. The optimization is useful because it changes several parameters simultaneously, allowing improvements that are not visible when each parameter is varied separately. This may not give an optimal design as the name optimization suggests, however, it does create good designs in terms of performance and demagnetization robustness.

Table 6.2: Optimized rotor geometry parameters results for the investigated magnet cases.

Magnet case	Original values	45SH	42SH	Custom Test 6, Opt. 1	Custom Test 6, Opt. 2
Pole Arc Ratio L1/L2 [-]	0.80/0.70	0.68/0.57	0.86/0.55	0.72/0.65	0.71/0.65
Web Thickness Ratio L1/L2 [-]	0.57/0.53	0.61/0.46	0.55/0.44	0.54/0.66	0.54/0.66
Magnet Bar Width Ratio L1/L2 [-]	0.97/0.98	0.95/0.71	0.85/0.79	0.99/0.74	0.99/0.74
Web Length Ratio L1/L2 [-]	0.43/0.22	0.48/0.17	0.49/0.11	0.49/0.13	0.45/0.29
Magnet Thickness L1/L2 [mm]	3.20/2.80	6.00/3.93	5.77/4.33	5.43/2.80	5.01/2.80
Pole V Angle L1/L2 [°]	79.09/151.40	99.71/115.70	95.46/141.14	102.06/129.51	102.23/111.51
Magnet Post L1/L2 [mm]	2.00/1.00	2.00/2.23	3.55/1.00	2.01/1.00	2.01/1.00
Magnet Separation L1/L2 [mm]	7.20/3.20	9.91/6.96	10/4.14	2.00/7.20	2.00/6.98
Bridge Thickness L1/L2 [mm]	1.00/1.00	1.28/1.02	1.11/2.04	1.57/1.30	1.17/1.19
Magnet Weight [kg]	3.00	4.08	4.56	4.41	4.13

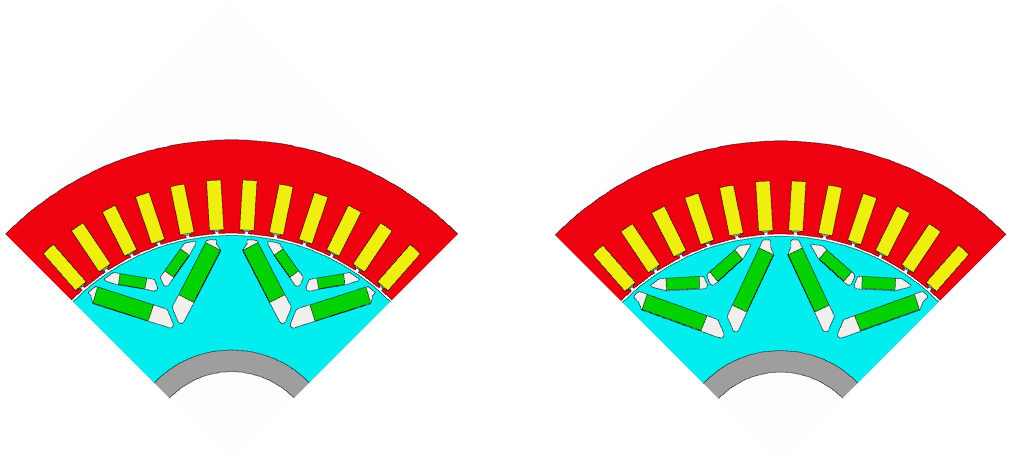

(a) Optimized 45SH

(b) Optimized 42SH

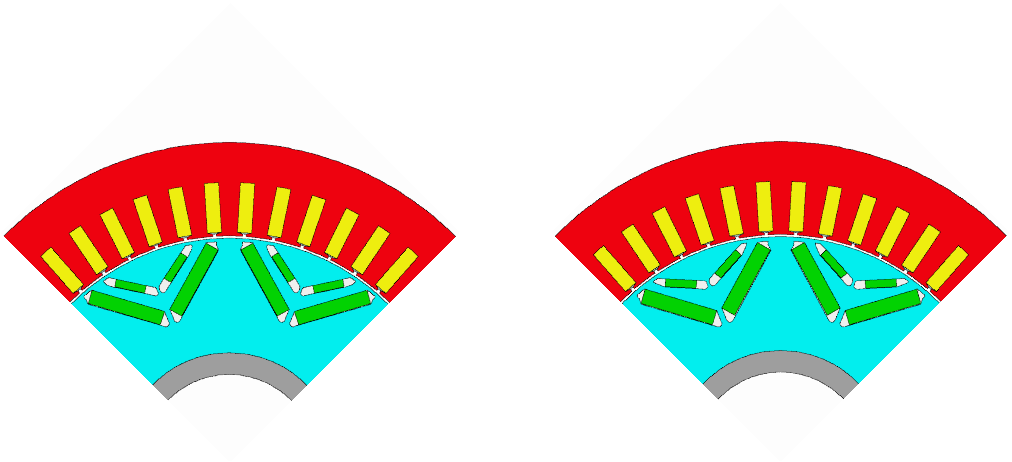

(c) Custom magnet Test 6 (increased H_{cj} with constant B_r), optimization 1

(d) Custom magnet Test 6 (increased H_{cj} with constant B_r), optimization 2

Figure 6.56: Optimized rotor geometries for the investigated magnet cases.

The following subsections present the optimization results for the previously selected 45SH, 42SH, and custom magnet cases. The coefficient of importance, Pareto front validation, and linear correlation results are used to evaluate how the geometry parameters influence magnet weight, demagnetization percentage, and peak shaft torque. The detailed linear correlation coefficients for each geometry parameter are provided in Appendix C.

Optimization Results for 45SH

Table 6.3 presents the coefficient of importance (CoI) for the optimization using the 45SH magnet. The CoI indicates the relative importance of each input parameter for the evaluated outputs.

For the magnet weight, the inputs of highest importance are the pole arc ratio and magnet thickness in Layer 1 at 6% and 13%, respectively. This is expected since increasing the magnet thickness or changing the magnet arc directly affects the amount of magnet material in the rotor. The magnet bar width ratio and pole V angle in Layer 1 stand at a CoI of 3% and 4%. The pole arc ratio and magnet thickness in Layer 2 both have an CoI of 1%.

For the demagnetization percentage, the highest inputs with highest CoI are the magnet width ratio, magnet thickness and magnet post in Layer 1 at 10%, 19% and 9%, respectively as well as the magnet post in Layer 2 at 11%. This shows that demagnetization is affected both by the magnet dimensions and by the local rotor geometry around the magnets. In particular, the Layer 1 parameters have a clear influence, which is consistent with the previous rotor geometry study.

Lastly, the most important parameter for the torque is the pole V angle in Layer 1 at 8%, followed by the magnet post and magnet bar width ratio in Layer 1 with bot hat 3% CoI. This indicates that the torque is sensitive to how the magnet flux is directed toward the air gap, rather than only to the amount of magnet material.

Table 6.3: Table with Coefficient of Importance for optimization of original model configured with the 45SH magnet

Input Parameters	Magnet Weight	Demagnetization Percentage	Peak Shaft Torque At 3000 rpm
Pole Arc Ratio L1/L2	6%/1%	2%/0%	2%/1%
Web Thickness Ratio L1/L2	0%/0%	2%/1%	2%/0%
Magnet Bar Width Ratio L1/L2	3%/0%	10%/3%	3%/0%
Web Length Ratio L1/L2	0%/0%	0%/1%	0%/0%
Magnet Thickness L1/L2	13%/1%	19%/3%	2%/0%
Pole V Angle L1/L2	4%/0%	0%/3%	8%/0%
Magnet Post L1/L2	0%/0%	9%/11%	3%/2%
Magnet Separation L1/L2	0%/0%	4%/3%	1%/0%
Bridge Thickness L1/L2	0%/0%	3%/1%	1%/0%

Fig. 6.57 illustrates the Pareto front and the validated designs from the optimization with the 45SH magnet. The predicted Pareto points represent the designs predicted by the meta model, while the validated points correspond to the same designs recalculated in Motor-CAD. This comparison is important because the meta model is used to identify promising design candidates, but the final evaluation must be based on the validated Motor-CAD results.

The horizontal axis shows the peak shaft torque objective with a negative sign, since optiSLang formulates the objective as a minimization problem. Therefore, points further to the left correspond to higher torque. The vertical axis shows the demagnetization percentage, where lower values are better.

For the demagnetization percentage objective the validated designs show a percentage of approximately 5% to 5.5%, while the predicted designs are mostly between 7% and 10%. Furthermore, the peak shaft torque objective at 3000 rpm also shows an disparity with the validated designs being between 535 Nm and 540 Nm while the predicted torque is mostly in the range of 554 Nm and 558 Nm. This means that the meta model overestimates the torque and demagnetization percentage for this case.

This difference indicates a discrepancy between the meta-model prediction and the validated Motor-CAD results. The prediction error obtained from the optiSLang validation statistics gives root mean square (RMS) error of 3.29 percentage points (pp) and a maximum error of 13.85 pp. for the demagnetization percentage. For the peak shaft torque, the RMS error is 15.79 Nm and the maximum error is 48.76 Nm. Therefore, the validated Motor-CAD results are used when evaluating whether the optimized design satisfies the torque and demagnetization requirements since the maximum error is so large.

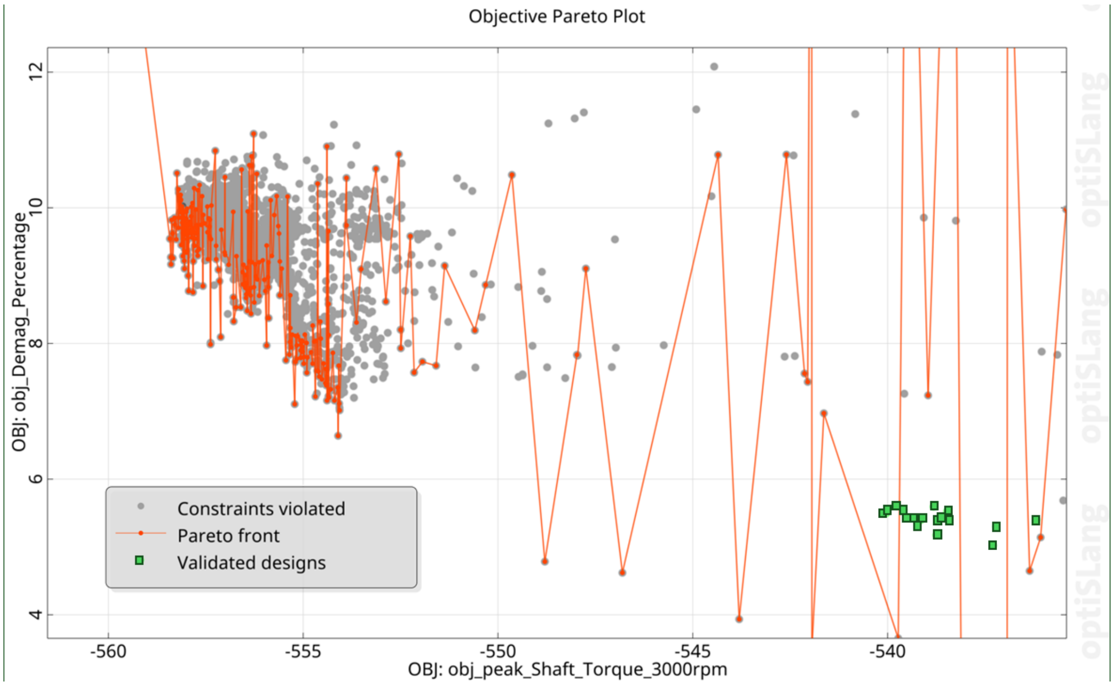

Figure 6.57: Pareto front from optimization with 45SH showing predicted outcomes with validated outcomes.

The linear correlation results are summarized in Fig 6.58, where the effects on demagnetization robustness and torque are compared directly for Layer 1 and Layer 2. Positive values indicate a beneficial effect for the corresponding objective, while negative values indicate an unfavourable effect.

For the 45SH magnet, the comparison shows that magnet thickness in Layer 1 has a positive effect on both torque and demagnetization robustness. Magnet bar width in Layer 1 also improves torque, but has a negative effect on demagnetization robustness. In contrast, magnet post and bridge thickness tend to improve demagnetization robustness, but reduce torque. This indicates that some geometry changes that protect the magnets can also reduce the useful air-gap flux.

In Layer 2, a similar trade off is observed. Magnet post gives the strongest positive effect on demagnetization robustness, while bridge thickness and pole V angle have negative effects on torque. Overall, the results show that the optimized geometry must balance torque production, demagnetization robustness, and magnet weight, rather than relying on one parameter alone.

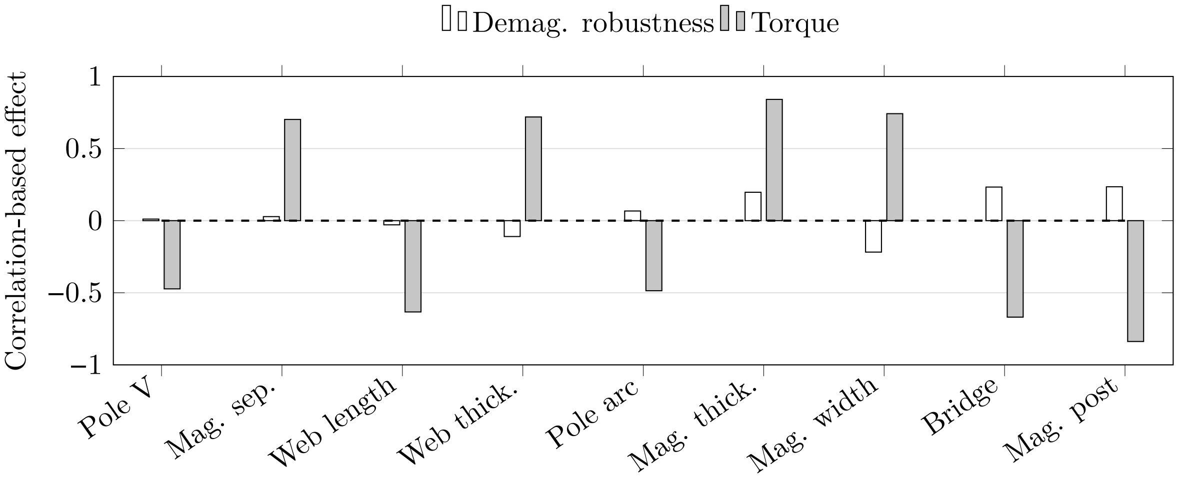

(a) Layer 1

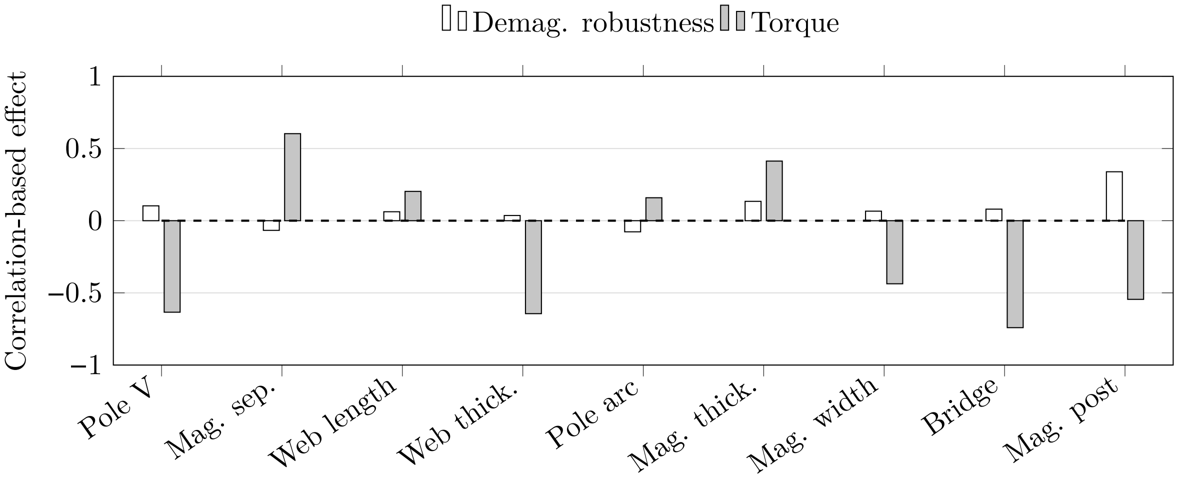

(b) Layer 2

Figure 6.58: Linear correlation comparison of demagnetization robustness and torque effects for rotor geometry parameters using the 45SH magnet.

Optimization Results for 42SH

In Table 6.4 the CoI for the optimization with the selected 42SH magnet is presented. For the magnet weight, the highest importance inputs are the pole arc ratio and magnet thickness in Layer 1 at 11% and 26%. The highest CoI for the demagnetization percentage are the magnet bar width ratio, magnet thickness and magnet post in Layer 1 at 12%, 25% and 11%, respectively as well as the magnet post in Layer 2 at 15%. The parameter of highest importance for the peak shaft torque is the pole V angle in Layer 1 at 14%.

Compared with the 45SH case, the 42SH optimization is more strongly influenced by magnet thickness in Layer 1, both for magnet weight and demagnetization percentage. This indicates that the weaker magnet grade requires a larger geometry compensation to reduce irreversible demagnetization while maintaining torque performance.

Table 6.4: Table with Coefficient of Importance for optimization of original model configured with the 42SH magnet

Input Parameters	Magnet Weight	Demagnetization Percentage	Peak Shaft Torque At 3000 rpm
Pole Arc Ratio L1/L2	11%/5%	3%/4%	5%/2%
Web Thickness Ratio L1/L2	0%/0%	0%/0%	3%/0%
Magnet Bar Width Ratio L1/L2	5%/0%	12%/0%	4%/0%
Web Length Ratio L1/L2	0%/0%	0%/0%	0%/0%
Magnet Thickness L1/L2	26%/2%	25%/4%	4%/0%
Pole V Angle L1/L2	7%/0%	1%/0%	14%/0%
Magnet Post L1/L2	0%/0%	11%/15%	4%/5%
Magnet Separation L1/L2	1%/0%	3%/0	1%/0%
Bridge Thickness L1/L2	0%/0%	5%/3%	1%/1%

Fig. 6.59 shows the Pareto front and the validated designs for the optimization with 42SH. The predicted demagnetization percentage is mostly in the range of 8% to 11%, while the validated designs show higher values of approximately 15%. For the peak shaft torque at 3000 rpm, the predicted values are mainly between 523 Nm and 540 Nm, while the validated designs are between approximately 521 Nm and 524 Nm.

This means that the validated 42SH designs have both higher demagnetization and lower torque than expected from the meta model. The optimization still improves the rotor compared with the original 42SH case, but the validation shows that this magnet grade is more difficult to optimize toward both requirements. The RMS error is 3.42 percentage points for the demagnetization percentage, with a maximum error of 8.39 percentage points. For the peak shaft torque, the RMS error is 18.13 Nm and the maximum error is 66.73 Nm. Therefore, like for the 45SH case, the validated Motor-CAD results are used when assessing the optimized design.

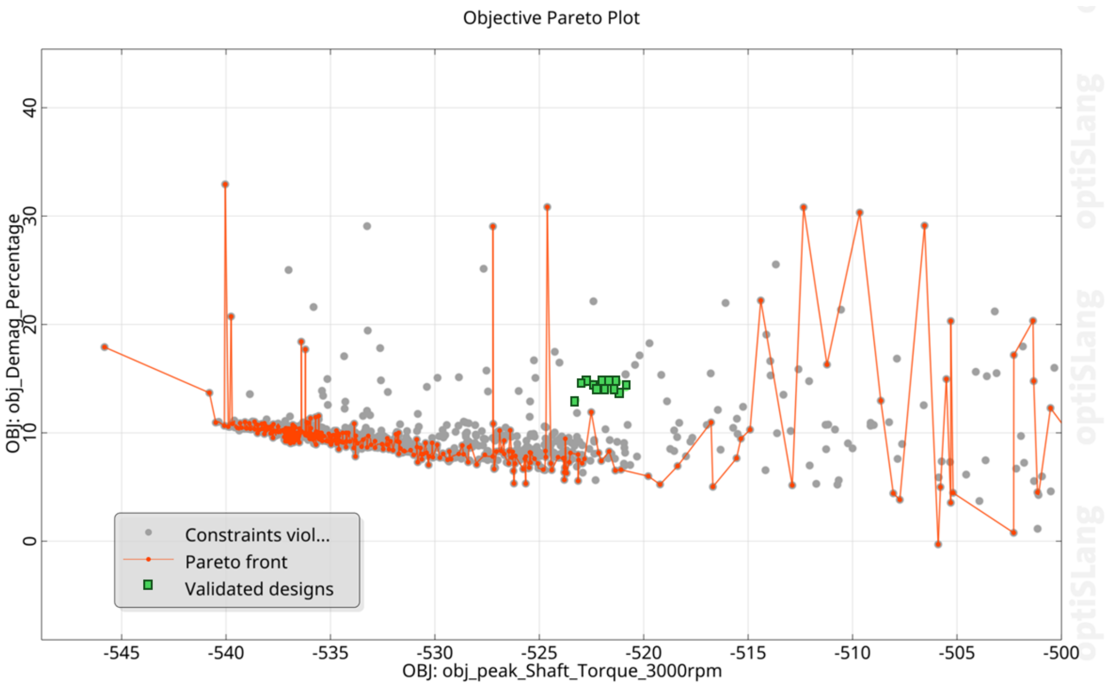

Figure 6.59: Pareto front from optimization with 42SH showing predicted outcomes with validated outcomes.

The linear correlation-based comparison for the 42SH magnet is shown in Fig. 6.60. Compared with the 45SH case, the same general trade off between torque and demagnetization robustness is observed, but the 42SH case shows a stronger dependence on magnet thickness. In Layer 1, magnet thickness has a clear positive effect on both torque and demagnetization robustness, while magnet bar width mainly improves torque but has an unfavourable effect on demagnetization robustness.

For Layer 2, magnet thickness again has a positive torque effect, while magnet post gives the strongest positive effect on demagnetization robustness but has a negative effect on torque. This indicates that the weaker 42SH magnet requires more geometry compensation, especially through increased magnet thickness, to maintain torque while reducing demagnetization.

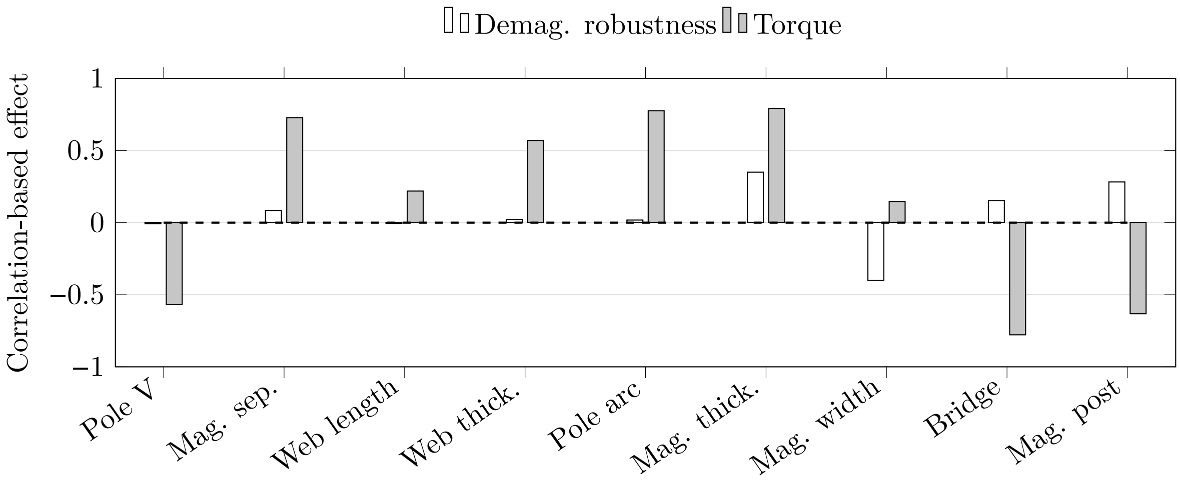

(a) Layer 1

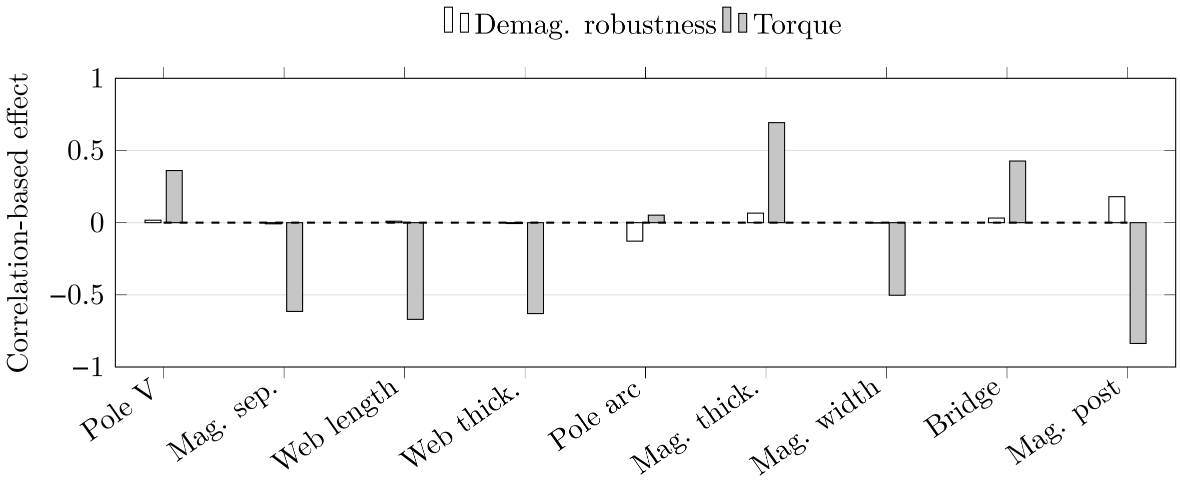

(b) Layer 2

Figure 6.60: Linear correlation comparison of demagnetization robustness and torque effects for rotor geometry parameters using the 42SH magnet.

Optimization Results for the Custom Magnet

In Table 6.5 the CoI of the inputs for the optimization with the custom magnet is presented. For the magnet weight the inputs with highest CoI are the pole arc ratio, magnet thickness and pole V angle in layer 1 at 7%, 27% and 6%, respectively. Furthermore, for the demagnetization percentage the inputs of highest importance are the magnet bar width ratio and magnet thickness in layer 1 at 8% and 15%. Lastly, the input of highest importance for the torque is the pole V angle in layer 1 at 5%.

Compared with the selected 45SH and 42SH cases, the CoI values for torque and demagnetization are generally lower and more distributed. This indicates that the custom magnet is less sensitive to one single geometry parameter, mainly because the higher intrinsic coercivity already improves the demagnetization resistance.

Table 6.5: Table with Coefficient of Importance for optimization of original model configured with the custom magnet

Input Parameters	Magnet Weight	Demagnetization Percentage	Peak Shaft Torque At 3000 rpm
Pole Arc Ratio L1/L2	7%/2%	2%/3%	1%/2%
Web Thickness Ratio L1/L2	0%/0%	3%/3%	2%/1%
Magnet Bar Width Ratio L1/L2	3%/0%	8%/0%	2%/1%
Web Length Ratio L1/L2	1%/1%	3%/2%	1%/0%
Magnet Thickness L1/L2	27%/3%	15%/5%	2%/1%
Pole V Angle L1/L2	6%/1%	2%/2%	5%/0%
Magnet Post L1/L2	0%/1%	2%/4%	2%/1%
Magnet Separation L1/L2	1%/1%	2%/2	2%/1%
Bridge Thickness L1/L2	0%/1%	2%/5%	1%/1%

The pareto front and validated designs from the optimization of the original design with the custom magnet is presented in Fig. 6.61. For the peak shaft torque at 3000 rpm, the prediction is between 580 Nm and 585 Nm. The validated designs have higher spread and show torque values between 564 Nm and 598 Nm. For the torque, the RMS error of the prediction is 19.84 Nm and a maximum error of 63.68 Nm. The predicted values for the demagnetization percentage are between 0.5% and 10%, while the validated designs have a similar spread of the demagnetization percentage which is between 0.5% and 9%. Furthermore, the RMS error of the prediction is 1.51 pp and has a maximum error of 8.41 pp. Compared with the 45SH and 42SH cases, the demagnetization prediction is more accurate for the custom magnet case.

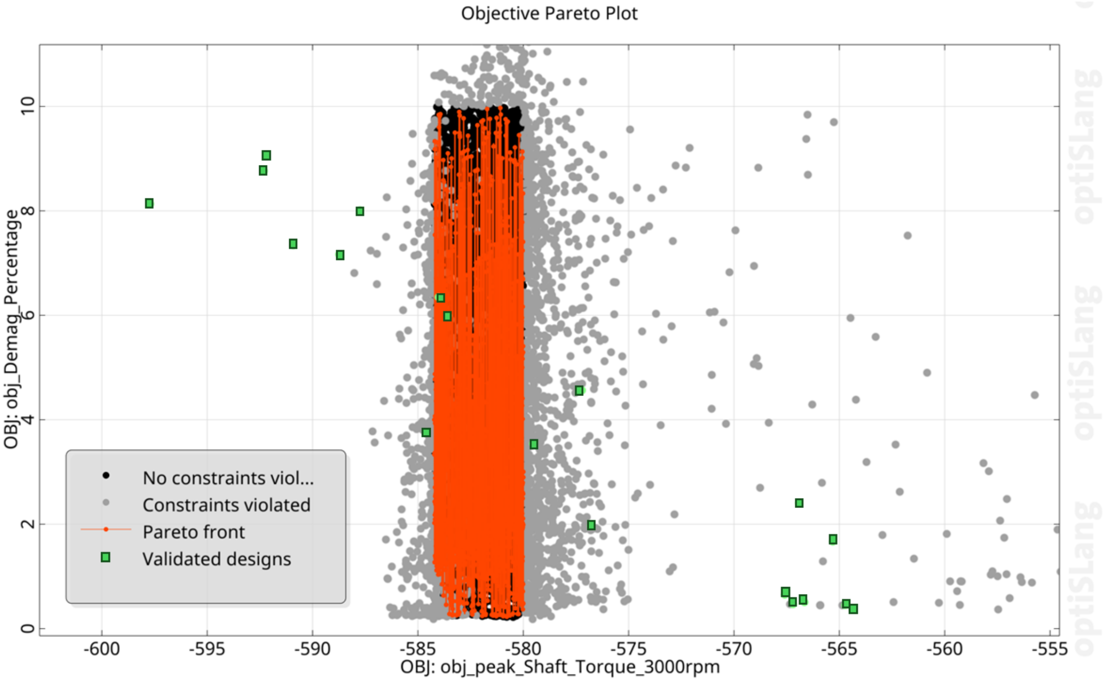

Figure 6.61: Pareto front from optimization with the custom magnet configuration showing predicted outcomes with validated outcomes.

The linear correlation comparison for the custom magnet is shown in Fig. 6.62. Compared with the selected 45SH and 42SH magnets, the correlation effects are generally smaller and more distributed. This indicates that the custom magnet is less dependent on one single geometry parameter, since the higher intrinsic coercivity already improves the demagnetization robustness.

In Layer 1, bridge thickness has the strongest positive effect on demagnetization robustness, while magnet thickness and pole arc ratio have the strongest positive effects on torque. This shows that the custom magnet still requires a balance between field shaping and torque production, even though the material itself is more robust.

In Layer 2, magnet thickness has the strongest positive effect on demagnetization robustness, while the torque correlations are generally weaker. This supports the optimized geometry result, where the custom magnet does not require the same increase in Layer 2 thickness as the selected 45SH and 42SH magnets.

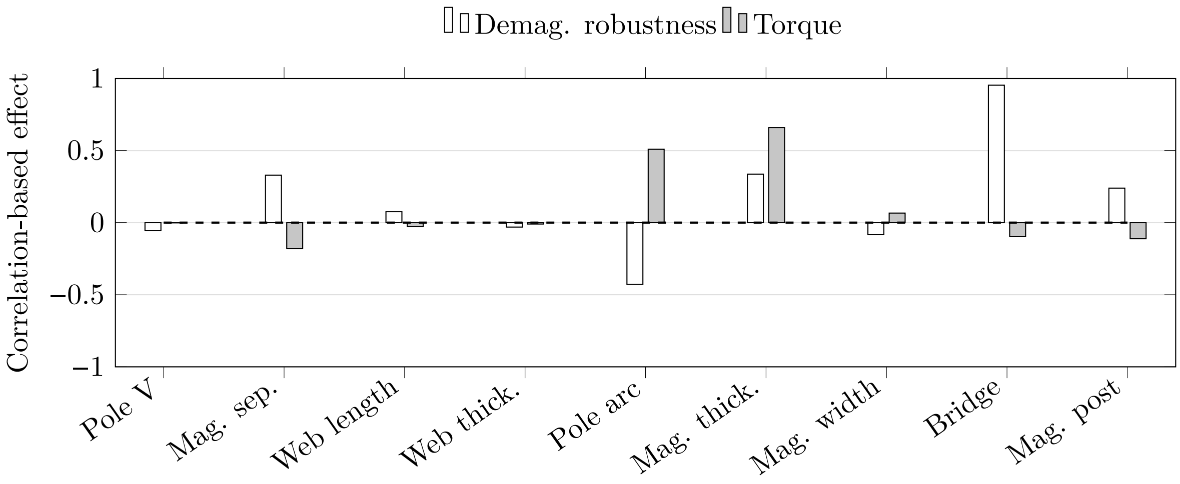

(a) Layer 1

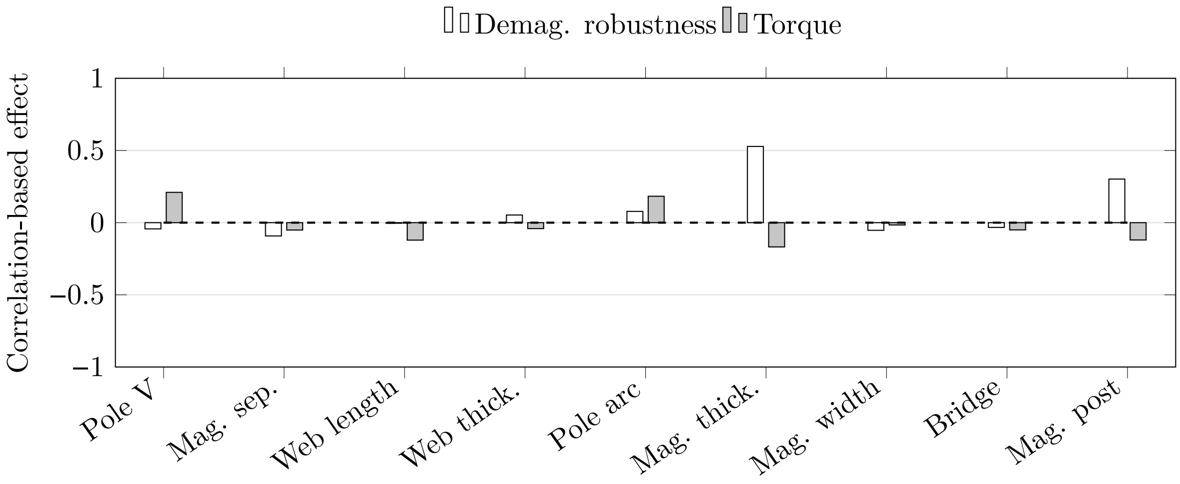

(b) Layer 2

Figure 6.62: Linear correlation comparison of demagnetization robustness and torque effects for rotor geometry parameters using the custom magnet.

Overall Interpretation of the Optimization Results

Overall, the optimization results show that the best design is obtained by balancing demagnetization resistance and torque production. Parameters such as magnet post and bridge thickness can reduce the local demagnetizing field acting on the magnets, but can at the same time reduce torque if they decrease the useful air-gap flux. In contrast, parameters such as magnet thickness and magnet bar width ratio can improve torque by increasing the effective flux path magnet area, but they may also increase magnet weight or affect demagnetization depending on the local field distribution.

The linear correlation results should also be interpreted with care, since they only describe linear relationships within the investigated design space. Some parameters may still be important through non-linear effects or through interactions with other geometry parameters. More importantly, there are differences in the correlation figures between the grades. For example, as seen in Fig. 6.58 with the 45SH magnet the web length ratio in Layer 1 has a negative effect on the torque, while Fig. 6.60 shows it has an positive effect in the 42SH case. Given that from Table 6.3 and 6.4 the parameter has a 0% CoI in both cases, showing that in the optimization these parameters are not of importance. This could contribute to the discrepancy shown in Fig. 6.58 and Fig. 6.60.

6.7 Benchmarking

The optimized HRE-free rotor designs are benchmarked against their corresponding original rotor cases and against the original HRE-based reference design. The purpose is to evaluate whether the optimized HRE-free designs can approach the performance and demagnetization robustness of the original reference machine.

Their torque retention as a function of temperature for SCC and NOC are illustrated in Fig. 6.63. Under NOC all simulations keep 100% torque retention during the whole temperature range.

Under SCC, the original HRE-based reference design with the N42UH magnet shows the best robustness. The torque retention decreases only from 100% at 100°C to approximately 92% at 140°C. In comparison, the original rotor geometry with the HRE-free 45SH and 42SH magnets shows a much larger reduction, decreasing from approximately 92% at 100°C to 60% and 57%, respectively, at 140°C. This shows once again that replacing only the magnet material is not sufficient, since the original rotor geometry does not provide enough protection for the HRE-free magnets during SCC.

The optimized HRE-free designs show a clear improvement. The optimized 45SH and 42SH designs both start at 100% torque retention at 100°C and decrease to approximately 94% and 90%, respectively, at 140°C. The custom magnet also benefits from optimization. In the original rotor geometry, the custom magnet decreases from 100% to approximately 80%, while the two optimized custom designs retain approximately 96% and 94% at 140°C. This shows that rotor geometry optimization strongly improves the SCC robustness of the HRE-free magnet designs.

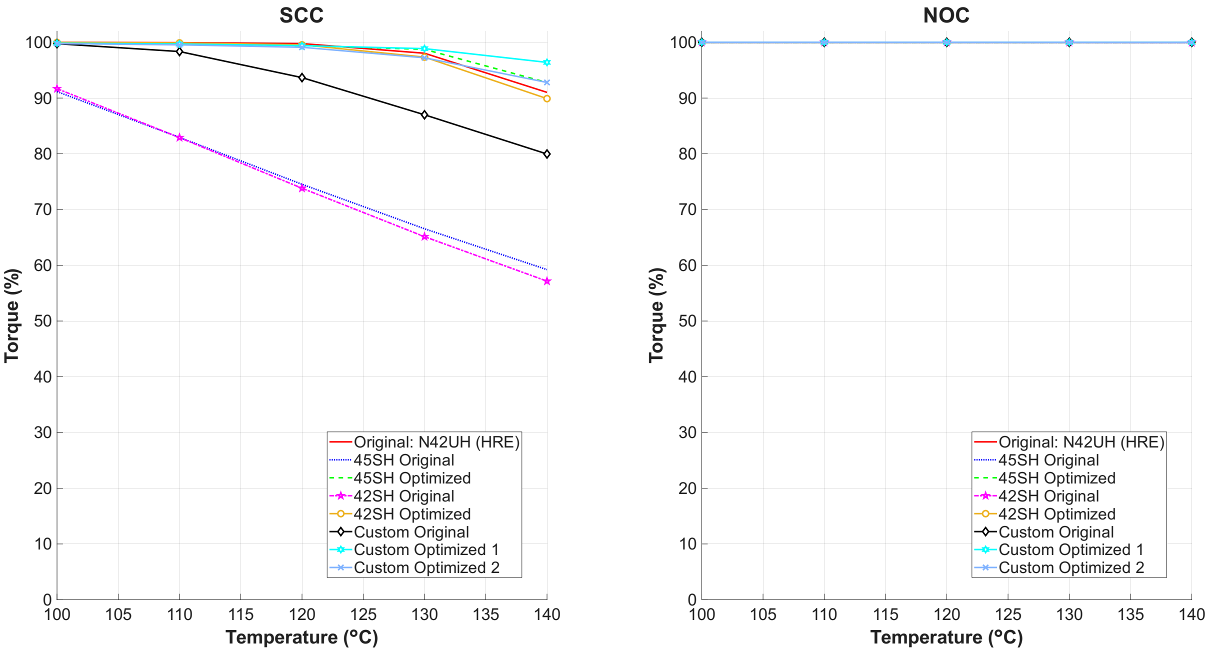

Figure 6.63: Torque retention (%) under SCC and NOC as a function of temperature ($°C$), comparing the original design with original magnets, the original design with HRE-free magnets, and optimized designs using HRE-free magnets.

The average torque before and after demagnetization is shown in Fig. 6.64. Before demagnetization, the original HRE-based reference design decreases slightly from approximately 560 Nm at 100°C to 555 Nm at 140°C. The original designs with 45SH and 42SH decrease from 575 Nm and approximately 562 Nm respectively at 100$°C$ to 570 Nm and 555 Nm respectively at 140$°C$. Their respective optimized designs have decreased in torque before demagnetization in both cases. For 45SH it has decreased to approximately 555 Nm at 100$°C$ and 545 Nm at 140$°C$ and for 42SH it has decreased to approximately 540 Nm at 100$°C$ and 530 Nm at 140$°C$. This indicates that part of the optimization improvement is achieved by sacrificing some initial torque capability.

After demagnetization under SCC, the difference between the original and optimized HRE-free designs becomes clear. The original HRE-based design decreases from approximately 560 Nm at 100°C to 505 Nm at 140°C. The original 45SH and 42SH rotor cases decrease much more, reaching only approximately 335 Nm and 320 Nm at 140°C. After optimization, the 45SH design reaches approximately 505 Nm at 140°C, which is comparable to the HRE-based reference design. The optimized 42SH design improves compared with its original case, but reaches only approximately 475 Nm at 140°C and therefore remains below the 500 Nm target.

The custom magnet gives the strongest HRE-free torque result after optimization. In the original rotor geometry, it decreases to approximately 450 Nm at 140°C after demagnetization under SCC. However, the two optimized custom designs reach approximately 570 Nm and 550 Nm at 140°C for the same operating condition. This shows that the combination of higher intrinsic coercivity and optimized rotor geometry gives a more favourable balance between torque and demagnetization resistance than the selected HRE-free magnet cases.

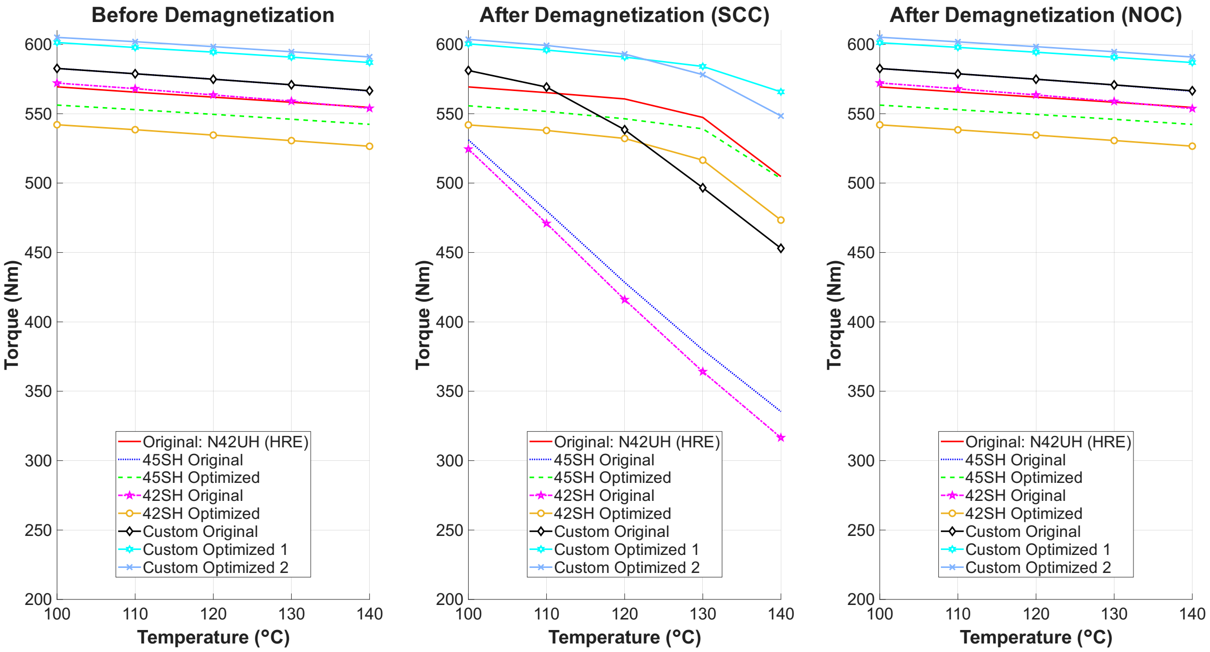

Figure 6.64: Average torque (Nm) before and after demagnetization under SCC and NOC as a function of temperature ($^\circ C$) for benchmarking, comparing the original design with original magnets, the original design with HRE-free magnets, and optimized designs using HRE-free magnets.

Fig. 6.65 shows the back EMF retention under SCC and NOC. After demagnetization under NOC, all cases remain at approximately 100% over the full temperature range. However, under SCC the original HRE-based magnet decreases from 100% at 100°C to approximately 85% at 140°C. The original HRE-free rotor cases show much stronger degradation, where 45SH and 42SH decrease to approximately 27.5% and 22.5%, respectively, at 140°C.

After optimization, the selected HRE-free designs improve significantly, with both optimized 45SH and 42SH retaining approximately 80% back EMF at 140°C. The custom magnet also improves through optimization. The original custom magnet case decreases to approximately 63%, while the optimized custom designs retain approximately 90% and 81% at 140°C. This supports the torque results and confirms that the optimized geometries preserve a larger part of the magnet flux after SCC.

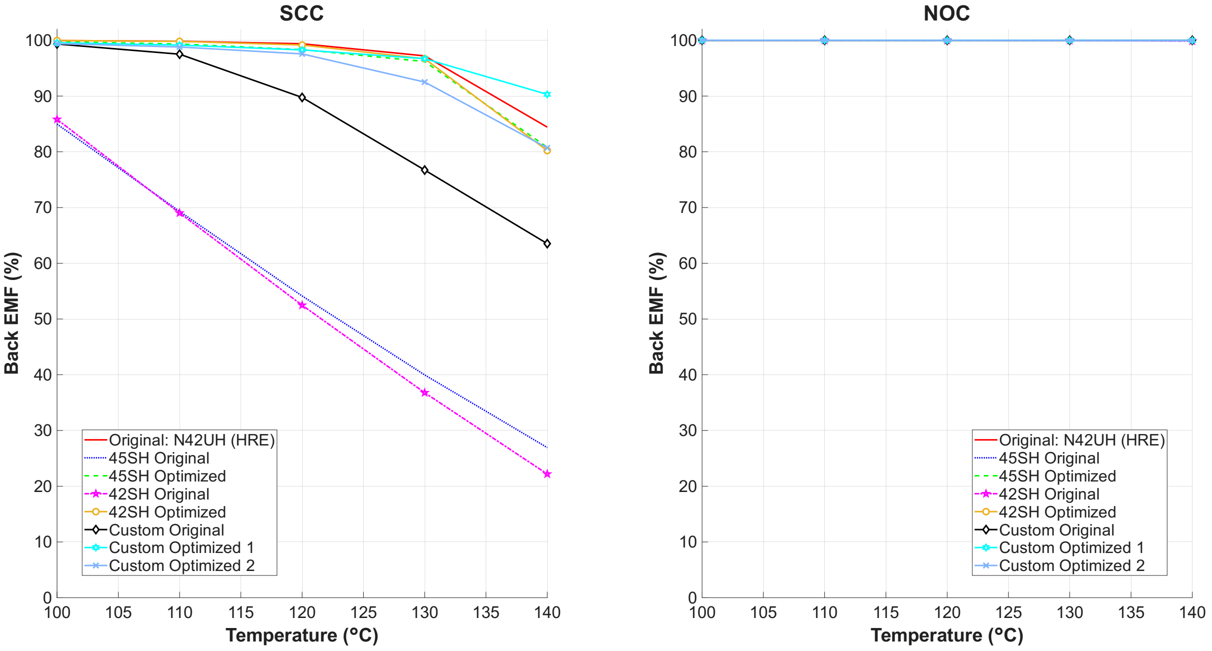

Figure 6.65: Back EMF retention (%) under SCC and NOC as a function of temperature ($^{\circ}C$), comparing the original design with original magnets, the original design with HRE-free magnets, and optimized designs using HRE-free magnets.

The short circuit current amplitude is shown in Fig. 6.66. The original HRE-based design decreases from approximately 1910 A at 100°C to 1825 A at 140°C. The original 45SH and 42SH rotor cases decrease from approximately 1980 A and 1925 A to 1900 A and 1825 A, respectively.

The optimized 45SH design shows a similar current level to the original 45SH case, decreasing from approximately 1975 A to 1895 A. For the optimized 42SH design, the current increases to approximately 2090 A at 100°C and 1975 A at 140°C. The optimized custom magnet designs show the highest short circuit current amplitudes, decreasing from approximately 2205 A and 2190 A to 2080 A and 2050 A, respectively. This is due to the larger width of the magnets optimized designs, which increases the flux path cross-sectional area and in turn the flux, flux linkage and lastly the current.

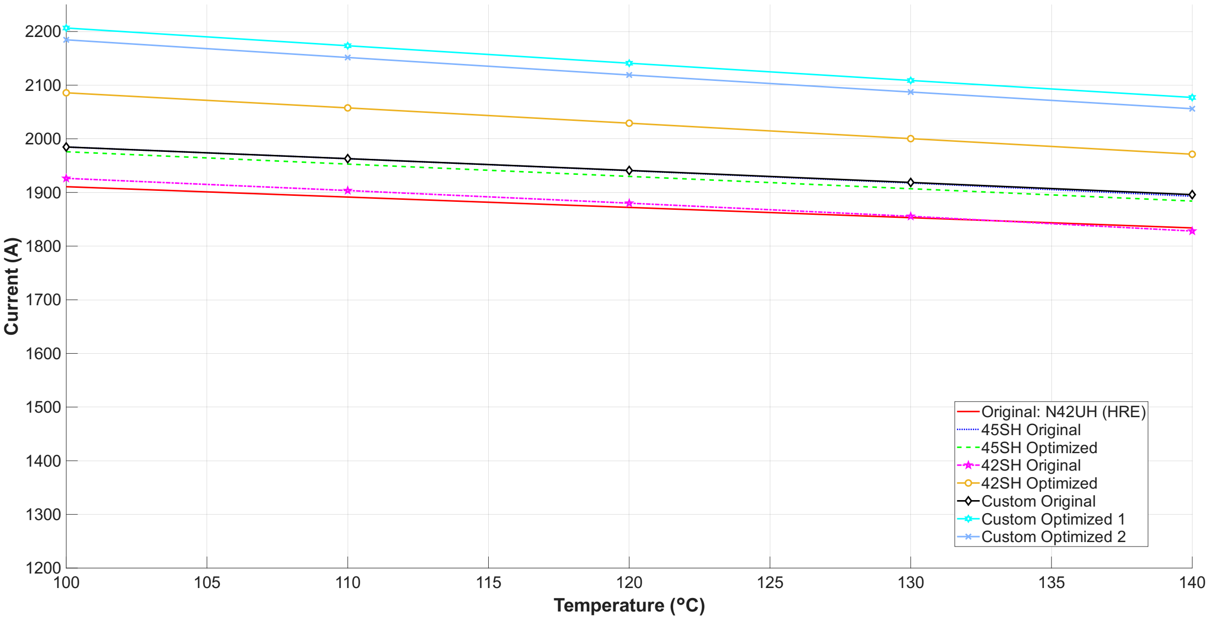

Figure 6.66: Short circuit current amplitude (A) as a function of temperature ($^{\circ}C$), comparing the original design with original magnets, the original design with HRE-free magnets, and optimized designs using HRE-free magnets.

The percentage reduction of average $\boldsymbol{B_r}$ in Layer 1 and Layer 2 is shown in Fig. 6.67. The original HRE-based reference design shows almost no reduction up until higher temperatures and reaches only approximately 9% reduction at 140°C. This confirms its strong demagnetization resistance under SCC.

The original HRE-free rotor cases show much larger degradation. At 140°C, the 45SH and 42SH cases reach approximately 60% and 64% reduction in Layer 1, and approximately 72% and 76% in Layer 2, respectively. After optimization, the reduction is greatly reduced. For the optimized 45SH design, Layer 1 reaches approximately 10% reduction at 140°C, while Layer 2 remains essentially unchanged. For the optimized 42SH design, the reduction reaches approximately 12% in Layer 1 and 13% in Layer 2 at 140°C.

For the custom magnet, the original rotor case reaches approximately 28% reduction in Layer 1 and 31% in Layer 2 at 140°C. After optimization, the two custom designs show lower reduction, with Layer 1 reaching approximately 7% and 16%, while Layer 2 remains essentially unchanged. This indicates that the optimized geometries are especially effective in protecting Layer 2, which was more sensitive to demagnetization in the original HRE-free rotor cases.

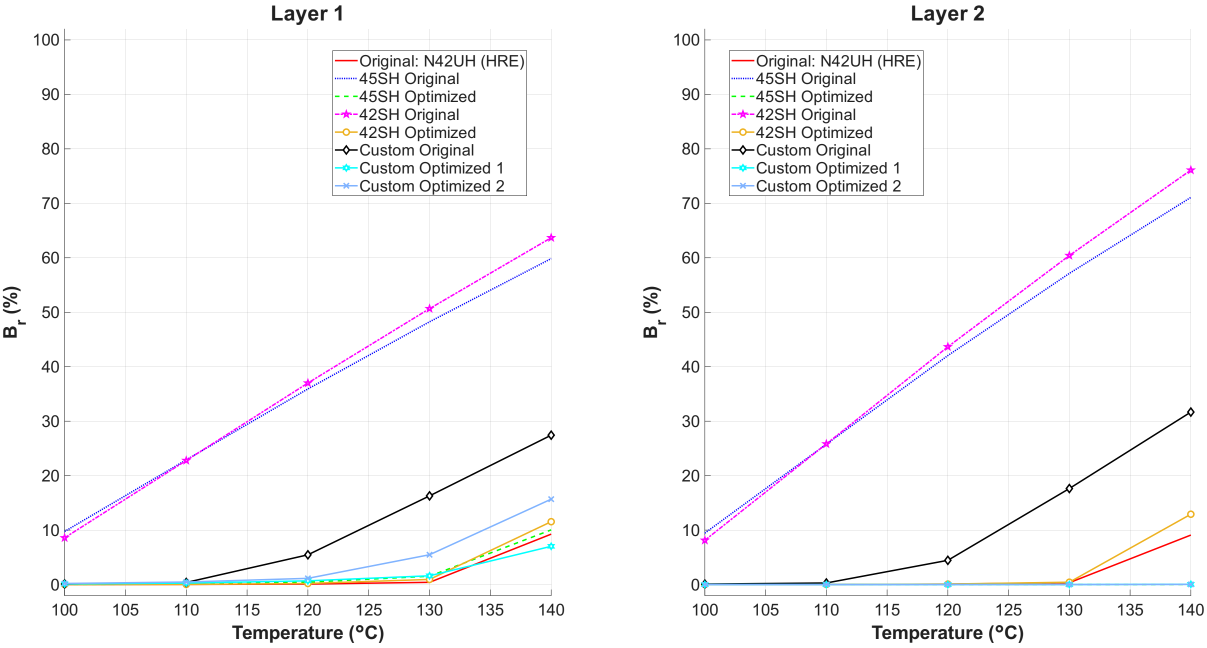

Figure 6.67: Percentage reduction of average B$_r$ (%) in layers 1 and 2 as a function of temperature (°C), comparing the original design with original magnets, the original design with HRE-free magnets, and optimized designs using HRE-free magnets.

Figure 6.68 shows the effective remanent flux density distribution for the optimized 42SH design at 100°C and 140°C. At 100°C, most of the magnet area remains close to the upper part of the scale, with values mainly around 1.125 to 1.25 T. At 140°C, the distribution shifts to lower values, with large parts of the magnets located around 0.84 to 1.08 T. Local reductions are mainly visible near the magnet tips and edges in both layers.

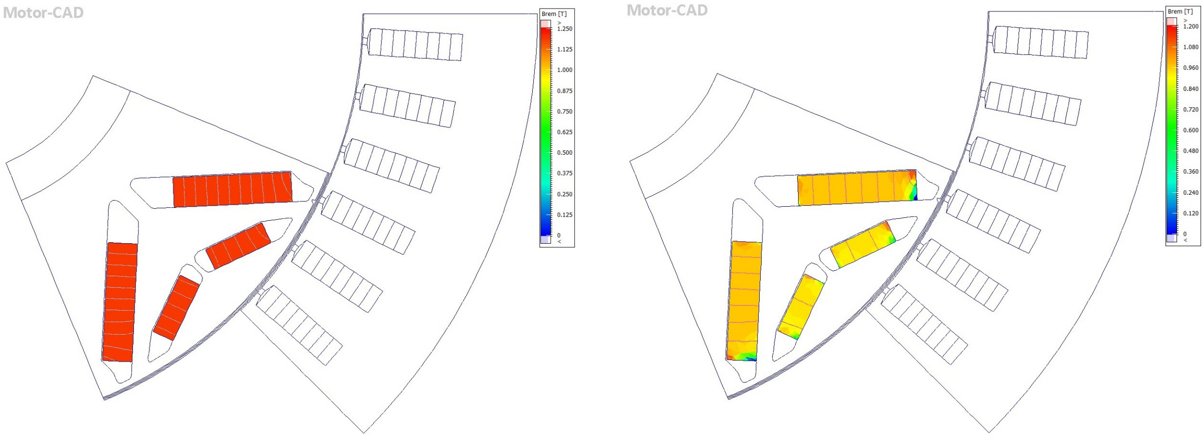

(a): 100°C

(b): 140°C

Figure 6.68: Effective remanent flux density distribution, B_r, for the optimized 42SH at 100°C and 140°C.

The corresponding FEA result for the optimized 45SH design is shown in Fig. 6.69. Since the 100°C result shows a similar high B_r distribution as the previous optimized case, the main difference is observed at 140°C. At this temperature, most of the magnet area remains in the upper part of the scale, while the lower B_r values are mainly limited to local regions near the edges of Layer 1. Layer 2 does not show the same clear reduction, which is consistent with the average B_r result where Layer 2 remains essentially unchanged for the optimized 45SH design.

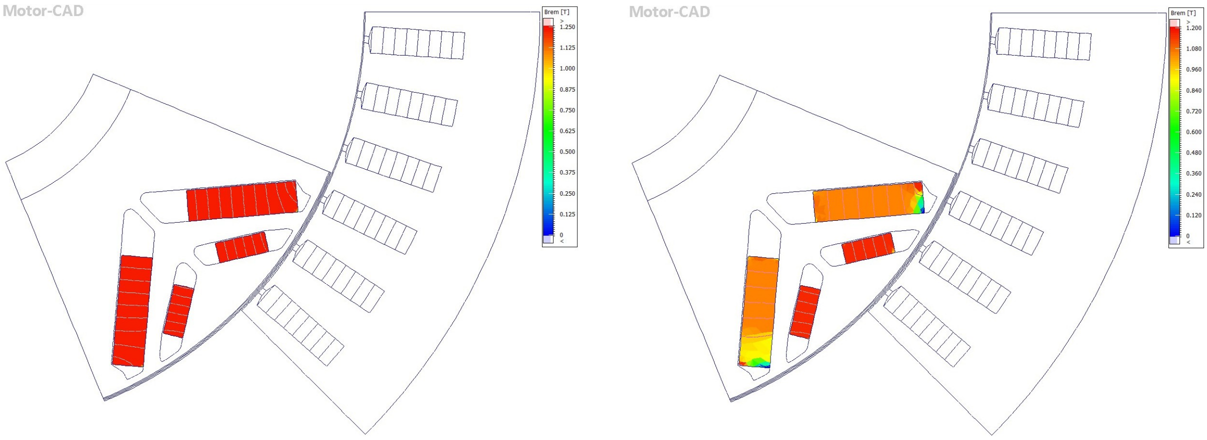

(a): 100°C

(b): 140°C

Figure 6.69: Effective remanent flux density distribution, B_r, for the optimized 45SH at 100°C and 140°C.

The FEA results for the two custom optimized designs are shown in Fig. 6.70 and Fig. 6.71. For both designs, the 100°C case shows that most of the magnet area remains close to the upper part of the scale. At 140°C, the reduction in B_r is still mainly local and appears close to the magnet tips and edges. In custom optimized 1, most of the magnet area remains at relatively high values, while only smaller local regions shift toward lower values. In custom optimized 2, a slightly larger part of Layer 1 shifts toward lower values at 140°C, especially close to the magnet edges. Layer 2 remains relatively well preserved in both cases.

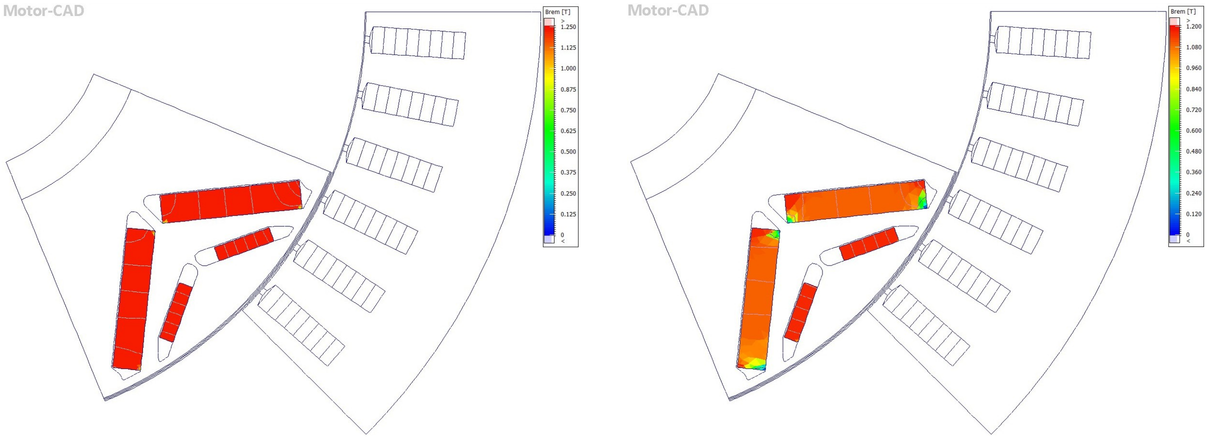

(a): 100°C **(b):** 140°C

Figure 6.70: Effective remanent flux density distribution, $\boldsymbol{B_r}$, for custom optimized 1 at 100°C and 140°C.

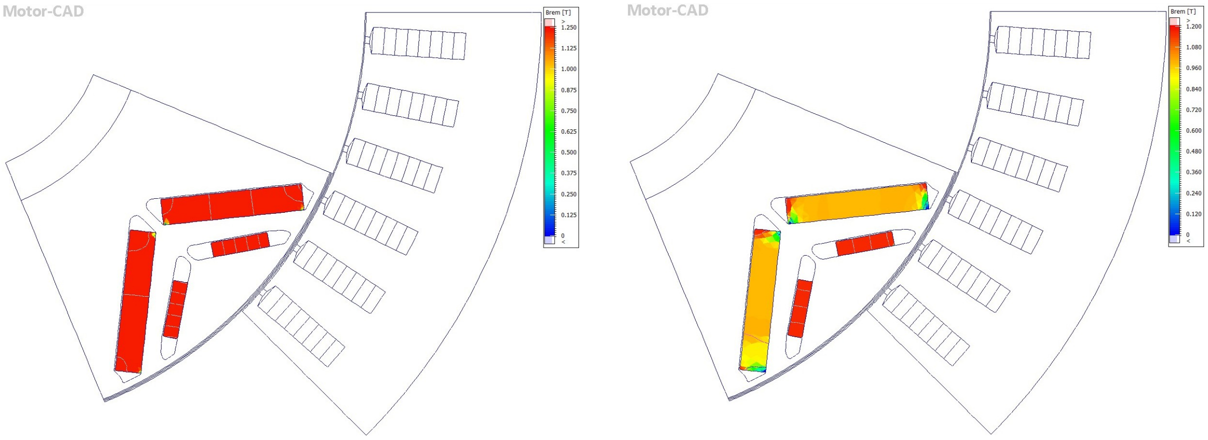

(a): 100°C **(b):** 140°C

Figure 6.71: Effective remanent flux density distribution, $\boldsymbol{B_r}$, for custom optimized 2 at 100°C and 140°C.

The FEA results also show that the spatial demagnetization pattern changes after optimization. In the original rotor geometry with HRE-free magnets, Layer 2 was generally more sensitive to irreversible demagnetization than Layer 1. After optimization, this behaviour is less pronounced. This indicates that the optimized rotor geometries redistribute the magnetic field during SCC and reduce the local reverse field acting on the outer magnet layer. However, the FEA plots also show that local demagnetization can still occur near magnet tips and edges. This is especially important when geometry changes, such as increased magnet separation, move parts of the magnet closer to the air gap. A similar tendency was observed in the combined rotor geometry study, where magnet separation could increase local exposure to the stator field.

The benchmarking results show that the original HRE-based reference magnet still provides the strongest resistance to irreversible demagnetization under SCC. This is expected and linked to the fact that the HRE magnet has higher coercivity and likely lower RTCs also improve the thermal stability of NdFeB magnets. As a result, the original N42UH magnet retains its performance better at elevated temperature compared with the HRE-free magnets in the original rotor geometry.

However, the optimized HRE-free designs significantly reduce the gap. The optimized 45SH design reaches approximately the same average torque after SCC at 140°C as the HRE-based reference design, while the optimized custom magnet designs exceed it. This is further emphasized with the custom magnet that has a $\boldsymbol{H_{cJ}}$ similar to the one with HREEs. The custom magnet, is demagnetized at a slower rate compared to its HRE-free counterparts. However, even though its $\boldsymbol{H_{cJ}}$ is identical at reference temperature, it demagnetizes at higher rate than the original magnet with HREEs. This further emphasizes the importance of taking the RTCs into account when evaluating the demagnetization of the magnets. A high coercivity at 20°C is therefore not sufficient if the coercivity decreases too rapidly with temperature.

The 42SH design improves substantially after optimization, but remains below the 500 Nm torque target and shows larger $\boldsymbol{B_r}$ reduction than the optimized 45SH and custom designs.

The results also show that the final HRE-free rotor design cannot be selected based only on one parameter. Increased magnet thickness improves demagnetization resistance and helps preserve torque, but it also increases magnet weight. Wider and thinner magnet designs become more feasible when the magnet has higher $\boldsymbol{H_{cJ}}$, as shown by the optimized custom magnet cases. Therefore, the best HRE-free rotor solution requires a combined selection of magnet material properties, rotor geometry, torque capability, and demagnetization resistance rather than only replacing the magnet material in the original rotor.

7

Conclusions

This chapter summarized the main conclusions of the thesis. The conclusions are divided into sustainability conclusions and simulation conclusions, followed by suggestions for future work.

7.1 Sustainability Conclusions

The sustainability analysis of REEs has shown that several challenges are associated with the current use of HRE-based magnets. Based on the initial assumptions, it was expected that removing HRE elements would improve sustainability in terms of availability, cost, environmental impact, and supply chain resilience.

Overall, the availability of REEs is not limited by geological scarcity, but rather by geopolitical concentration, processing capacity, and long development timelines. The strong dependence on China for both mining and processing creates a significant supply risk for Europe, particularly for HREEs where China currently dominates the global market. Although several promising deposits have been identified within Europe, such as in Kiruna and Norway, these resources are not expected to contribute significantly in the short term due to long permitting processes and environmental considerations. This creates a mismatch between rapidly increasing demand and the slow development of domestic supply. Furthermore, while alternative sources outside China exist, many of these are associated with environmental, social, and governance risks, which may conflict with the sustainability goals defined in the CRMA. As a result, simply diversifying supply geographically does not necessarily guarantee a secure or sustainable supply chain.

Regarding cost, the analysis supports the initial assumption that HRE elements contribute significantly to material costs. This is mainly due to their low abundance in ores combined with high demand, which results in considerably higher prices compared to LREs. Therefore, replacing or eliminating HREs is expected to reduce overall material cost. However, the cost of REEs is not only determined by material composition, but also by supply-demand dynamics and co-production effects, where increasing production of certain elements may lead to oversupply of others. It should also be noted that cost reductions depend on manufacturing methods, material availability, and market demand, which introduces uncertainty. As a result, while the assumption is partly supported, the actual cost benefit of reducing HRE content will depend on future market conditions and cannot be fully predicted.

From an environmental perspective, the results clearly align with the hypothesis. The impact of REEs is driven not only by the extraction process, but even more by energy intensive processing and chemical separation steps. The results show that both greenhouse gas emissions and water consumption increase significantly with growing demand, highlighting the environmental burden associated with scaling up REE production. In particular, as expected HREEs exhibit higher environmental impact per kilogram compared with LREEs when emissions are allocated based on economic value. This means that reducing HRE content can contribute to lowering the environmental impact at the material level. However, the total environmental impact of an electric machine also depends on the overall material usage, where materials such as copper may dominate due to their larger quantities. In addition, the environmental impact is strongly influenced by external factors such as the energy mix and production location. REE production in regions with fossil based electricity results in significantly higher emissions compared to regions with low carbon energy systems. This highlights that supply route selection is a key factor in determining the overall environmental footprint.

Regarding supply chain resilience, recycling offers a promising pathway to reduce dependence on primary extraction, but current recycling rates remain very low, mainly due to difficulties in collection, disassembly, and material recovery. In addition, the performance and quality of recycled magnets can be affected by changes in material composition and microstructure, which may require additional processing. Recycling also needs to be economically competitive with highly optimized primary production such as in China which in turn limits its large-scale implementation. These findings indicate that while recycling can contribute to a more resilient supply chain, it does not fully support the initial hypothesis that recycling alone can significantly improve supply chain resilience. Instead, the results show that a combination of strategies, including improved recycling technologies, design for recycling, diversification of supply, and increased processing capacity outside dominant regions, is required.

Overall, reducing or removing HREs from NdFeB magnets can improve the sustainability of PMSM rotor designs by reducing material cost, lowering the environmental burden associated with HREE production, and decreasing dependence on some of the most critical elements. However, HRE reduction does not remove all sustainability challenges related to REE-based magnets. A sustainable HRE-free rotor design must also consider responsible sourcing, cleaner processing routes, recycling potential, material efficiency, and supply chain diversification. Therefore, HRE reduction should be seen as an important step toward more sustainable electric machine designs, not as a complete solution on its own.

7.2 Simulation Conclusions

The simulation results show that repeated short circuit transients do not lead to cumulative demagnetization. The main degradation occurs during the initial fault event, and subsequent transients do not further reduce machine performance. As expected, this allows the demagnetization behavior to be accurately evaluated using a single short circuit event.

The initial magnet screening showed that replacing the original HRE-based magnet with available HRE-free magnets in the unchanged rotor geometry is not sufficient to meet the performance and demagnetization requirements. Several magnet grades experienced irreversible demagnetization and torque reduction already at 100°C under SCC. At 140°C, several magnets retained only approximately 48–55% of the original torque under SCC, while the best selected SH magnets reached higher values, around 68%. Under NOC, the degradation was less severe, and no magnet grade dropped below approximately 60% torque retention. The results therefore confirm that SCC is the critical operating condition for demagnetization.

The results further confirmed that magnet grades with stronger coercivity retention at elevated temperatures showed significantly better torque robustness. SH-type magnets generally performed better than M-, H- or N-type magnets. However, variations between sources were also observed, indicating that nominal grade alone is not sufficient. For example, the comparison of 45SH magnets from different sources showed that the torque retention under SCC at 140°C varied from approximately 45% to 59%, even though the magnets had the same nominal grade. This shows that temperature-dependent material data, especially $\boldsymbol{H_{cJ}}$ and its reduction with temperature, must be included when evaluating demagnetization robustness.

The back EMF results showed even stronger sensitivity to demagnetization than the torque results. Under SCC, the remaining back EMF for the original HRE-free rotor cases could decrease below 30% at 140°C, and some weak magnet grades approached 0%. In contrast, finite torque still remained because of the reluctance torque contribution in the interior PMSM. The short circuit current response followed the same general material-dependent trend, where weaker magnets showed reduced current, torque, and back EMF. This confirms that a lower short circuit current does not necessarily represent improved robustness, but can instead reflect a weakened magnetic state after demagnetization.

The demagnetization percentage directly confirmed the permanent loss of magnetization. In the original HRE-free rotor geometry, the remaining average $\boldsymbol{B_r}$ decreased strongly with temperature. At 140°C, many magnets retained only approximately 20–30% of the original $\boldsymbol{B_r}$ in Layer 1 and approximately 10–20% in Layer 2. This provided a clear explanation for the degradation observed in torque, back EMF and current, and highlights that HRE-free magnets require sufficient coercivity retention to maintain acceptable performance under fault conditions. The results also showed that Layer 2 was generally more sensitive to irreversible demagnetization than Layer 1 in the original rotor geometry.

Also, the nominal magnet grade alone is not sufficient to predict demagnetization robustness. Instead, detailed material data, including temperature dependent properties, must be considered in the design process in order to accurately evaluate the performance under fault conditions which was seen when 45SH from different sources was compared.

The comparison of magnets with different remanence at approximately constant coercivity showed that higher $\boldsymbol{B_r}$ can increase the risk of irreversible demagnetization, even when the torque and short-circuit current levels are similar. This means that high remanence is not beneficial for fault robustness. Instead, $\boldsymbol{H_{cJ}}$ remains the dominant parameter for demagnetization resistance, while $\boldsymbol{B_r}$ mainly influences torque and back EMF performance.

The custom magnet study showed that increasing $\boldsymbol{H_{cJ}}$ improves resistance to demagnetization by preventing the operating point from reaching the knee point. When $\boldsymbol{H_{cJ}}$ was increased while $\boldsymbol{B_r}$ was kept constant, the torque retention under SCC at 140°C increased from approximately 50% for the lowest test case to close to 100% for the highest test cases. The back EMF retention showed a similar improvement, increasing from approximately 11% to almost 100%. When both $\boldsymbol{H_{cJ}}$ and $\boldsymbol{B_r}$ were increased, the best overall performance was obtained, since the magnet could maintain both high torque and strong demagnetization resistance. However, the required coercivity levels reached approximately 2000–2200 kA/m, which approaches UH-grade material levels and may not be available within the current HRE-free SH magnet class.

The rotor geometry study showed that demagnetization behaviour can be improved through manual parameter variations. The most influential geometric parameter was magnet thickness. Increasing the magnet thickness by 2 mm increased the torque after SCC from approximately 335 Nm to 440 Nm at 140°C, while the torque loss between NOC and SCC decreased from approximately 230 Nm to 170 Nm. At the same time, the average $\boldsymbol{B_r}$ reduction decreased from approximately 60% to 42% in Layer 1 and from approximately 72% to 47% in Layer 2. However, this improvement also increased the short circuit current from approximately 1900 A to 2500 A and increased the magnet volume.

The studies of pole V-angle and web thickness showed that these parameters mainly affect the local field distribution rather than providing large torque improvements. The pole V-angle could slightly improve the SCC response when selected carefully, especially in Layer 2, but it did not provide a monotonic improvement. Web thickness reduced the average $\boldsymbol{B_r}$ reduction, but the torque after SCC increased only by approximately 5–10 Nm. These results show that magnet thickness is the dominant parameter.

The combined rotor geometry study confirmed that geometry parameters must be changed together to improve the design. Several combinations reduced the average $\boldsymbol{B_r}$ reduction below the acceptable limit of 10% at 140°C. However, the corresponding torque levels under SCC still remained below the required 500 Nm. This means that although the geometry modifications improved demagnetization resistance, they were not sufficient to meet both the demagnetization and torque requirements simultaneously. The FEA results also showed that average $\boldsymbol{B_r}$ reduction should not be evaluated alone, since local reductions can still appear near magnet tips and edges, especially when magnet separation is included.

The optimization results further confirmed the trade-off between torque capability, demagnetization resistance, and magnet weight. For the selected 45SH and 42SH magnets, the optimized designs required thicker magnets than the original rotor. The Layer 1 magnet thickness increased from 3.20 mm to 6.00 mm for 45SH and to 5.77 mm for 42SH, while Layer 2 increased from 2.80 mm to 3.93 mm and 4.33 mm, respectively. This increased the magnet weight from approximately 3.00 kg in the original design to 4.08 kg for 45SH and 4.56 kg for 42SH. The custom magnet optimizations required less increase in Layer 2 thickness, which remained at 2.80 mm, due to the higher intrinsic coercivity. This shows that improved magnet material properties can reduce the need for aggressive geometry changes.

From the benchmarking, it is evident that it is not sufficient to use the reference design with HRE-free magnets if a safety state such as ASC is to be used due to the risk of demagnetization. However, it also showed that the optimized HRE-free designs strongly reduced irreversible demagnetization. For the original 45SH and 42SH rotor cases, the average $\boldsymbol{B_r}$ reduction at 140°C reached approximately 60–64% in Layer 1 and 72–76% in Layer 2. After optimization, the corresponding reduction decreased to approximately 10–12% in Layer 1 and approximately 0–13% in Layer 2. For the optimized custom magnet designs, Layer 2 remained almost unchanged, while Layer 1 showed approximately 7% and 16% reduction. The FEA results showed that the optimized geometries also changed the spatial demagnetization pattern, with Layer 2 being better preserved than in the original HRE-free rotor cases.

Overall, the simulation results show that an HRE-free PMSM rotor for heavy-duty applications is possible only if magnet material properties and rotor geometry are designed together. Replacing the HRE-based magnet with an available HRE-free magnet in the original rotor geometry is not sufficient. A suitable HRE-free design requires high coercivity retention at elevated temperature, sufficient remanence for torque production, and rotor geometry modifications that reduce local demagnetizing fields while maintaining useful air-gap flux. The optimized 45SH design can approach the HRE-based reference performance, while the optimized custom magnet designs can exceed the torque requirement, but only with improved coercivity and carefully optimized rotor geometry.

7.3 Future Work

The sustainability benefits of an HRE-free design should also be evaluated in relation to the complete electric machine and its full life cycle. This includes the extraction and processing of magnet materials, magnet manufacturing, machine production, operation, recycling, and end-of-life treatment.

Since rare earth elements remain critical from both availability and a supply chain perspective, recycling can play an important role in reducing the dependence on primary raw material extraction. Future work should therefore evaluate how HRE-free magnets behave when recycled material is used, and whether recycling magnet grades can provide sufficient remanence and coercivity. In addition, the rotor design should be studied from a design-for-recycling perspective, where magnet accessibility, separation, and reuse are considered already during the design stage.

From a simulation perspective, future work should focus on improving the demagnetization evaluation by including a coupled electromagnetic and thermal model. The risk of irreversible demagnetization is strongly dependent on magnet temperature, since both remanence and coercivity decrease as temperature increases. A thermal model would make it possible to evaluate the actual magnet temperature distribution during operation and identify local hot spots that may increase the risk of partial demagnetization. This would also make it possible to investigate how much demagnetization can be accepted in practice, since this work mainly evaluates critical demagnetization conditions.

Future studies should also include full drive cycle simulation, where the machine is exposed to varying torque, speed, current, and temperature conditions over time. This would provide a better understanding of how partial demagnetization develops during repeated load cycles and transient events, rather than only under selected critical operating points.

Another important continuation is to include inverter effects and control strategy. Current harmonics, PWM ripple, and transient current peaks may influence both losses and local demagnetizing fields and the magnets. This is especially relevant during active short circuit events and field weakening operation, where negative d-axis current can move the magnet working point closer to the knee point of the demagnetization curve.

Future work should also improve the magnet material modeling by using more detailed BH-curve data. In this work, the available material data from different sources did not always include complete BH-curves for all magnet grades and temperatures. In several cases, the material description was mainly based on values of remanence and intrinsic coercivity at a limited number of temperature points. More complete BH-curve data, with several data points at each relevant temperature, would improve the accuracy of the magnet models and provide a more reliable prediction of the demagnetization behaviour.

Another interesting aspect would be to analyze the demagnetization at all operating points. What can be done is to map the motor considering the demagnetization in a torque-speed curve to gain knowledge on what operating points are most critical. This could be used to set a reasonable limit on how much demagnetization is allowed since the worst case scenario may not happen often enough.

Future work could also investigate material processing strategies, such as grain size refinement, to increase $\boldsymbol{H_{cJ}}$ in HRE-free NdFeB magnets. This is relevant since high coercivity was found to be critical for improving demagnetization resistance in this work.

Further studies should also investigate design solutions for reducing magnet temperature and improving demagnetization robustness. Beyond the rotor geometry variations studied in this work, this could include further magnet segmentation, improved cooling methods, and the use of different magnet grades in different rotor layers. Since Layer 2, located closer to the air gap, showed a higher tendency for demagnetization than Layer 1, a higher-coercivity magnet could be used in Layer 2 while a lower-cost magnet could be used in Layer 1. This could reduce cost and HRE dependency while maintaining sufficient demagnetization resistance in the most critical rotor regions.

Bibliography

[1] S. Kalantzakos, *China and the geopolitics of rare earths.* Oxford University Press, 2017.

[2] T. Raminosoa, R. Wiles, J. E. Cousineau, K. Bennion, and J. Wilkins, "A High-Speed High-Power-Density Non-Heavy Rare-Earth Permanent Magnet Traction Motor", English, Detroit, MI: IEEE, 2020, pp. 61–67, ISBN: 9781728158266. DOI: `10.1109/ECCE44975.2020.9235704`.

[3] P. Kumar, A. Al-Qarni, R. Wilson, and A. El-Refaie, "Retrofitting of a Chevy-Bolt IPM Motor with a PM-Assisted Synchronous Reluctance Rotor Enabled with a Blend of Heavy-Rare-Earth-Free Neodymium and Ferrite Magnets", in *International Electric Machines and Drives Conference, IEMDC 2025*, Institute of Electrical and Electronics Engineers Inc., 2025, pp. 1190–1195, ISBN: 9798350376593. DOI: `10.1109/IEMDC60492.2025.11061037`.

[4] Z. S. Du and J. Tangudu, "Performance comparison between Rare earth and Non-Rare Earth based SPM machines using High Silicon Steel", English, Baltimore, MD: IEEE, 2019, pp. 3952–3959, ISBN: 9781728103952. DOI: `10.1109/ECCE.2019.8912531`.

[5] W. Feng et al., "Design of high power density 100 kW surface permanent magnet machine with no heavy rare earth material using current source inverter for traction application", in *2021 IEEE Transportation Electrification Conference and Expo, ITEC 2021*, Institute of Electrical and Electronics Engineers Inc., Jun. 2021, pp. 1–6, ISBN: 9781728175836. DOI: `10.1109/ITEC51675.2021.9490037`.

[6] Y. Yoshida, T. Yanagisawa, and K. Tajia, "Consideration of Asymmetrical Magnetic Pole IPMSM Using Bonded Rare-earth Magnet", Hamamatsu, Tech. Rep., 2020, pp. 720–723. DOI: `10.23919/ICEMS50442.2020.9291226`.

[7] M. S. Islam, S. Agoro, R. Chattopadhyay, and I. Husain, "Heavy Rare Earth Free High Power Density Traction Machine for Electric Vehicles", in *2021 IEEE International Electric Machines and Drives Conference, IEMDC 2021*, Institute of Electrical and Electronics Engineers Inc., May 2021, ISBN: 9781665405102. DOI: `10.1109/IEMDC47953.2021.9449585`.

[8] A. Al-Qarni and A. El-Refaie, “On Eliminating Heavy Rare-Earth PM Elements for High Power Density Traction Application Motors”, in *2021 IEEE International Electric Machines and Drives Conference, IEMDC 2021*, Institute of Electrical and Electronics Engineers Inc., May 2021, ISBN: 9781665405102. DOI: `10.1109/IEMDC47953.2021.9449542`.

[9] J. H. L. Voncken, *The Rare Earth Elements An Introduction.* Springer, 2016, ISBN: 978-3-319-26809-5. DOI: `10.1007/978-3-319-26809-5`.

[10] N. Dushyantha et al., *The story of rare earth elements (REEs): Occurrences, global distribution, genesis, geology, mineralogy and global production*, Jul. 2020. DOI: `10.1016/j.oregeorev.2020.103521`.

[11] “Alkaline Rocks”, in *Encyclopedia of Geology*, D. Alderton and S. A. Elias, Eds., 2nd ed., vol. 5, Elsevier, 2021. [Online]. Available: `https://www.sciencedirect.com/topics/earth-and-planetary-sciences/alkaline-rock`.

[12] B. D. Cullity and C. D. Graham, *Introduction to magnetic materials*, English, Second. 2009, Section 1.3, 1.5, 1.6, ISBN: 978-0-471-47741-9.

[13] Y. Ghorbani, I. M. Ilankoon, N. Dushyantha, and G. T. Nwaila, *Rare earth permanent magnets for the green energy transition: Bottlenecks, current developments and cleaner production solutions*, Jan. 2025. DOI: `10.1016/j.resconrec.2024.107966`.

[14] Y. V. Murty, M. Anne, A. Jack, and P. Lifton, *Rare Earth Metals and Minerals Industries*, English. Springer International Publishing AG, Dec. 2023, p. 299, ISBN: 9783031318665.

[15] I. R. Harris and G. W. Jewell, *Functional Materials for Sustainable Energy Applications*, J. A. Kilner, S. J. Skinner, S. J. C. Irvine, and P. P. Edwards, Eds. Woodhead Publishing, 2012, pp. 600–639, ISBN: 978-0-85709-059-1. DOI: `https://doi.org/10.1533/9780857096371.4.600`.

[16] M. Hossain and S. S. Sikder, “Hysteresis loop properties of rare earth doped spinel ferrites: A review”, *Jounral of Magnetism and Magnetic Materials*, vol. 564, 2022, ISSN: 0304-8853. DOI: `https://doi.org/10.1016/j.jmmm.2022.170095`.

[17] S. R. Trout, “A Second Look at the Reversible Temperature Coefficients of Permanent Magnets”, Apr. 2018. DOI: `10.1109/LMAS.2104.2312178`. [Online]. Available: `https://www.khanacademy.org/math/ap-calculus-ab/advanced-differentiation-`.

[18] G. F. Olson, A. Bojoi, P. Pescetto, S. Ferrari, L. Peretti, and G. Pellegrino, “Active Short-Circuit Strategy for PMSMs Enabling Bounded Transient Torque and Demagnetization Current”, *IEEE Access*, vol. 12, pp. 109 001–109 011, 2024, ISSN: 21693536. DOI: `10.1109/ACCESS.2024.3440015`.

[19] R. Du et al., “Stepwise incorporation of heavy rare earth elements for the preparation of Nd-Fe-B magnets with ultra-high coercivity”, *Materials Letters*, vol. 403, 2026, ISSN: 0167-577X. DOI: `https://doi.org/10.1016/j.matlet.2025.139512`.

[20] S. B. Narang and K. Pubby, “Nickel Spinel Ferrites: A review”, *Journal of Magnetism and Magnetic Materials*, vol. 519, 2021, ISSN: 0304-8853. DOI: `https://doi.org/10.1016/j.jmmm.2020.167163`.

[21] M. S. Shafie et al., “Magnetic M-H loops family characteristics in the microstructure evolution of BaFe12O19”, *Journal of Materials Science: Materials in Electronics*, vol. 25, no. 9, pp. 3787–3794, 2014, ISSN: 1573482X. DOI: `10.1007/s10854-014-2090-0`.

[22] Z. x. Li, G. l. Yang, Y. m. Fan, and J. h. Li, “Irreversible demagnetization mechanism of permanent magnets during electromagnetic buffering”, *Defence Technology*, vol. 17, no. 3, pp. 763–774, Jun. 2021, ISSN: 22149147. DOI: `10.1016/j.dt.2020.05.005`.

[23] Advanced Magnets, *Sintered NdFeB Magnet Grades*. [Online]. Available: `https://www.advancedmagnets.com/how-to-understand-the-rare-earth-permanent-magnets-grades-part-1-sintered-neodymium-iron-boron-magnets/`.

[24] J. Cui et al., *Manufacturing Processes for Permanent Magnets: Part I—Sintering and Casting*, 2022. DOI: `10.1007/s11837-022-05156-9`.

[25] K. Opelt et al., “Upscaling the 2-Powder Method for the Manufacturing of Heavy Rare-Earth-Lean Sintered didymium-Based Magnets”, *Advanced Engineering Materials*, vol. 23, no. 10, Oct. 2021, ISSN: 15272648. DOI: `10.1002/adem.202100459`.

[26] Z. Liu, J. He, and R. V. Ramanujan, *Significant progress of grain boundary diffusion process for cost-effective rare earth permanent magnets: A review*, Nov. 2021. DOI: `10.1016/j.matdes.2021.110004`.

[27] Y. Liu, J. Tang, N. Sharma, and A. Rodionov, “Electrical Machines-Design and Analysis , 1st Edition”, Tech. Rep., 2019.

[28] J.-C. Urresty, J.-R. Riba, H. Saavedra, and L. Romeral, “Detection of Inter-Turns Short Circuits in Permanent Magnet Synchronous Motors Operating under Transient Conditions by means of the Zero Sequence Voltage”, Tech. Rep. [Online]. Available: `www.mcia.upc.edu`.

[29] L. Niu and M. Zhang, “The optimal design and research of interior permanent magnet synchronous motors for electric vehicle applications”, *The Journal of Engineering*, vol. 2023, no. 4, Apr. 2023, ISSN: 2051-3305. DOI: `10.1049/tje2.12258`.

[30] T. Deng, Z. Su, J. Li, P. Tang, X. Chen, and P. Liu, “Advanced Angle Field Weakening Control Strategy of Permanent Magnet Synchronous Motor”, *IEEE Transactions on Vehicular Technology*, vol. 68, no. 4, pp. 3424–3435, Apr. 2019, ISSN: 19399359. DOI: `10.1109/TVT.2019.2901275`.

[31] K. E. Portney, *Sustainability*. MIT Press, 2015, pp. 1–4. [Online]. Available: `https://books.google.se/books?hl=sv&lr=&id=WXr6CgAAQBAJ&oi=fnd&pg=PP6&dq=sustainability&ots=umUqf8tUE8&sig=tkoacfl823NDOWgPS4_kWeg4iGQ&redir_esc=y#v=onepage&q&f=false`.

[32] European Commission., *Critical Raw Materials Act.* [Online]. Available: `https://single-market-economy.ec.europa.eu/sectors/raw-materials/areas-specific-interest/critical-raw-materials/critical-raw-materials-act_en`.

[33] M. Grohol and C. Veeh, "Study on the Critical Raw Materials for the EU 2023 – Final Report", Tech. Rep., May 2023. DOI: `10.2873/725585`.

[34] European Commission, *Rare earth elements, permanent magnets, and motors.* [Online]. Available: `https://single-market-economy.ec.europa.eu/sectors/raw-materials/areas-specific-interest/rare-earth-elements-permanent-magnets-and-motors_en`.

[35] European Commission, *European Critical Raw Materials Act.* [Online]. Available: `https://commission.europa.eu/topics/competitiveness/green-deal-industrial-plan/european-critical-raw-materials-act_en`.

[36] LKAB, *Europe's largest deposit of rare earth metals located in Kiruna area*, Jan. 2023. [Online]. Available: `https://lkab.com/en/press/europes-largest-deposit-of-rare-earth-metals-is-located-in-the-kiruna-area/`.

[37] K. M. Goodenough et al., *Europe's rare earth element resource potential: An overview of REE metallogenetic provinces and their geodynamic setting*, Jan. 2016. DOI: `10.1016/j.oregeorev.2015.09.019`.

[38] LKAB, *LKAB becomes main owner in REEtec AS, builds strong Nordic industry for rare earth elements*, Nov. 2022. [Online]. Available: `https://lkab.com/en/press/lkab-becomes-largest-owner-in-reetec-as-builds-a-strong-nordic-industry-for-rare-earth-elements/`.

[39] G. de Souza Vieira, *Simplified World Map.* [Online]. Available: `https://commons.wikimedia.org/wiki/File:Simplified_World_Map.svg`.

[40] S. L. Liu et al., "Global rare earth elements projects: New developments and supply chains", *Ore Geology Reviews*, vol. 157, Jun. 2023, ISSN: 01691368. DOI: `10.1016/j.oregeorev.2023.105428`.

[41] Steinbeis Europa Zentrum, *Findings by EU project REEsilience show: exploiting a fraction of low-risk deposits could mitigate EU's rare earth elements supply risk*, Jul. 2025. [Online]. Available: `https://steinbeis-europa.de/en/post/findings-by-eu-project-reesilience-show-exploiting-a-fraction-of-low-risk-deposits-could-mitigate-eu-s-rare-earth-elements-supply-risk`.

[42] X. Yin, C. Martineau, I. Demers, N. Basiliko, and N. J. Fenton, "The potential environmental risks associated with the development of rare earth element production in Canada", *Environmental Reviews*, vol. 29, no. 3, pp. 354–377, 2021, ISSN: 11818700. DOI: `10.1139/er-2020-0115`.

[43] C. Spandler, P. Slezak, and T. Nazari-Dehkordi, *Tectonic significance of Australian rare earth element deposits*, Aug. 2020. DOI: `10.1016/j.earscirev.2020.103219`.

[44] A. Ford et al., “A national-scale mineral potential assessment for carbonatite-related rare earth element mineral systems in Australia”, *Ore Geology Reviews*, vol. 161, Oct. 2023, ISSN: 01691368. DOI: `10.1016/j.oregeorev.2023.105658`.

[45] Rare Earths Norway, *Europe’s largest deposit of rare earth elements discovered at Fen Norway*, Jun. 2024. [Online]. Available: `https://rareearthsnorway.com/europes-largest-deposit-of-rare-earth-elements-discovered-at-fen-norway`.

[46] P. Meehan, M. Sadan, and D. S. Lawn, “The Myanmar borderlands as a green energy transition ‘sacrifice zone’: A case study of rare earth mining in Kachin state”, *Extractive Industries and Society*, vol. 22, Jun. 2025, ISSN: 22147918. DOI: `10.1016/j.exis.2024.101579`.

[47] V. Balaram, “Rare earth elements: A review of applications, occurrence, exploration, analysis, recycling, and environmental impact”, *Geoscience Frontiers*, vol. 10, no. 4, pp. 1285–1303, Jul. 2019, ISSN: 16749871. DOI: `10.1016/j.gsf.2018.12.005`.

[48] European Commission, *Questions and Answers on the Critical Raw Materials Act*, May 2024. [Online]. Available: `https://ec.europa.eu/commission/presscorner/detail/en/qanda_24_2749`.

[49] K. Binnemans, P. T. Jones, K. Van Acker, B. Blanpain, B. Mishra, and D. Apelian, “Rare-earth economics: The balance problem”, *JOM*, vol. 65, no. 7, pp. 846–848, Jul. 2013, ISSN: 10474838. DOI: `10.1007/s11837-013-0639-7`.

[50] A. Nordelöf and A. Bongards, “Allocating the environmental burdens in co-production of rare earth elements for EV magnets”, Tech. Rep.

[51] S. R. Golroudbary, I. Makarava, A. Kraslawski, and E. Repo, “Global environmental cost of using rare earth elements in green energy technologies”, *Science of the Total Environment*, vol. 832, Aug. 2022, ISSN: 18791026. DOI: `10.1016/j.scitotenv.2022.155022`.

[52] H. Ritchie and P. Rosado, “Energy”, Tech. Rep., 2025. [Online]. Available: `https://ourworldindata.org/profile/energy/china`.

[53] Energiföretagen, “Energiåret 2024”, Tech. Rep.

[54] A.-M. Tillman et al., “Elmaskiner för fordon i en cirkulär ekonomi”, Tech. Rep. [Online]. Available: `www.chalmers.se`.

[55] T. Elwert et al., *Current developments and challenges in the recycling of key components of (Hybrid) electric vehicles*, 2016. DOI: `10.3390/recycling1010025`.

[56] Z. Li, A. Kedous-Lebouc, J. M. Dubus, L. Garbuio, and S. Personnaz, “Direct reuse strategies of rare earth permanent magnets for PM electrical machines-an overview study”, *EPJ Applied Physics*, vol. 86, no. 2, 2019, ISSN: 12860050. DOI: `10.1051/epjap/2019180289`.

[57] T. Klier, F. Risch, and J. Franke, “Disassembly, Recycling, and Reuse of Magnet Material of Electric Drives”, Tech. Rep., 2013, pp. 88–90. DOI: `10.1109/ISAM.2013.6643495.`.

[58] S. Högberg et al., "Direct Reuse of Rare Earth Permanent Magnets-Wind Turbine Generator Case Study", Tech. Rep.

[59] A. Rob, N. Mann, J. Farthing, A. Mahendran, and A. Walton, "Executive summary of Recent Technical Progress by HyProMag Ltd-June 2025", Tech. Rep.

A

Temperature Dependent Magnet Data

Table A.1: B_r and H_{cj} ranges for the investigated magnet grades at different temperatures.

20°C

Grade	B_r [T]	H_{cj} [kA/m]
35SH	1.18–1.19	1592–1703
38SH	1.22	1592
40SH	1.26–1.30	1592–1743
42SH	1.29–1.31	1592–1800
45SH	1.33–1.35	1592–1814
48SH	1.37	1602
48H	1.37	1353
50H	1.39	1353
50SH	1.42	1615
52H	1.42–1.44	1355–1409
52M	1.42	1114
54M	1.44	1114
N56	1.48	955
N58	1.50	876

100°C

Grade	B_r [T]	H_{cj} [kA/m]
35SH	1.07–1.08	820–882
38SH	1.11	820
40SH	1.14–1.18	805–833
42SH	1.17–1.20	763–926
45SH	1.21–1.23	750–945
48SH	1.25	633
48H	1.25	640
50H	1.27	630
50SH	1.29	761
52H	1.29–1.31	620–649
52M	1.29	500
54M	1.31	500
N56	1.34	420
N58	1.36	380

120°C

Grade	B_r [T]	H_{cj} [kA/m]
35SH	1.03–1.05	670–709
38SH	1.11	670
40SH	1.10–1.15	618–683
42SH	1.13–1.16	639–756
45SH	1.17–1.20	640–783
48SH	1.22	570
48H	1.21	510
50H	1.23	500
50SH	1.29	610
52H	1.25–1.28	490–508
52M	1.25	400
54M	1.27	400
N56	1.30	330
N58	1.32	330

140°C

Grade	B_r [T]	H_{cj} [kA/m]
35SH	0.99–1.00	540–548
38SH	1.03	540
40SH	1.06–1.10	487–553
42SH	1.00–1.11	470–606
45SH	1.13–1.16	476–641
48SH	1.18	394
48H	1.17	400
50H	1.19	390
50SH	1.215	478
52H	1.21–1.24	380–418
52M	1.21	320
54M	1.23	320
N56	1.26	270
N58	1.28	240

B

Additional Rotor Geometry Variations

Results of the rotor geometry variation simulations that were not presented in Chapter 6.

B.1 Magnet Separation

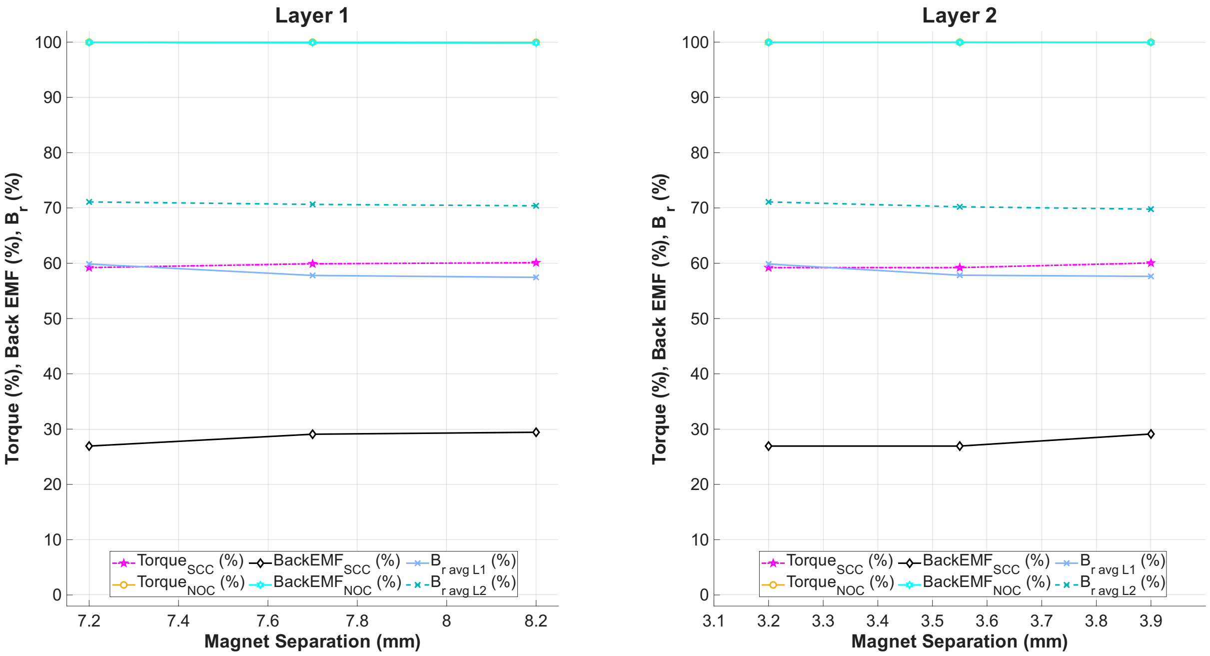

Figure B.1: Torque and Back EMF behaviour for short circuit and maximum normal operating conditions and percentage reduction of average B$_r$ with varying magnet separation in layers 1 and 2, at 140°C.

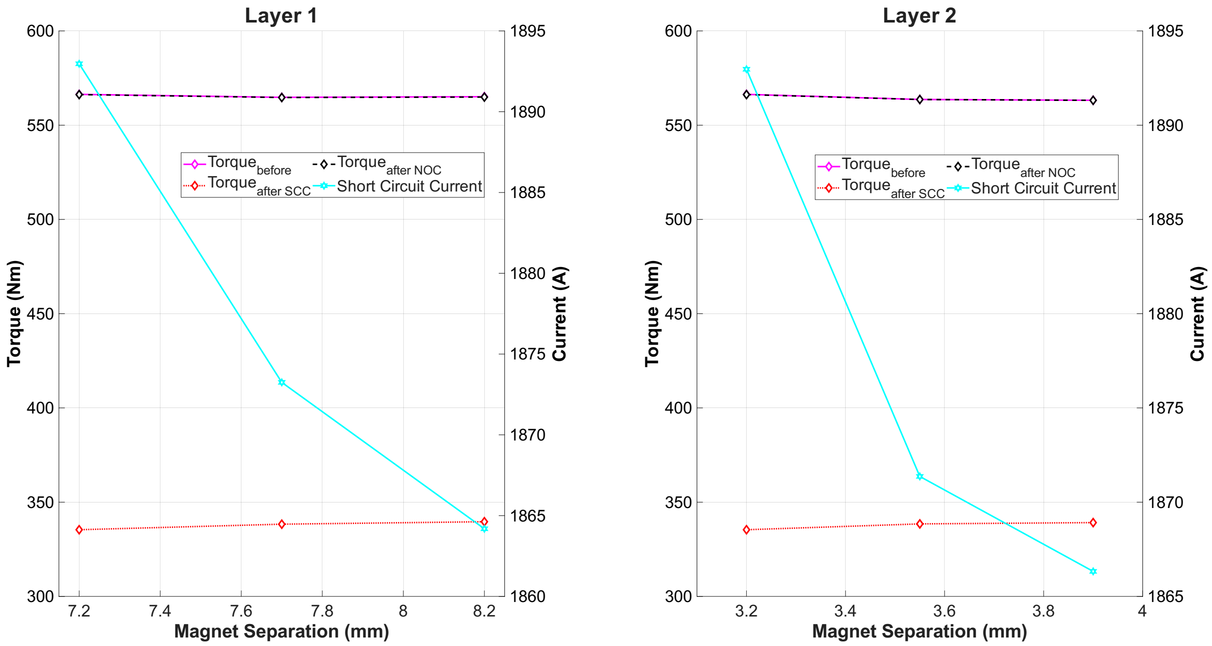

Figure B.2: Average torque before and after demagnetization due to short circuit and maximum normal operating conditions (left y-axis, diamond shaped markers) and short circuit current amplitude (right y-axis, hexagram markers) as functions of magnet separation in layers 1 and 2 at 140°C.

B.2 Magnet Post

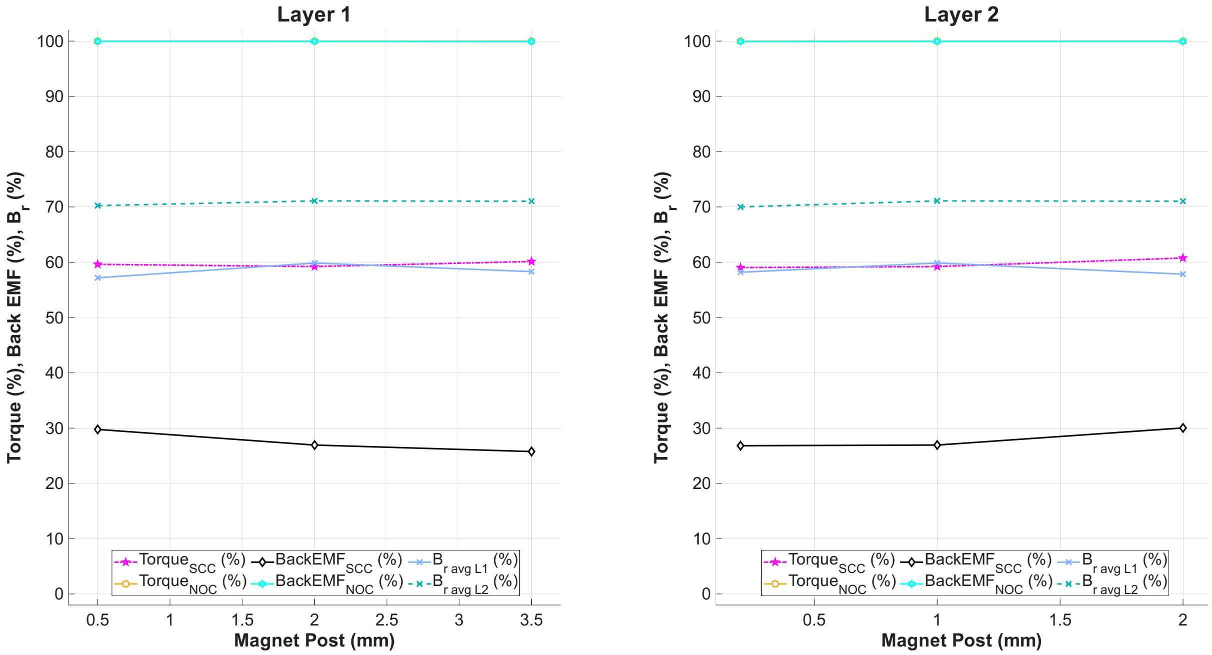

Figure B.3: Torque and Back EMF behaviour for short circuit and maximum normal operating conditions and percentage reduction of average B$_r$ with varying magnet post in layers 1 and 2, at 140°C.

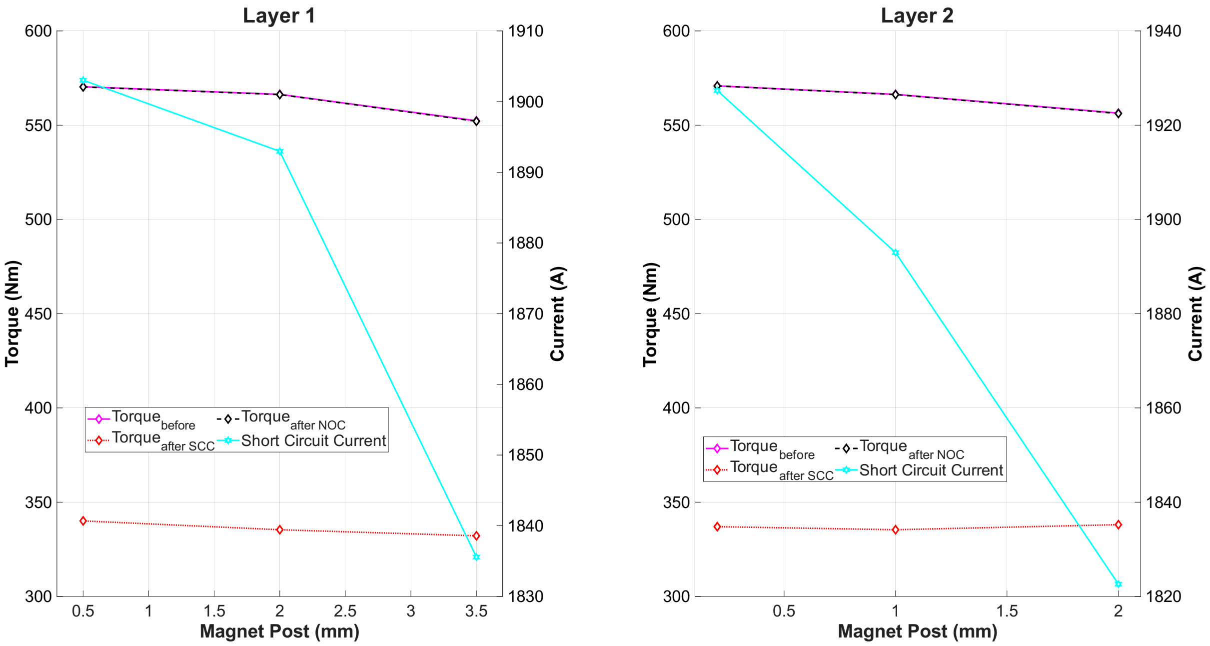

Figure B.4: Average torque before and after demagnetization due to short circuit and maximum normal operating conditions (left y-axis, diamond shaped markers) and short circuit current amplitude (right y-axis, hexagram markers) as functions of magnet post in layers 1 and 2 at 140°C.

B.3 Web Length

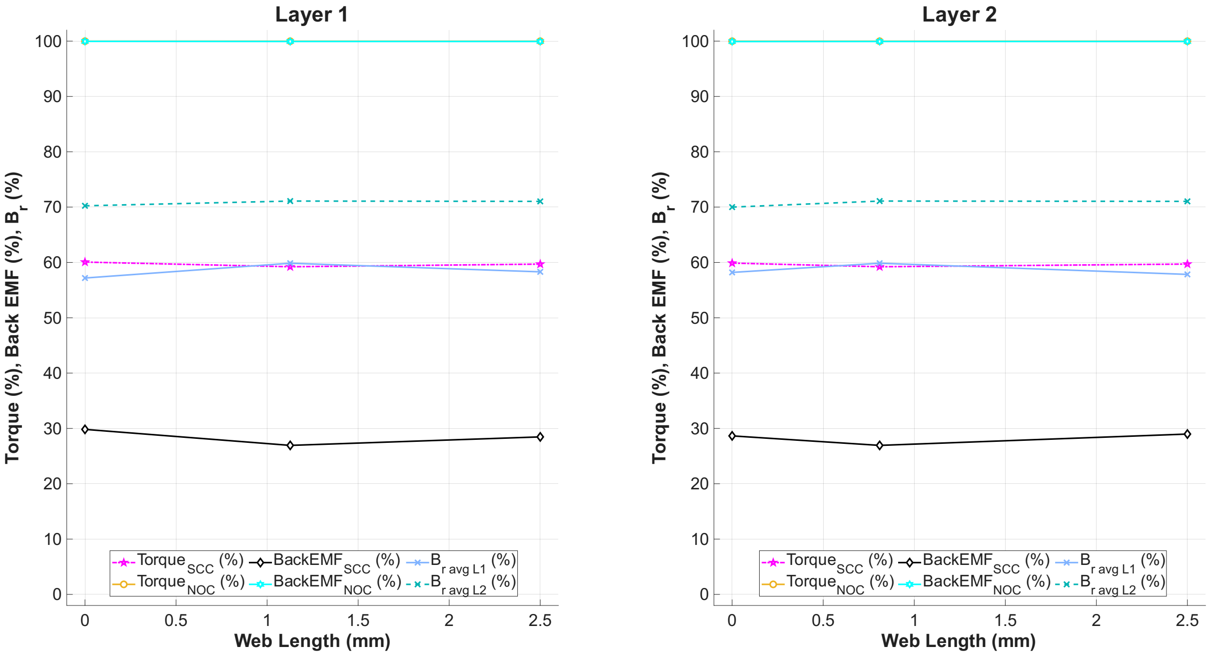

Figure B.5: Torque and Back EMF behaviour for short circuit and maximum normal operating conditions and percentage reduction of average B$_r$ with varying web length in layers 1 and 2, at 140°C.

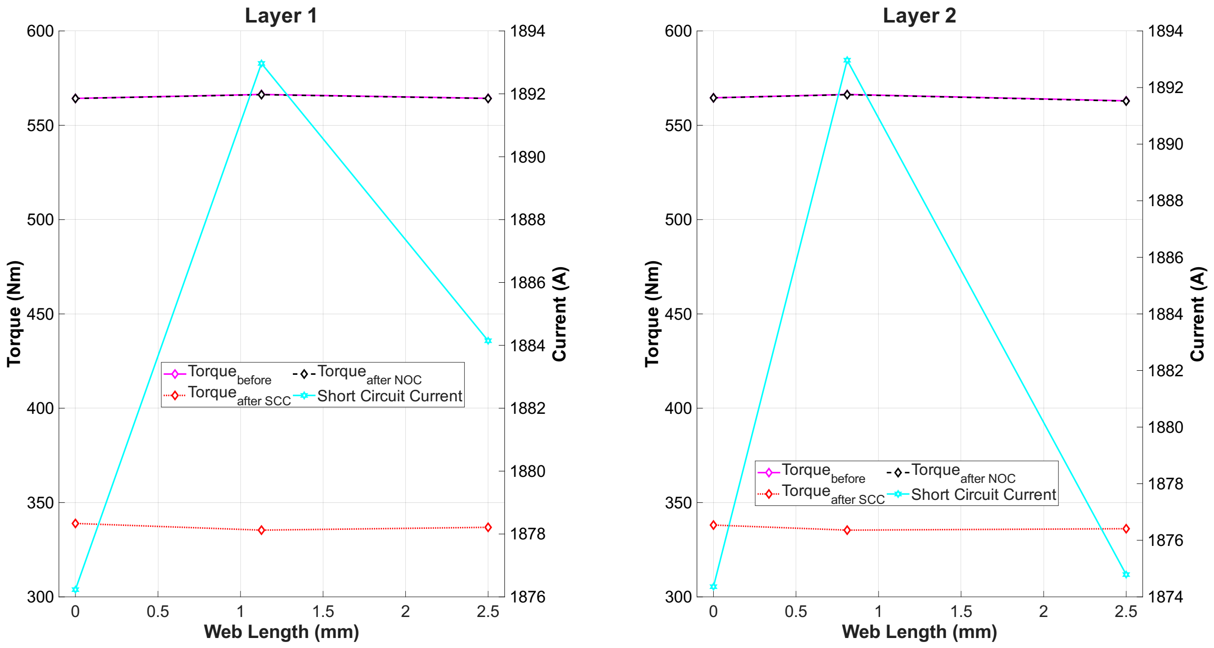

Figure B.6: Average torque before and after demagnetization due to short circuit and maximum normal operating conditions (left y-axis, diamond shaped markers) and short circuit current amplitude (right y-axis, hexagram markers) as functions of web length in layers 1 and 2 at 140°C.

B.4 Combined Rotor Geometry Models

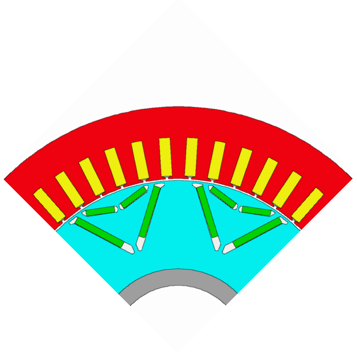

Figure B.7: Original

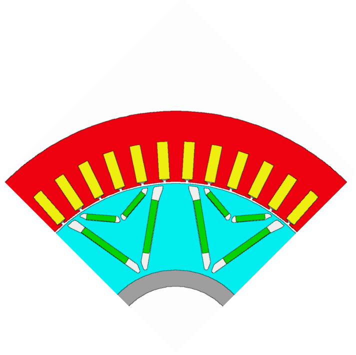

Figure B.8: Combination 1

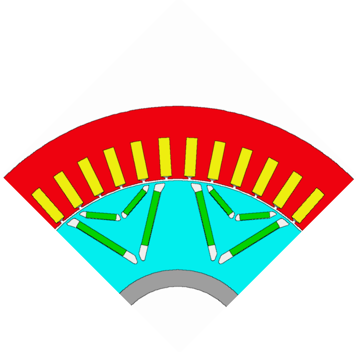

Figure B.9: Combination 2

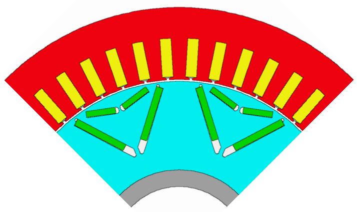

Figure B.10: Combination 3

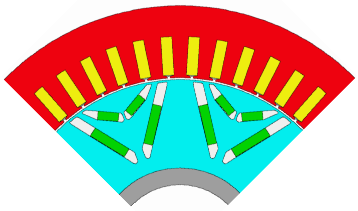

Figure B.11: Combination 4

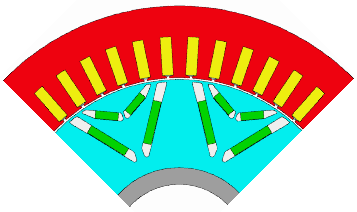

Figure B.12: Combination 5

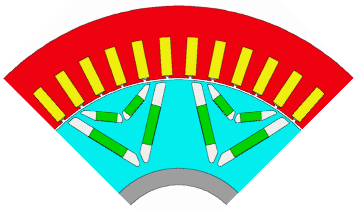

Figure B.13: Combination 6

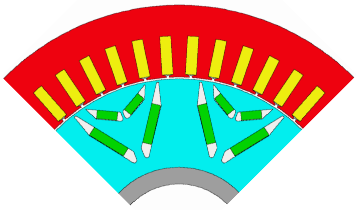

Figure B.14: Combination 7

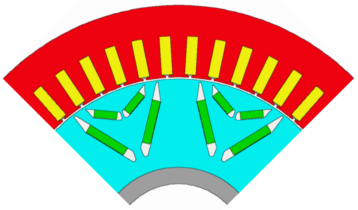

Figure B.15: Combination 8

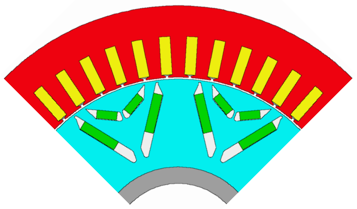

Figure B.16: Combination 9

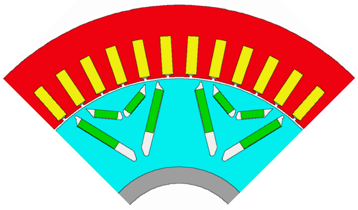

Figure B.17: Combination 10

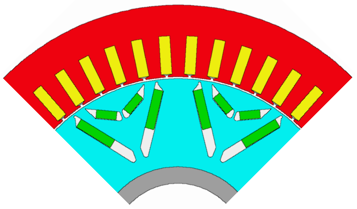

Figure B.18: Combination 11

C

Linear Correlation of Rotor Geometry

B.0.1 45SH Magnet

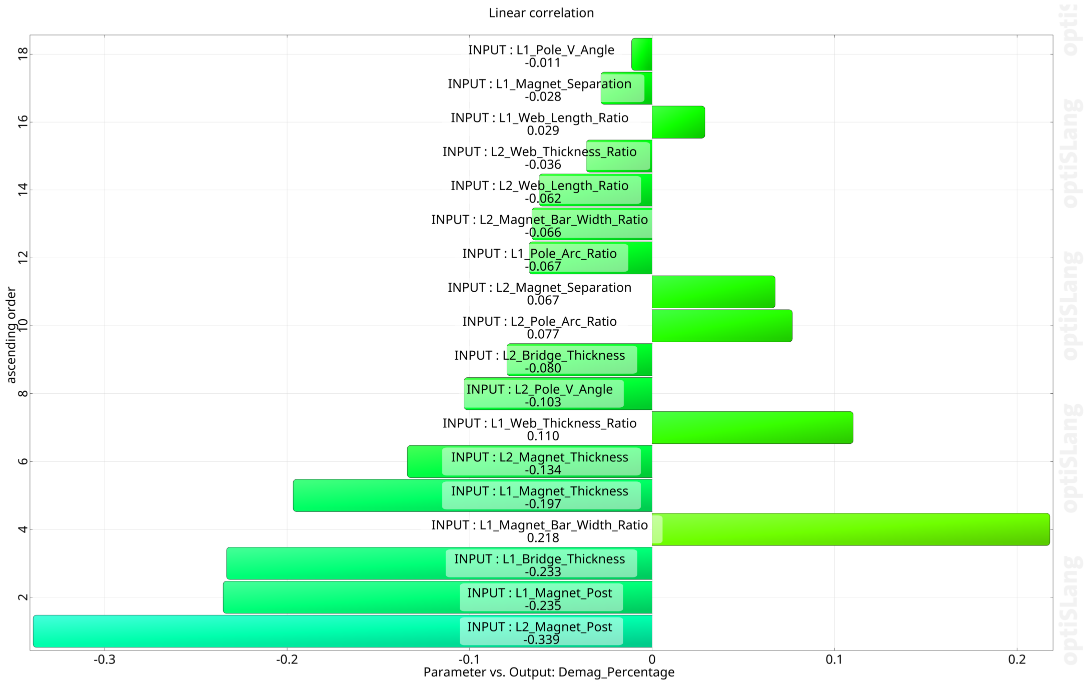

Figure C.1: Linear correlation coefficients between the input parameters and the demagnetization percentage for the 45SH magnet.

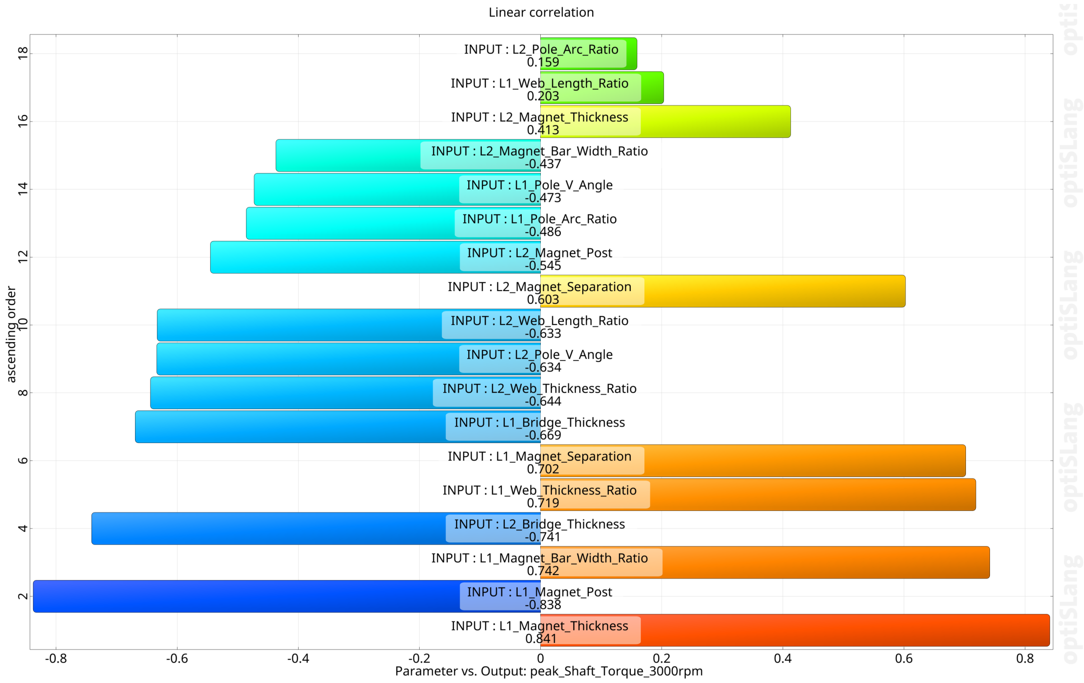

Figure C.2: Linear correlation coefficients between the input parameters and the peak shaft torque at 3000 rpm for the 45SH magnet.

B.0.2 42SH Magnet

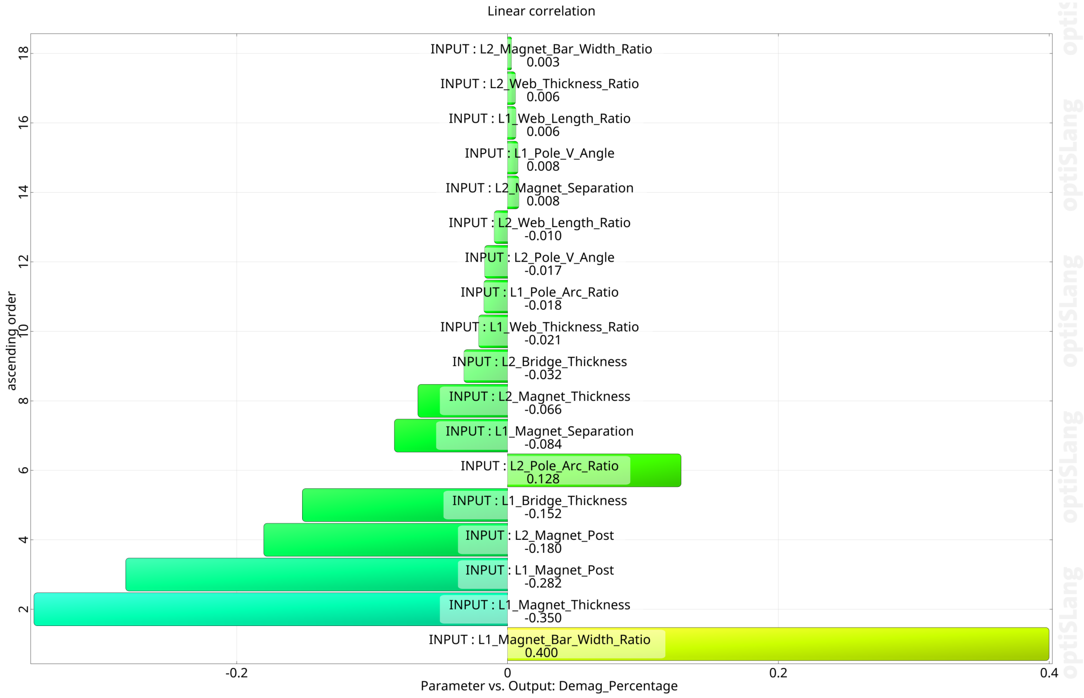

Figure C.3: Linear correlation coefficients between the input parameters and the demagnetization percentage for the 42SH magnet.

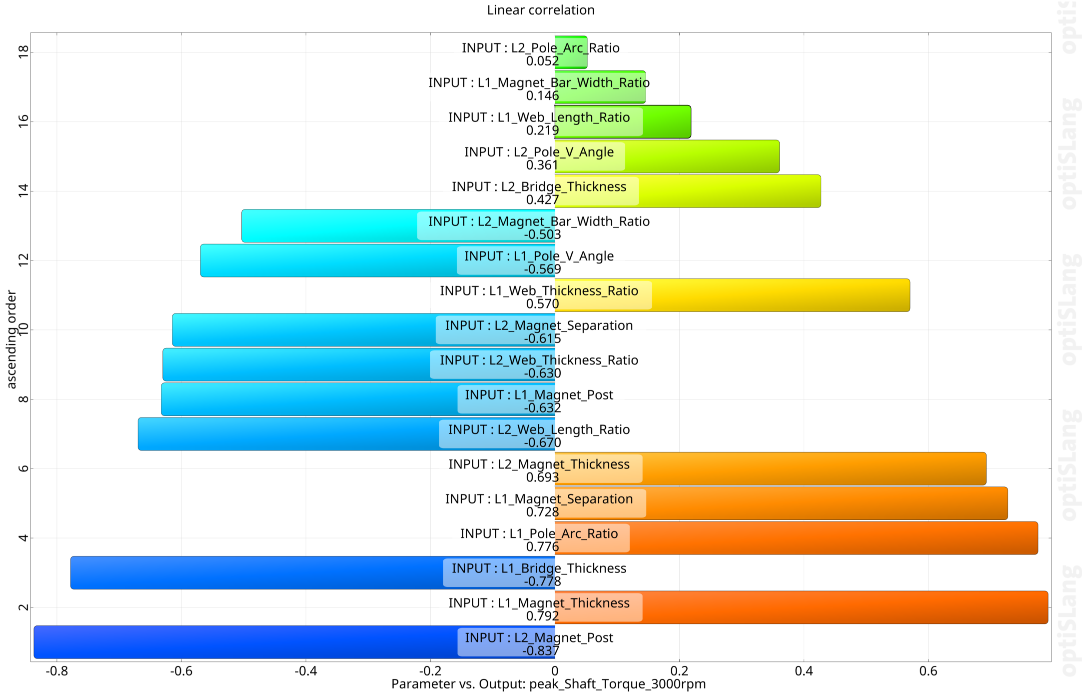

Figure C.4: Linear correlation coefficients between the input parameters and the peak shaft torque at 3000 rpm for the 42SH magnet.

B.0.3 Custom Magnet

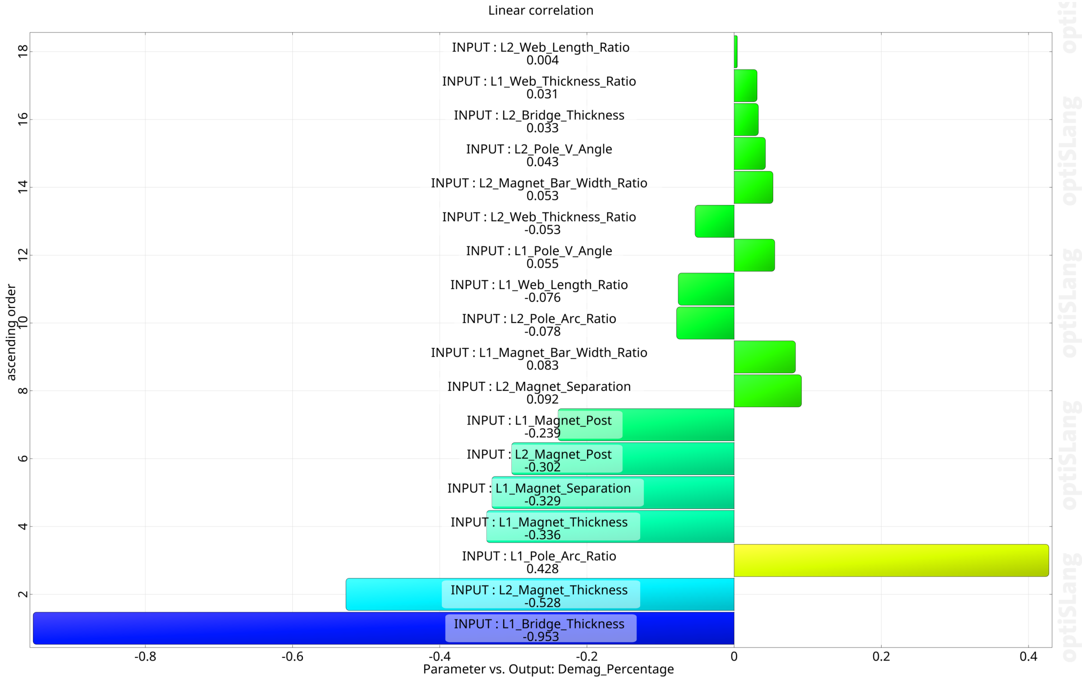

Figure C.5: Linear correlation coefficients between the input parameters and the demagnetization percentage for the custom magnet

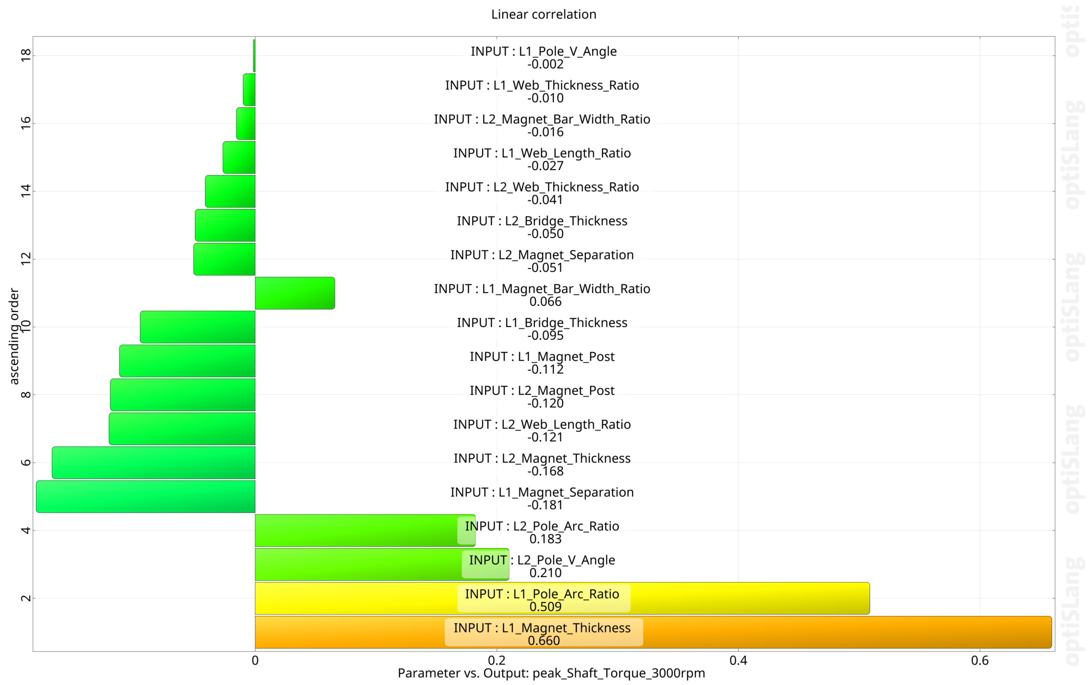

Figure C.6: Linear correlation coefficients between the input parameters and the peak shaft torque at 3000 rpm for the custom